Energy Efficient Wireless System Design

Dinuka Kudavithana

Submitted in total fulfilment of the requirements of the degree of

Doctor of Philosophy

Department of Electrical and Electronic Engineering
THE UNIVERSITY OF MELBOURNE

November 2015

Produced on archival quality paper.

Abstract

THE demand on telecommunication networks is increasing rapidly, and wireless access is a major contributor to this trend. On the other hand, wireless is considered to be the least energy efficient transmission medium mainly due to its unguided nature. The general focus of increasing the energy efficiency of wireless systems is on the reduction of their transmit power. However, this strategy may not save energy in short distance communication systems as the processing energy in hardware becomes more significant compared to the transmit radio energy. This thesis focuses on looking at the energy consumption of wireless systems by modeling the energy consumption as a function of several parameters such as receiver SNR, RF bandwidth, information rate, modulation scheme and code rate. We propose energy models for synchronization systems and other digital signal processing modules by considering the computational complexity of the algorithm and the required circuitry.

Initially we focus on the synchronization aspects of wireless receivers, and we study various algorithms for symbol timing recovery, carrier frequency recovery and carrier phase recovery. We compare the performance of these approaches in order to identify suitable algorithms to operate within various SNR regions. We then develop energy models of these synchronization sub-systems by analyzing the computational complexity of their circuitry based on their number of arithmetic, logic and memory operations. We define a new metric – energy consumption to achieve a given performance as a function of SNR – in order to compare the energy efficiency of different estimation algorithms.

Next, we investigate the energy-efficiency trade-offs of a point-to-point wireless system by developing energy models of both transmitters and receivers that include practical aspects such as error control coding, synchronization and channel equalization. In our system, a multipath Rayleigh-fading channel model and a low-density parity check (LDPC) coding scheme are chosen. We then develop a closed-form approximation for the total energy consumption as a function of receiver SNR and use it to find a minimum-energy transmission configuration. The results reveal that low SNR operation (i.e. low transmit power) is not always the most energy efficient strategy, especially in short distance communication. We present an optimal-SNR concept which can save a significant amount of energy mainly in short-range transmission systems.

We then focus on cooperative relay systems. We investigate the energy efficiency trade-offs of single–relay networks by developing a complete energy model of the systems for two relay strategies: amplify-and-forward (AF) and detect-and-forward (DF). We then optimize the location and power allocation of the relay to minimize the total energy consumption. The optimum location is found in two-dimensional space for constrained and unconstrained scenarios. We then optimize the total energy consumption over the spectral efficiency and derive expressions for the optimal spectral efficiency values. We use numerical simulations to verify our results.

Finally, we focus on energy efficiency of multi-hop systems by considering a two-relay cooperative system using a detect-and-forward (DF) protocol with full diversity. We propose a location-and-power-optimization approach for the relays to minimize the transmit radio energy. We then minimize the total system energy from a spectral efficiency perspective for two scenarios: throughput-constrained and bandwidth-constrained configurations. Our proposed approach reduces the transmit energy consumption compared to an equal-power allocated and equidistant-located relay system. Finally, we present an optimal transmission scheme as a function of distance by considering single-hop and multi-hop schemes. The overall results imply that more relays are required as the transmission distance increases in order to maintain a higher energy efficiency.

Declaration

This is to certify that

1. the thesis comprises only my original work towards the PhD,
2. due acknowledgement has been made in the text to all other material used,
3. the thesis is less than 100,000 words in length, exclusive of tables, maps, bibliographies and appendices.

Dinuka Kudavithana, November 2015

Acknowledgements

First of all, I would like to thank my supervisors Associate Professor Brian Krongold, Professor Jamie Evans and Dr. Qasim Chaudhari for their guidance and support. I thank them for sharing their expertise, and specially for making time in their busy schedules to provide advice with my research. I have endured a number of setbacks along this journey and they have never given up on me and always believed and encouraged me to reach my goals. This thesis would not have been possible without your support, and working under your supervision was a privilege.

I would like to thank the University of Melbourne, and Center for Energy-Efficient Telecommunications (CEET) laboratory, for providing great facilities, and a good work environment to conduct my research. I acknowledge the University of Melbourne, the State Government of Victoria and Alcatel-Lucent Bell Labs for providing financial support towards my studies. I would like to also thank The University of Moratuwa, Sri Lanka, the institution at which I did my undergraduate degree, for providing me a sound technical foundation to carry out post-graduate studies and research.

In addition to my supervisors, I would like to express my gratitude to my advisory committee chair Dr. Kerry Hinton for his feedback and suggestions during my PhD candidature. Special thanks should go to Dr. Bipin Pillai, Dr. Jack Li, Dr. Rob Ayre, Dr. Jeff Cheong, Dr. Saman Atapattu and Hamid Khodakarami for the insightful discussions we had over the last four years.

Throughout my PhD candidature, I have met number of amazing friends and made memories that I will treasure for the rest of my life. I would like to thank my friends at University of Melbourne - Chrispin, Fatemeh, Rajitha, Tharaka, Senaka, Hamid, Gitansh, Farzad, Xiaoxi, Jack, Chathurika, Chamil, Imali, Sandu, Meng, Sascha, Olivia, Tony, Marco and Ashrar. I wish them all the best for their future endeavors. I specially like to thank my best friends Chamath, Kashyapa and Chamara. I would also like to thank IEEE Student Branch members at University of Melbourne and IEEE Victorian Section, especially for being a part of my life.

My sincere thanks extend to my loving parents Shelton and Manel Kudavithana and my brother Hashan for their love, care and encouragement especially during the hard times and being there for me and shaping me to be who I am today.

I will be forever grateful to my noble friends for helping me in every possible way to achieve my goals.

To my family and my friends, for their love and support

Contents

List of Figures

List of Tables

Chapter 1

Introduction

THE telecommunication industry is an integral part of the world economy as it facilitates various services such as voice, video and the Internet, and connects the global market. Over the last few decades the capacity of telecommunication networks has expanded rapidly and is expected to rise further [8]. The growing popularity of cloud services and social media as well as future 5G (fifth generation)technologies will catalyze the rise of telecommunication system capacities. The advancement of the Internet-of-Things (IoT), with an expectancy of between 50 - 200 billion devices by 2020, will only increase these demands [9].

As the network capacity is expected to increase exponentially, the focus on the energy consumption of telecommunication systems has become prominent. Information and communication technology (ICT) is accountable for 2% to 4% of the global carbon footprint [10, 11]. This is an important fact not only from an environmental perspective, but also from the economic perspective of telecommunication service providers because energy costs contribute a significant portion of their operational costs [12, 13]. For instance, mobile operators' concerns about increasing energy bills were discussed in [13, 14].

The energy consumption of telecommunication systems has been analyzed by various researchers [10, 15–19]. Reports indicate that the majority of telecommunication networks' energy is spent by the access network [16, 18]. Among different types of access networks, wireless is identified as the least energy efficient transmission medium compared to guided media such as optical fiber. For example, wireless technologies such as the Universal Mobile Telecommunications System (UMTS) and WiMax consume more than 10 times the energy of passive optical networks (PON) and digital subscriber lines

(DSL), hybrid fiber coaxial (HFC) and point-to-point optical technologies [16]. Other studies have revealed that the energy consumption of a number of mobile operators was dominated by the radio access network which consumed 55–70% of total energy [20, 21].

The evolution of cellular communication standards such as long-term evolution (LTE), has also focused on achieving more capacity by using the limited available bandwidth of wireless channels. For instance, the LTE standard uses technologies such as orthogonal frequency-division multiple access (OFDMA) in the downlink to achieve high spectral efficiencies. However, the use of orthogonal frequency-division multiplexing (OFDM) as the carrier modulation results in a higher peak-to-average power ratio (PAPR), hence it provides low energy efficiencies [22].

The main reason for the low energy efficiency of wireless transmission is the spreading of radio energy around the area due to the transmission being unguided.

On the other hand, the energy efficiency of communication systems, especially in mobile communications, is growing at a slow pace in comparison with the dramatic expansion of the traffic requirement [23]. As energy consumption increases with network capacity, the efficiency of mobile systems needs to improve significantly in order to satisfy future capacity requirements and at the same time keeping network energy costs affordable.

In order to address this major gap, several organizations have been formed and a number of projects launched. One such project is Green Radio (2009-2012) which focused on a 100-fold reduction of energy in high data rate services [20]. The EARTH (Energy Aware Radio and Network Technologies) project was rolled-out in 2010 with the aim of reducing the energy usage of mobile cellular networks by a factor of two [24]. The recently concluded GreenTouch consortium focused on reducing energy consumption per bit by a factor of 1000 by 2015 and had a strong interest in wireless systems' energy reduction [25]. This thesis was initially motivated by projects driven by GreenTouch.

The most common approach to improving energy efficiency of wireless systems is to reduce the transmit power; however, this results in reducing the signal to noise ratio (SNR) at the receiver end; therefore, wireless systems need to be optimized to operate in the low SNR region. From an information theoretical perspective, according to Shannon's capacity theorem, capacity decreases when the SNR is reduced [26]. It also introduces errors due to high noise levels at detection. In order to combat the noise, powerful error-control coding schemes need to be introduced while more bandwidth is required to support the additional coding overheads [20,21].

Although the bandwidth expansion seems to be a difficult task to achieve in practical systems with regard to current demand, future wireless systems may allow additional bandwidth per user with the adaptation of smaller cells with high frequency reuse factors [27]. It is expected that future wireless communication standards proposed for 2020 and beyond will focus more on energy efficiency.

1.1 Problem Statement

Although low SNR operation is considered to increase energy efficiency in terms of the transmit power, several issues arise as a result and need to be addressed. One major challenge is the receiver design.

Wireless receivers perform many important functions such as carrier synchronization, symbol synchronization, channel estimation and equalization, noise and interference mitigation, error detection and correction and data demodulation. These functions can be categorized into two types, inner receiver and outer receiver. The inner receiver engages with carrier and symbol synchronization, and channel estimation and equalization. The outer receiver is responsible for the remaining functions such as noise and interference mitigation, error detection and correction, and data demodulation. Most of the modern wireless literature assumes perfect performance of the inner receiver functions, that is perfect synchronization in carrier frequency, carrier phase, sampling rate and symbol timing. These assumptions are quite accurate when the receivers operate in the high SNR region; however, in low SNR operation, the accuracy of these estimates may be poor and the assumption of perfect synchronization may not be valid. Moreover, the performance of synchronization as a function of SNR and the related complexities are interesting problems worth investigating. This provides insights into practical considerations of wireless systems within an energy efficiency framework.

As the transmission parameter configuration is changed according to the relevant SNR value, the complexity of signal processing operations also changes. The signal processing energy consists of the energy consumption of analog components such as mixers and digital signal processing components such as decoders. The lowest SNR operation, therefore, may not be the most energy efficient configuration because the circuit energy consumption is expected to rise at low SNR. The total energy consumption, which can be calculated by adding the transmit radio energy and signal processing energy of circuitry, can be expressed as a function of SNR. As SNR varies with different configurations of bandwidth and other system variables such as modulation and channel coding, the total energy can be expressed as a function of these parameters.

Therefore, it is important to develop a complete energy model for a simple wireless transmission systems such as a point-to-point link. The energy model should consider both analog and digital components of the wireless system and should reflect relationships with SNR, bandwidth, modulation scheme and code parameters. In terms of digital energy consumption, the energy consumption of error control codes, channel equalizers and synchronizers should be considered. Moreover, it is important to analyze the energy consumption of practical wireless systems such as multi-point systems and multi-user systems. The effects of the bandwidth and SNR allocation can be formulated into optimization problems and will provide deep insights into these systems from a practical implementation perspective.

1.2 Background

This section provides an overview of the literature pertaining to energy modeling and energy efficiency improvement approaches in wireless systems. Much of the research on energy efficient wireless has been undertaken since 2000. There was a significant boost in research in this area after 2010.

Hasan et al. discussed novel insights for green cellular systems after carrying out a detailed survey [28]. Power breakdowns of various parts of a cellular system and a base station were thoroughly analyzed before presenting green metrics to measure the energy efficiency. Hasan et al. discussed several energy saving approaches for base stations such as improving the power amplifier, zooming cells, and changing the network architectures. Adaptation of future technologies as well as changing network planning strategies were also investigated before presenting the potential energy savings that could be achieved by the proposed methodologies. Fundamental trade-offs for energy efficient wireless systems were analyzed using a framework of four metrics by Chen et al. [20]. Energy efficiency versus spectral efficiency trade-off and power versus bandwidth trade-off were considered with practical concerns such as circuit energy. Energy efficiency-deployment efficiency trade-off was discussed from an economic perspective whereas power-delay trade-off was analyzed from a system requirement perspective. Among many other related works, there have been several investigations into energy efficiency trade-offs in wireless systems [29–32].

Cui et al. studied the energy efficiency of wireless systems for two modulation types, quadrature amplitude modulation (QAM) and frequency-shift keying (FSK), by modeling the transmit energy and analog circuit components [33]. The authors referred to previous power models of analog components such as filters, digital-to-analog converters (DACs), analog-to-digital converters (ADCs) and mixers. The energy consumption was derived for both uncoded and trellis-coded transmission. The analog power models used by Cui et al. are comparatively old, and the failure to include digital circuit energy has resulted in the final energy consumption differing from realistic values for modern equipment. Finally, the energy consumption of each system was analyzed and minimized as a function of spectral efficiency using numerical calculations. More accurate power models for wireless transceiver front-ends were presented later by Li et al. by referring to different types of recent designs [34]. Here, power models for ADC, DAC, low noise amplifier (LNA), filters and power amplifiers were developed as functions of RF bandwidth, noise power, supply voltage, symbol rate, and carrier frequency.

On the other hand, digital circuit energy consumption was modeled and introduced by Desset et al. using energy-complexity conversion tables [35]. Desset et al. used complementary metal-oxide semiconductor (CMOS) based implementation to measure the average energy consumption for arithmetic operations such as real additions and real multiplications, memory operations such as ROM access and RAM writing/reading and logical operations. In the original work [35], the complexities of different error correction schemes including turbo codes, convolution codes and Reed-Muller codes and Reed-Solomon codes are modeled and converted to respective energy consumption values. The encoder and decoder energy costs are then compared with coding gains to evaluate the energy efficiency of channel coding schemes for applications with different requirements. Howard et al. used different power models to investigate the energy efficiency of error control schemes [36]. In this study, Howard et al. presented a pathloss dependent transmit radio energy model to compare with the circuit energy consumption. They referred to existing implementations of different encoders and decoders from Reed-Solomon, BCH, Viterbi and LDPC code families and used their power ratings and throughput values to calculate the absolute energy efficiency. However, these studies [35,36] did not focus on both the analog and digital circuit components and did not develop an energy model based on bandwidth, code rate and SNR.

Theory-based energy models for a decision feedback channel equalizer and message passing decoder were derived by Grover et al. [37]. Grover extended this work to derive lower bounds on the decoding power to illustrate the fundamental trade-off between transmit and decoding power [38]. The results were compared with Shannon's limit to show that the total power diverges to higher values as the error probability reaches zero due to the decoder energy consumption. Grover et al. investigated the lower power-bounds of coded communication further [39] and their work was influenced by complexity analysis of very-large-scale integration (VLSI) circuits [40]. The energy efficiency of decoders was further analyzed by Kienle et al. and Xiong et al. [41,42].

An end-to-end energy model for a long haul optical transmission system was developed by Pillai et al. with consideration of analog and digital processing components in an optical communication system [43]. The analog power models are derived using previous work and the digital processing energy was modeled using the computational complexity of circuit level implementations. This paper provides energy efficient solutions for optical system design based on link length and provides insights for wireless system energy modeling.

1.3 Focus of the Thesis

In this thesis, we aim to develop a better understanding of the energy consumption of wireless systems. We use energy consumption per information bit as the main metric to investigate the energy efficiency. We focus on total energy consumption by considering both transmit radio energy as well the signal processing circuit energy, which accounts for practical aspects such as synchronization and channel imperfections. We initially look at the synchronization capability at lower SNRs to support our main work that follows. We aim to understand the relation between the energy consumption of wireless systems by answering the following fundamental questions:

- How do the synchronization systems perform at low SNR? Which architectures are best suited for operation over all SNR values?

- How does the processing energy of the circuit impact the total energy consumption of the wireless systems? What is the relationship of SNR, bandwidth, modulation orders and code rates to the total energy consumption?

- What are the optimal configurations for wireless transmission systems for given user requirements?

As discussed in the literature review, a straightforward solution to low-energy wireless communication is to use a larger bandwidth and trade-off spectral efficiency for energy efficiency as outlined by Shannons information theory [44]. As a result of transmit power reduction, the received SNR is also decreased; however, lowering the receiver SNR may have an impact on inner receiver operations such as carrier synchronization, symbol synchronization, channel estimation and channel equalization. We first focus on the trade-off's of different synchronization systems as a function of SNR and propose a synchronization system architecture to be used in later chapters. We then develop energy models for synchronization systems and then compare the energy-performance trade-offs by defining a new metric.

Our main focus is modeling the total energy consumption of wireless systems. As discussed in the literature review, power models for analog components are used to obtain energy costs of wireless systems without considering digital signal processing energy. In contrast, different approaches are taken to model the digital energy consumption, especially for encoders and decoders; however, to the best of our knowledge a complete energy model has not been presented in the literature. Throughout this thesis, we use analytical expressions and optimization techniques when possible. We use prediction and curve fitting approaches to evaluate the energy consumption of wireless systems when the analytical expressions are not derivable.

We initially investigate and optimize the energy consumption of a basic point-to-point wireless link and then extend our models to more advanced wireless systems such as relay networks. In relay systems, we consider resource allocation for the relays to optimize energy efficiency.

We use an all-digital approach for our receiver [45,46]. In today's practical receivers, most of the signal processing functions are implemented in the digital domain, by moving the analog-to-digital converter to the front end of the receiver. This approach enables the receiver designers to use powerful digital processing techniques for carrier synchronization, timing synchronization, channel estimation and equalization processes.

Throughout this thesis, we focus on single-carrier transmission as multi-carrier systems such as OFDM suffer from high peak-to-average power ratio (PAPR) which reduces their energy efficiency; however, we exploit the advantages of frequency domain processing tools using single-carrier frequency domain equalizers [47]. We focus on different channels; frequency selective fading (Chapter 4) and frequency flat channels (Chapter 5 and 6). We assume randomly generated channel coefficients following a Rayleigh distribution [48]. We also look at the synchronization of signals, we especially choose the most appropriate algorithms for the operating criteria. In Chapter 4 we use low-density parity check (LDPC) error control coding schemes to obtain coding gains in point-to-point transmission.

1.4 Contributions and Outline of Thesis

In the following section, we give an outline of the thesis and state the contributions of the thesis.

Chapter 2 investigates the performance of synchronization systems in low SNR regions in order to facilitate the low SNR operation of wireless receivers. We review the literature and identify appropriate carrier synchronization and timing synchronization algorithms and observe their performance as a function of SNR and other related parameters. We conclude this chapter by presenting a synchronization system architecture designed for low SNR operation.

Chapter 3 analyzes the energy consumption of the synchronization systems discussed in Chapter 2. We develop energy consumption models for different algorithms and segments of synchronization systems including carrier frequency estimators, carrier phase estimators and timing estimators. We initially analyze the computational complexity of each algorithm and component using their implementation block diagrams with consideration to arithmetic, memory and logical operations. Then we use energy tables to convert the complexity into energy consumption. We then define a new metric to compare the performance and energy consumption of frequency, phase and timing estimators as a function of SNR.

In Chapter 4, we analyze the energy consumption of practical point-to-point wireless systems. We use previously developed synchronization energy models in Chapter 3 and available power models of analog functions. In addition, we develop energy models for other components such as frequency domain equalizers. The transmit energy is modeled as a function of distance, pathloss exponent, received SNR and noise spectral density. The circuit energy is modeled as a function of bandwidth, modulation order and data rate. We use a numerical evaluation to investigate the energy consumption as a function of the above parameters and then derive conclusions for energy efficient transmission.

We then focus on more advanced wireless systems such as single-relay and multi-relay networks. Chapter 5 analyzes the energy consumption of cooperative single relay systems considering two relaying protocols: amplify-and-forward (AF) and detect-and-forward (DF). We obtain an expression for the transmit energy which is a convex function of relay location and power allocation. We present optimal solutions for power allocations and relay location for constrained and unconstrained scenarios. We then, optimize the energy consumption as a function of modulation order and distance. We verify the accuracy of our analytical expressions using numerical evaluations.

After optimizing single relay systems, we focus on multi-relay systems with consideration of a dual–relay system in Chapter 6. We assume that the relays and destination utilize full diversity by combining signals using a maximal ratio combiner. As we concluded in Chapter 5, DF relays are more energy efficient, therefore, in the multi-relay system we use DF relays. We derive an expression for the transmit energy as a function of relay location and power allocation. We develop a complete energy model by calculating the circuit energy consumption of this system; however, due to the complexity of the expressions, analysis of the energy consumption is not possible; therefore, we use numerical simulations to investigate energy consumption. Next, we present the optimal relay locations and power allocations as a function of pathloss of the environment, bit error rate and spectral efficiency. Finally, we compare the energy consumption of dual–relay systems with direct transmission and single–relay systems as a function of source-destination distance. Chapter 7 concludes the thesis.

1.5 List of Publications

Journal Papers

1. D.U. Kudavithana, Q. Chaudhari, B. S. Krongold and J. S. Evans, "Energy Consumption Modeling and Optimization of Cooperative Relay Transmission," *In preparation for submission to IEEE Transactions on Vehicular Technology*, 2016.

2. D.U. Kudavithana, Q. Chaudhari and B. S. Krongold, "Energy Consumption Modeling of a Point-to-Point Wireless Transmission System," *Submitted to Physical Communication (Elsevier) Journal*, Aug. 2015.

Conference Papers

1. D.U. Kudavithana, Q. Chaudhari, B. S. Krongold and J. S. Evans, ″On the Energy Efficiency of Coherent Communication in Multipath Fading Channels,″ in *Proc. IEEE Global Telecommunications Conference* (GLOBECOM2014 - 2nd Workshop on Green Broadband access: energy efficient wireless and wired network solutions), Austin, TX, USA, Dec. 2014.
2. D.U. Kudavithana, Q. Chaudhari, B. S. Krongold and J. S. Evans, ″Energy Modeling and Optimization of Cooperative Dual-Relay Systems,″ *Submitted to IEEE Global Telecommunications Conference (GLOBECOM2016).*

Poster Presentations

1. D.U. Kudavithana, B. S. Krongold and J. S. Evans, ″Energy Efficiency Comparison of Coherent QPSK and Differential QPSK,″ *IEEE Australian Communication Theory Workshop*(AusCTW 2013), Sydney, Australia, Feb. 2014.

Other Presentations

1. ″Energy modeling of synchronization algorithms for wireless receivers,″ in *GreenTouch members meeting*, Shanghai, China, May 2013.
2. ″Synchronization of low SNR wireless receivers,″ in *GreenTouch members meeting*, Dallas, USA, June 2012.

Chapter 2

Synchronization of Wireless Systems

This chapter discusses about synchronization subsystems of wireless receivers. The symbol timing recovery, carrier frequency recovery and carrier phase recovery algorithms are investigated and compared in order to identify the suitable algorithms to operate at different SNR regions, especially at low SNR. We propose a synchronization system architecture for low SNR operation and choose appropriate algorithms after a careful performance and limitation investigation.

2.1 Introduction

IN wireless communication, the dynamic nature of wireless channels results in multipath fading and Doppler frequency shifts [48]. In addition, the non-ideal operations of hardware such as oscillator phase noise and frequency mismatch, amplifier nonlinearities and non-ideal filtering also contribute towards a distorted signal at the receiver. Finally, the noise generated in hardware components also corrupts the received signal. In order to overcome such effects, several functions are performed at the receiver; synchronization, channel estimation and equalization, and error correction and detection [49]. A channel equalizer overcomes the multi-path fading effects after explicitly or implicitly estimating the channel. In order to overcome noise and other distortions, error detection and correction schemes are used. Synchronization removes the carrier frequency and phase offsets and also samples the signal at optimal SNR instants where eye opening of matched filter output is at its maximum.

Synchronization of a wireless system can be categorized into several segments:

- Symbol rate synchronization - The symbol rate may not be exactly equivalent to an integer multiple of the receiver sampling rate. Therefore, it is important to make sure that the receiver generates exactly the same symbol rate as the transmitter.

- Symbol timing synchronization - This segment is responsible to sample the received signal at positions where the SNR is highest (i.e. maximum opening of the eye-diagram). Naturally a receiver cannot predict the optimum position beforehand. Therefore, this segment is placed after the matched filter to correct the sampling error and to fix the symbol phase error.

- Carrier frequency synchronization - The carrier frequency of the received signal and the frequency of the receiver oscillator may be different due to various reasons such as frequency drifts in the oscillator and Doppler effects occurred during the transmission. The carrier frequency recovery unit is used to correct the frequency mismatches at the receiver front end.

- Carrier phase synchronization - Coherent detection is performed based on the instantaneous phase of the signal constellation diagram. However, the received symbols may contain phase errors due to delays in the channel as well as due to the phase ambiguities in the hardware filters. This segment is responsible for fixing the phase offsets in the received signal prior to signal detection.

A scatter plot of a perfectly synchronized 4-QAM modulated signal with a SNR of 20 dB is shown in Figure 2.1. All the symbols are centered around the four original constellations points $\left\{\left(\frac{-1}{\sqrt{2}}, \frac{-1}{\sqrt{2}}\right), \left(\frac{-1}{\sqrt{2}}, \frac{1}{\sqrt{2}}\right), \left(\frac{1}{\sqrt{2}}, \frac{1}{\sqrt{2}}\right), \left(\frac{1}{\sqrt{2}}, \frac{-1}{\sqrt{2}}\right)\right\}$. The noise in the AWGN channel results in spreading the constellation around the original four points.

Symbol rate errors change the sampling point of the received signal with time and hence the required output rate gets changed. As the timing recovery unit uses interpolation to correct sampling errors, symbol rate mismatches can be corrected using that. Usually the oscillator errors are quite small compared to carrier frequency errors, and therefore they can be corrected without using a separate unit [49].

When the received signal is not sampled at the optimum point, it creates additional noise due to timing jitters. Figure 2.2 shows a 4-QAM modulated signal of a SNR of 20 dB with a normalized timing offset of 0.25. The timing offsets result in moving the signal

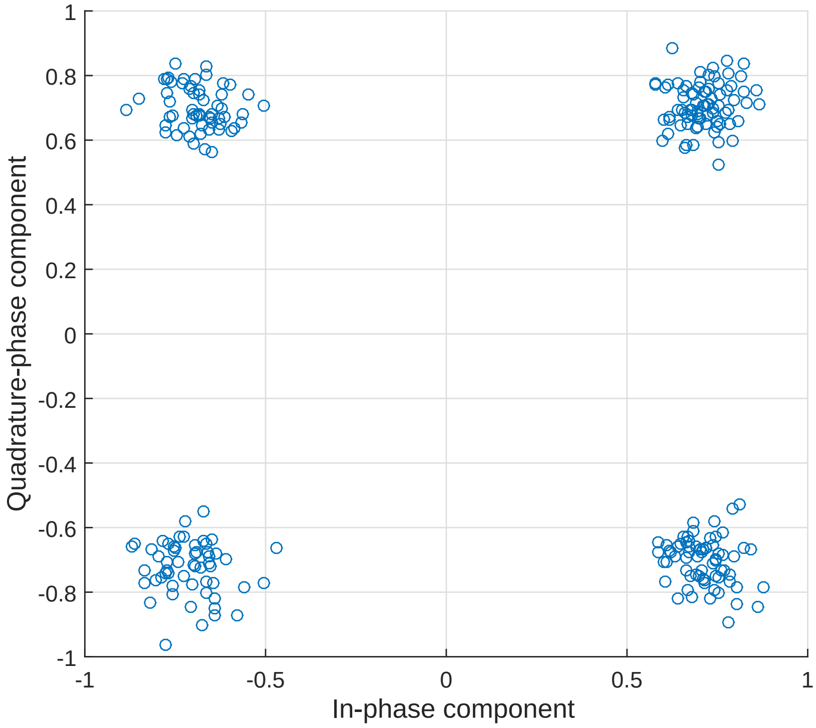

Figure 2.1: Scatter diagram of 4-QAM signal with perfect timing, frequency and phase recovered signal.

samples around the original constellation points. At lower SNR operations, this distorts the signal detection process.

The received signal frequency changes from that of the transmitted signal mainly due to Doppler effect which occur during the transmission and due to oscillator frequency mismatches. This results in a frequency offset and it changes the phases of the received symbols at a constant rate. Hence the received symbol constellation rotates as shown in Figure 2.3. Therefore, it is important to estimate the frequency offset and then de-rotate each of the received symbols to cancel out the frequency errors.

Finally, towards the end of synchronization process, phase recovery unit is used to overcome the phase offsets. Phase offsets occur due to the channel phase shifts as well as the phase changes occur due to hardware components such as filters. Phase offsets rotate the signal constellation of an entire block by a fixed angle. Figure 2.4 illustrates a signal

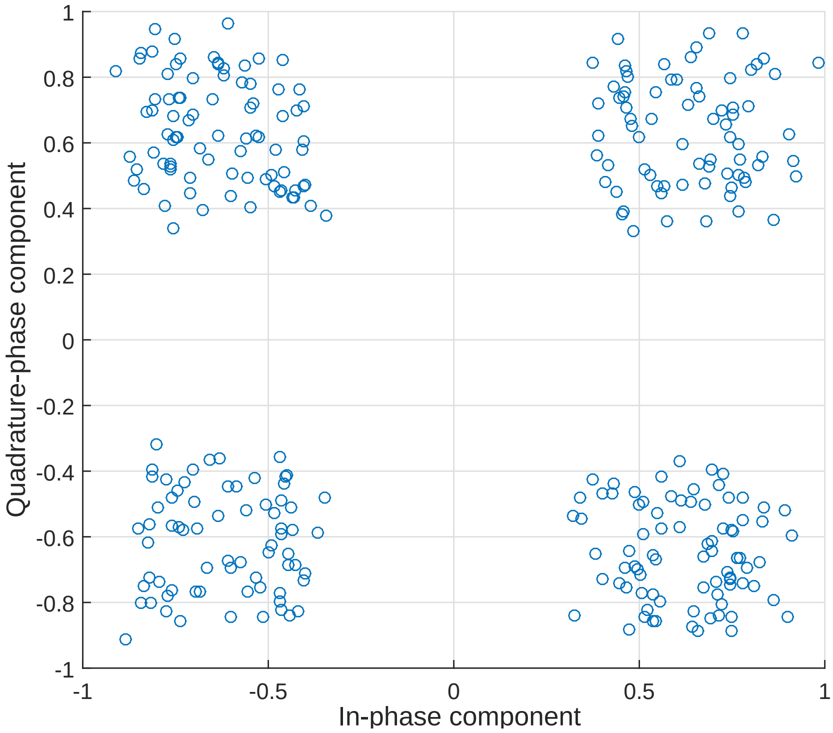

Figure 2.2: Scatter diagram of 4-QAM signal with a normalized timing offset of 0.25 (SNR = 20 dB).

constellation of 4-QAM signal with a phase offset of 20 degrees.

Wireless receiver synchronization systems can be designed according to different topologies [49–51]. Depending on the requirement, the strategies of synchronization are changed. The initial parameters are estimated at the beginning of the transmission and it is known as acquisition. Acquisition stage uses specific approaches that usually use training symbols to estimate the initial parameters within a short period of time. After initial acquisition, data transmission starts with small carrier frequency, phase and timing variations still remaining. So, tracking algorithms which track the minor variations of synchronization parameters are used to achieve this goal. Generally these algorithms have less complexity compared to the acquisition algorithms.

In early days of communications, most transmission systems used feedback based synchronizers which operate using phase locked loops (PLL). However, PLLs suffer from hang-up phenomenon which results in a prolonged dwell time when large phase errors occur [52]. Nowadays, burst mode transmission has become more popular with high

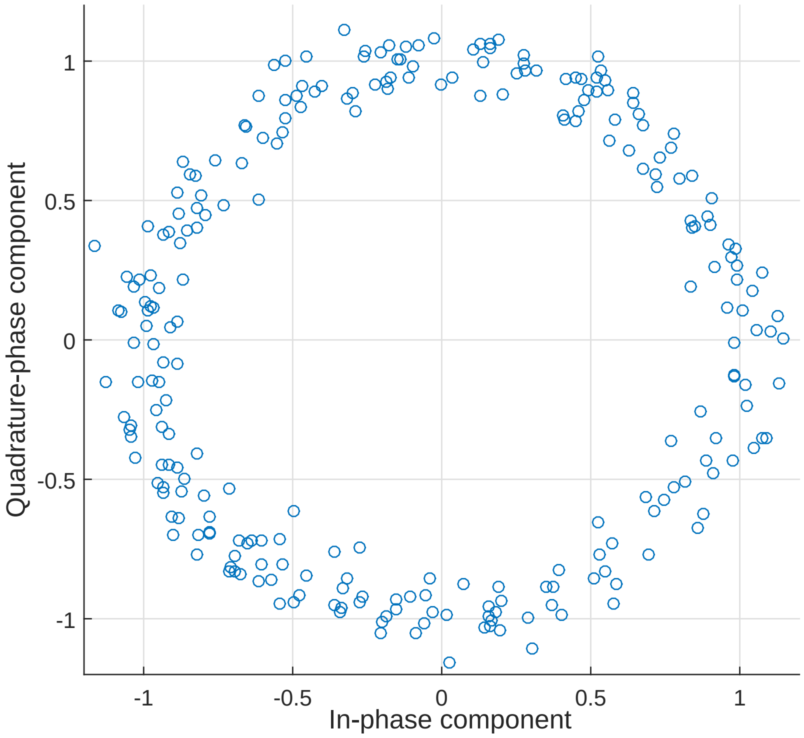

Figure 2.3: Scatter diagram of 4-QAM signal with a normalized frequency offset of 0.01 (SNR = 20 dB).

speed data communication such as LTE and WiFi. These systems need rapid carrier and clock acquisition using short bursts of data. Therefore, feed-forward techniques are proposed to achieve this objective. Feed-forward techniques can be used to acquire and track the parameters using preambles and data respectively.

Synchronization algorithms can be categorized again based on the type of information used in estimation: data-aided (preamble), decision directed or non-data-aided [51]. In data-aided operation, the received preamble is fully known at the synchronizer and hence accurate estimates can be formed. Decision-directed and non-data-aided mode operations are used without any training. In decision-directed mode, the output of symbol detector is used to estimate the synchronization parameters. In non-data-aided mode, mathematical approaches are used to overcome the effect of modulation schemes, for instance, modulation of a QPSK modulated signal is removed by obtaining the fourth power so that all the modulated symbols would end up in the same phase angle.

Apart from the parameter synchronization, the receiver has additional tasks to per-

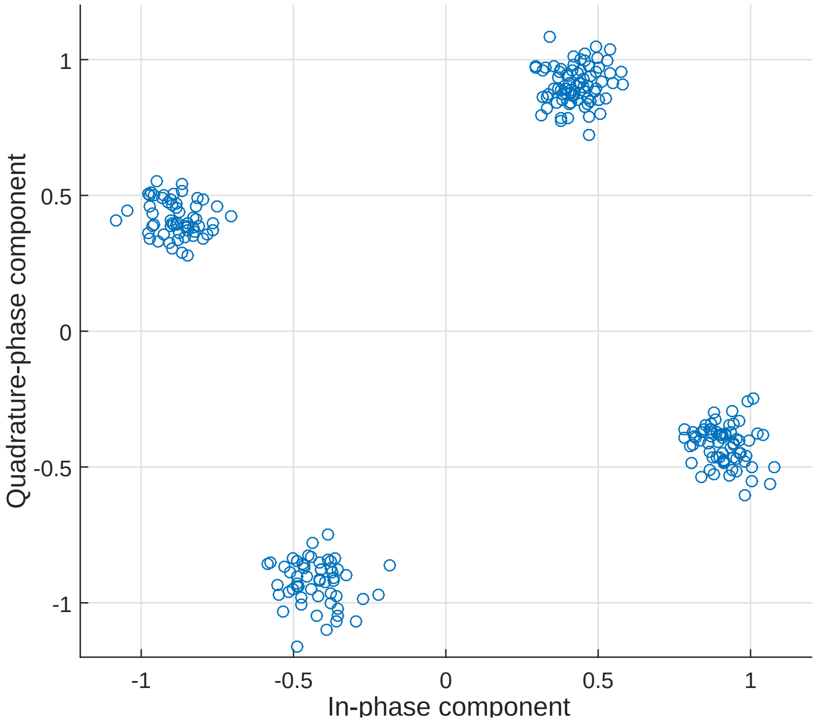

Figure 2.4: Scatter diagram of 4-QAM signal with a normalized phase offset of 20^0 (SNR = 20 dB).

form such as frame detection [49, 53]. However, we will not focus on frame synchronization aspects in this thesis.

The rest of the chapter is organized as follows. Section 2.2 describes the system model we used in the rest of this chapter and establishes basic notations and variables. Section 2.3 discusses the performance of timing synchronization algorithms at low SNR regions. Section 2.4 discusses the performance of carrier frequency synchronization at low SNR. The performance of carrier phase recovery systems are discussed in Section 2.5. Section 2.6 concludes the chapter by summarizing the proposed synchronization algorithms for low SNR operations.

2.2 System model

Throughout this chapter, we consider a single-carrier transmission with a single antenna system assuming a Gaussian channel model. Quadrature amplitude modulation (QAM) is considered in our system as it provides a higher spectral efficiency than other modulation schemes. The received signal at the antenna undergoes regular analog signal processing such as band filtering, amplification (by a low noise amplifier), gain controlling and down conversion to baseband before entering the matched filter. We assume that the frequency of the down converter is different from the received signal frequency and this frequency difference is defined as the carrier frequency offset. We define the output of matched filter as

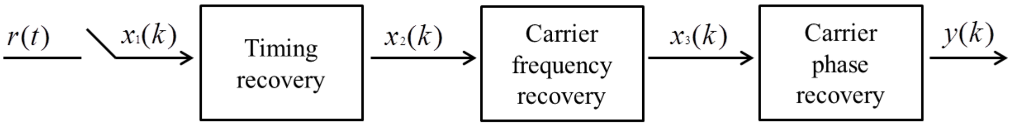

Figure 2.5: Receiver block diagram of the synchronization system.

$$r(t) = e^{j(2\pi f_d t+\theta)} \sum_k c_k g(t - kT_s - \tau) + w(t) \ , \tag{2.1}$$

where the variables are denoted as follows:

- f_d is the carrier frequency offset
- θ is the carrier phase offset
- τ is the time delay from the optimum sampling point
- T_s is the symbol time
- T is the sampling time
- c_k is unit amplitude transmitted information symbol at kth instance
- $g(t)$ is raised cosine Nyquist pulse
- $w(t)$ is the complex Gaussian noise with power spectral density of N_0.

The signal is sampled at $t = iT + \hat{\tau}$ where the time delay estimate is defined as $\hat{\tau}$. The samples are sent to timing recovery unit are given as

$$x_1(iT + \hat{\tau}) = \sum_k c_k e^{j(2\pi f_d (iT+\hat{\tau})+\theta)} g(iT + \hat{\tau} - \tau) + w(iT + \hat{\tau}) \tag{2.2}$$

The oversampling rate N is defined as $N = \frac{T_s}{T}$. A block diagram of our synchronization system is presented in Figure 2.5. The output of the timing synchronizer $x_1(i)$ has only one sample per symbol and is fed into the frequency recovery system. Its output $x_2(i)$ is then sent to the carrier phase synchronizer. SNR is defined as the symbol energy to noise spectral density at the receiver.

2.3 Symbol timing recovery

The timing recovery system estimates the timing error and corrects the sampling instance to maximize the SNR of the signal. The optimum sampling point minimizes the inter-symbol-interference (ISI). Some symbol timing estimators can perform independently of the carrier frequency offset, provided that this offset is small. On the other hand, carrier recovery systems perform quite poor in the presence of timing errors. Therefore, in our proposed system, timing synchronization is carried out prior to carrier synchronization.

Wireless receivers use different architectures to recover the timing errors, namely, synchronous sampling and non-synchronous sampling [51]. Synchronous sampling systems use previous signal samples to decide the current sampling instance in real-time. Non-synchronous sampling systems sample the signal at fixed rates and send the samples into the timing recovery circuit to overcome the timing errors. Timing recovery circuits use a timing error detector (TED), a loop filter, an interpolation controller and an interpolator. Non-synchronous sampling as more frequently used as it allows to carry out more operations in the digital domain using powerful signal processing concepts.

According to our system model in Figure 2.5, the timing error $\tau_e = \hat{\tau} - \tau$ needs to be eliminated and the signal should be sampled at optimum points to generate a perfectly sampled signal. In addition to that, the timing recovery unit possesses timing rate correction capability. Unlike carrier frequency offsets, timing frequency offsets are small in practice, hence it is not needed to correct the timing rate errors separately. It can be recovered using a timing recovery loop or timing phase un-wrapper [49]. As described in the introduction, there are two main timing recovery approaches available; feedback recovery and feed-forward recovery.

2.3.1 Feedback based timing recovery systems

Feedback based timing recovery systems have the distinct advantage of correcting sampling rates. A block diagram of a non-synchronous feedback based timing recovery loop is given in Figure 2.6. The received signal $r(t)$ is first sampled using a free running oscillator with an oversampling factor of N. Since the sampling may not be perfect, the samples produced at this point may not align with the symbol boundaries (at maximum opening of the eye diagram). Next, the samples are sent through a digital matched filter followed by an interpolator which generates optimum sampling points according to the timing error estimates.

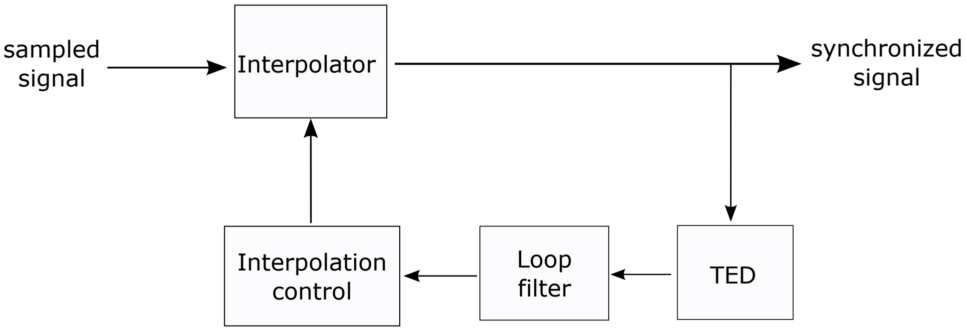

Figure 2.6: Feedback based timing recovery loop.

Different types of interpolators proposed in literature [45, 51]. Piecewise polynomial interpolator is quite common and performs with high accuracy. Polynomial order can be selected as linear (1), parabolic (2) or cubic (3). The performance of these interpolators increase with the order at the cost of complexity. Another type of interpolation technique, polyphase filter bank interpolation [54], utilizes several different banks of interpolators with different in-built timing offsets which produce different timing corrections. Most suitable filter should be selected after calculating and selecting the smallest timing errors from all the interpolator banks. As this technique needs more hardware resources in practical implementation, it consumes higher complexity and energy compared to the piecewise polynomial interpolators.

The output of the interpolator is taken and timing error is calculated by TED. The timing error is fed to a loop filter. Usually 2nd order loop is utilized with proportional and integrator paths. Interpolator controller is used to provide timing indices and fractional offsets to the interpolator. Modulo 1 counter based control and recursive interpolation control are two popular approaches used in practical systems [45,55].

Next, we discuss about some popular TED algorithms used in communication systems.

Maximum Likelihood Timing Error Detector (MLTED)

The theoretical optimal timing error detector is given by maximum likelihood based TED which uses the slope of the matched filtered signal to calculate the timing error [45,51]. A noise free signal gives a zero slope at the optimum sampling position of the matched filter output. MLTED uses this phenomenon to track the timing error. When it is operated in data-aided mode, MLTED uses the knowledge of preamble symbols to remove the modulation. In decision-directed mode, the preambles are replaced by the output of detector. However, digital implementation of the derivative matched filter has a higher complexity. MLTED estimation for a QPSK modulated signal is given by [45],

$$e(k) = a_0(k)\dot{x}(kT_s + \hat{\tau}) + a_1(k)\dot{y}(kT_s + \hat{\tau}) \ , \tag{2.3}$$

where $a_0(k)$ and $a_1(k)$ represent in-phase and quadrature-phase components of the symbols. Then $x(t)$ and $y(t)$ are in-phase and quadrature-phase components of the received signal at time t. Therefore, $\dot{x}(kT_s + \hat{\tau})$ and $\dot{y}(kT_s + \hat{\tau})$ represent the slope of in-phase and quadrature-phase signals sampled at $t = kT_s + \hat{\tau}$. The above equation is defined for the data aided mode and when operating in the decision directed mode, the decisions $\hat{a}_0$ and $\hat{a}_1$ are used instead of a_0 and a_1.

Early-Late Timing Error Detector (ELTED)

Early-Late TED uses time differences between samples to approximate the derivatives of the pulse given in (2.3) [56]. ELTED can operate at different oversampling rates, but commonly use two samples per symbol. Both MLTED and ELTED suffer from self noise, which results in a non-zero derivative at the perfect sampling point when consecutive transmit symbols are same. ELTED algorithm for a QPSK modulated signal with oversample rate of two is defined as [56] follows:

$$\begin{aligned} e(k) &= a_0(k)[x((k+1/2)T_s+\hat{\tau})-x((k-1/2)T_s+\hat{\tau})] \\ &\quad +a_1(k)[y((k+1/2)T_s+\hat{\tau})-y((k-1/2)T_s+\hat{\tau})] \end{aligned} \tag{2.4}$$

Zero-Crossing Timing Error Detector (ZCTED)

Zero-Crossing TED operates based on the concept of finding the points where the signal crosses zero in the eye diagram. It is defined for an oversampling rate of two. ZCTED has a lower self noise compared to the MLTED and ELTED. ZCTED algorithm for a QPSK modulated signal is mathematically represented as [51],

$$\begin{aligned} e(k) &= x((k-1/2)T_s+\hat{\tau})[a_0(k-1)-a_0(k)] \\ &\quad +y((k-1/2)T_s+\hat{\tau})[a_1(k-1)-a_1(k)] \end{aligned} \tag{2.5}$$

Gardner Timing Error Detector (GTED)

Gardner introduced a pure non-data aided TED by replacing the data symbols in ZCTED with signal samples [57]. This also operates at an oversampling rate of two. Unlike the previously discussed TEDs, GTED is capable of estimating the timing errors independent of the carrier phase, hence, GTED is suitable for timing recovery prior to carrier recovery in coherent communication systems. GTED algorithm for a QPSK modulated signal is given by [57] as

$$\begin{aligned} e(k) &= x((k-1/2)T_s+\hat{\tau})[x((k-1)T_s+\hat{\tau})-x(kT_s+\hat{\tau})] \\ &\quad +y((k-1/2)T_s+\hat{\tau})[y((k-1)T_s+\hat{\tau})-y(kT_s+\hat{\tau})] \end{aligned} \tag{2.6}$$

Mueller & Muller Timing Error Detector (MMTED)

Mueller et al. presented MMTED which operates at one sample per symbol [58]. The low sampling rate is important to reduce the ADC's sampling rate. MMTED has a lower self noise compared to above TEDs. MMTED is defined as follows for a QPSK signal [45]:

$$\begin{aligned} e(k) &= a_0(k-1)x(kT_s+\hat{\tau}) - a_0(k)x((k-1)T_s+\hat{\tau}) \\ &\quad +a_1(k-1)y(kT_s+\hat{\tau}) - a_1(k)y((k-1)T_s+\hat{\tau}) \end{aligned} \tag{2.7}$$

Among the above algorithms ZCTED, GTED and MMTED perform better than ELTED in high noise environments [51]. ZCTED and GTED perform better when the pulse bandwidth is increased while the performance of MMTED degrades with the pulse bandwidth [51].

2.3.2 Feed-forward based timing recovery systems

Feedback based recovery systems take longer to acquire the lock, and hence, a higher number of samples are needed for an initial estimate. Feedback systems may also acquire false locks which could result in hang-up phenomenon. Therefore, for application which require fast acquisition, feed-forward based recovery schemes are proposed to estimate timing errors within a short period of time using a determined number of symbols. As in feedback schemes, ML based approaches have been followed to derive practical estimators.

The MSE variance of feed-forward timing estimators is lower bounded by modified Cramer-Rao bound (MCRB) [51]. It is defined for a QPSK signal as follows:

$$MCRB(\hat{\tau}) = \frac{1}{8\pi^2 L\xi E_s/N_0T_s^2}\ , \tag{2.8}$$

where, L is the number of symbols used in the estimator, ξ is the normalized mean square bandwidth of pulse shaping filter and E_s/N_0 is the ratio of symbol energy to noise spectral density.

Oerder & Meyr (SLN) estimator

Oerder et al. proposed a non-data aided feed-forward timing estimator which operates at an oversampling rate of four [1]. This estimator is also known as square-law non-linear

(SLN) estimator because it takes the second power of the amplitude.

The received signal is first sent through a low pass filter or a matched filter. The filtered output samples $x(kT_s)$ are then squared, and each sample is multiplied by $e^{-j2\pi k/N}$ where k is the sample number. The multiplied outputs are then added together, and next the phase angle of the complex signal is measured to obtain the timing estimate. A normalizing factor of $-\frac{T_s}{2\pi}$ is used to calculate the final estimate. This estimator is unbiased and its performance increases with wide pulse bandwidth.

SLN estimator can be mathematically defined as [1],

$$\hat{\tau} = -\frac{T_s}{2\pi} \arg \left\{ \sum_{k=0}^{4L-1} |x(kT)|^2 e^{-j\pi k/2} \right\} \tag{2.9}$$

LOGN and AVN based estimators

Morelli et al. presented improvements for the SLN estimator and proposed three new estimators [59]. The logarithmic nonlinearity estimator (LOGN) is derived based on ML estimation. The other estimators are named as absolute value nonlinearity (AVN) estimator and fourth-law nonlinearity (FLN) estimator [7]. The fourth-law nonlinearity (FLN) estimator performs quite poorly compared to the other estimators [59].

LOGN estimator is defined as [59],

$$\hat{\tau} = -\frac{T_s}{2\pi} \arg \left\{ \sum_{k=0}^{4L-1} f[x(kT)] e^{-j\pi k/2} \right\} , \tag{2.10}$$

where, $f(z) = \ln[1 + |z|^2(\frac{E_s}{N_0})^2]$.

AVN estimator is defined as [59],

$$\hat{\tau} = -\frac{T_s}{2\pi} \arg \left\{ \sum_{k=0}^{4L-1} |x(kT)| e^{-j\pi k/2} \right\} \tag{2.11}$$

The LOGN and AVN estimators perform better than SLN estimator when a low bandwidth pulse is used.

Zhu estimator

Zhu et al. presented a timing error estimator which uses two samples per symbol [2]. This estimator exploits both the in-phase and quadrature-phase components of the received signal and multiplies the complex modulated signal with half symbol rate exponential. Low pass filters with a cutoff frequency of $\alpha/2T_s$ are used prior to squaring and averaging operations. Zhu et al. propose to use Kalman filters to improve the performance of this estimator [2].

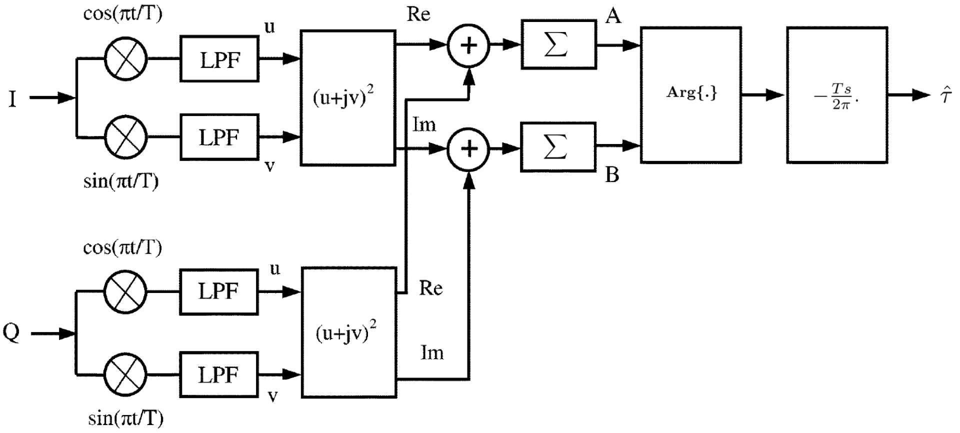

Figure 2.7: Block diagram of Zhu timing estimation algorithm.

Zhu estimator is defined as [2],

$$\hat{\tau} = -\frac{T_s}{2\pi} \arg \left\{ \sum_{k=0}^{2L-1} y_I^2(kT) + y_Q^2(kT) \right\} , \tag{2.12}$$

where, the signals at various points of the estimator are shown in Figure 2.7 and $y_I(t) = u_I(t) + v_I(t)$ and $y_Q(t) = u_Q(t) + v_Q(t)$.

Lee estimator

Lee introduced a non-data aided feed-forward symbol timing estimator which also uses a lesser sampling rate compared to the previous estimators - two samples per symbol [60]. It contains a lower computational complexity compared to Zhu estimator because of the avoidance of low pass filters.

Lee estimator is defined as [60],

$$\hat{\tau} = -\frac{T_s}{2\pi} \arg \left\{ \sum_{k=1}^{2L} |x(kT)|^2 e^{-jk\pi} + Re[x(kT)x^*((k-1)T)]e^{-j(k-0.5)\pi} \right\} \tag{2.13}$$

2.3.3 Performance investigation of timing estimators

In this section, the performance of SLN, AVN, LOGN and Lee estimators are investigated using computer simulations and compare with MCRB. The performance of the above mentioned estimators depends on the pulse bandwidth, SNR and block size. We used Nyquist pulse shaping filter with two values of excess bandwidth 0.35 and 0.75. Block lengths of 32 and 128 are considered. The initial timing errors were uniformly distributed as $\tau = (-0.5, -0.4, ...0.4, 0.5)$.

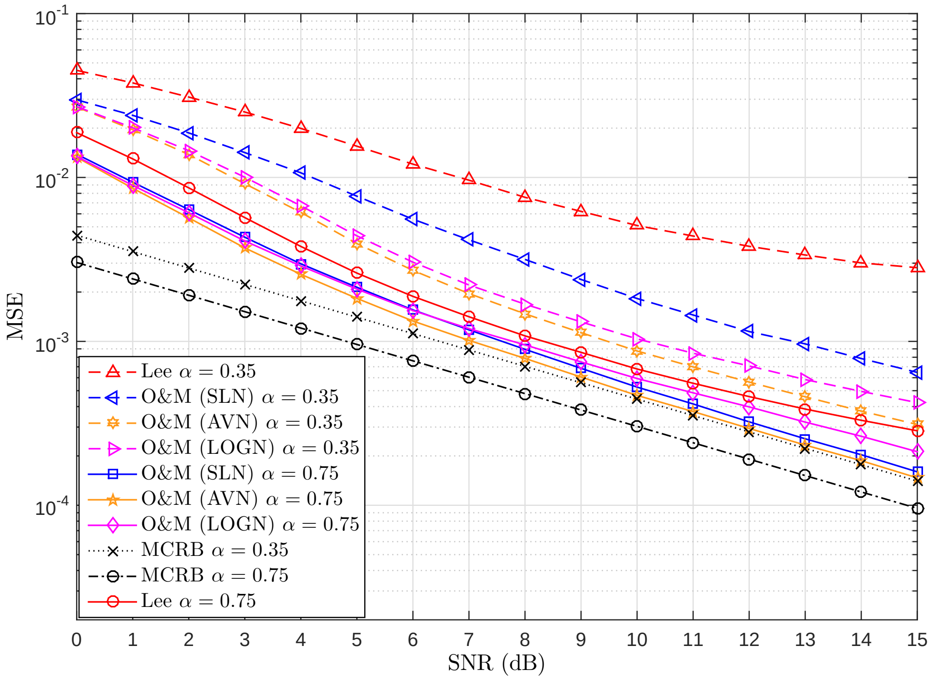

Figure 2.8: Performance comparison of timing estimators ($L = 32$).

Figure 2.8 shows MSE performances of feed-forward timing estimators for two pulse bandwidths when the block size is 32. It can be observed that the two-sample based Lee

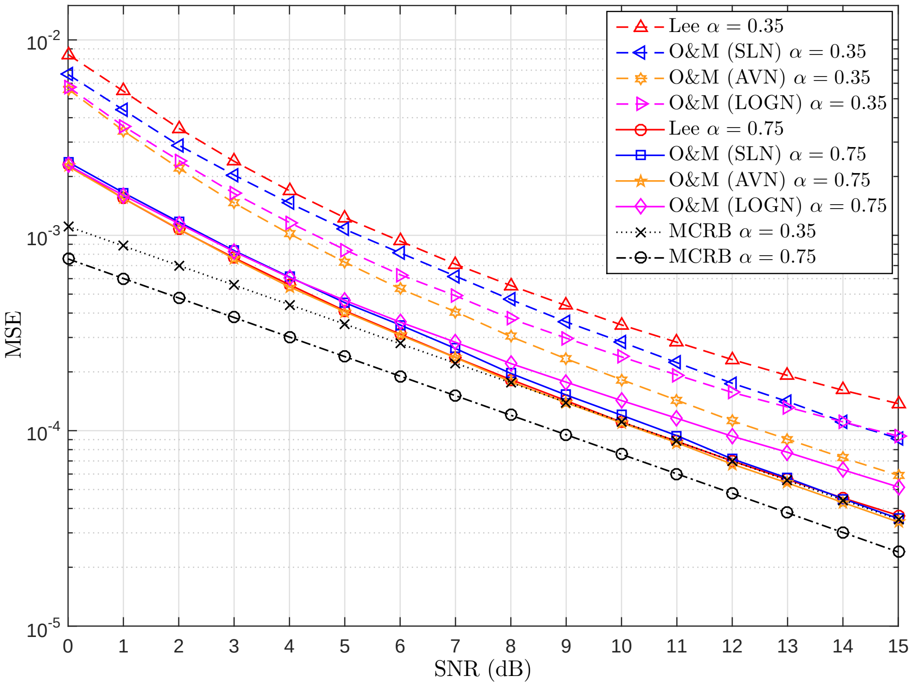

Figure 2.9: Performance comparison of timing estimators ($L = 128$).

estimator performs quite poorly when low pulse bandwidth ($\alpha = 0.35$) is used. SLN estimator also performs poorly with low bandwidth, but performs better than the Lee estimator. AVN and LOGN estimators perform close to each other when $\alpha = 0.35$. But when α is increased to 0.75, AVN and LOGN estimators perform closer to MCRB at high SNR region. It can be observed that AVN estimator records lower MSE for both pulse bandwidths within the considered SNR region.

However, the performance of each estimator improves when the block size is increased to 128 as illustrated in Figure 2.9. It shows that the performance gains between the estimators also reduce when L is increased from 32 to 128. All four estimators behave similarly at low SNR when $\alpha = 0.75$. The performance of Lee estimator increases compared to $L = 32$ when the α is increased. Based on the above two figures, it can be concluded that AVN estimator is the best estimator for low SNR operation. SLN is suitable for high pulse bandwidths and LOGN for low pulse bandwidths.

We investigated the bit-error rate (BER) performance after timing recovery and presented in Figure 2.10. AVN estimator is used as the timing estimator and block length of

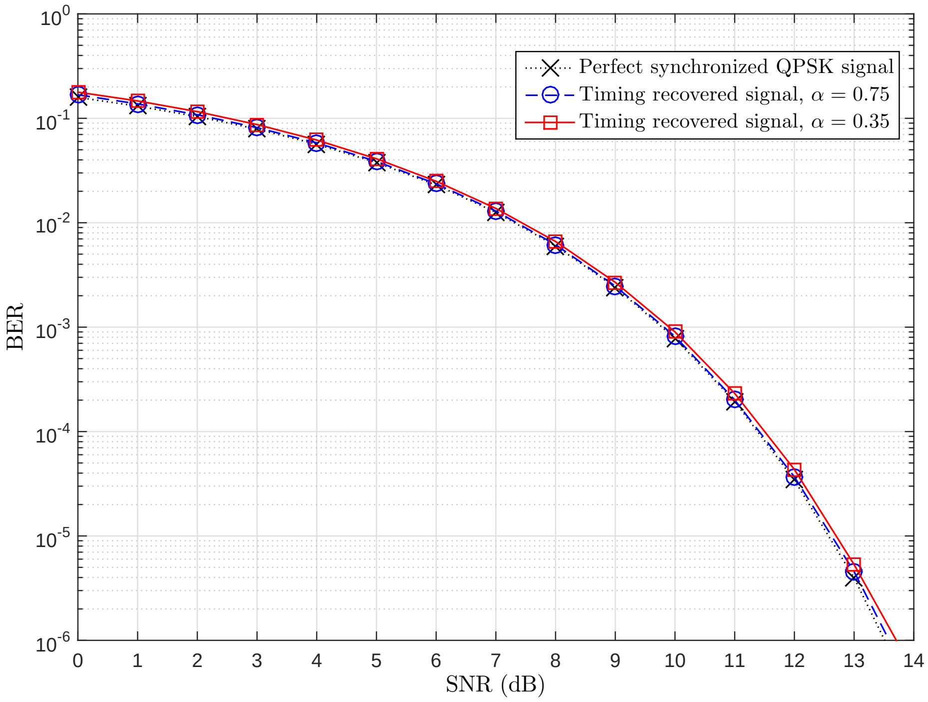

Figure 2.10: BER performance after timing recovery ($L = 32$).

32 is used. It can be observed that the BER curve of the timing recovered signal is quite close to the perfect BER curve when α is 0.75. When α is reduced to 0.35, the system performance degrades. The performance gap between the timing recovered signal and perfect signal at SNR of 3 dB is about 0.1 dB with $\alpha = 0.75$ and 0.3 dB with $\alpha = 0.35$. The performance gap reduces to about 0.03 dB with $\alpha = 0.75$ and 0.1 dB with $\alpha = 0.35$ at 14 dB.

The BER performance loss due to timing error is approximated [61] as follows,

$$\Delta \cong \frac{10}{\ln(10)} \left[A + 2B \frac{E_s}{N_0} \right] \mathrm{Var}(\hat{\tau}) \text{ (in dB)} , \tag{2.14}$$

where A and B constants are calculated according to the pulse shaping filter parameters.

The performance of these timing estimators is investigated at the presence of carrier frequency offsets. Figure 2.11 shows the MSE of AVN estimator when the normalized carrier frequency offset is 0.01 and 0.1 (1% and 10%). The performance degradation due to a frequency offset of 0.01 is very small while a frequency offset of 0.1 degrades the performance considerably. The performance degradation due to frequency offsets increases when the pulse bandwidth is reduced. Based on the observations it can be concluded that timing recovery systems perform accurately in the presence of small carrier frequency errors (less than 0.1) and the AVN estimator is suitable to be used as the timing estimator when operate at low SNR.

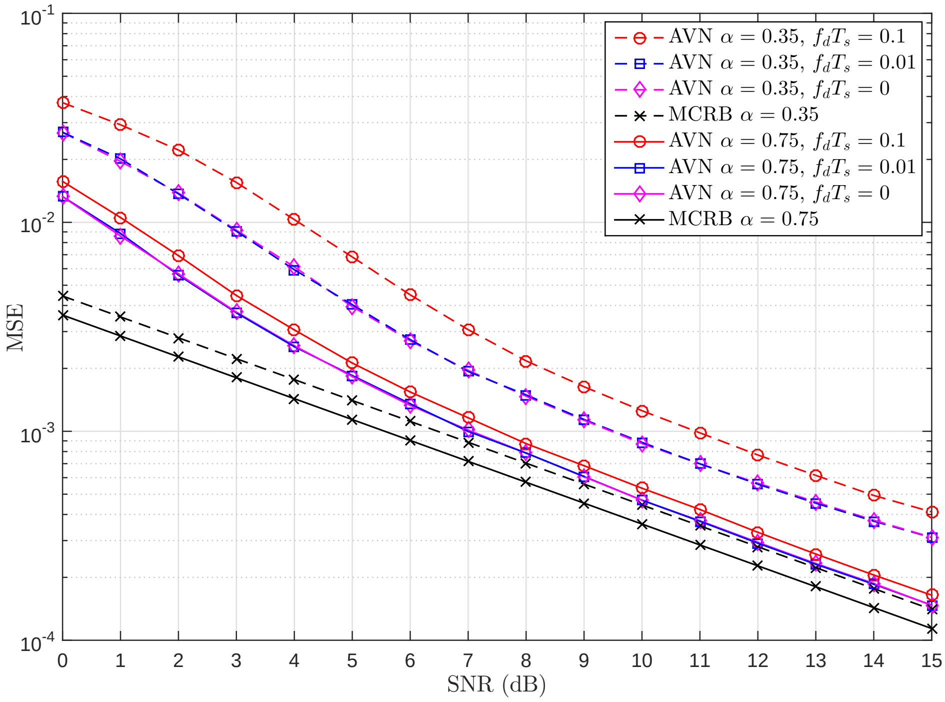

Figure 2.11: MSE performance of LOGN and AVN timing estimators at the presence of carrier frequency offsets ($L = 32$).

2.4 Carrier Frequency Recovery

Carrier frequency recovery is a very sensitive operation in coherent communication systems. Even a small frequency offset could entirely destroy the final signal constellation and also the performance of the system [49, 51]. Carrier frequency recovery can be achieved using different types of approaches. One approach is to transmit the unmodulated carrier prior to the data transmission which helps the receiver to extract the carrier frequency offset of the received signal. Such methods were used in early days of the wireless communication where a low throughput was required. But sending an unmodulated carrier is a waste of resources and energy. The most common approach is to estimate the frequency offset from the modulated signal and it is adopted in our system. As in the timing synchronization system, frequency recovery can also be divided into several categories.

Feedback based closed loop carrier recovery architectures are mostly used in continuous mode transmission using frequency locked loops and phase locked loops. But due to the high acquisition time and the possibility of occurrence of the 'hang-up' phenomenon, feed-forward approaches are more popular [62]. So, we use feed-forward schemes to estimate the frequency errors. However, most of the systems still use feedback based phase-locked loops to track residual small frequency errors after the initial acquisition. Phase locked loops are discussed in later sections of this chapter.

There are many frequency estimation algorithms proposed for single carrier transmission. In this section, we focus on some popular algorithms which were developed based on different methodologies. Usually, the frequency offset is estimated using preambles at the beginning of the transmission. Several data-aided frequency estimators are discussed in [49, 51]. A simple implementation of ML frequency estimator is not available due to the high complexity [51].

According to Figure 2.5, the input signal of the frequency recovery unit can be defined as

$$x(k) = c_k e^{j[2\pi f_d k T_s + \theta]} + w'(k) \ , \tag{2.15}$$

where, f_d is the carrier frequency offset, θ is the carrier phase offset, T_s is symbol time, c_k is a QAM modulated complex symbol with the index k, where the region is defined as $0 \le k \le L-1$. The total number of symbols used in the estimator is given by L. $w(k)$ is complex Gaussian noise sample with power spectral density N_0. (2.15) is derived assuming perfect timing recovery. We remove the modulation of PSK or 4-QAM symbol by multiplying (2.15) with c_k^* as $z(k) \triangleq x(k)c_k^*$.

$$z(k) = e^{j[2\pi f_d k T_s + \theta]} + w''(k) \ , \tag{2.16}$$

where $w''(k) \triangleq w'(k)c_k^*$ has the same mean and variance as $w(k)$. The MRCB of frequency estimators for a QPSK modulated system is defined as follows [51]:

$$MCRB(\hat{f}_d) = \frac{3}{8\pi^2 L_0^3 E_s/N_0 {T_s}^2} \;, \tag{2.17}$$

where, T_s is the symbol time, L is the block length and E_s/N_0 is the ratio of symbol energy to noise spectral density.

2.4.1 Kay estimator

Kay presented an unbiased frequency estimator which achieves MCRB at high SNR region [3]. This estimator is derived by multiplying $z(k)$ with conjugate of the previous symbol $z^*(k-1)$. It results in a complex number where the phase angle is equivalent to the normalized frequency offset and an additive noise sample. Weighting factors $\gamma(k)$ are calculated based on the autocorrelations of relevant noise samples. The final frequency estimate is obtained by adding the weighted angles of L symbols and normalizing the result. Kay estimator is defined as [3],

$$\hat{f}_d = \frac{1}{2\pi T_s} \sum_{k=1}^{L-1} \gamma(k) \arg\{z(k)z^*(k-1)\} \;, \tag{2.18}$$

where $\gamma(k)$ is defined as,

$$\gamma(k) = \frac{3}{2}\frac{L}{L^2-1}\left[1 - \left(\frac{2k-L}{L}\right)^2\right], k = 1, 2..., L-1$$

2.4.2 Lovell and Williamson (L&W) estimator

Lovell et al. presented an improved version of the Kay algorithm [63]. L&W estimator uses the phase differences of consecutive symbols $z(k)$ and $z(k-1)$. L&W estimator is defined as [63],

$$\hat{f}_d = \frac{1}{2\pi T_s} \arg\left\{\sum_{k=1}^{L-1} \gamma(k)\; \exp\{j[\arg\{z(k)\} - \arg\{z(k-1)\}]\}\right\} \;, \tag{2.19}$$

where weighting factors are defined as,

$$\gamma(k) \triangleq 6k(L-k)/[L(L^2-1)]$$

2.4.3 Fitz estimator

Fitz developed a frequency estimator based on the correlation of the received symbols [6]. $R(m)$ vector is calculated using autocorrelations of $z(k)$ as follows:

$$R(m) \triangleq \frac{1}{L-m} \sum_{k=m}^{L-1} z(k)z^*(k-m), 1 \leq m \leq L-1 \;, \tag{2.20}$$

where $1 \leq m \leq L-1$. It can be simplified as

$$R(m) = e^{j2\pi m f_d T_s} + w'''(m) \;, \tag{2.21}$$

where $w'''(m)$ is a zero mean noise term and$|w'''(m)|$ can be neglected at high SNR region. By measuring the phase of $R(m)$ and taking the summation over N autocorrelations, Fitz estimator can be obtained as follows [6]:

$$\hat{f}_d = \frac{1}{\pi N(N+1)T_s} \sum_{m=1}^{N} \arg\{R(m)\} \;, \tag{2.22}$$

where N must satisfy the two requirements $N \leq 1/(f_d T_s)$ and $N \leq L/2$.

2.4.4 Luise and Reggianni (L&R) estimator

Luise et al. proposed another frequency estimator which utilizes the autocorrelations of the input vector [4]. This estimator sums the autocorrelations $R(m)$ prior to calculating the phase. L&R estimator is defined as [4],

$$\hat{f}_d = \frac{1}{\pi T_s(N+1)} \arg\left\{\sum_{m=1}^{N} R(m)\right\} \;, \tag{2.23}$$

where N is limited by $N \leq L/2$ and $N \leq 1/(f_d T_s)$ conditions.

2.4.5 Mengali and Morelli (M&M) estimator

Mengali et al. presented an autocorrelation based algorithm overcoming the 2π phase ambiguity of autocorrelation vector $\arg(R(m))$ which suffered in Fitz estimator [64]. M&M estimator replaces the phase angles of the autocorrelations in Fitz estimator with phase angle difference between the neighboring components in autocorrelation vectors $\arg\{R(m)R^{*}(m-1)\}$. M&M estimator is mathematically defined as [64],

$$\hat{f}_d = \frac{1}{2\pi T_s}\sum_{m=1}^{N}\gamma(m)\left[\arg\{R(m)\} - \arg\{R(m-1)\}\right]_{2\pi}, \tag{2.24}$$

where, $\gamma(m) \triangleq 3[(L-m)(L-m+1)-N(L-N)]/[N(4N^2-6NL+3L^2-1)]$ and $N \leq L/2$.

2.4.6 Other frequency estimators

All the above estimators were proposed to be used when preambles are transmitted in a single block. Palmer et al. presented two frequency estimators when the preambles are distributed throughout a burst along with data [65]. These have the advantage of overcoming burst errors where the first block (preamble block) is lost during the transmission. The proposed estimators, namely, phase-incremental estimator and autocorrelation-based estimator achieve MCRB at high SNR region [65].

The previously discussed frequency estimators can be used in decision-directed mode or non-data aided mode by canceling the modulation (e.g. take the Mth power for a M-PSK modulated signal) [51]. A pure non-data aided and non-timing aided feed-forward estimator is suggested, which uses delayed samples of the signal [66]. the cost is its poor performance compared to data-aided and timing-aided estimators and hence is not suitable for low SNR operation.

2.4.7 Performance investigation of frequency estimators

We investigate the performance of frequency estimators using computer simulations. MSE of each estimator is compared with MCRB as a function of SNR. Nyquist pulse is used with an excess bandwidth $\alpha = 0.5$. Two block sizes 32 and 128 are considered with an initial frequency offset of 0.

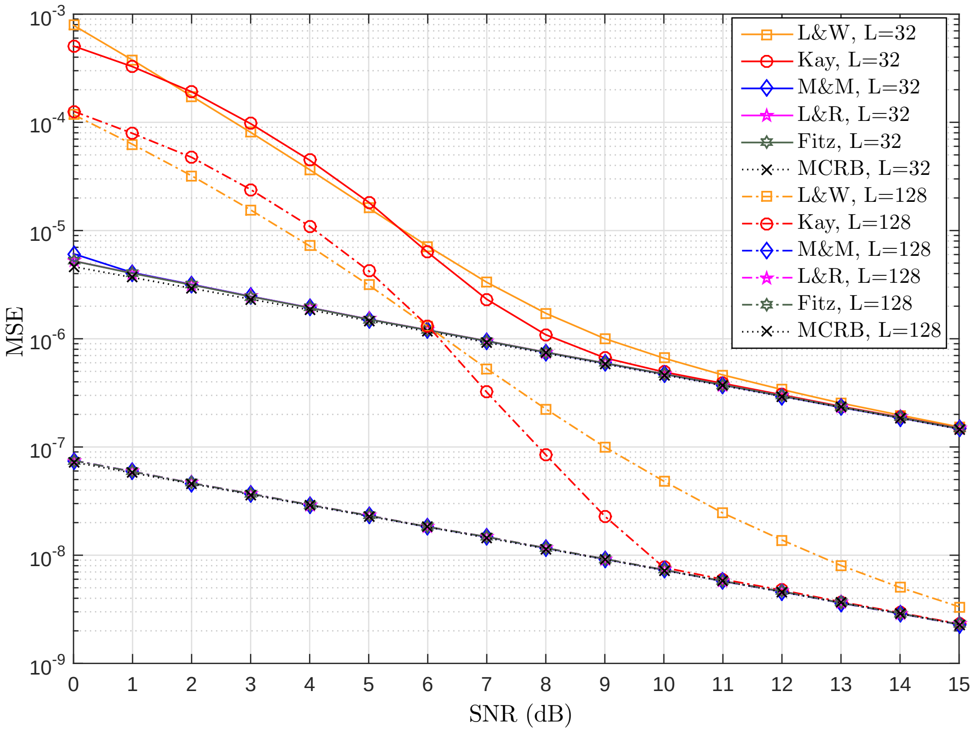

Figure 2.12: MSE performance of frequency estimators ($L = 32$ & $L = 128$).

According to Figure 2.12, when the block size is 32, all the frequency estimators achieve MCRB at high SNR values over 14 dB. L&W and Kay estimators perform poorly when SNR is lower than 13 dB and 9 dB respectively. M&M estimator achieves MCRB at a low SNR of 1 dB. Fitz and L&R estimators perform well at low SNR by reaching MCRB. When the block size is increased to 128, L&W estimator fails to achieve MCRB till 15 dB and Kay estimator achieves MCRB at 9 dB. The performance of M&M algorithm improves compared to a block size of 32 and it achieves MCRB before 0 dB. Fitz and L&R estimators also reach MCRB at negative SNR values. Therefore, based on MSE investigation, it can be concluded that data-aided M&M, Fitz and L&R estimators are suitable for low SNR operation.

Estimation range is another key metric to compare frequency estimators. It measures the maximum frequency offset that the estimators can track and it is also named as the S-curve. In our investigation the initial frequency offset is varied from -0.1 to 0.1. The operating SNR is chosen as 15 dB and block sizes of 32 and 128 are considered. The

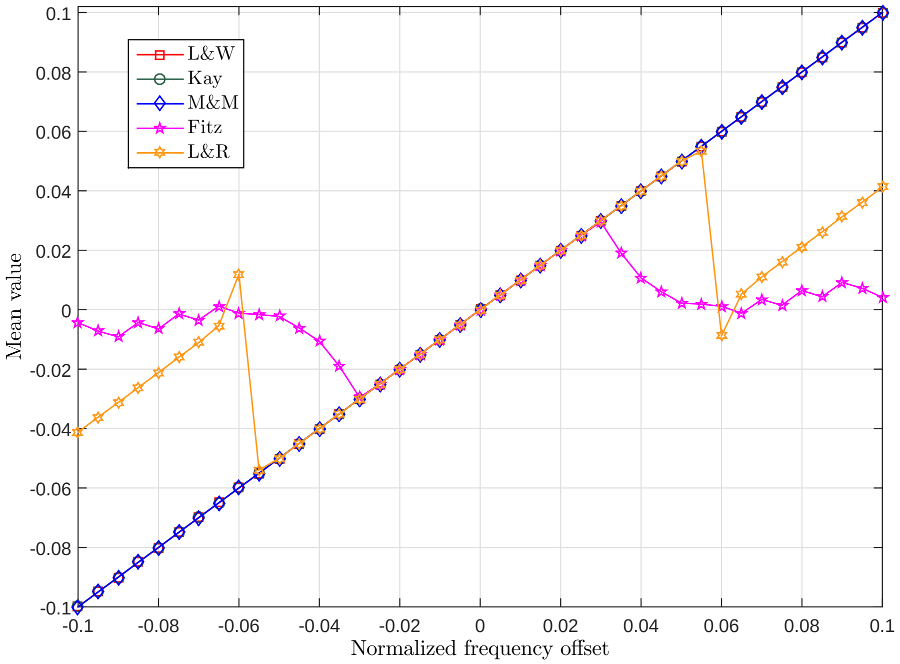

Figure 2.13: S curves of frequency estimators ($L = 32$).

estimation ranges for block size of 32 are presented in Figure 2.13. Kay, L&W, and M&M estimators have a wide estimation range about 0.3, 0.45 and 0.45 Hz per symbol. These three estimators use the phase differences between the consecutive symbols to calculate the frequency offset. Therefore, block length do not affect these estimators. However, on the other hand, Fitz estimator and L&R estimator use the auto correlation and phase differences among the symbols in entire block. So these estimators have a maximum in terms of the estimation range depending on the phase difference between the first and last symbol of the block. When $N = 32$ Fitz estimator records the lowest estimation range of 0.03 among the considered algorithms. L&R estimator is capable of measuring the normalized frequency offsets up to 0.05.

Higher block sizes result in lower estimation ranges for Fitz and L&R. Figure 2.14 shows the estimation ranges when the block size is increased to 128. L&W, Kay and M&M estimators still operate with the same range, higher than 0.1 Hz per symbol. However, the normalized ranges of Fitz and L&R estimators have fallen to 0.005 and 0.01 respectively.

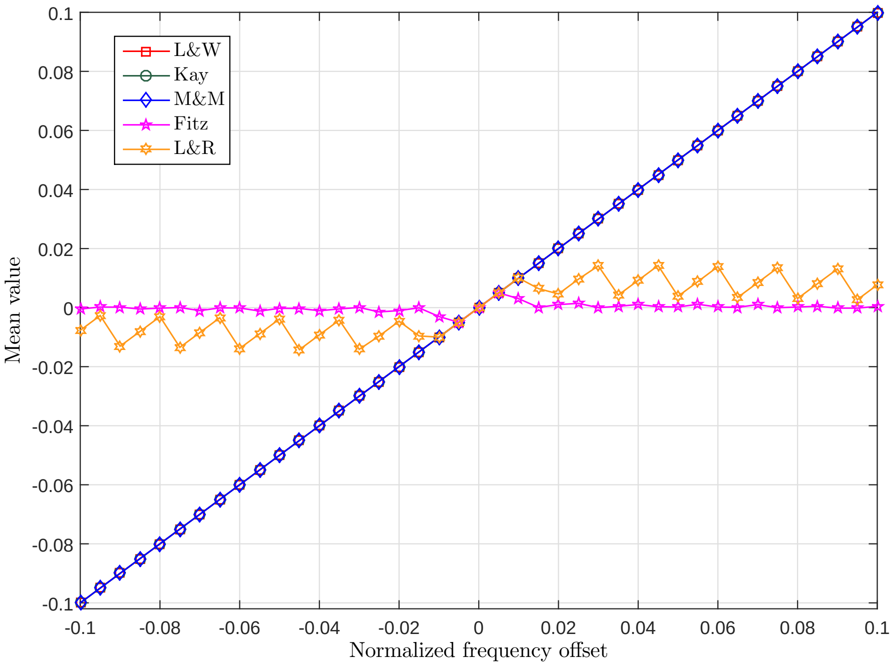

Figure 2.14: S curves of frequency estimators ($L = 128$).

We also investigate the performance of these algorithms for non-data aided operation. Instead of performing the process defined in (2.16), we remove the modulation by taking the received signal to its fourth power since QPSK modulation is used. Therefore, we re-write $z(k)$ as

$$z(k) = e^{j[2\pi 4 f_d (kT)]} + n'(k) \tag{2.25}$$

The remaining part of the derivations is the same, except for the division of estimators by a factor of 4 to obtain $\hat{f}_d$ being the final step. Estimation range of the NDA estimators are also reduced by a factor of 4 compared to the data-aided versions, because of the fourth power operation.

MSE performance for NDA frequency estimators are presented in Figure 2.15. The NDA estimators perform quite poorly compared to DA estimators at low SNR. When block size is 32, all the estimators fail to achieve MCRB below SNR of 16 dB. However, Fitz and L&R estimators start performing better, when SNR is higher than 10 dB. M&M estimator aligns with Fitz and L&R estimators at 12 dB. However, L&W estimator behaves poorly within the considered SNR region.

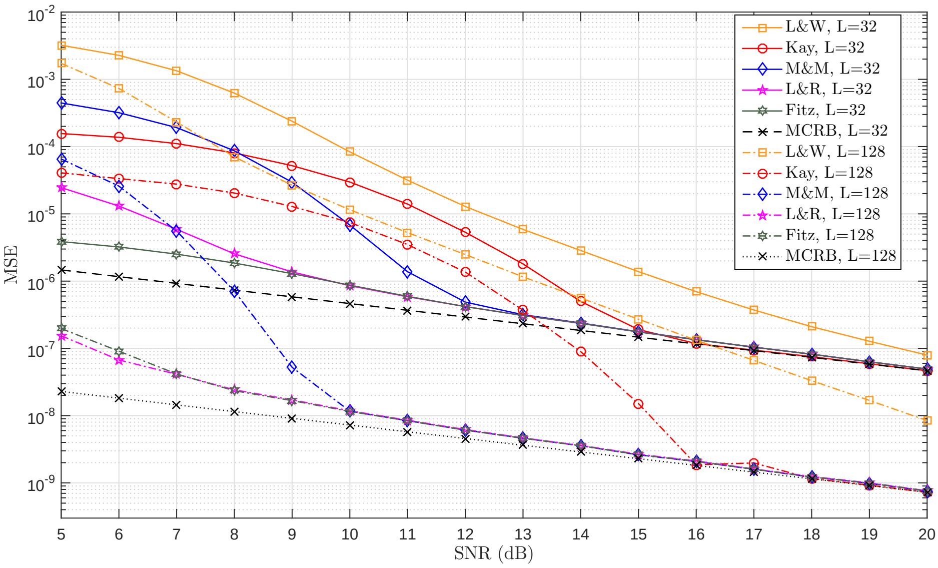

Figure 2.15: MSE performance of frequency estimators (Non data-aided) ($L = 32$ & $L = 128$).

The performance of some NDA estimators improve when the block size is increased to 128. Fitz and L&R estimators perform close to MCRB from a SNR of 7 dB and M&M estimator starts to reach MCRB from 10 dB. Kay and L&W estimators result in higher MSE compared to other estimators. However, the MSE gap of Fitz and L&R with MCRB, increases when SNR gets lower. Therefore, we realize that non data-aided mode is not suitable for the low SNR operation.

Based on the above observations, we select data-aided M&M estimator as the most appropriate frequency estimator, due to its superior performance at low SNR (around 0 dB) and the wider estimation range.

Performance of frequency estimators at the presence of timing errors

The behavior of M&M frequency estimator in the presence of timing errors is investigated and presented in Figure 2.16 when the block size is 32. It is observed that the MSE is not converging to the MCRB at high SNRs. This is because at high-SNR, timing errors have more impact than the Gaussian noise, resulting in a higher MSE compared to the perfectly-sampled scenario. At the presence of worst timing error of 0.5, variance of

M&M converges to 10^{-5}. Therefore, it is important to perform the timing recovery prior to the frequency recovery.

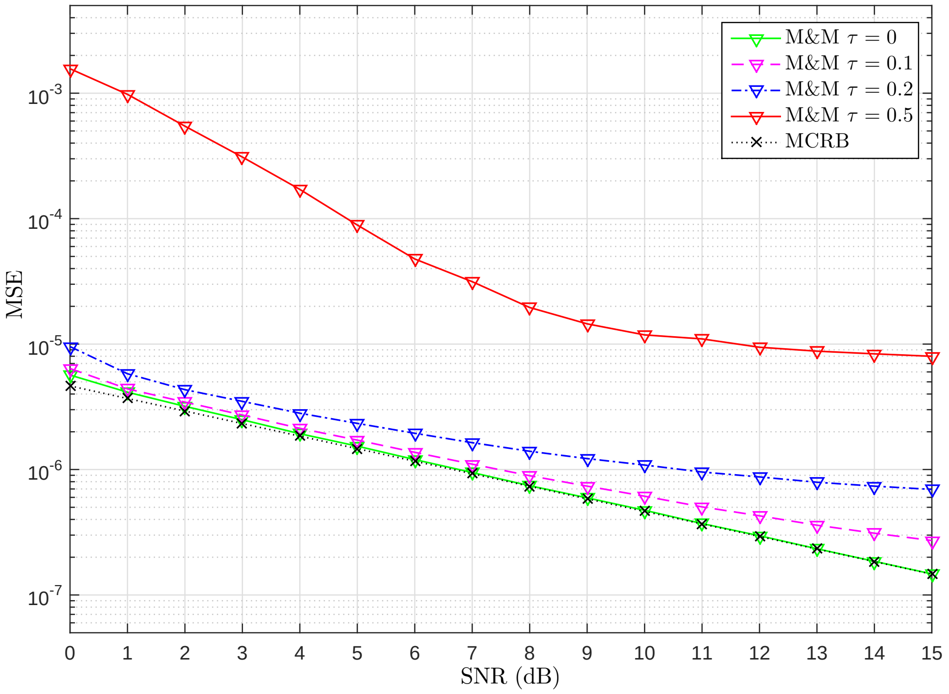

Figure 2.16: MSE performance of M&M estimators at the presence of timing offsets ($L = 32$).

2.5 Carrier Phase Synchronization

Carrier phase synchronization is a necessary component in coherent communication systems. It needs to correct both the initial phase offsets as well as the phase errors occurring due to residual frequency errors. Especially in low SNR region, the residual frequency errors can be large enough to distort the received signal constellation. It is important to recover the carrier phase continuously throughout the data transmission. Therefore, non-data aided or decision-directed estimators are needed to operate during the data transmission. As preamble is already supplied for the training stage, data-aided operation can be conducted to obtain a more accurate estimate of the initial phase offset.

Assuming perfect timing and frequency recovery, the input of carrier phase recovery unit can be written as follows:

$$x(k) = c_k e^{j\theta} + w'(k) \tag{2.26}$$

2.5.1 Feedback based carrier recovery loop

Carrier phase recovery loops are widely used in current communications systems. They are mostly suitable in continuous mode operations where it is needed to track small phase variations over a long period of time. A typical carrier recovery loop consists of a phase error detector, a loop filter and a direct digital synthesizer (DDS). Usually maximum likelihood phase detector is used as it calculates the optimal phase error. Second order loop filters are widely used due to their capability of tracking small frequency errors with a low complexity.

2.5.2 Feed-forward based carrier recovery system

As feedback based carrier recovery loops may require a long time to acquire the initial lock, an alternative approach can be used for fast acquisition during the burst transmission. Feed-forward synchronizers are proposed to achieve this requirement. We focus on data-aided ML estimator [51] and non data-aided Viterbi & Viterbi estimator [7] in this section.

The Cramer-Rao bound (CRB) is defined for QPSK modulated phase estimators as follows [51]:

$$MCRB(\hat{\theta}) = \frac{1}{2LE_s/N_0}\ , \tag{2.27}$$

where, L is the number of symbols used in the estimator.

Maximum likelihood (ML) phase estimator

ML based feed-forward and data-aided phase estimator performs with a high accuracy even at low SNR values around -2 dB and is widely used during the training mode [51]. It basically removes the modulation by multiplying the matched filter output $x(k)$ with the conjugate of preambles. Then average phase angle over a block of L symbols is calculated as the final estimate. ML estimator is mathematically represented as follows [51]:

$$\hat{\theta}_{ML} = \arg\left\{\sum_{k=0}^{L-1} c_k^* x(k)\right\} , \tag{2.28}$$

Viterbi & Viterbi (V&V) estimator

Viterbi et al. presented a non data-aided and feed-forward estimator for PSK modulated signals which is widely used in modern wireless and optical communication systems [7]. V&V algorithm estimates the phase of middle symbol when a small frequency error is present. The performance of V&V estimator varies with two parameters use in the estimator: window size (L) and non-linear transformation function.

The input signal can be written as, $x(k) = a_k + jb_k$, where $a_k = \text{real}(x(k))$ and $b_k = \text{imaginary}(x(k))$. The parameters of the estimator, are calculated as $\rho_k = \sqrt{a_k^2 + b_k^2}$ and $\phi_k = \tan^{-1}(b_k/a_k)$.

The nonlinear transformation function is defined as $F = \rho_k^n$ where n is the order of the non linearity and $n = 0, 1$ and 2.

Then new variables a_k' and b_k' are calculated as

$$a_k' + jb_k' = F(\rho_k)e^{jM\phi_k}$$

The final phase estimate is obtained as follows:

$$\hat{\theta}_k = \frac{1}{M}\tan^{-1}\left\{\frac{\sum\limits_{k=0}^{N} b_k'}{\sum\limits_{k=0}^{N} a_k'}\right\} , \tag{2.29}$$

where M is the signal constellation size. V&V estimator gives a rise to an M-fold ambiguity in the phase estimate. Practical systems overcome this phase ambiguity by adapting differential encoding and decoding. However, adopting differential encoding and decoding will result in a higher bit error rate, by approximately two times at high SNR region. Another method to overcome this phase ambiguity is to use a phase un-wrapper [1]. A phase un-wrapper resolves the phase ambiguity through accumulating the phase estimate around the discontinuities.

2.5.3 Performance investigation of phase estimators

Figure 2.17 and 2.18 illustrate MSE for ML and V&V estimators with different non-linear transformation functions. It can be seen that ML estimator achieves CRB even at low SNR values for both block sizes chosen. All the V&V estimators perform poorly compared to the ML estimator at low SNR region, however, the performances improve at high SNR values. V&V estimator with unit magnitude ($F(\rho) = 1$) gives the worst performance when SNR is less than 11 dB. For SNR values less than 5 dB, square non-linear function ($F(\rho) = \rho^2$) performs superior to other two functions. Absolute non-linear function ($F(\rho) = \rho$) performs better than other two only during the mid SNR region around 5 dB to 11 dB, however, the performance gain over square non-linear function is very small.

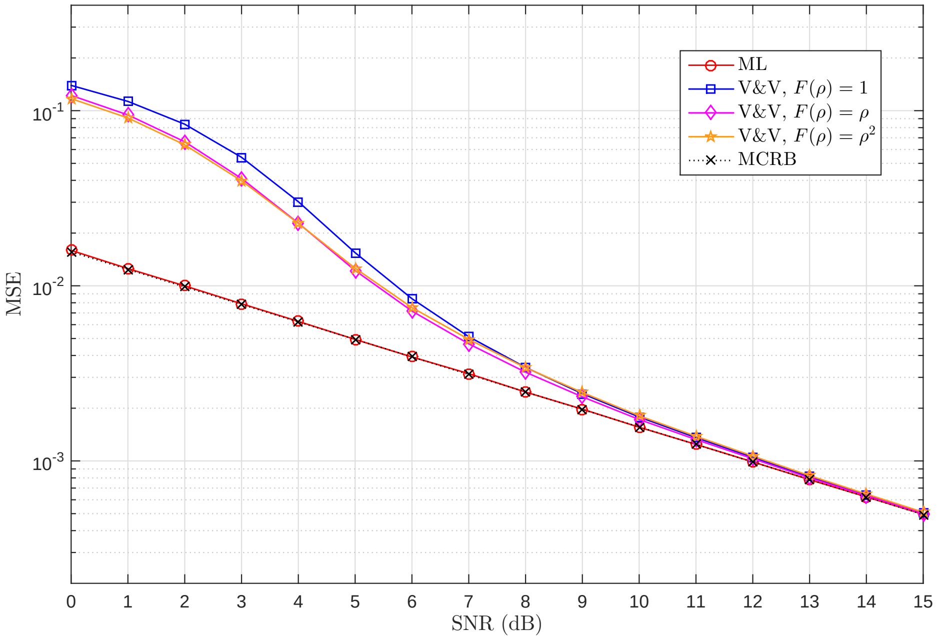

Figure 2.17: Performance comparison between of phase estimators ($L = 32$).

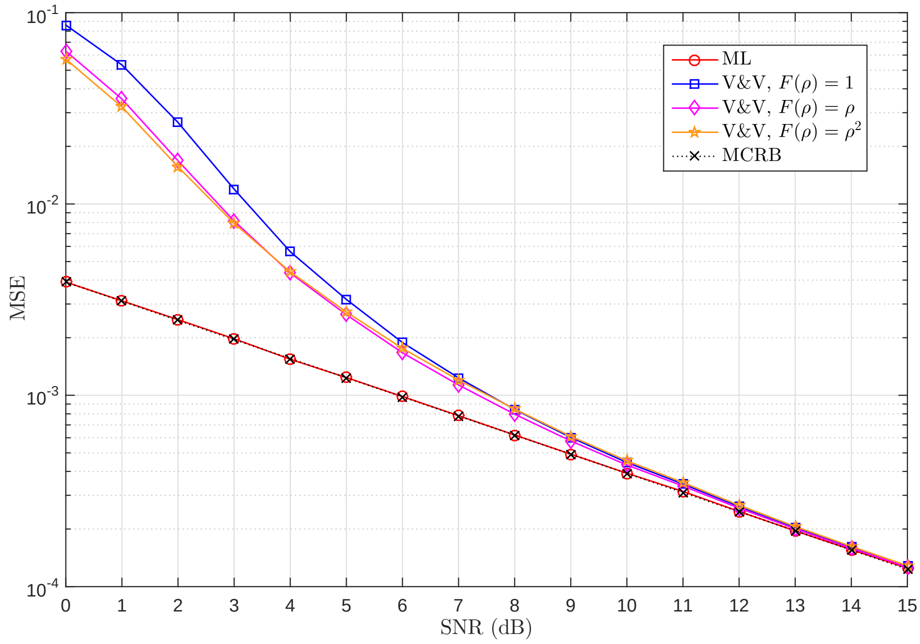

Figure 2.18: Performance comparison phase estimators ($L = 128$).

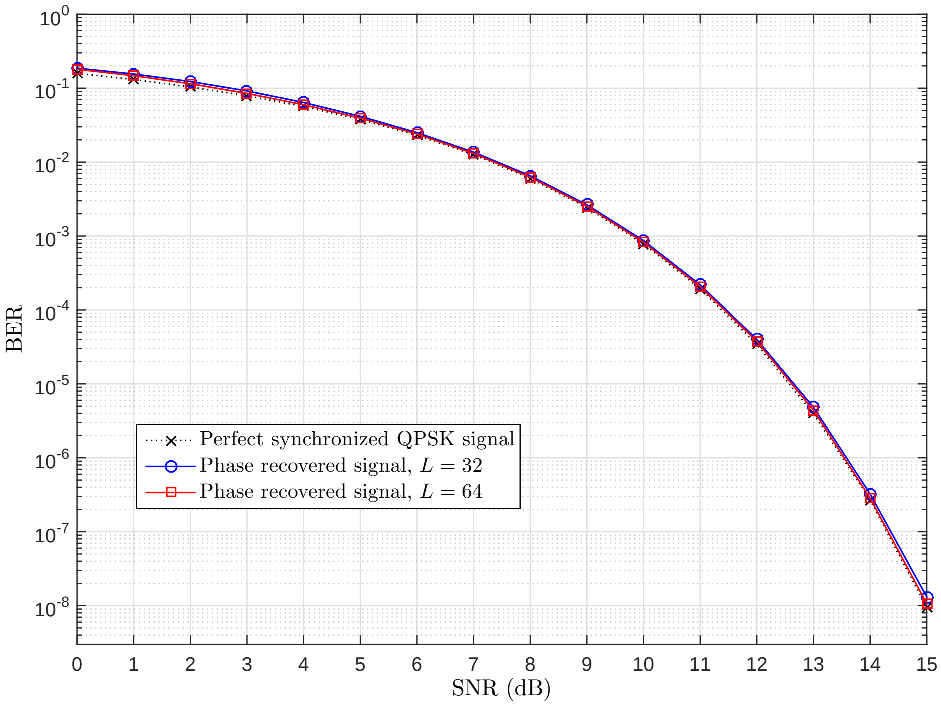

Figure 2.19: BER performance after phase recovery ($L = 32$ & $L = 64$).

We also observe the BER performance after the carrier phase recovery and presented in Figure 2.19. V&V estimator ($F(\rho) = \rho^2$) is implemented with block sizes of 32 and 64. The phase recovered signal suffers a loss of 0.4 dB compared to the perfect synchronized signal at SNR of 3 dB and a 0.07 dB loss at SNR of 10 dB when block size is 32. The number of errors is reduced when block size is increased to 64, the signal suffers losses of 0.2 dB and 0.03 dB at SNR's of 3 dB and 10 dB respectively. Therefore, by using a large enough block size, V&V estimator provides a near perfect BER performance.

BER for a perfectly synchronized un-coded QPSK signal is given by [50] as,

$$BER_{\text{QPSK}} = Q\left(\sqrt{\frac{E_s}{N_0}}\right) \tag{2.30}$$

An analytical expression is available for the BER loss (Δ) due to the variance of phase estimation $\text{Var}(\hat{\theta})$ [61]. This expression is highly accurate when the phase variance is low.

$$\Delta \cong \frac{10}{\ln(10)}\left[1 + \frac{E_s}{N_0}\right]\text{Var}(\hat{\theta})\ \text{(in dB)} \tag{2.31}$$

We also investigate the performance of V&V algorithm in the presence of frequency errors. The average symbol phase increases in proportion to the frequency error present. In such scenarios, V&V estimator produces an estimate of the middle symbol in the block. In order to avoid this problem, a lower block size should be used. However, at low SNR, small block sizes give inaccurate estimates. Therefore, it is important to decide the optimum block size depending on the possible frequency offsets and operating SNR [67].

One issue with feed-forward phase estimators is the phase wrapping due to frequency offsets. Therefore, the output of the phase estimator needs to be tracked and un-wrapped as proposed in [1].

The maximum variance of the phase estimator in the presence of frequency error is given by [67] as

$$\sigma^2_{\hat{\theta},max} = \sigma^2_{\hat{\theta}} + 4\pi^2 L_\theta^2 f_e^2 T_s^2\ , \tag{2.32}$$

where, $\sigma^2_{\hat{\theta}}$ is the phase error variance of the central symbol, $f_e T_s$ is the normalized frequency error, $2L_\theta + 1$ is the number of symbols used in the phase estimator.

Figure 2.20 shows the MSE of V&V estimator for small frequency errors of 10^{-3}, 10^{-4} and 0 for three block sizes 32, 128 and 256. The signal with highest frequency error of 10^{-3} produces large phase variance due to the frequency error when long block size is used ($L = 128$ and $L = 256$). The phase variance is dominated by the second term in (2.32). When the block size is 32, the total phase variance due to frequency error is small compared to the phase estimator variance. So all three graphs almost overlap with each other. When $L = 256$ and frequency error is high (10^{-3}), V&V estimator is unable to estimate the phase correctly as the phase of the symbols in the block exceeds the estimation range of $(-\pi/2, \pi/2)$. But smallest block size of 32 produces similar performance for all three signals. The performances for signals with small frequency error 10^{-4} and no frequency error are quite similar for these block sizes. Based on our investigation, we conclude that the initial phase acquisition should be carried out using data-aided ML phase estimator. However, small residual frequency errors can still exist after the frequency recovery. Those frequency errors should be tracked continuously, and therefore, a non-data aided estimator has to be used. For low SNR operation of PSK modulated systems, V&V esti-

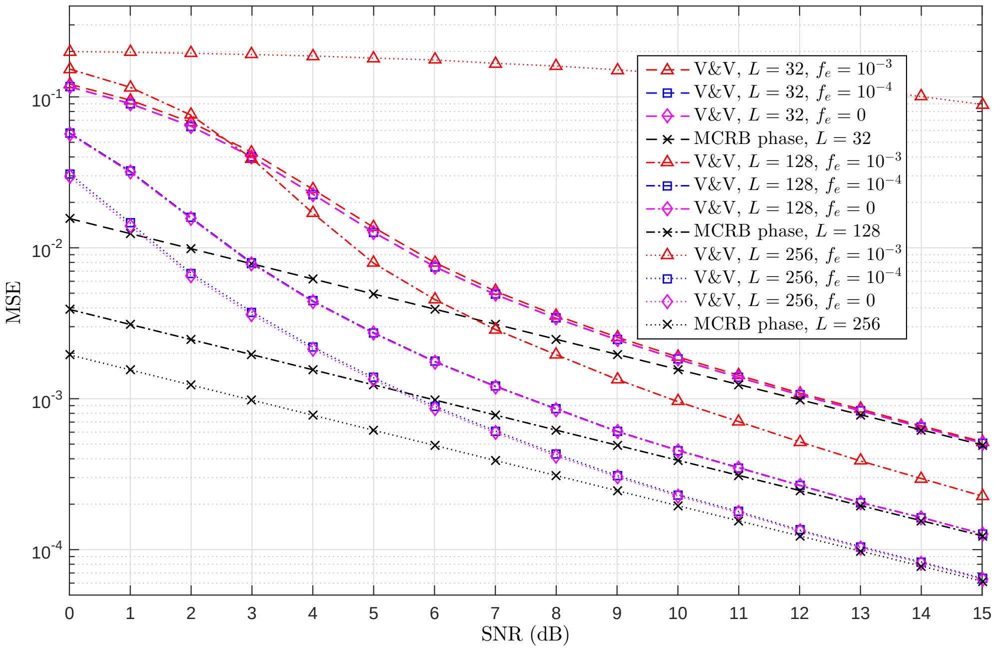

Figure 2.20: Performance comparison of Viterbi & Viterbi estimator at the presence of frequency errors ($L = 32$ & $L = 128$).

mator should be used with non-linearity of $F(\rho) = \rho$ or $F(\rho) = \rho^2$ depending on the exact operating SNR. However, for high order QAM signals, carrier recovery loops need to be used for tracking after the initial phase is acquired by feed-forward ML phase estimator, because V&V phase estimator performs quite poorly in that case.

2.5.4 Performance of combined timing and carrier synchronization systems

Based on our investigations and conclusions of individual scheme performances, we simulated a combined timing and carrier phase recovery system[1]. We have chosen absolute value non-linearity (AVN) based feed-forward timing estimator [59] as to estimate the timing error. We then use correct the phase offset using Viterbi and Viterbi estimator [7]. Nyquist pulse with excess bandwidth of $\alpha = 0.35$ is used with different block sizes 32, 64 and 256. The initial timing and phase offsets were evenly distributed. The BER results are presented in Figure 2.21.

The BER degradation due to the non-perfect synchronization reduces as the number of symbols or the block size (N) is increased. At a BER of 10^{-1}, there is SNR degradation of 0.8 dB when 32 symbols are used in the estimators. But the SNR degradation reduces to 0.4 dB when the block size is increased to 64. At a lower BER value of 10^{-4}, 32 and 64 blocks require to operate at 11.6 dB and 11.5 dB while the perfect synchronized system only needs 11.4 dB. When 256 blocks are used for synchronization, the performance closely aligns with perfect synchronized signal. When compared with individual estimated BER performances - timing recovered in Figure 2.10 and phase recovered in Figure 2.19 - the joint synchronized system performance is slightly poor mainly due to the effect of non-perfect timing recovered signal fed into phase estimator. However, by selecting a large enough number of symbols for the estimators (e.g. $N = 256$) near perfect synchronization can be achieved for a given application.

---

[1] Even though the synchronization parameter estimates are evaluated in MSE, a complete system performance is more meaningful to evaluated using BER. In practice, when the carrier synchronizer fails to mitigate the frequency offset, it results in a frequency error. In the presence of a frequency error, the symbol constellation rotates and in such situations the BER renders meaningless (e.g. by converging to 0.5 for QPSK). Considering such a scenario into BER calculation would provide inaccurate results. Therefore, we did not consider the frequency synchronization in the BER simulation and we only considered timing and phase recovery in Figure 2.21

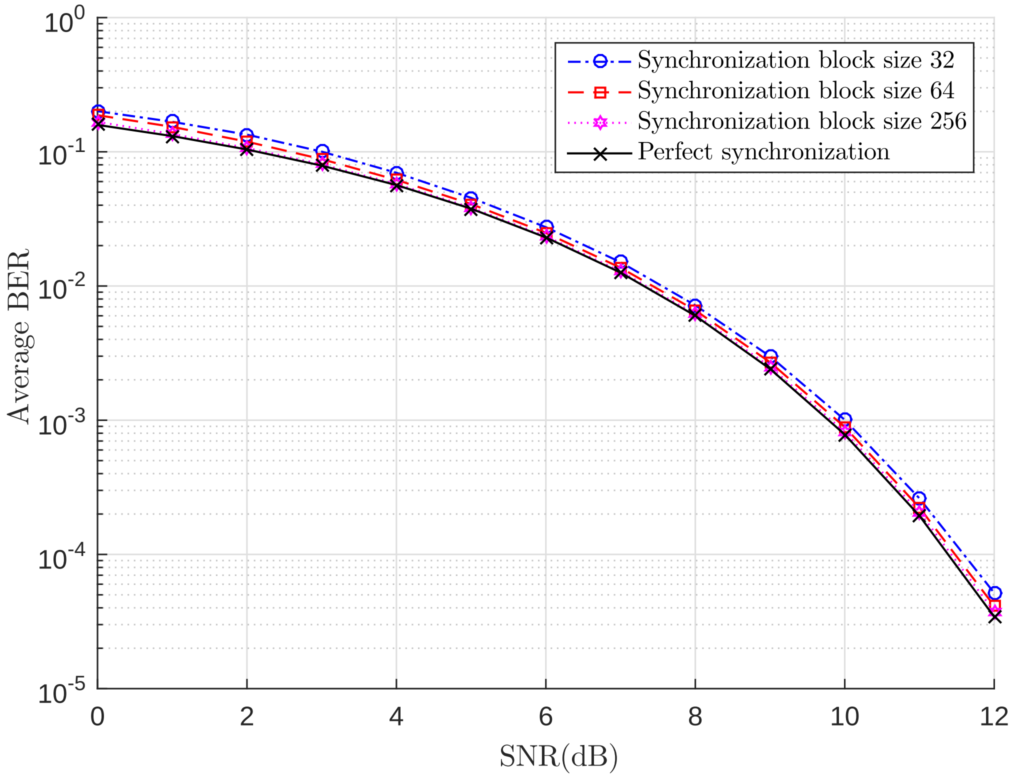

Figure 2.21: BER performance with joint timing and carrier phase synchronization ($L = 32$ & $L = 64$).

2.6 Conclusions

In this chapter, we evaluate the performance of various synchronization architectures and algorithms for single-carrier transmission in AWGN channel. We propose a synchronization system architecture with appropriate algorithms for low SNR operations. It is important to use a preamble to train the receiver, especially for the low SNR region. The preamble can be used to acquire the initial parameters such as timing offset, carrier frequency offset and phase offset. Then, non-data aided algorithms and decision directed algorithms can be used during the data transmissions to track the synchronization parameters.

Timing error is corrected first as timing estimators can perform independently of small carrier frequency errors. We propose to use absolute value non-linearity (AVN) based feed-forward timing estimator [59] or Gardner TED [57] in the timing recovery system. We propose to adopt Mengali et al. algorithm to estimate the large frequency offsets using a preamble [64]. Using the initial frequency estimation, the frequency error should be correct throughout the data transmission.

The small residual frequency errors can be corrected by phase recovery subsystem during the data transmission. Feed-forward Viterbi and Viterbi estimator [7] can be used for 4-QAM modulated transmission, and a feedback loop with decision directed ML carrier recovery loop [51] is recommended for any M-QAM modulated transmission.

Chapter 3

Energy Modeling of Synchronization Systems

This chapter presents energy models for different synchronization systems which were discussed earlier in Chapter 2. We initially analyze the computational complexity of synchronization system components considering arithmetic, logic and memory based operations. The energy consumption of digital signal processing (DSP) circuitries is then modeled using a computational complexity–energy framework assuming complementary metal-oxide-semiconductor (CMOS) implementation. The computational complexity of parameter estimation algorithms and other segments are studied according to available implementation architectures. We also define a new metric to compare the energy efficiency of synchronization estimators by considering both MSE performance and operating SNR.

3.1 Introduction

As discussed in the Chapter 2, many estimators are available for carrier frequency [3, 4, 6, 64], carrier phase [7, 51] and symbol timing synchronization [1, 59, 60]. We compare the performance of these algorithms using various metrics such as mean squared error (MSE), estimation range and bit-error rate (BER). Another important metric which is useful in practice is computational complexity. The complexity of these algorithms can be calculated based on the required number of computational operations and the required circuitries for completing each operation. The computational complexity can be categorized into arithmetic operations, logical operations and memory accesses. These computations are performed by digital circuits and it results in circuit processing energy consumption. Energy consumption for a given algorithm also depends on the hardware implementation platform and the technology.

Complementary metal-oxide-semiconductor (CMOS) is commonly-used technology in constructing digital electronic circuits for communication systems [68, 69]. One of the main advantages of CMOS technology is that it enables chips that are small in size to have features like high operating speeds and efficient usage of energy [70]. Another important characteristics of CMOS technology is its low static power consumption, making it possible for low-power high-speed application [70]. Devices using CMOS technology also have a high degree of noise immunity, and for these reasons, many leading telecommunication standards were fabricated using CMOS technology in the last few decades.

The complexity of digital circuits was initially investigated in VLSI systems using area and time-based computational designs [40,71]. New investigations have been carried out recently to analyze the energy consumption of decoders [37,38]. Grover et al. introduced simple energy models for equalizers and decoders [37]. This study is later extended to derive fundamental lower bounds for complexity and to model power consumption for LDPC encoders and decoders [38, 39].

A computational complexity – energy conversion framework is presented by Desset et al. for wide range of operations covering arithmetic, logic and memory operations [35]. The authors used this framework to model the energy consumption of Hamming codes, Reed-Solomon codes, Reed-Muller codes and turbo codes. It is later used to model energy more accurately in different code families such as Reed-Solomon [72] and LDPC [43].

To the best of our knowledge, however, a computational complexity based complete model for a whole synchronization system in wireless receivers is not available. It is important to model the energy costs of synchronization systems due to two main reasons:

- Low power devices such as wireless sensor nodes and IoT transceivers generally use batteries with limited stored energy. In such cases, the energy consumption of digital processing becomes more significant, therefore, modeling the circuit energy for the synchronization system provides insights on energy efficient system design.
- Circuit energy is more important at low SNR operation. As the received SNR is reduced, the coding overhead needs to increase in order to overcome the additional errors that occur due to the high noise power. This results in receivers to process

more bandwidth, which results in higher circuit processing energy. The selection of algorithms could also change at different SNRs, and therefore, the circuit energy will change.

In order to address the gap this area, we model the energy consumption of synchronization systems. This chapter is organized as follows: Section 3.2 consists of a description of a framework for our system. Section 3.3 provides the analysis and energy modeling details of timing recovery subsystem. Frequency system complexity analysis and energy modeling are presented in Section 3.4. Section 3.5 consists of complexity analysis for different phase synchronization algorithms and details of the energy models. Finally, Section 3.6 summarizes and concludes the chapter.

3.2 Energy Modeling Framework for DSP Circuits

In this chapter, we use the complexity–energy framework presented by Desset et al. [35] with necessary modifications to match modern processing technologies. This framework is then used to derive energy models from different parts of the synchronization systems.

The complexity-energy framework provides energy consumption estimates of DSP components for basic operations such as addition, multiplication, register access, read-only memory (ROM) access and logic gate operations. Desset et al. presented the energy consumption values for an operating voltage of 1.8 V and CMOS technology of 180 nm. The original energy consumption details are listed in Table 3.1 and represent the average equivalent energy consumed by each basic operation [35]. The parameter n is defined as the average bit resolution of the DSP module. The energy costs are estimated on the basis of data sheets as well as on practical experience. The energy values include related overheads such as interconnection [35]. The energy consumption for a given DSP module is a sum of energy costs of all individual operations.

In our system, registers are used to store temporary variables that are needed later. ROMs are used to save fixed constants used in arithmetic operations. Most of the components in our system use complex numbers; therefore, complex operations need to be

Table 3.1: Energy consumption basic framework [35] ($0.18\,\mu$m CMOS implementation with a supply voltage of 1.8 V).

Operation	**Energy consumption per operation (pJ)**
Logic gate	0.4
Flip-flop	2 (write)
n-bit Adder	$1.5n$
n-bit Multiplier	$1.5n^2$
RAM	10 per bit (read or write)
m-input ROM	m per bit (read)

carried out. A complex addition is realized using two real additions. A common approach to implement complex number multiplication is to use four real multiplications and two real additions, but an alternative approach can be taken by using three real multiplications and five real additions [73]. Both approaches have different trade-offs, which depend on the bit resolution of the system. But the second approach requires different DSP clock frequencies, which affects the throughput of the system [74]. Therefore, first approach is used to implement a complex multiplication in our calculations.

Table 3.2: Energy consumption for different operations in our system (45 nm CMOS implementation and with a supply voltage of 1 V).

Operation	**Energy consumption per operation (pJ)**
Logic gate	0.03
Register (read & write)	1.23
Real adder	0.93
Real multiplier	7.41
RAM	6.17
ROM (read)	6.17 (read)
Sin, Cosine, Tangent	6.17
Complex exponential	12.34
Argument	6.17
Logarithm	6.17
Root, Power	6.17

In addition to basic mathematical and memory operations, the estimators need to calculate non-linear complex functions such as trigonometric and logarithmic functions. The easiest method to calculate the value of these functions is to use look-up tables (LUT) and read values from the ROM. The accuracy of the function values depend on the resolution of the LUT. The second approach uses COordinate Rotation DIgital Computer (CORDIC) architectures. CORDIC can be used to provide calculations with higher accuracy [75]. The fundamental operation of CORDIC is based on vector rotations, and realized using a set of iterative shifts and additions; however, CORDIC requires a higher number of computations than LUTs and is suitable for applications that need very high accuracy. A third approach - Taylor series approximation - is also available to perform complex functions. Taylor series approximation uses basic arithmetic operations to calculate values of a complex function. The accuracy of the Taylor series expression, however, depends on the number of terms used in the approximation; therefore, highly accurate implementation may consume higher complexity. In our system, we assume that complex functions are implemented using LUTs due to its simpler implementation with sufficient accuracy [43].

LUT-based implementation for an n-bit ROM with a resolution of 2^m consumes mn pJ energy. Functions such as $\sin$, $\cos$, $\tan$, $\log$, $\exp$, $\arg$, roots and powers of variables are implemented using LUTs as shown in Table 3.2.

CMOS circuit energy consumption changes according to the supply voltage and processor technology [76]. In our system, 45nm CMOS technology and 1 V supply voltage are assumed as they are equivalent to today's common practice. The original energy framework given in Table 3.1 is scaled according to the relevant rules [76] and presented in Table 3.2. We assume a bit-resolution of 8 to represent arithmetic values in our system.

3.3 Timing Recovery Systems

In this section, we first analyze computational complexity of the timing recovery system and then develop relevant energy models. A block diagram of our timing recovery system is illustrated in Figure 3.1. We start with feed-forward based timing synchronization system.

3.3.1 Feed-forward Timing Estimators

Timing error is first estimated using a timing estimator and then we use timing phase un-wrapper to track the errors continuously. An interpolator is used to correct the timing error. The computational complexity of the entire system is derived by analyzing each segment and adding individual contributions together. We analyze complexity of the timing estimators which were discussed in Section 2.3.2.

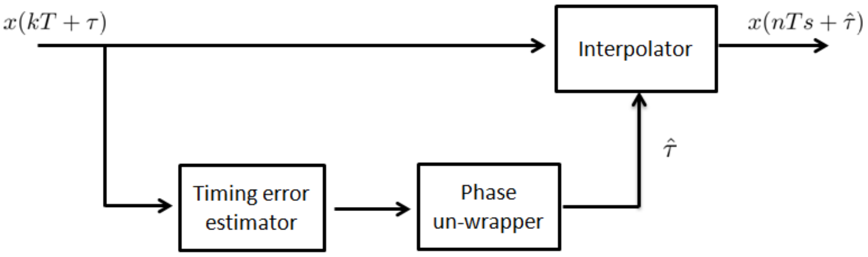

Figure 3.1: A block diagram of the timing recovery system.

Oerder & Meyr (SLN) estimator

Oerder & Meyr (SLN) estimator is given by [1] as follows:

$$\hat{\tau} = -\frac{T_s}{2\pi} \arg \left\{ \sum_{k=0}^{4L-1} |x(kT)|^2 e^{-j\pi k/2} \right\} , \tag{3.1}$$

where, the variables are defined as follows:

- τ is the time delay from the optimum sampling point
- T_s is symbol time
- T is sampling time
- $x(kT)$ is the received sample belongs to the time instance kT
- L is the block size used in the estimator

- $\hat{\tau}$ is the estimator output

A block diagram of SLN estimator is presented in the original publication [1] and shown in Figure 3.2.

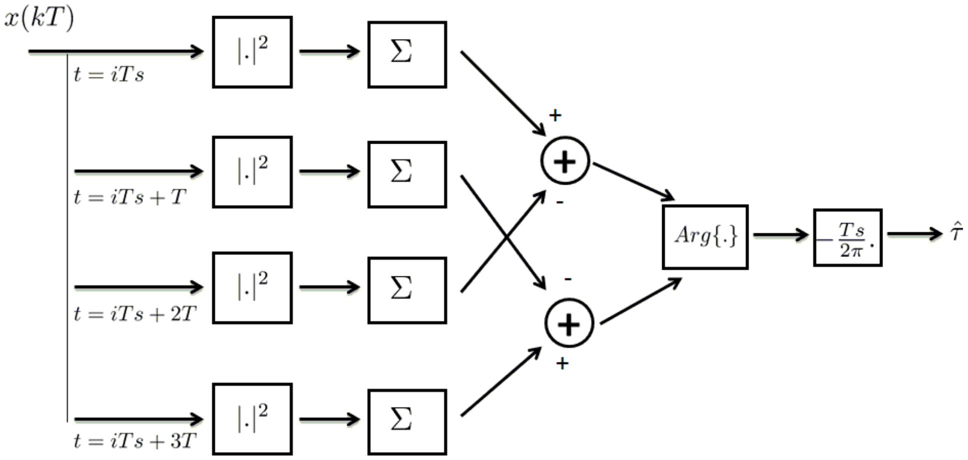

Figure 3.2: Hardware implementation architecture of the Oerder & Meyr estimator ([1]).

This estimator operates on four samples per symbol. Four parallel paths are used to perform the calculation for the four samples of each symbol more efficiently allowing its operation at high data rates. This realization avoids the use of sinusoidal multipliers and saves LUT access for sine and cosine functions. The squared magnitude of the signal was calculated using two real multiplications and one real addition. Finally, a summation over a block of L symbols were taken and the angle of the complex output was calculated using the LUT to obtain the final estimator.

The required number of computations to obtain one estimate for an L size block is presented in the Table 3.3.

Table 3.3: Computational complexity of the Oerder & Meyr ([1]) estimator.

Operation	**No. of operations**
Real additions	$8L - 2$
Real multiplications	$8L + 1$
Argument	1
ROM access	1

LOGN and AVN estimators

Modified Oerder & Meyr algorithms can also be implemented similar to the SLN algorithm. The LOGN based feed-forward estimator [59] can be implemented as SLN estimator (Figure 3.2), by replacing the squared magnitude function with the function $f(z) = ln[1 + |z|^2(SNR)^2]$. SNR is defined as the ratio of symbol energy to noise spectral density for the remainder of this Chapter and can be found at the matched filtered output of the previous symbol block. The analysis of the computational complexity of the LOGN estimator is presented in Table 3.4.

Table 3.4: Computational complexity of the LOGN feed-forward estimator.

Operation	**No. of operations**
Real additions	$12L - 2$
Real multiplications	$12L + 2$
Logarithm	$4L$
Argument	1
ROM access	2

Table 3.5: Computational complexity of the AVN feed-forward estimator.

Operation	**No. of operations**
Real additions	$4L - 2$
Real multiplications	1
Absolute value	$4L$
Argument	1
ROM access	1

Similarly, the AVN based feed-forward estimator [59] can also be implemented according to Figure 3.2 by performing the absolute value function instead of the squared magnitude function. The analysis of the computational complexity of this estimator is given in Table 3.5.

Zhu estimator

An implementation architecture for a two-sample Zhu estimator is presented in Figure 3.3 [2]. The in-phase and quadrature-phase components of the input signal are first multiplied with sinusoidal constants before sending through low pass filters. Then the resulting complex numbers are squared and sent to arithmetic processes prior to calculating the timing error using the argument function. The low pass filters are assumed to be 1st-order infinite impulse response (IIR) filters. It is assumed that two multiplications, one addition and one register shifting are required to perform low-pass filtering.

Zhu algorithm is presented as [2]

$$\hat{\tau} = -\frac{T_s}{2\pi} \arg \left\{ \sum_{k=0}^{2L-1} y_I^2(kT) + y_Q^2(kT) \right\} , \tag{3.2}$$

where, the signals at various points of the estimator are shown in Figure 3.3 and $y_I(t) = u_I(t) + v_I(t)$ and $y_Q(t) = u_Q(t) + v_Q(t)$.

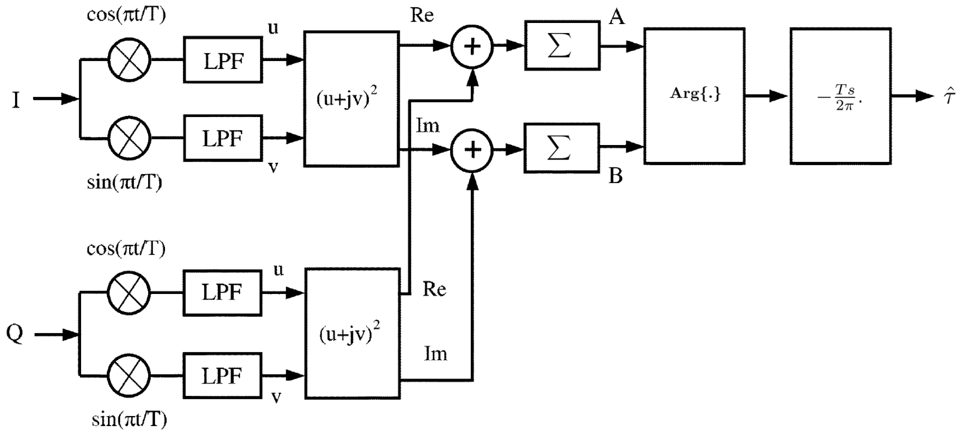

Figure 3.3: Hardware implementation architecture of the Zhu estimator [2].

The computational complexity of the Zhu estimator is summarized in Table 3.6.

Table 3.6: Computational complexity of Zhu estimator.

Operation	**No. of operations**
Real additions	$16L-2$
Real multiplications	$24L$
Argument	1
ROM access	4
LPF	$8L$

Lee estimator

The Lee estimator [60] is proposed to implement by using low complexity architecture with four parallel data lines as shown in Figure 3.4. Each sample of the two-sample based algorithm is sent through two parallel lines to calculate the timing error. The Lee estimator′s computational complexity is presented in Table 3.7.

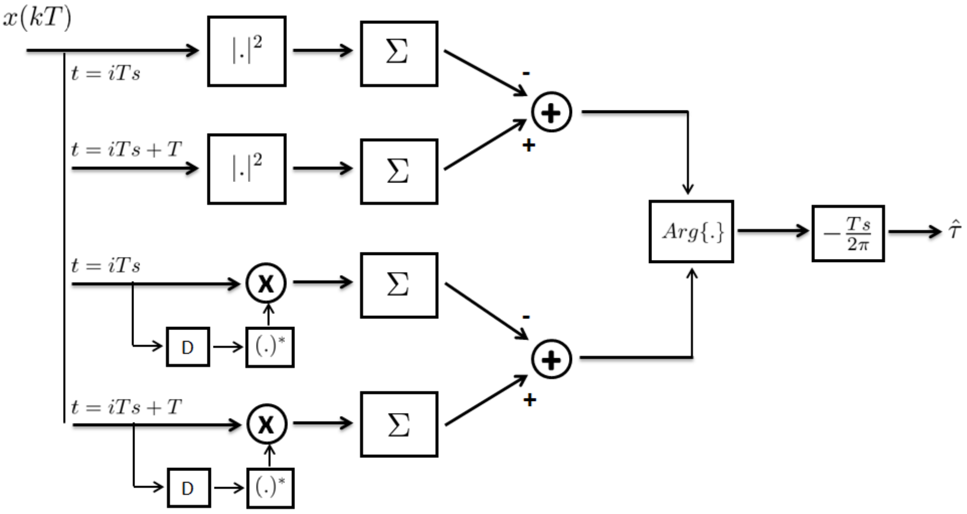

Figure 3.4: Hardware implementation architecture of the Lee estimator.

Lee estimator is defined as [60]

$$\hat{\tau} = -\frac{T_s}{2\pi} \arg\left\{ \sum_{k=1}^{2L} |x(kT)|^2 e^{-jk\pi} + Re[x(kT)x^*((k-1)T)] e^{-j(k-0.5)\pi} \right\} \tag{3.3}$$

Table 3.7: Computational complexity of the Lee estimator.

Operation	**No. of operations**
Real additions	$8L - 2$
Real multiplications	$8L + 1$
Argument	1
ROM access	1
Register shifting	$4L$

3.3.2 Interpolation

The operation of interpolators was discussed in Section 2.3.1. The complexity of two popular types of piece-wise polynomial interpolators–parabolic and cubic–are discussed by Erup et al. [77] and is summarized in Table 3.8, where N is the oversampling factor.

Table 3.8: Computational complexity of piece-wise polynomial interpolators (Per interpolator).

Operation	**Parabolic** No. of operations	**Cubic** No. of operations
Real additions	$9NL$	$11NL$
Real multiplications	$2NL$	$3NL$
Register shifting	$5NL$	$8NL$
ROM access	1	3

3.3.3 Energy consumption of timing recovery systems

We summarize the computational complexity of previously discussed algorithms and interpolators in Table 3.9 where a piece-wise parabolic interpolator is assumed to be used. An over-sampling factor of four is considered for Oerder & Meyr estimators (SLN, AVN and LOGN), while an over-sampling factor of two is considered for Zhu and Lee estimators. L symbols are considered to generate one estimate.

We then convert the complexity into energy consumption by applying the energy framework and present the energy consumption as a function of block size L in Table

Table 3.9: Computational complexity summary of the timing recovery system.

Operation	**SLN**	**AVN**	**LOGN**	**Zhu**	**Lee**	**Interpolator (N=4)**	**Interpolator (N=2)**
Real additions	$8L-2$	$8L-2$	$12L-2$	$16L-2$	$8L-2$	$72L$	$36L$
Real multiplications	$8L+1$	$8L+1$	$12L+2$	$24L$	$8L+1$	$16L$	$8L$
Argument	1	1	1	1	1	-	-
ROM access	1	1	2	4	1	1	1
Square-root	-	$4L$	-	-	-	-	-
Logarithm	-	-	$4L$	-	-	-	-
Register shifting	-	-	-		$4L$	$40L$	$20L$
LPF	-	-	-	$8L$	-	-	-

Table 3.10: Energy budget variation of the timing recovery systems with L (in nJ).

Block length (L)	**SLN**	**AVN**	**LOGN**	**Zhu**	**Lee (N=4)**	**Interpolator (N=2)**	**Interpolator**
16	1.1	1.5	2.1	5.3	1.2	3.0	1.5
32	2.1	2.9	4.1	10.5	2.3	6.1	3.0
64	4.3	5.9	8.1	21.0	4.6	12.2	6.1
128	8.6	11.7	16.1	42.1	9.2	24.4	12.2
256	17.1	23.4	32.0	84.1	18.3	48.8	24.4

3.10.

As Oerder & Meyr estimators (SLN, AVN and LOGN) require four samples per symbol, interpolator with an over sampling factor of four should be adopted with the estimators. In these systems, interpolators consume higher levels of energy mainly due to the high number of samples being used. In comparison with SLN and AVN, the LOGN estimator consumes higher levels of energy, mainly due to the additional arithmetic operations and memory accesses.

Zhu and Lee estimators operate with interpolators of two samples per symbol. Even though the Zhu estimator operates at a lower sampling rate at than the Oerder & Meyr estimator, it consumes more energy than other estimators. This is mainly due to the fact that it requires a higher number of arithmetical calculations and low pass filters. However, the Lee estimator-based system gives the lowest energy consumption for a fixed block size due to the lower interpolator energy.

Figure 3.5 shows a new metric to compare the energy consumption of SLN, AVN, LOGN and Lee estimator–based timing recovery systems to achieve a given MSE as a function of SNR. MSE values of 10^{-3} and 10^{-2} are considered. Both the estimator energy and interpolator energy are considered in the analysis. The MSE simulation similar to that described in Section 2.3.3 have been used with a roll–of–factor of 0.35 and the initial timing offsets uniformly distributed between -0.5 and 0.5.

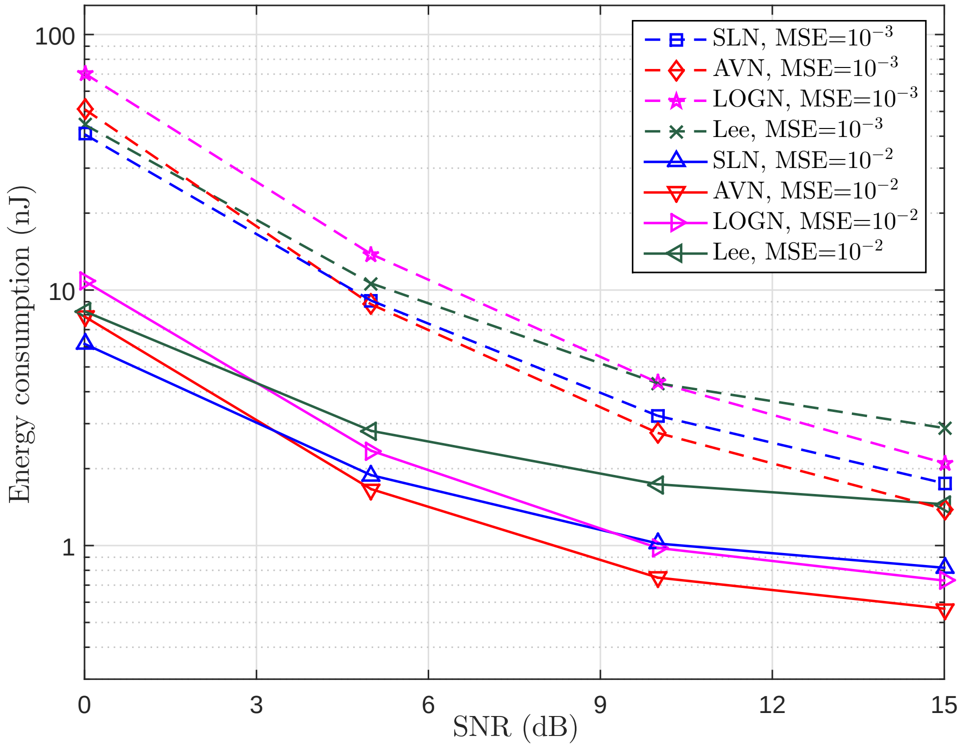

Figure 3.5: Energy consumption comparison of different timing recovery systems.

According to Figure 3.5, the Lee estimator consumes the highest levels of energy with an MSE of 10^{-2}, when the SNR is higher than 5 dB. For an MSE of 10^{-3}, it consumes less energy than Oerder & Meyr systems when the SNR is less than 10 dB. The main reason for the high energy consumption of the Lee based system is that its MSE performance is poor in comparison with other estimators; therefore, it needs a high number of symbols which results in more energy consumption, even though it uses fewer of samples. However, in order to count the effect of sampling rate, we need to consider the energy consumption of the interpolator and analog-to-digital converter (ADC).

AVN and LOGN estimators have more complexity than others; however, AVN produces the best MSE performance for a SNR higher than 5 dB and LOGN performs poorly when SNR is less than 10dB. The AVN requires fewer symbols to obtain the given MSE values, hence AVN consumes the lowest levels of energy when SNR is higher than 5 dB. When SNR is at 0 dB, SLN is the most energy efficient.

This result was affected by the selection of excess bandwidth of Nyquist pulse. Over-sampling rate also has a strong influence on devices such as ADC, which operate prior to the timing recovery system. Therefore, these need to be considered when making decisions in relation to output of energy budget.

3.3.4 Feedback-based Timing Recovery Systems

In this section, we analyze the complexity and energy consumption of feedback-based timing recovery systems. A block diagram of the proposed feedback-based timing recovery system is shown in Figure 3.6. Our system consists of a TED, a loop filter, an interpolation controller and an interpolator. We focus on Gardner TED [57] (GTED), Zero Crossing TED (ZCTED) [51], and Mueller & Muller TED (MMTED) [58] as they are quite popular in practical receivers [45, 51]. Proportional and integrator loop filters were used due to their ability to correct the small symbol rate mismatches. Piece-wise parabolic interpolators were used as in the previous section. Interpolation controllers were used to feed the precise timing error to the interpolator and to sample the symbol at the optimum position. N is the over-sampling factor which takes the value of two when ZCTED and GTED are used, and the value of one when MMTED is used.

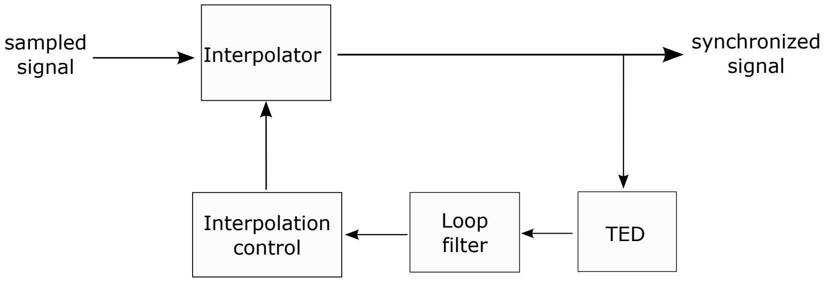

Figure 3.6: A block diagram of a feedback-based timing recovery system.

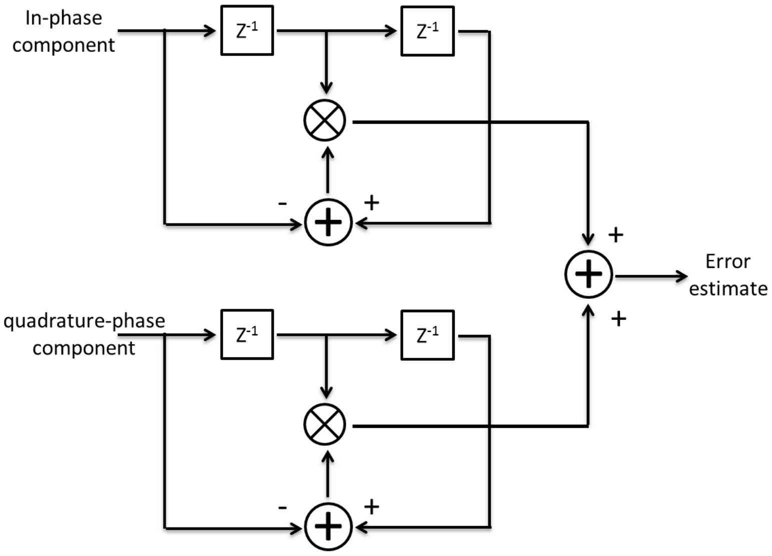

Figure 3.7: Hardware implementation architecture of the Gardner TED.

The output of GTED is defined as [57] follows:

$$\begin{aligned} e(k) &= x((k-1/2)T_s+\hat{\tau})[x((k-1)T_s+\hat{\tau})-x(kT_s+\hat{\tau})] \\ &\quad +y((k-1/2)T_s+\hat{\tau})[y((k-1)T_s+\hat{\tau})-y(kT_s+\hat{\tau})]\,, \end{aligned} \tag{3.4}$$

where $a_0(k)$ and $a_1(k)$ represent in-phase and quadrature-phase components of the symbols. Then $x(t)$ and $y(t)$ are in-phase and quadrature-phase components of the received signal at time t. $\hat{\tau}$ is previous timing estimate.

The output of ZCTED is defined as [51] follows:

$$\begin{aligned} e(k) &= x((k-1/2)T_s+\hat{\tau})[a_0(k-1)-a_0(k)] \\ &\quad +y((k-1/2)T_s+\hat{\tau})[a_1(k-1)-a_1(k)] \end{aligned} \tag{3.5}$$

MMTED output is mathematically represent as follows [45]:

$$\begin{aligned} e(k) &= a_0(k-1)x(kT_s+\hat{\tau})-a_0(k)x((k-1)T_s+\hat{\tau}) \\ &\quad +a_1(k-1)y(kT_s+\hat{\tau})-a_1(k)y((k-1)T_s+\hat{\tau}) \end{aligned} \tag{3.6}$$

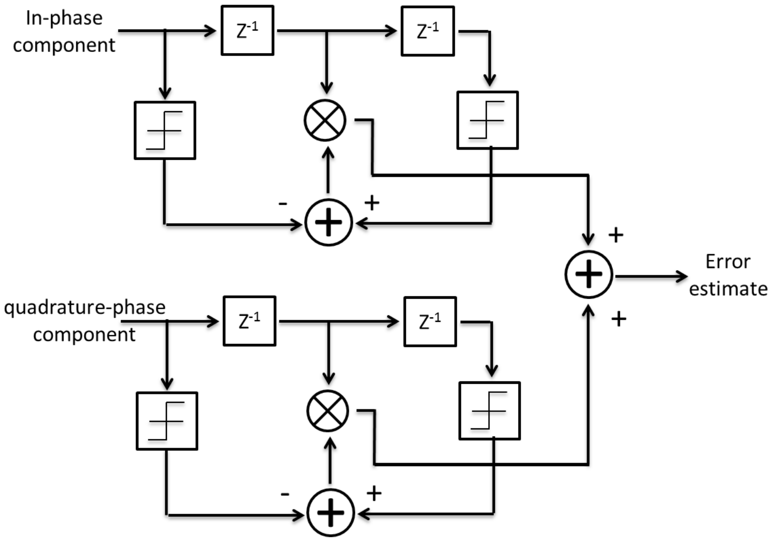

Figure 3.8: Hardware implementation architecture of the Zero Crossing TED.

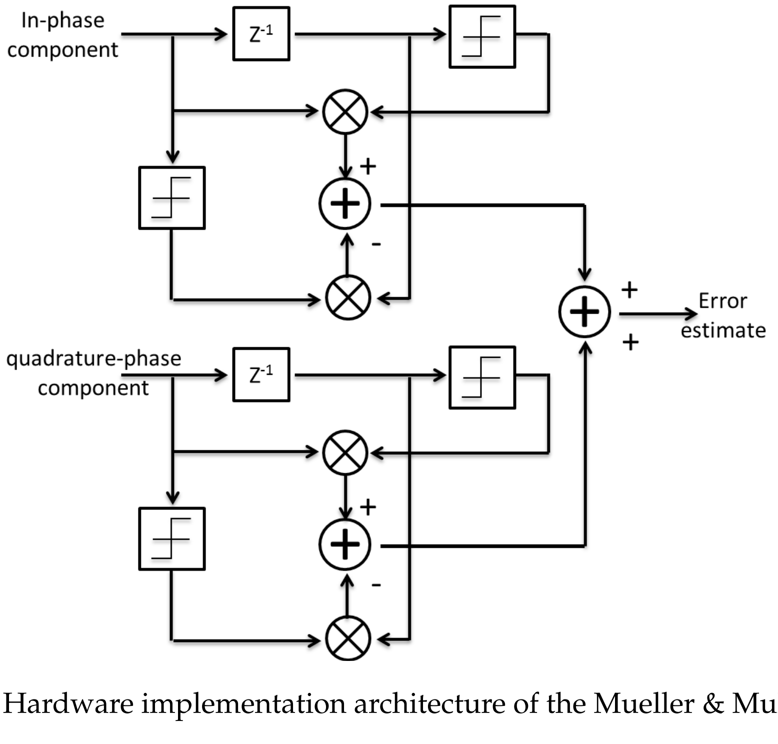

Figure 3.9: Hardware implementation architecture of the Mueller & Muller TED.

Computational complexity summary of different modules of the timing recovery system is presented in Table 3.11 based on the implementation block diagrams of interpo-

Table 3.11: Computational complexity summary of feed-back based timing recovery systems.

Operation	**Gardner TED**	**ZCTED**	**MMTED**	**Loop filter**	**Interpolation controller**	**Interpolator**
Real additions	3	3	3	$2N$	$2N+1$	$18N$
Real multiplications	2	2	4	$2N$	-	$4N$
Register shifts	4	4	2	N	-	$10N$
Divisions	-	-	-	-	1	-
ROM access	-	-	-	-	-	2

lation controller and loop filters. The complexity of TEDs can be derived from the block diagrams in Figure 3.7, 3.8 and 3.9. The complexity of TEDs is given as number of computations carry out in a symbol duration (i.e. GTED and ZCTED operates twice). After applying the complexity–energy framework, energy consumption of different components and algorithms were developed and presented in Table 3.12.

Table 3.12: Energy consumption of feed-back based timing recovery systems (in pJ per symbol).

Gardner TED	**ZCTED**	**MMTED**	**Loop filter**		**Interpolation controller**		**Interpolator**	
			$N=2$	$N=1$	$N=2$	$N=1$	$N=2$	$N=1$
22.53	22.53	34.89	35.82	17.91	12.06	10.2	129.70	71.02

According to Table 3.12, Gardner-based and ZCTED-based timing recovery loops consume 200.11 pJ in total per symbol. The MMTED-based timing recovery system consumes 134.02 pJ in total per symbol; therefore, the single-sample-based timing recovery loop consumes less energy. However, the actual energy efficiency can only be measured after considering the performance of these estimators.

3.4 Frequency Recovery Systems

In this section, we analyze the computational complexity and energy consumption of carrier frequency recovery systems. Unlike timing recovery systems, the majority of the complexity in frequency recovery systems belongs to the estimators. Some estimators can be realized using different architectures.

A block diagram of a feed-forward frequency recovery system is given in Figure

3.10. This system consists of a preamble processing unit, a frequency estimator and a frequency correction unit. During the training mode, preambles are used to make the initial estimate. During the data mode, either previous estimate with frequency correction or decision-directed operation of frequency estimators are used. In these figures, $x(k)$ represents the perfectly sampled received signal; c_k^* represents the conjugate of complex-modulated symbols and $z(k)$ represents the received signal after removal of the modulation.

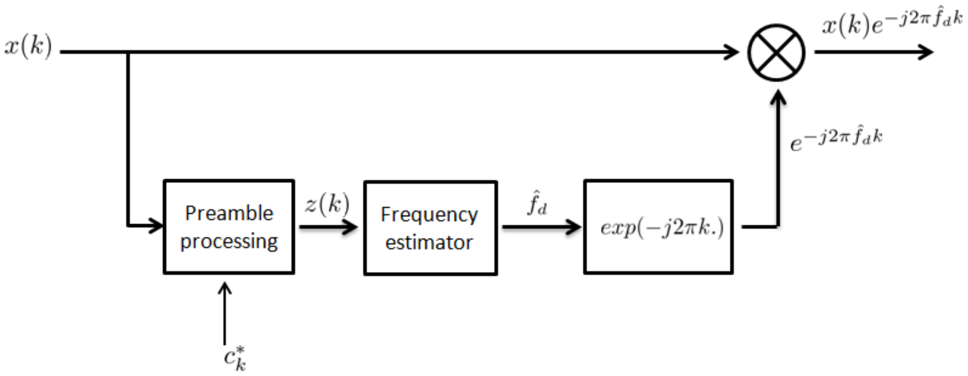

Figure 3.10: A block diagram of the frequency recovery system.

3.4.1 Preamble processing unit

The frequency estimators use preambles to remove the modulation of the received symbols. The received symbols are multiplied with the complex conjugate of the relevant preambles. Figure 3.11 represents the preamble processing unit. The complexity of this unit is presented in Table 3.13.

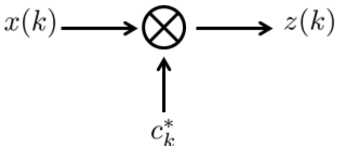

Figure 3.11: Hardware implementation architecture of the preamble processing unit.

Table 3.13: Computational complexity of the preamble processing unit.

Operation	**No. of operations**
Real additions	$2L$
Real multiplications	$4L$

3.4.2 Frequency estimators

The computational complexity of several feed-forward frequency estimators is discussed by Morelli et al. using several approximations [5]. The autocorrelations–based estimators can be implemented in both time and frequency domains. In time domain based implementation, computational complexity increases exponentially with the block size L of the estimator. In frequency domain calculations, autocorrelation becomes multiplication, which reduces complexity in comparison with time domain [5]. Fast Fourier Transform (FFT) can be used for efficient implementation of frequency domain conversion of discrete signals; therefore, a suitable implementation approach should be chosen depending on the block length.

Kay estimator

The Kay estimator can be implemented in hardware as shown in Figure 3.12 [3]. The incoming data is used to calculate the difference between neighboring phase angles which consume $L-1$ additions. The final estimator can be taken after $L-1$ multiplications and $L-2$ additions at the mixer and accumulator. The total computations needed for the Kay estimator are summarized in Table 3.14.

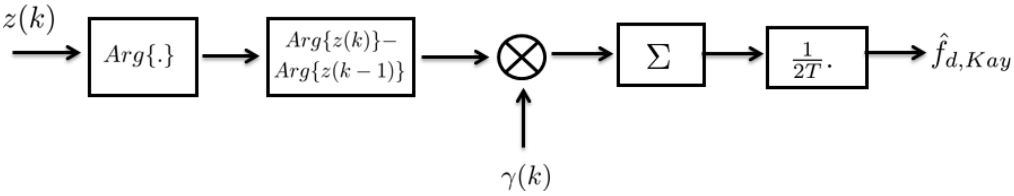

Figure 3.12: Hardware implementation architecture of the Kay estimator [3].

Kay estimator is defined as [3],

$$\hat{f}_d = \frac{1}{2\pi T_s} \sum_{k=1}^{L-1} \gamma(k) \arg\{z(k)z^*(k-1)\} \tag{3.7}$$

where, $\hat{f}_d$ is the estimate of carrier frequency offset, T_s is symbol time, $z(k)$ are the received symbols after modulation removal using preamble. $\gamma(k)$ are the weighting factors.

Table 3.14: Computational complexity of the Kay estimator.

Operation	**No. of operations**
Real additions	$2L-3$
Real multiplications	L
Argument	L
ROM access	L
Register shifting	$L-1$

Luise and Reggianni estimator

An implementation block diagram of the Luise and Reggianni (L&R) estimator, which was first is shown in Figure 3.13 and proposed by authors in their original paper [4]. The autocorrelation vector $R(m), m = 1, 2, ...N$ was calculated in parallel using multiple paths. Shift registers, complex multipliers and complex adders were used to calculate the autocorrelation vector. At each clock cycle the content of each register is shifted to the following one and multiplied by a constant and then summed together. All the additions and multiplications up to the final accumulator are performed as complex numbers. The computational complexity summary of the L&R estimator is presented in column three of Table 3.15.

L&R estimator is defined as [4] follows:

$$\hat{f}_d = \frac{1}{\pi T_s (N+1)} \arg\left\{\sum_{m=1}^{N} R(m)\right\}, \tag{3.8}$$

where N is limited by $N \leq L/2$ and $N \leq 1/(f_d T_s)$ conditions.

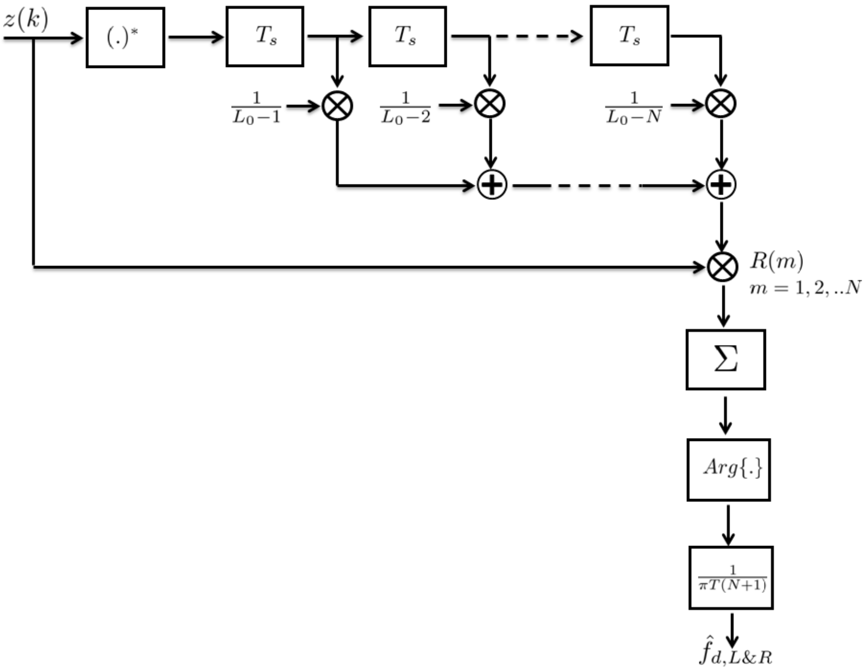

Figure 3.13: Hardware implementation architecture (time domain) of the L&R estimator [4].

The L&R algorithm can be implemented using frequency domain autocorrelation calculation approach [5] as in Figure 3.14 where FFT is used to perform DFT operation [78]. First, N zeros are added to L number of symbols to perform the FFT operation on $L + N$ sized block. The absolute square of the FFT output $Z(n)$ is calculated and then the inverse fast Fourier transform (IFFT) is performed. Using the last L values in the IFFT output $y(m)$, the autocorrelation vector is calculated. Radix-2 based FFT implementation is assumed in our system. The resultant complexity is included in Table 3.15.

Fitz estimator

An efficient implementation model of the Fitz estimator is presented by the author in the original paper [6] as shown in Figure 3.15. Parallel paths are used to calculate the autocorrelation vector $R(m)$. In each path, a shift register, a complex conjugate operator,

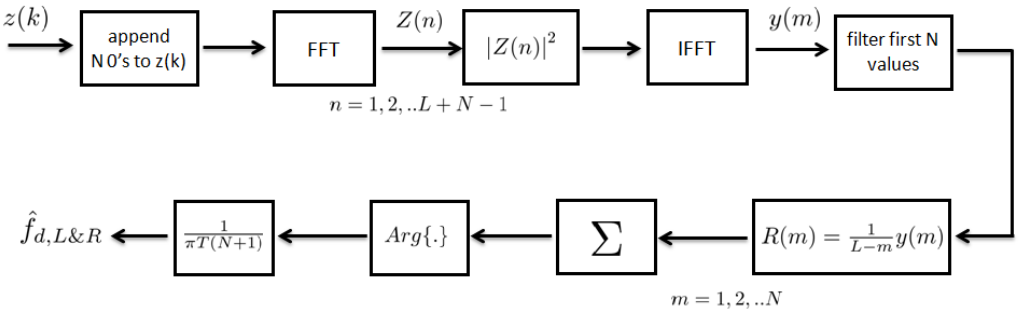

Figure 3.14: Hardware implementation architecture (FFT-based) of the L&R estimator [5].

Table 3.15: Computational complexity of the L&R estimator.

Operation	**Time domain implementation**	**FFT-based implementation**
	No. of operations	No. of operations
Real additions	$2NL + N - 1$	$6(L + N)\log_2(L + N) + L + 2N - 1$
Real multiplications	$2NL + 4L + 1$	$4(L + N)\log 2(L + N) + 2L + 3N + 1$
ROM access	$N + 1$	$(L + N)\log 2(L + N) + N + 1$
Argument	1	1
Register shifting	$NL - N$	–

two multipliers, an accumulator, and an argument operator is used. A complete block diagram of the Fitz algorithm is shown in Figure 3.15.

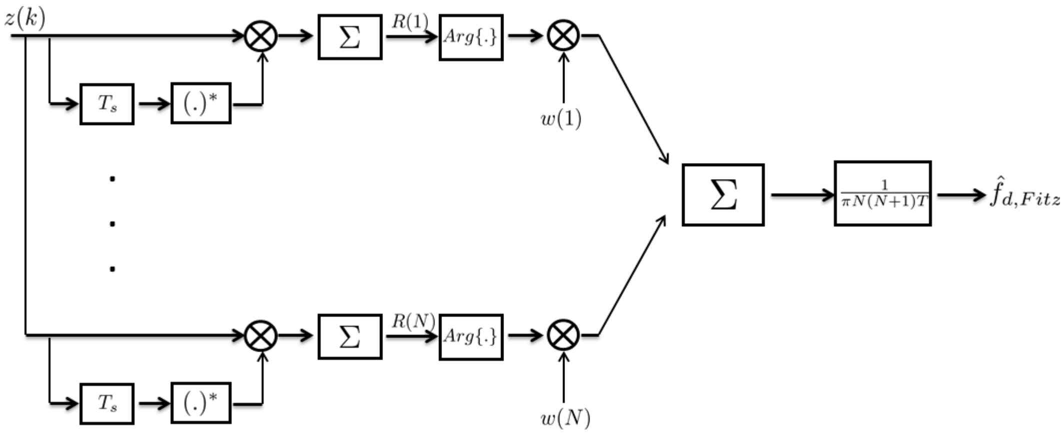

Figure 3.15: Hardware implementation architecture (time domain) of the Fitz estimator [6].

Fitz estimator is defined as [6]

$$\hat{f}_d = \frac{1}{\pi N(N+1)T_s} \sum_{m=1}^{N} \arg\{R(m)\} \;, \tag{3.9}$$

where N satisfies the conditions $N \leq 1/(f_d T_s)$ and $N \leq L/2$.

The Fitz algorithm can be implemented using FFTs similar to the Luise & Reggianni algorithm. A computation analysis for time domain and frequency domain implementations of the Fitz estimator are included in Table 3.16.

Table 3.16: Computational complexity of the Fitz estimator.

Operation	**Time domain implementation** No. of operations	**FFT-based implementation** No. of operations
Real additions	$4NL - 2N^2 - 3N - 1$	$6(L+N)\log_2(L+N) + L + 2N - 1$
Real multiplications	$4NL - 2N^2 - N + 1$	$4(L+N)\log_2(L+N) + 2L + 4N + 1$
ROM access	$N+1$	$(L+N)\log_2(L+N) + N + 1$
Argument	N	N
Register shifting	$NL - N^2/2 - N/2$	–

Mengali and Morelli estimator

The Mengali & Morelli estimator can be implemented using a similar architecture as the Fitz estimator. The autocorrelations are calculated as in Fitz model, then the phase differences are calculated prior to multiplying by the weighted constants $w(m)$ and an accumulator. A complete block diagram of this estimator is shown in Figure 3.16.

M&M estimator is mathematically defined in [64] as

$$\hat{f}_d = \frac{1}{2\pi T_s} \sum_{m=1}^{N} \gamma(m)\left[\arg\{R(m)\} - \arg\{R(m-1)\}\right]_{2\pi} \;, \tag{3.10}$$

where, $\gamma(m)$ are the weighting factors and $N \leq L/2$.

A frequency domain based implementation similar to the Fitz estimator is also considered. Required number of computations were analyzed and are presented in Table

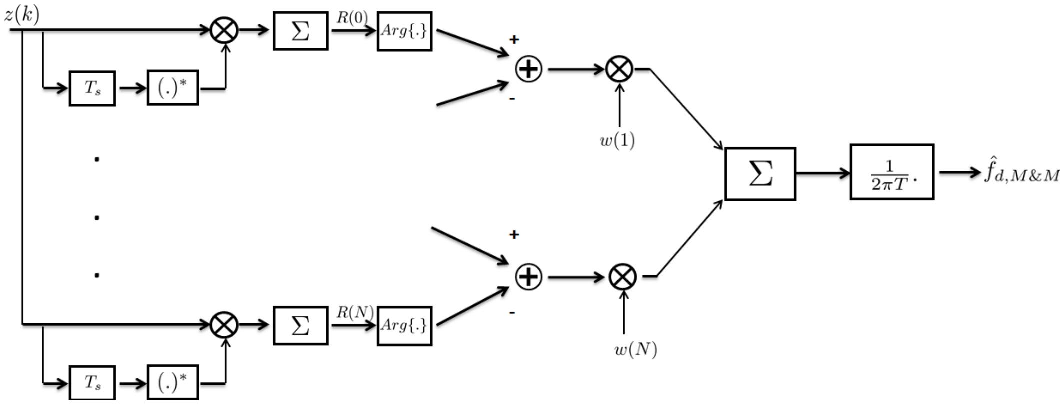

Figure 3.16: Hardware implementation architecture (time domain) of the Mengali & Morelli estimator.

Table 3.17: Computational complexity of the Mengali & Morelli estimator.

Operation	**Time domain implementation** No. of operations	**FFT-based implementation** No. of operations
Real additions	$4NL + 4L - 2N^2 - 2N - 3$	$6(L+N)\log_2(L+N) + L + 3N - 1$
Real multiplications	$4NL + 4L - 2N^2 - N + 1$	$4(L+N)\log_2(L+N) + 2L + 4N + 2$
ROM access	$N + 1$	$(L+N)\log_2(L+N) + 2N + 2$
Argument	$N + 1$	$N + 1$
Register shifting	$NL - N^2/2 - N/2$	$-$

3.17.

3.4.3 Frequency correction

The estimated frequency errors are corrected by the frequency correction unit. It can be simply implemented as shown in Figure 3.17. The phase angle for each symbol is calculated using the frequency error and multiplied by the received symbol to de-rotate the constellation. The computational cost for the frequency correction unit is given in Table 3.18.

3.4.4 Energy consumption of frequency recovery systems

The computational complexity of frequency recovery systems is summarized in Table 3.20. The preamble processing energy is also added to the estimator as it is compulsory

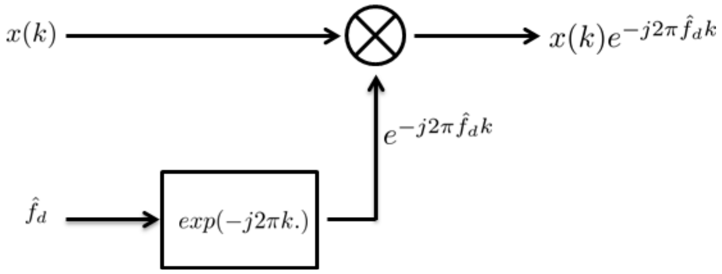

Figure 3.17: A block diagram of the frequency correction unit.

Table 3.18: Computational complexity of the frequency correction unit.

Operation	**No. of operations**
Real additions	$3L$
Real multiplications	$5L$
Register shifting	$2L$
Complex exponential	L

for the estimation. For autocorrelation based estimators, we assume $N = L/2$, which is half of the symbol block size. We calculated the energy consumption for different block sizes of frequency estimators and the frequency correction unit, and the results are presented in Table 3.19.

Table 3.19: Energy budget variation of frequency recovery systems with L (in nJ).

Block length (L)	**Kay**	**L&R**	**L&R (FFT)**	**Fitz**	**Fitz (FFT)**	**M&M**	**M&M (FFT)**	**Frequency correction**
16	0.9	3.5	4.9	3.9	5.0	4.5	5.0	0.7
32	1.8	11.8	11.4	14.8	11.7	15.9	11.8	1.5
64	3.6	43.3	26.3	57.0	26.7	59.2	26.9	3.0
128	7.1	164.9	59.3	224.2	60.1	228.5	60.6	5.9
256	14.2	643.4	132.1	888.5	133.8	897.2	134.7	11.8
512	28.4	2541.1	291.2	3537.6	294.7	3554.9	296.5	23.6

Table 3.20: Computational complexity summary of frequency recovery systems.

Operation	**Kay**	**L&R**	**L&R (FFT)**	**Fitz**	**Fitz (FFT)**	**M&M**	**M&M (FFT)**	**Frequency correction**
Real additions	$4L-3$	$L^2+2.5L$ -1	$9L\log_2(1.5L)$ $+4L-1$	$1.5L^2+0.5L$ -1	$9L\log_2(1.5L)$ $+4L-1$	$1.5L^2+5L$ -3	$9L\log_2(1.5L)$ $+4.5L-1$	$3L$
Real multiplications	$5L$	L^2+8L $+1$	$6L\log_2(1.5L)$ $+7.5L+1$	$1.5L^2+3.5L$ $+1$	$6L\log_2(1.5L)$ $+8L+1$	$1.5L^2+7.5L$ $+1$	$6L\log_2(1.5L)$ $+8L+2$	$5L$
ROM access	L	$0.5L+1$	$0.5L+1$	$0.5L+1$	$0.5L+1$	$0.5L+1$	$L+2$	-
Argument	L	1	1	$0.5L$	$0.5L$	$0.5L+1$	$0.5L+1$	-
Register shifting	$2L-2$	L^2-L	-	$0.75L^2-0.5L$	-	$0.75L^2-0.5L$	-	$2L$
Complex exponential	-	-	-	-	-	-	-	L

As Table 3.19 reveals the autocorrelation based estimators consume more energy than the Kay estimator, due to the fact that autocorrelation calculation requires significantly high complexity. Another important observation is that for larger blocks, the complexity of FFT-based implantations have a lower energy cost than time domain implementations; therefore, frequency domain implementation becomes more energy efficient as block size increases.

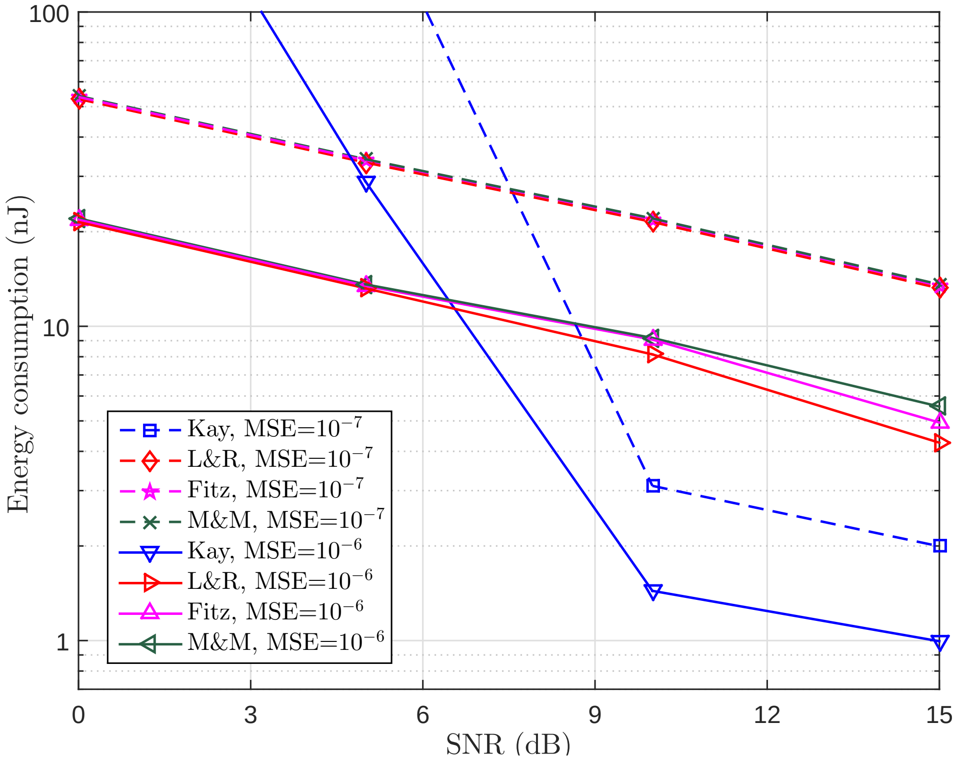

Figure 3.18: Energy consumption comparison of different frequency estimation algorithms.

We now investigate the energy consumption of four frequency estimators by making the MSE fixed at different SNR values. Two different MSE values were considered: 10^{-6} and 10^{-7}, and the required number of symbols to achieve the given MSE was found using simulations. Then the energy consumption was calculated from Table 3.19 .

The energy consumption of the Kay estimator [3], Luise & Reggianni estimator[4], Fitz estimator [6] and Mengali & Morelli estimator [64] are calculated and presented as a function of SNR in Figure 3.18. The vertical axis represents the energy consumption in nJ in logarithmic scale.

The Kay estimator is a least square-based estimator and the other three estimators are autocorrelation based estimators. We used the least complex approach for time domain and frequency domain implementations for a given block size. The energy consumption of autocorrelation based estimators are higher than the Kay estimator when SNR is greater than 10 dB, due to the high computational cost of autocorrelation estimators. We observed that the energy consumption of the Kay estimator increases rapidly and exceeds the energy consumption of autocorrelation estimators when SNR is less than 5 dB. The main reason for this behavior is that the Kay estimator performs poorly at low SNRs (< 10 dB); i.e. the Kay estimator needs a very high block size in order to achieve the same MSE as the other three estimators. It is, therefore, inefficient to use the Kay estimator for low SNR operation.

As indicated in Table 3.19, the Mengali & Morelli estimator has the highest complexity, thus consuming the most energy. However, as the required MSE is reduced from 10^{-6} to 10^{-7}, energy consumption of all autocorrelation algorithms converge to approximately the same value.

According to the Figure 3.18, we can conclude that the Kay estimator is most energy efficient when SNR is higher than 10 dB, and autocorrelation based estimators are most energy efficient when operating in low SNR region. When selecting an algorithm, however, it is also important to consider the estimation range as discussed in section 2.4.

3.5 Phase Recovery Systems

This section presents the computational complexity and energy costs of carrier phase recovery systems for feed-forward and feedback-based approaches. A block diagram of a feed-forward carrier phase recovery system is shown in Figure 3.19. This system consists of a phase estimator, a phase un-wrapper and a phase correction unit. We focus on two phase estimators: data-aided ML phase estimator and non data-aided Viterbi & Viterbi (V&V) estimator with different configurations of non-linear function ($F(\rho) = 1$, ρ and ρ^2). When calculating the computational complexity of the ML estimator, preamble

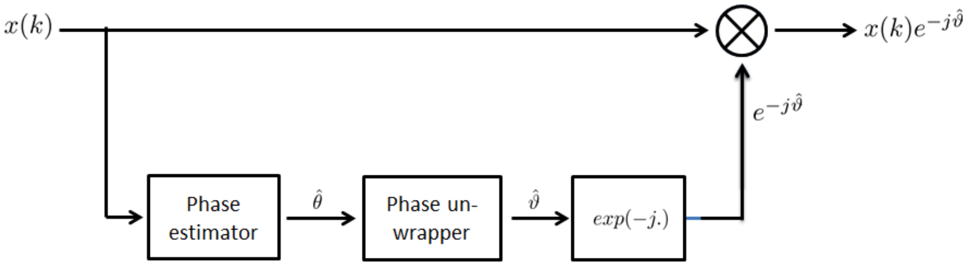

Figure 3.19: A block diagram of the phase recovery system.

processing was considered.

As the phase estimators have limited estimation ranges, higher phase errors produce phase ambiguities, for example, $\pi/4$ for Viterbi & Viterbi estimators. In addition, residual frequency errors result in changing the phase offsets at constant rates. Therefore, it is important to track and correct the phase errors continuously. A phase un-wrapper is used to achieve this objective. The complexity of the phase un-wrapper is considerably small as it operates only once per estimate, hence the computational cost of the phase un-wrapper is negligible in comparison with other modules in the phase recovery system.

ML phase estimator

In data-aided ML phase estimator, modulation of the received symbols is removed with the aid of preambles. The average angle of symbols is then calculated to estimate the phase offset of the received signal as in Figure 3.20. The computational cost of the ML phase estimator is summarized in Table 3.21. ML estimator is defined as follows [51]:

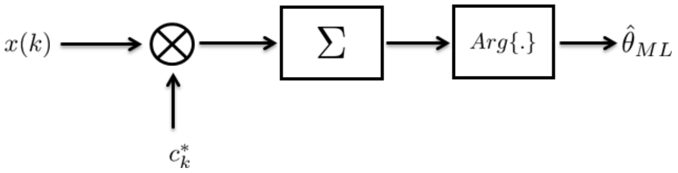

Figure 3.20: A block diagram of the ML phase estimator.

$$\hat{\theta}_{ML} = \arg\left\{\sum_{k=0}^{L-1} c_k^* x(k)\right\} , \tag{3.11}$$

where $x(k)$ is the input signal at kth instance c_k^* is the complex conjugate of the preamble at kth instance. $\hat{\theta}_{ML}$ is the estimate and L is the block size.

Table 3.21: Computational complexity of the ML phase estimator.

Operation	**No. of operations**
Real additions	$4L-2$
Real multiplications	$4L$
Argument	1

Viterbi & Viterbi phase estimator

The Viterbi & Viterbi phase estimator has different configurations based on the non-linear function ($F(\rho) = 1$, ρ and ρ^2). An implementation block diagram for the general model of V&V estimator is presented in Figure 3.21.

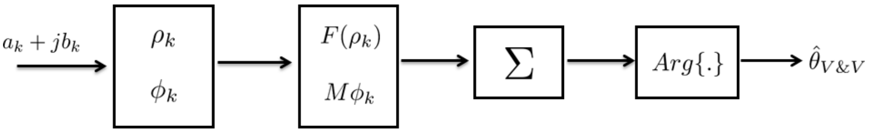

Figure 3.21: A block diagram of the Viterbi & Viterbi phase estimator [7].

The input complex signal is $x(k)$. It can be written as, $x(k) = a_k + jb_k$, where $a_k =$ real$(x(k))$ and $b_k =$ imaginary$(x(k))$. The parameters of the estimator, are calculated as $\rho_k = \sqrt{a_k^2 + b_k^2}$ and $\phi_k = \tan^{-1}(b_k/a_k)$. The nonlinear transformation function is defined as $F = \rho_k^n$ where n is the order of the non linearity and $n = 0, 1$ and 2.

Then new variables a'_k and b'_k are then calculated as

$$a'_k + jb'_k = F(\rho_k)e^{jM\phi_k}$$

The final phase estimate is defined as follows [7]:

$$\hat{\theta}_k = \frac{1}{M}\tan^{-1}\left\{\frac{\sum_{k=0}^{N} b'_k}{\sum_{k=0}^{N} a'_k}\right\}, \tag{3.12}$$

where M is the signal constellation size.

The computational complexity for each configuration of Viterbi & Viterbi estimator is analyzed and presented in Table 3.22.

Table 3.22: Computational complexity of the Viterbi & Viterbi phase estimator.

Operation	**No. of operations** $F(\rho) = 1$	**No. of operations** $F(\rho) = \rho$	**No. of operations** $F(\rho) = \rho^2$
Real additions	$2L - 2$	$3L - 2$	$3L - 2$
Real multiplications	$L + 1$	$5L + 1$	$6L + 1$
Complex exponential	L	L	L
Argument	$L + 1$	$L + 1$	$L + 1$
Square root function	$-$	L	L

3.5.1 Phase un-wrapper

An implementation block diagram of a phase un-wrapper is shown in Figure 3.22 and its computational cost is summarized in Table 3.23. The output of the phase estimator is taken and compared with the un-wrapped output using a SAW function [1]. SAW function can be implemented in hardware with low complexity.

Table 3.23: Computational complexity of the phase un-wrapper

Operation	**No. of operations**
Real additions	2
Register shifting	1
SAW function	1

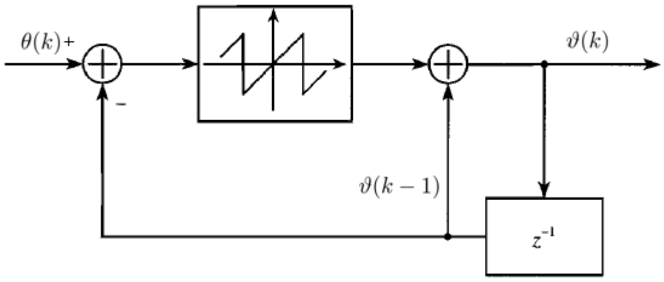

$$\vartheta(k) = \vartheta(k-1) + SAW[\theta(k) - \vartheta(k-1)]$$

Figure 3.22: A block diagram of the phase un-wrapper [1].

3.5.2 Phase correction

The final component in the feed-forward phase recovery system is the phase correction unit. It is used to de-rotate the signal constellation according to the phase estimates. An implementation model of a phase correction unit is shown in Figure 3.23. The computational cost for the phase correction unit is given in Table 3.24.

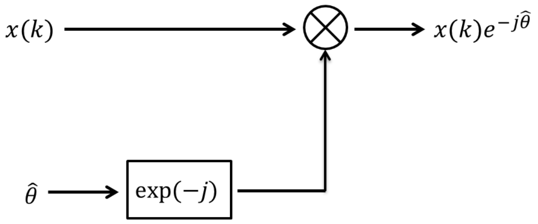

Figure 3.23: A block diagram of the phase correction unit.

Table 3.24: Computational complexity of the phase correction unit.

Operation	**No. of operations**
Real additions	$2L$
Real multiplications	$5L$
Complex exponential	1

3.5.3 Energy consumption of phase recovery systems

A summary of the computational complexity of different phase recovery systems is presented in Table 3.25. We calculated the energy consumption for each algorithm as a function of block size and the results are presented in Table 3.26.

Table 3.25: Computational complexity summary of phase recovery systems.

Operation	**ML**	**V&V (F(ρ) = 1)**	**V&V (F(ρ) = ρ)**	**V&V (F(ρ) = ρ^2)**	**Phase correction**
Real additions	$4L-2$	$2L-2$	$3L-2$	$3L-2$	$2L$
Real multiplications	$4L$	$L+1$	$5L+1$	$6L+1$	$5L$
Argument	1	$1L+1$	$1L+1$	$1L+1$	-
Complex exponential	-	L	L	L	1
Square-root	-	-	L	L	-

Table 3.26: Energy budget variation of phase recovery systems with L (in nJ).

Block length (L)	**ML**	**V&V (F(ρ) = 1)**	**V&V (F(ρ) = ρ)**	**V&V (F(ρ) = ρ^2)**	**Phase correction**
16	0.5	0.4	1.0	1.1	0.5
32	1.0	0.9	2.0	2.3	1.0
64	2.1	1.8	4.1	4.6	2.0
128	4.3	3.6	8.3	9.2	4.0
256	8.5	7.1	16.5	18.4	8.0

According to Table 3.26, the V&V estimator with square non-linear function consumes the highest levels of energy for a given block size. The data-aided ML estimator has the lowest energy consumption; however, compared with estimating algorithms, the phase correction unit consumes a significant amount of energy.

Energy consumption of data-aided ML algorithm and V&V algorithms are now compared by fixing the target MSE at 10^{-2} and 10^{-3}. V&V1, V&V2 and V&V3 represent the Viterbi & Viterbi algorithm with non-linear factors of $F(\rho) = 1$, $F(\rho) = \rho$ and $F(\rho) = \rho^2$ respectively. We changed the block size for each algorithm to achieve the same MSE at a given SNR.

The ML estimator achieves MCRB for all the SNR in the given range (0 - 15 dB), but Viterbi & Viterbi algorithms achieve MCRB after 10 dB. According to Figure 3.24, the

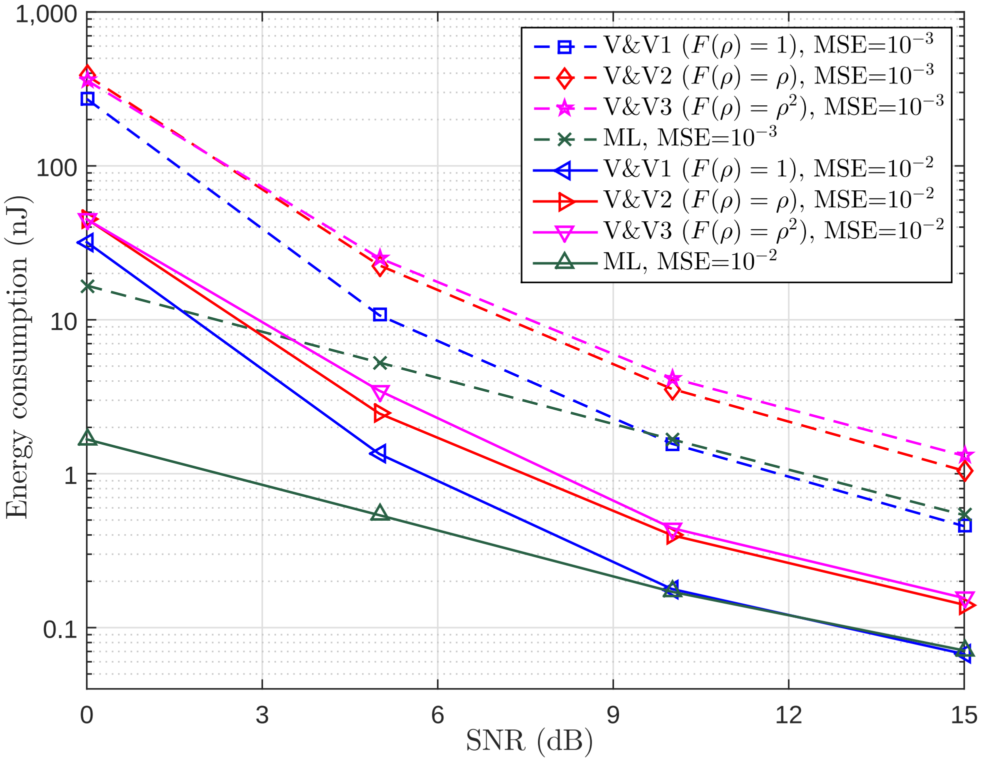

Figure 3.24: Energy consumption comparison of different phase estimation algorithms.

ML algorithm and V&V1 algorithm consume similar energy and the least in the higher SNR region (SNR >10 dB). But in the lower SNR region, energy consumption of V&V1 is higher than ML. The energy costs for V&V2 and V&V3 are almost the same, but higher than V&V1 because implementation of $F(\rho) = 1$ results in a simple computational model. Being non data-aided, they perform quite poorly at low SNR. Therefore, more symbols are needed to achieve the same MSE as ML at lower SNRs. According to Figure 3.24, V&V1 is the most energy efficient among the non-data-aided phase estimators.

3.5.4 Feedback-based Carrier Recovery Systems

This section presents the computational complexity of a feedback-based carrier synchronization system. A block diagram of our phase recovery system is given in Figure 3.25 [45]. This system consists of a phase error detector, a loop filter and a DDS. We used a digital phase-locked loop (PLL) with a first order proportional and integrator loop filter. This loop filter is capable of correcting small carrier frequency errors. The ML-based decision-directed phase error detector is adopted in our system. A direct digital synthesizer (DDS) is used to accumulate the phase of the PLL, which is equivalent to voltage control oscillator in an analog PLL [45, 51].

A summary of the computational complexity analysis of the feedback-based phase recovery system is presented in Table 3.27. The computational complexity is calculated for number of operations required in one symbol cycle.

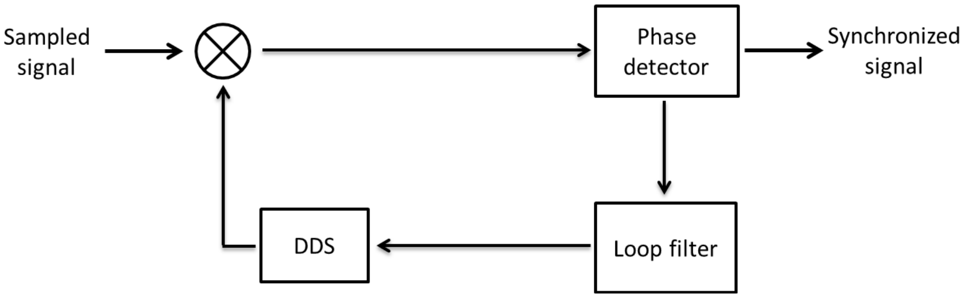

Figure 3.25: A block diagram of a feedback-based carrier recovery system.

Table 3.27: Computational complexity summary of feed-back based phase recovery systems.

Operation	**ML phase detector**	**Loop filter**	**DDS**	**Phase corrector**
Real additions	1	2	1	-
Real multiplications	2	-	-	2
Multiplications by a constant	-	2	-	-
Decisions	2	-	-	-
Sine & Cosine functions	-	-	2	-
Register shifts	-	1	1	-

We then derive the energy consumption of the phase recovery system and presented in Table 3.28. We have ignored the complexity of the decision making device, as it can be taken from the detector/decoder and it is in outside of the synchronization system.

Based on our calculations, the energy cost of the ML-based decision-directed phase recovery system was 62.98 pJ per symbol; this is far more energy efficient than feed-

Table 3.28: Energy consumption of feed-back based phase recovery systems (in pJ per symbol).

ML phase detector	Loop filter	DDS	Phase corrector
15.75	17.91	14.5	14.82

forward estimators.

3.6 Conclusions

In this chapter, we developed energy models for synchronization systems. These energy models provide energy costs for different synchronization functions, i.e. how much energy is consumed to remove frequency and phase offsets and to sample the signal at the optimum eye opening point.

We use our energy models to compare the energy efficiency of different estimation algorithms using a new metric: energy cost to achieve a given MSE. By doing so, we carried out a fair evaluation of synchronization algorithms from an energy efficiency perspective.

Considering the energy consumption of a combined synchronization system, typically, frequency estimators consume the highest energy due to the higher complexity (e,g, auto correlation calculations), and timing and phase estimators consume energy in a similar range. According to Table 3.10, 3.19 and 3.26, when block size of 256 is used, frequency (M&M), timing (AVN) and phase (V&V) estimators consume 134.7 nJ, 23.4 nJ, and 16.5 nJ per each estimate respectively. In general frequency estimation consists of the highest complexity among the feedforward estimators.

Our energy framework is developed based on computational complexity. While the actual energy consumption of these algorithms may vary, we considered many low-level operations such as memory access and register access along with the complexity of arithmetic operations, and our results should therefore provide a reasonably close approximation to actual energy consumption. More accurate energy costs can be measured by implementing the circuits on software platforms and simulating for power consumption.

Chapter 4

Energy Efficiency of Point-to-Point Wireless Transmission

A widely-used approach to increase the energy efficiency of wireless systems is to reduce transmit power. Although this approach is beneficial for high-power wireless systems, it may not save energy in small area networks and short distance transmission as the computational energy in digital hardware becomes more significant compared to the transmit radio energy. In this chapter, we investigate the energy-efficiency trade-offs of a point-to-point wireless system by developing energy models of both the transmitter and receiver that include practical aspects such as error control coding, synchronization and channel equalization. We assume a multipath Rayleigh-fading channel model and use a frequency-domain equalizer, regular low-density parity check (LDPC) codes with girth 6 and column weight 3, and fix specific synchronization algorithms for our energy models. The total energy consumption of this wireless system is modeled as a function of spectral efficiency, data rate, bandwidth spectrum, and received signal-to–noise ratio per bit $\frac{E_b}{N_0}$*. We develop a closed form analytical expression that approximates the total energy consumption as a function of* $\frac{E_b}{N_0}$ *and compare it to results from numerical simulation. A minimal-energy transmission configuration as a function of distance is determined, and results show that low-SNR-per-bit receiver operation is not always the most energy-efficient strategy, especially at very short distances. The digital component energy consumption is noteworthy at short distances and can reach upwards of 20% of the total system energy. This percentage varies non-monotonically as a function of distance due to changes in the optimal energy configuration (modulation order and code rate).*

4.1 Introduction

THE capacity of telecommunication networks has been growing rapidly over the last decade, and wireless access is identified as a key contributor to this fast growing traffic distribution [79]. While wireless is very convenient for user access, it is far less energy efficient compared to guided media like fiber and copper access technologies [23]. The spreading of wireless energy over the surrounding area causes this major inefficiency, which is further worsened by the low efficiency of wireless hardware.

Over the last decade, researchers have been working to reduce the energy consumption of wireless systems. Among the major projects, Green Radio, EARTH and GreenTouch investigated different approaches to improve the energy efficiency of wireless systems. [20] investigated fundamental tradeoffs of energy efficiency by considering four categories: bandwidth-power, delay-power, spectral efficiency-energy efficiency and deployment efficiency-energy efficiency. Among the recommendations for energy-efficient wireless systems, reduction of transmit power, adoption of beamforming techniques for multi-antenna systems, and implementation of heterogeneous cell concepts are widely popular.

In conventional wireless systems, energy consumption is mainly dominated by the transmitter power amplifier [80]. A direct approach to reduce energy consumption is to simply decrease the transmit power. This lowers the received signal-to-noise ratio (SNR) and increases the bit-error rate (BER) at the receiver. In order to compensate for the increased error performance, strong error-control coding (more redundancy) is required, which ends up lowering the spectral efficiency. Additional bandwidth is needed to support this extra redundancy to maintain the same information rate. The additional coding and increased bandwidth also result in a rise of signal processing load (mainly at the receiver), which increases the computational energy of the system. This chapter investigates the achievable energy gains of error-control coding while considering main transceiver functions such as amplification, sampling, equalization and synchronization.

Most of the energy-efficient wireless research has focused on saving transmit radio energy. The tradeoffs of energy efficiency with bandwidth, power and modulation schemes are discussed in [81] using a basic power-throughput model. Similar work is presented in [82] by investigating the energy efficiency and deployment efficiency tradeoffs for different cell types. [83] presents the bandwidth-power tradeoff in heterogeneous networks considering site-sleeping strategies and small-cell deployments. An overview of different energy-efficiency approaches such as radio resource management, network deployment, multiple-input multiple-output (MIMO), orthogonal frequency-division multiple access (OFDMA) and cross-layer design technologies were proposed in [30].

Energy-efficiency improvements in base stations and the transmitter side are proposed widely in the literature, but there still are some open problems to consider from the receiver-side perspective, including joint optimization of the transmitter and receiver energy consumption. This is particularly important for applications where energy is a critical resource due to being derived from batteries or harvested from solar, mechanical vibration, or wireless induction. Such scenarios may be commonplace in an internet of things (IoT) network made of sensors and other battery-powered and/or energy-harvested devices.

The overall energy savings of error-control coding schemes in low-power wireless systems is analyzed in [35] using a computational-complexity-based energy model of complementary metaloxide-semiconductor (CMOS) technology. Similar work is carried out in [36] by comparing the energy efficiency of various error-control codes with a distance-based path-loss model. However, this work uses constant energy consumption for the decoder which is independent of operating parameters. More advanced and accurate energy models for Reed-Solomon (RS) [72], BCH [84] and low-density parity check (LDPC) encoders and decoders [43] have been developed based on their computational complexity analysis. All of these works assume an additive white Gaussian noise (AWGN) channel, and therefore ignore the fading conditions present in practical wireless channels and relevant signal processing. [37] discusses energy efficiency in multipath fading channels by proposing basic energy models for a decision-feedback equalizer and an iterative LDPC decoder. Cui et al. in [33] studied the energy efficiency of wireless systems for two modulation types, quadrature amplitude modulation (QAM) and frequency-shift keying (FSK), by modeling the transmit energy and analog circuit components. More recently, [84] presented an energy-efficiency optimization approach that used BCH coding, but, the RF and baseband power consumption of the system were assumed to be constant irrespective of the transmission configuration (i.e. modulation scheme and code rate) which may lead to inaccurate energy modelling in low-power devices.

In this chapter, we consider a more complete wireless receiver energy model compared to previous works by including a detailed modelling of digital processing segments such as equalization and synchronization of carrier, phase and timing. To the best of our knowledge, this depth of energy analysis of both digital and analog components in wireless receivers has not been investigated previously. The more complete receiver modeling allows for the investigate the energy efficiency trade-offs of a point-to-point wireless transmission system by evaluating the computational complexity of hardware algorithms and modeling their corresponding energy consumption. The energy models are investigated as a function of modulation order, data rate, signal bandwidth, code rate, received SNR per bit and multipath channel parameters. We then simulate a system with practical characteristics such as multipath fading and channel coding. The total energy is then approximated analytically, and optimum solutions are derived for a given system requirement.

The organization of this chapter is as follows. Section 4.2 presents our system model and the signal processing algorithms used in it. In Section 4.3, we present the energy models of the various system components. In Section 4.4, we minimize the energy consumption of a point-to-point wireless transmission using numerical analyses. Finally, we summarize the results and give concluding remarks in Section 4.5.

4.2 System Model

We consider a point-to-point system with a single transmitter and receiver, with no other end users in the system and no interferers. A block diagram of our transmitter model is shown in Figure 4.1. We focus on a burst-mode, single-carrier, single-antenna transmission system in our work. A single-carrier system is chosen over orthogonal frequency-division multiplexing (OFDM) due to its lower peak-to-average power ratio (PAPR), which results in a higher energy efficiency at the transmit power amplifier compared to OFDM.

We employ a frequency-domain equalizer (FDE) due to its lower computational complexity compared to time-domain equalizers when the number of channel taps is large

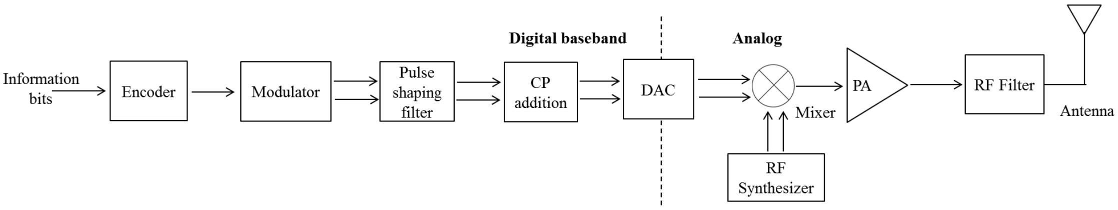

Figure 4.1: Block diagram of the transmitter analog and digital functions.

[47]. The information bits generated by upper layers are encoded, and these coded bits are linearly modulated into multiple quadrature amplitude modulation (M-QAM) symbols and passed through a pulse-shaping filter. Additional transmit samples are then added in the form of a cyclic prefix (CP) to help alleviate inter-symbol-interference (ISI) effects by allowing linear channel convolution to be modeled as circular convolution. The digital signal is then fed through a digital-to-analog converter (DAC). This analog signal is then up-converted to a carrier frequency and amplified using a power amplifier (PA) before transmission through a radio frequency (RF) filter and an antenna.

In our system, we consider a multipath Rayleigh fading channel with additive white gaussian noise. A direct conversion architecture [85] is employed with the block diagram shown in Figure 4.2. The received signal at the antenna is first filtered using a band-select RF filter. The signal then is amplified using a low-noise amplifier (LNA), followed by down-conversion to baseband. The baseband signal is then amplified using baseband amplifiers (BA), filtered and then sampled using analog-to-digital converters (ADC). The sampled signal after the digital front-end is assumed to be oversampled at two samples per symbol and matched filtered after removing the CP.

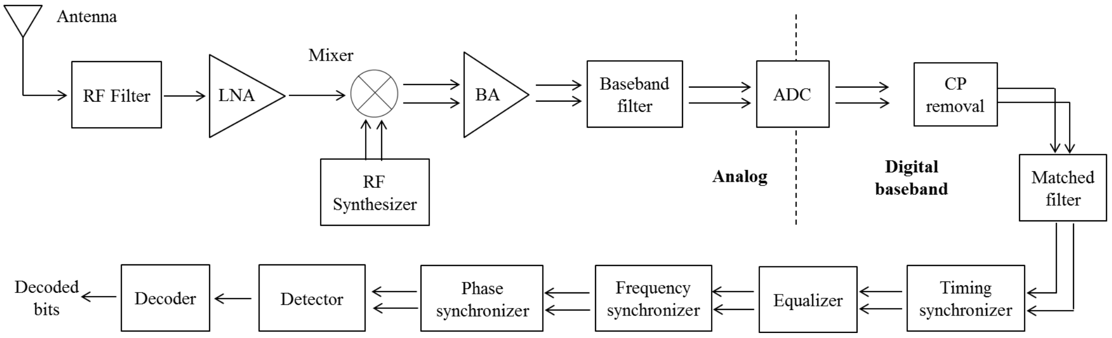

Figure 4.2: Block diagram of the receiver analog and digital functions.

4.2.1 Timing Recovery

Feedback-based timing recovery with a phase-independent timing error detector like Gardner [57] is utilized for our timing synchronizer because there is no optimal pulse peak in the presence of ISI but the recovery of clock frequency - instead of the clock phase - is still required for proper functioning of the equalizer delay line. The timing phase-offset correction is then passed over to the equalizer. Feed-forward timing estimators, on the other hand, can only detect a timing phase offset that is constant throughout the whole block length [1], [60], [2]. The output rate of the timing recovery loop is kept at two samples per symbol, as our chosen equalizer needs more than one sample per symbol.

4.2.2 Channel Equalization

The signal is then passed through a channel equalizer to invert the channel effects and remove the ISI. Wireless signals undergo various types of fading, depending on the environment, that can result in ISI. Time-selective fading occurs due to the variation of the channel with time. A receiver should estimate the new channel and other parameters as the channel changes slowly. Frequency-selective fading is due to the multipath signal reception at the receiver. In our system, we chose a multipath Rayleigh random channel model with an exponentially-decaying power delay profile for the channel taps, where the ratio of the last and the first taps is set as $1/e$. The FDE inverts the channel, and is also capable of compensating for small timing and phase errors [86]. Preambles are used to train the FDE and then equalizer taps are updated during data transmission to track channel variations. We use the least mean square (LMS) based adaptive algorithm [87] to update the minimum mean square error (MMSE) equalizer coefficients. The equalizer operates at two samples per symbol and outputs one sample per symbol.

4.2.3 Carrier and Phase Synchronization

The ISI-mitigated signal is then fed to a frequency synchronizer to remove the residue carrier frequency offsets. We chose a data-aided, feed-forward based approach to recover the carrier frequency error due to needing fast frequency acquisition. The Kay algorithm [3] has a low complexity compared to the other auto-correlation based estimators like Luise & Reggiani [4], Lovel & Williamson [63] and Mengali & Morelli [64] algorithms. However, it performs poor in the low-SNR-per-bit regime. The Mengali & Morelli estimator has a wider estimation range compared to Luise & Reggiani and Lovel & Williamson estimators, and we therefore adopt this algorithm to estimate the initial frequency offset during preamble transmission. During data transmission, we use this frequency offset estimate to correct the frequency error.

The frequency corrected signal is then sent through a phase synchronizer, which is required for reliable coherent symbol detection. We use the data-aided maximum-likelihood (ML) based feed-forward phase estimator [51] to estimate the initial phase offset. We then adopt a decision-directed ML phase recovery loop with a second-order loop filter [51] to correct phase errors and small residual frequency errors. The popular non-data-aided, feed-forward phase estimator in [7] is capable of estimating phase errors in 4-QAM modulated signals. However, non-data-aided, feed-forward phase estimators perform quite poorly in higher order modulation schemes as shown in [51]. Therefore, in order to compare the performance of various M-QAM modulation schemes, we adopted a carrier recovery loop in our system.

4.2.4 Decoder

Finally, the synchronized signal is detected and decoded using an iterative decoder. We chose LDPC as the channel coding scheme due to its superior error-correcting capability [88]. In our initial work [89], we used Reed-Solomon codes and observed the achievable performance gain was limited at a bit-error rate of 10^{-4}. In this work, we use LDPC codes with girth six and column weight three quasi-cyclic [90]. Girth is defined as the shortest cycle in the bipartite graph representing the parity-check matrix of the LDPC code. Column weight denotes the number of ones in each column in the parity-check matrix. We use iterative LDPC soft decoding to recover the transmitted bits [91]. Each symbol in a received code block corresponds to a variable node unit (VNU) and each parity check constraint corresponds to a check node unit (CNU). The decoder uses the scaled min-sum algorithm for the CNU and VNU computations [43], [91]. We employ different rates of LDPC codes by first fixing the information bit length k, then allowing the code length n to vary, which results in the code rate k/n. We then scale the transmission bandwidth so that the data rate remains constant for all considered codes.[1]

4.2.5 Preamble Training

The receiver needs to be initialized using training sequences (preambles) to estimate several parameters such as the equalizer coefficients, symbol-timing error, carrier-frequency error and carrier-phase error. Apart from these, a practical receiver may also estimate the signal power, noise power and I-Q imbalance, the latter of which we ignore in our system model. We use 4-QAM symbols for our preambles which are transmitted using the same RF bandwidth allocated for data transmission. The required preamble size and percentage is calculated according to the application requirement and channel model.

We note that timing recovery is performed before equalization, frequency and phase recovery due to its ability to perform independently of the the channel, carrier phase and moderate frequency offsets. The initial estimates for frequency error and phase error are made during the preamble transmission using data-aided feed-forward estimators due to their fast acquisition.

4.3 Energy Models

The following notations are used in the subsequent sections: R_{d} is the required information bit rate and r_{c} is the code rate defined as the ratio between the input information block length of the encoder k and the output codeword block length of the encoder n (i.e. $r_{\mathrm{c}} = \frac{k}{n}$). We consider M-QAM modulation in our system, where M is the size of the signal constellation and is selected from 4, 16 or 64.

---

[1] For example, starting with an information bit length $k = 3000$, consider a $(3750, 3000)$ LDPC code that has rate 0.8 and operates with a bandwidth of 5 MHz. An equivalent information rate is achieved using a $(7500, 3000)$ code that has rate 0.4 and operates with a bandwidth of 10 MHz. Further note that when there is a change in modulation order, there will be a change in k as well to keep the operating rate of encoder and decoder same for all the symbol rates. This is seen later in the chapter in Table 4.9.

The information symbol rate R_s is defined as

$$R_\mathrm{s} = \frac{R_\mathrm{d}}{r_\mathrm{c} \log_2 (M)} \tag{4.1}$$

We define the FFT length used in the frequency-domain equalizer as N_Eq and the length of the CP as l, which is set equal to the number of effective channel taps in a worst-case scenario, i.e.

$$l = \left\lfloor \frac{\tau}{T'_\mathrm{s}} \right\rfloor , \tag{4.2}$$

where $\lfloor \cdot \rfloor$ is the integer floor operator and τ and T'_s denote the worst-case channel time length and transmit symbol time duration, respectively.

The CP is used during both preamble and information transmission. We define λ as the ratio of the preamble symbol length to the combined preamble and information symbol length. Therefore, the total symbol rate R'_s including both information symbols and preamble symbols is written as

$$R'_\mathrm{s} = \frac{1}{1-\lambda} \frac{N_\mathrm{Eq} + l}{N_\mathrm{Eq}} R_\mathrm{s} , \tag{4.3}$$

The required signal bandwidth of the transmit signal W is calculated as follows:

$$W = 2 (1 + \alpha) R'_\mathrm{s} , \tag{4.4}$$

where α is the excess bandwidth assuming a square-root raised-cosine pulse shape and chosen to be $\alpha = 0.5$ for the remainder of the chapter.

Our receiver is a multi-rate system, where the decoder and encoder operate at rate $\frac{R_\mathrm{d}}{r_\mathrm{c}}$, the timing synchronizer and the equalizer operate at rate $\frac{2R_\mathrm{s}}{1-\lambda}$, and all the other digital receiver functions operate at a rate of $\frac{R_\mathrm{s}}{1-\lambda}$.

The next three subsections present the analog, digital and total energy consumption models for the considered system. The notation used in the expressing these models is as follows:

- P_x is used to represent power consumption, where x is an identifier subscript for where this power is consumed.

- E_x is used to represent energy consumption per *information bit*, where again x is an identifier subscript.
- C_x represents a fixed constant used in the energy modeling of analog and digital blocks.

We also note that the energy consumption for transmitting or processing data symbols may differ from processing training (preamble) symbols. We distinguish these energy differences, when necessary, with either a 'D' or 'P' in the subscript of an energy figure.

4.3.1 Analog Components

Power consumption of analog components can vary significantly depending on the topology, implementation architecture and required system performance [34]. As such, power models need to be dependent on many system conditions. In this work, we choose CMOS 45 nm technology, which is used in modern wireless devices, and we assume reasonable power consumption values using recent designs. We assume a supply voltage of 1 V for our system and chose the power consumption values based on the designs in [92]–[93].

Table 4.1 presents operating specifications of wireless receiver front-end designs for different standards and applications, including WLAN, WiMAX, UMTS, DCS1800, LTE and general UWB systems.[2] We have normalized the power consumption of these designs to 45 nm technology and a 1 V supply voltage according to the analog power scaling rules[3] presented in [80]. The results show that the normalized designs consume about 1–10 mW, and the power consumption of our forthcoming RF front-end (4–8 mW for a bandwidth of 10 MHz) is in agreement with these results.

The receiver power consumption is attributed to various analog components, such as the a LNA, mixer, and frequency synthesizer (Syn). Where appropriate, we need to

---

[2] Some designs [92], [94], [95] are capable of operating in multiple standards.

[3] The analog power scaling from technology Y (in nm) to technology Z (in nm) is $\text{Power}(Z) = \text{Power}(Y) \cdot \frac{1 + 0.5 \cdot (Z/65\text{nm} - 1)}{1 + 0.5 \cdot (Y/65\text{nm} - 1)}$

Table 4.1: Power consumption of wireless RF front-ends.

	[92]	[94]	[96]	[97]	[95]	[98]	[99]
Standard	WLAN /WiMAX	UMTS /DCS1800 /WLAN	WLAN	UWB-IR	WiMAX /LTE	WLAN	M-WiMAX
CMOS Technology	180 nm	130 nm	180 nm	130 nm	90 nm	240 nm	130 nm
Supply voltage	1.8 V	1.2 V	1.8 V	1.35 V	1.2 V	2 V	1.5 V
Carrier frequency	2.6 GHz /3.6 GHz / 5.5 GHz	- -	2.4 GHz	7.875 GHz	700 MHz - 6 GHz	5 GHz	2.3 GHz
Signal bandwidth	-	-	22 MHz	1.25 GHz	30 MHz	23.5 MHz	30 MHz
Power consumption	45 mW - 48 mW	20 mW / 24 mW	47 mW	4.2 mW	10.2 mW	12.4 mW	40 mW
Normalized power consumption	6.2 - 6.6 mW	7.8 - 9.4 mW	6.5 mW	1.3 mW	5 mW	1.1 mW	10 mW

model the power consumption of each component as a function of bandwidth, which is variable in our system. Table 4.2 presents the power and energy models we used in this chapter, where we chose the most appropriate models and parameters from the literature.

Transmitter energy is usually dominated by the power amplifier in wireless systems, which needs to provide enough transmit power to maintain the received signal at a required SNR per bit. Its power consumption can be expressed in terms of the required received $\frac{E_b}{N_0}$, PAPR, losses occuring during transmission (including path loss, shadow fading and fading margin) and the noise floor at the receiver. A general path-loss-based transmit power model from [36] is used in our work and presented in Table 4.2. We note that PAPR, which depends on the modulation order, is a very important parameter in some analog components' power consumption as discussed in [34].

Among the other analog components, the power models of the ADC and DAC depend on the signal bandwidth and quantization resolution. Based on the models presented in [34], we assume that the power consumption of the frequency synthesizer (Syn), mixer, and LNA are independent of the operating RF bandwidth, while the BA power consumption is proportional to the signal RF bandwidth. We neglect the power

Table 4.2: Power consumption of different components in RF front-end of wireless transceivers.

Component	**Power model**	**Reference values**	**Parameter values**
PA	$P_{\text{PA}} = \frac{1}{\eta_{\text{PA}}} C_{\text{PA}}\, \text{PAPR}\, e^{\text{a}\frac{E_{\text{b}}}{N_0}} R_{\text{d}}\, d^{\gamma}$ [36] [4] $\text{PAPR} = 1.4\sqrt{3\,\frac{\sqrt{M}-1}{\sqrt{M}+1}}$ [34]	Depends on the required output power	$C_{\text{PA}} = 5.55 \times 10^{-14}$ mW, $\eta_{\text{PA}} = 0.5$, $\text{a} = \ln(10)$
Mixer	$P_{\text{Mixer}} = C_{\text{Mixer}}$ [34]	7.7 mW [100], 2.1 mW [98] 2.1 mW [98]	$C_{\text{Mixer}} = 1.25$ mW
Syn	$P_{\text{Syn}} = C_{\text{Syn}}$ [34]	6.9/1.8 mW [101], 3.2 mW [98]	$C_{\text{Syn}} = 1.25$ mW
LNA	$P_{\text{LNA}} = C_{\text{LNA}}$ [34]	2.5 mW [102]	$C_{\text{LNA}} = 1.25$ mW
DAC	$P_{\text{DAC}} = C_{\text{DAC}} r_{\text{DAC}}\, W$ [43][5]	5.4 mW [103]	$C_{\text{DAC}} = 5 \times 10^{-8}$ mW/Hz
ADC	$P_{\text{ADC}} = C_{\text{ADC}}\, r_{\text{ADC}}\, W$ [43][6]	2 mW [93]	$C_{\text{ADC}} = 3.4 \times 10^{-8}$ mW/Hz
BA	$P_{\text{BA}} = C_{\text{BA}}\, W$ [34]	5 mW [34], 2.4 mW [95]	$C_{\text{BA}} = 1.25 \times 10^{-7}$ mW/Hz

consumption of band filters used in our system as these passive analog filters consume negligible power.

The energy consumption per information bit of the analog section in the transmitter is written by dividing the average power by the information rate R_d:

$$E^{\text{Tx}}_{\text{Analog}} = \frac{2P_{\text{DAC}} + 2P_{\text{Mixer}} + P_{\text{Syn}} + P_{\text{PA}}}{R_{\text{d}}} . \tag{4.5}$$

The analog transmitter energy consumption per information bit for data mode is determined by multiplying this with the ratio of information symbols:

$$E^{\text{Tx}}_{\text{Analog-D}} = (1-\lambda) E^{\text{Tx}}_{\text{Analog}} . \tag{4.6}$$

Similarly, the preamble-mode transmit energy cost per information bit is written as,

$$E^{\text{Tx}}_{\text{Analog-P}} = \lambda E^{\text{Tx}}_{\text{Analog}} . \tag{4.7}$$

---

[4] The power amplifier energy model is derived using Eq. (10) in [36] assuming a carrier frequency of 1 GHz, receiver noise spectral density of -174 dBm/Hz, receiver noise figure and other losses and margins of 9 dB [104]. γ is the path loss exponent. The transmit distance d in the pathloss model is dimensionless as shown in [36]. $\frac{E_{\text{b}}}{N_0}$ is defined as the receiver SNR per bit in dB.

[5] The ADC and DAC energy models presented in [43] are used with proper scaling. The resolution of the ADC and DAC are given by r_{ADC} and r_{DAC}, respectively, and are defined as follows [43]: r_{ADC} is 6, 7 and 8 for 4-QAM, 16-QAM and 64-QAM, respectively, and r_{DAC} is 4, 5 and 6 for 4-QAM, 16-QAM and 64-QAM, respectively.

Likewise, the energy consumption per information bit of the receiver analog section is written as

$$E^{\text{Rx}}_{\text{Analog}} = \frac{P_{\text{LNA}} + 2P_{\text{Mixer}} + P_{\text{Syn}} + 2P_{\text{BA}} + 2P_{\text{ADC}}}{R_{\text{d}}} . \tag{4.8}$$

The analog receiver energy consumption per information bit for data mode can is determined by multiplying this with the ratio of information symbols:

$$E^{\text{Rx}}_{\text{Analog-D}} = (1 - \lambda)\, \frac{P_{\text{LNA}} + 2P_{\text{Mixer}} + P_{\text{Syn}} + 2P_{\text{BA}} + 2P_{\text{ADC}}}{R_{\text{d}}} . \tag{4.9}$$

Similarly the preamble-mode receiver analog energy cost per information bit is written as

$$E^{\text{Rx}}_{\text{Analog-P}} = \lambda\, \frac{P_{\text{LNA}} + 2P_{\text{Mixer}} + P_{\text{Syn}} + 2P_{\text{BA}} + 2P_{\text{ADC}}}{R_{\text{d}}} . \tag{4.10}$$

Note that the factors of 2 in Eqs. (4.5) – (4.10) are due to two converters, filters and mixers required in the direct conversion architecture.

4.3.2 Digital Components

The energy consumption of the digital signal processing blocks is derived based on computational complexity analysis. For the LDPC encoders and decoders, we used the energy models presented in [43]. For other digital blocks, we use the energy consumption models of arithmetic and memory operations proposed in [35], where we use the rules presented in [76] to scale the energy consumption for 45 nm CMOS technology with a 1 V supply voltage and assumed a DSP module resolution of 8-bits.[6] The equivalent energy consumption of the various operations are obtained from Table 3.2 in Chapter 3 and listed in Table 4.3. We assumed a radix-2 based implementation for the required FFT and IFFT modules, and a complex addition is constructed using two real additions while a complex multiplication is realized using four real multiplication and two real additions.

---

[6] Energy consumption is proportional to the technology length c and voltage V squared ($E \propto cV^2$), and we scale by the proportionality change between technologies.

Table 4.3: Energy consumption of different digital operations.

Operation	**Average energy consumption (pJ)**
Real multiplication (Mul)	7.41
Real addition (Add)	0.93
Register access (Reg)	1.23
ROM access (ROM)	6.17

The remainder of Section 4.3.2 presents the energy modeling details of the digital processing segments. We first analyse the computational complexity per symbol or block of each segment in terms of real additions, real multiplications, and memory operations. We then use Table 4.3 to convert the computations into energy per information symbol (i.e. non-CP and non-preamble symbols). Dividing this by the number of information bits per symbol, we obtain expressions of energy per information bit for all digital segments in terms of transmission variables M (constellation size), r_c (code rate) and n (code length), as well as some fixed constants (C_x's) and some block processing parameters (N_x's and l). For the synchronization blocks and the equalizer, we must determine the energies per information bit in preamble mode separately from data mode.

Note that we neglect the energy consumption of the digital transmit pulse-shaping and receiver matched filters in our energy modelling. Both filters will have less computations than other digital blocks, especially when exploiting the symmetry of the raised-root cosine filters and up/down-sampling operations which involve many samples that are either zeros or discarded.

Timing synchronizer

Figure 4.3 shows a block diagram of our timing synchronizer with an over-sampling rate of two. The timing error is detected using the Gardner timing error detectors (TEDs) [57] and corrected using a parabolic interpolator [55]. A second-order loop filter and an interpolation controller is used to control the feedback loop [45]. The computational complexity of our timing synchronizer is summarized in Table 4.4 based on Table 3.11 in Chapter 3.

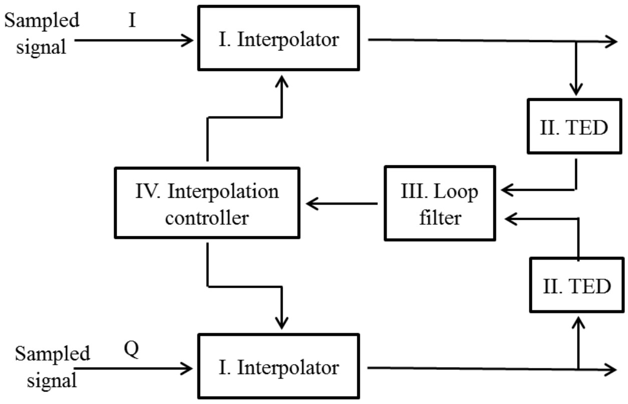

Figure 4.3: Block diagram of the timing synchronizer.

Table 4.4: Computation complexity of a timing synchronizer (per symbol).

Task	**Mul**	**Add**	**Reg**	**ROM**
I. Interpolator	12	32	20	–
II. Gardner TED	2	3	4	–
III. Loop filter	4	4	2	–
IV. Interpolator controller	2	4	2	2

After converting these computations into energies using Table 4.3, summing the result gives the energy consumption per symbol for timing recovery as the constant C_{TS}. Note that this energy is the same for both preamble and data symbols as the same algorithm is used on received symbols regardless of their designation.

In data mode, dividing C_{TS} by the number of information bits per symbol gices the the energy consumption per information bit, $E_{\text{TS-D}}$:

$$E_{\text{TS-D}} = \frac{1}{r_{\text{c}} \log_2(M)} \cdot C_{\text{TS}} \tag{4.11}$$

For preamble mode, the energy cost per information bit is

$$E_{\text{TS-P}} = \frac{1}{r_{\text{c}} \log_2(M)} \cdot \frac{\lambda}{1-\lambda} \cdot C_{\text{TS}} \tag{4.12}$$

where $\frac{\lambda}{1-\lambda} \cdot C_{\text{TS}}$ is the ratio of information symbols to preamble symbols.

Equalizer

A functional block diagram of our frequency-domain equalizer is shown in Fig. 4.4. The received samples, which are at twice the symbol rate, are transformed into the frequency domain using a $2N_{\mathrm{Eq}}$–point FFT operation. During training mode, the initial tap coefficients are estimated, while the received samples are equalized during data transmission mode. In addition, noise power is estimated using the ML-based estimation algorithm in [87], and this estimate is later used by the LDPC decoder. The over-sampling rate is reduced to one through a N_{Eq}-point IFFT operation to obtain the time-domain samples. The coefficient adaptation algorithm in [87] updates the equalizer taps with symbol decisions. The computational complexity of this equalizer for each of its five main tasks is listed in Table 4.5.

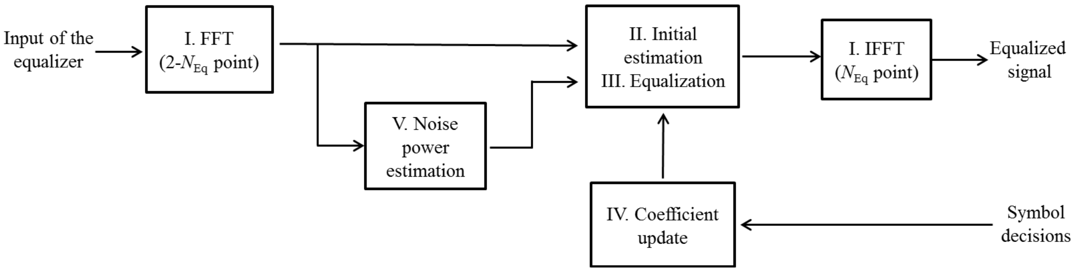

Figure 4.4: Block diagram of the frequency domain equalizer (FDE).

Table 4.5: Computation complexity of a frequency domain equalizer (per block).

Task	Mul	Add	Reg
I. FFT/IFFT operation	$6N_{\mathrm{Eq}}\log_2(N_{\mathrm{Eq}})$ $+4N_{\mathrm{Eq}}$	$9N_{\mathrm{Eq}}\log_2(N_{\mathrm{Eq}})$ $+6N_{\mathrm{Eq}}$	–
II. Initial tap estimation	$5N_{\mathrm{Eq}}$	$4N_{\mathrm{Eq}}$	–
III. Equalization	$8N_{\mathrm{Eq}}$	$4N_{\mathrm{Eq}}$	–
IV. Coefficient update	$2N_{\mathrm{Eq}}\log_2(N_{\mathrm{Eq}})$ $+14N_{\mathrm{Eq}}$	$3N_{\mathrm{Eq}}\log_2(N_{\mathrm{Eq}})$ $+13N_{\mathrm{Eq}}$	$4N_{\mathrm{Eq}}$
V. Noise power estimation	$N_{\mathrm{Eq}}+2$	$N_{\mathrm{Eq}}+2$	–

When the equalizer is in data mode, Tasks I, III, IV and V in Table 4.5 are required. Summing these computational operations per block and using Table 4.3 converts these computations into an energy per data block. Dividing by the number of information bits per block ($r_\mathrm{c}\ \log_2(M)\ N_\mathrm{Eq}$), results in the following equalizer energy per bit in data mode, $E_\text{Eq-D}$

$$E_\text{Eq-D} \;=\; \frac{1}{r_\mathrm{c}\ \log_2(M)}\left[C_\text{Eq-D1}\ \log_2(N_\mathrm{Eq}) + C_\text{Eq-D2}\right]. \tag{4.13}$$

Appendix A gives the computational details of this result and serves as a model for deriving the remaining energy-per-bit results.

Initializing the equalizer with a preamble block requires Tasks I, II and V in Table 4.5. Summing these operations and using Table 4.3, we convert these computations into an energy consumption per preamble block. Dividing by the block length gives the energy per preamble symbol, and the same scaling as in the time synchronizer case results in $E_\text{Eq-P}$, the equalizer energy per information bit in preamble mode:

$$E_\text{Eq-P} \;=\; \frac{1}{r_\mathrm{c}\ \log_2(M)} \cdot \frac{\lambda}{1-\lambda} \cdot \left[C_\text{Eq-P1}\ \log_2(N_\mathrm{Eq}) + C_\text{Eq-P2}\right]. \tag{4.14}$$

Frequency synchronizer

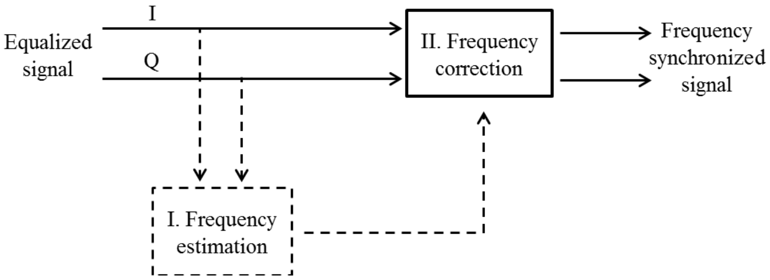

Figure 4.5: Block diagram of frequency synchronizer.

Frequency synchronization has two important tasks: carrier-frequency estimation is carried out in a blockwise fashion using preambles, while the frequency correction unit operates on all data symbols to compensate for the frequency error. We use the Mengali & Morelli's frequency estimator in our system, and a simple block diagram of the frequency synchronizer unit is shown in Fig 4.5. The computational complexity of the frequency estimator is analysed in Table in 3.20 in Chapter 3 using a FFT/IFFT-based approach and is shown in Table 4.6 for a block size N_{FS}.

Table 4.6: Computation complexity of the frequency synchronizer.

Task	**Mul**	**Add**	**Reg**	**ROM**
I. Mengali & Moreli estimation algorithm (per block)	$6N_{\text{FS}}\log_2(1.5N_{\text{FS}})$ $+4N_{\text{FS}}+2$	$9N_{\text{FS}}\log_2(1.5N_{\text{FS}})$ $+2.5N_{\text{FS}}-1$		$1.5N_{\text{FS}}\log_2(1.5N_{\text{FS}})$ $+1.5N_{\text{FS}}+3$
II. Frequency correction (per symbol)	5	3	1	2

The energy cost of the frequency recovery loop during training mode, which includes both frequency estimation and correction, is calculated by converting the computations in Tasks I and II in Table 4.6 into energy consumption. Note that the frequency estimate is made only once per block and the correction is carried on each individual QAM symbol. The resulting energy per information bit for frequency synchronization in preamble mode is written as,

$$E_{\text{FS-P}} = \frac{1}{r_{\text{c}}\ \log_2(M)} \cdot \frac{\lambda}{1-\lambda}\left[C_{\text{FS-P}\,1}\log_2(N_{\text{FS}}) + C_{\text{FS-P}\,2}\right], \tag{4.15}$$

where $C_{\text{FS-P}\,1}$ and $C_{\text{FS-P}\,2}$ are the coefficients of the dominant energy terms[7] when computations are converted to energy normalised by total number of bits used in the preamble ($2N_{\text{FS}}$).

The frequency correction energy per information bit, $E_{\text{FS-D}}$, for data mode is derived by calculating the energy cost per symbol, $C_{\text{FS-D}}$, to perform Task II in Table 4.6, then normalising by the number of information bits per symbol, $r_{\text{c}}\ \log_2(M)$ bits:

$$E_{\text{FS-D}} = \frac{1}{r_{\text{c}}\ \log_2(M)} \cdot C_{\text{FS-D}}, \tag{4.16}$$

Phase synchronizer

The initial phase offset is estimated using the feed-forward based maximum-likelihood (ML) phase estimator [51] with the aid of known preambles as shown in Fig. 4.6. Phase

---

[7] A negligible third term consisting of a smaller constant divided by a large block size N_{FS} is ignored in (4.15). Appendix A details a similar energy modelling reduction for the case of the equalizer.

unwrapping is used to overcome the phase ambiguities that occur during the initial phase estimation [51]. During data mode, a feedback-based decision-directed loop [51] is used to correct the phase errors as illustrated in Fig. 4.7. A ML-based decision-directed phase detector is used identify the initial phase error. A second-order loop filter and direct digital synthesizer (DDS) is then used to track and correct the phase error. The computational complexity of both approaches were investigated and are summarized in table 4.7 (based on Table 3.25 in Chapter 3). N_{PS} is the block size used in the feed-forward ML phase estimator.

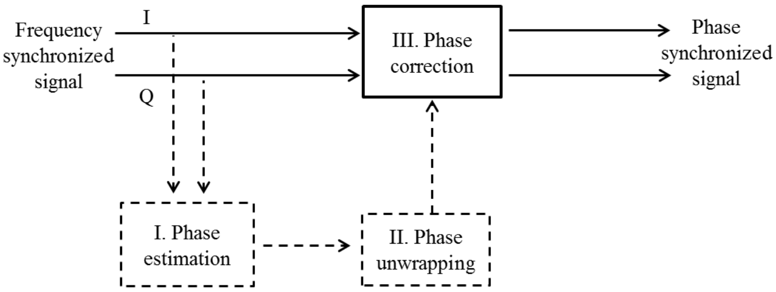

Figure 4.6: Block diagram of feed-forward phase synchronizer.

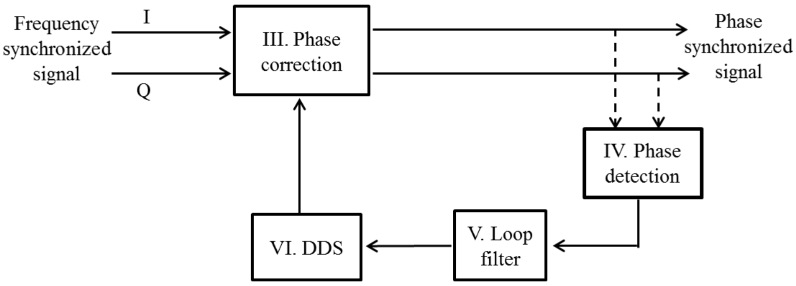

Figure 4.7: Block diagram of phase synchronization loop.

The computational energy for phase recovery in data mode, is calculated using Tasks III, IV, V and VI in Table 4.7 along with the energies in Table 4.3, and results in the energy per data symbol, $C_{\text{PS-D}}$. Normalizing by the number of information bits per symbol gives the energy per information bit for phase synchronization in data mode, $E_{\text{PS-D}}$:

$$E_{\text{PS-D}} = \frac{1}{r_{\text{c}} \log_2(M)} \cdot C_{\text{PS-D}} \tag{4.17}$$

Table 4.7: Computation complexity of phase synchronizers (per symbol, unless labeled otherwise).

Task	**Mul**	**Add**	**Reg**	**ROM**
I. Data-aided ML feed-forward estimator (per block)	$4N_{\text{PS}}$	$4N_{\text{PS}}-2$	–	2
II. Phase un-wrapper	–	2	1	1
III. Phase correction unit	5	2	–	2
IV. ML phase detector	2	1	–	–
V. Loop filter	2	2	1	–
VI. DDS	–	1	1	2

The computational energy for phase recovery during receiver training is obtained using Tasks I, II and III in Table 4.7 along with the energies in Table 4.3. Note that Task I and II are performed per block (N_{PS} symbols), while Task III in performed per symbol. The resulting computational energy per preamble symbol, $C_{\text{PS-P}}$, is scaled as in (4.12) to give $E_{\text{PS-P}}$, the phase synchronization energy per information bit in preamble mode:

$$E_{\text{PS-P}} = \frac{1}{r_{\text{c}}\,\log_2(M)} \cdot \frac{\lambda}{1-\lambda} \cdot C_{\text{PS-P}} \tag{4.18}$$

Encoder and decoder

A detailed energy model of the LDPC encoder and iterative decoder is presented in [43] and summarized in (4.19) and (4.20). The computational complexity of the encoder increases with code length n and the number of redundancy bits $(n-k)$. The encoder energy consumption per bit is given by

$$E_{\text{Enc}} = \frac{(1-r_{\text{c}})(n\,r_{\text{c}}\,C_{\text{Enc}\,1}-1)C_{\text{Enc}\,2}+C_{\text{Enc}\,3}}{r_{\text{c}}}\ , \tag{4.19}$$

where $C_{\text{Enc}\,1}$ is the generator matrix average ratio of ones per column, $C_{\text{Enc}\,2}$ is the average energy per gate operation, and $C_{\text{Enc}\,3}$ is the energy per register access.

The decoder energy consumption per bit is calculated as

$$E_{\text{Dec}} = \frac{f_{av}\ w_c}{r_{\text{c}}}\left(C_{\text{Dec}\,1}-r_{\text{c}}\,C_{\text{Dec}\,2}\right)\ , \tag{4.20}$$

where f_{av} is the average number of iterations and w_c is the column weight. $C_{\text{Dec}\,1}$ and $C_{\text{Dec}\,2}$ are calculated using the computational analysis presented in [43] and according to our code specifications. We verified that the row weight of the generating matrix is inversely proportional to the code rate, and hence included in the above energy model.

Table 4.8 gives the energy model numerical parameters calculated for the digital components. Timing synchronizer, frequency synchronizer and phase synchronizer parameters were obtained from Chapter 3.

Table 4.8: Parameters of digital component energy models.

Component	**Parameter values (pJ)**
Channel equalizer	$C_{\text{Eq-P}\,1}$ = 52.8, $C_{\text{Eq-P}\,2}$ = 84.3, $C_{\text{Eq-D}\,1}$ = 70.4, $C_{\text{Eq-D}\,2}$ = 227.3, N_{Eq} = 1024
Timing synchronizer	C_{TS} = 235.0
Frequency synchronizer	$C_{\text{FS-P}\,1} = 62.1$, $C_{\text{FS-P}\,2} = 130.9$, $C_{\text{FS-D}} = 53.4$, N_{FS} = 256
Phase synchronizer	$C_{\text{PS-P}}$ = 84.6 , $C_{\text{PS-D}}$ = 99.4, N_{PS} = 256
Encoder	$C_{\text{Enc}\,1}$ = 5, $C_{\text{Enc}\,2}$ = 0.03, $C_{\text{Enc}\,3}$ = 0.15
Decoder	$C_{\text{Dec}\,1}$ = 7.58, $C_{\text{Dec}\,2}$ = 0.53, w_c = 3, f_{av} = 12 [43]

4.3.3 Total energy consumption

In this section we give the expression for total energy consumption using the previous energy models. We also derive an approximate analytical expression for predicting energy costs that is used in Section IV.

The total energy per information bit in data mode, and write this using the analog and digital results in the last two subsections:

$$\begin{aligned} E^{\text{Data}} &= (E^{\text{Tx}}_{\text{Analog-D}} + E^{\text{Rx}}_{\text{Analog-D}}) + (E_{\text{TS-D}} + E_{\text{Eq-D}} + E_{\text{FS-D}} \\ &\quad + E_{\text{PS-D}} + E_{\text{Enc}} + E_{\text{Dec}}) \end{aligned} \tag{4.21}$$

where the first grouped terms represent the analog energy (including mixed signal energy) and the second group of six summed terms represents the digital energy per information bit in the point-to-point system.

The energy per information bit to transmit preambles and train the receiver is written as

$$\begin{aligned} E^{\text{PreAm}} &= (E^{\text{Tx}}_{\text{Analog-P}} + E^{\text{Rx}}_{\text{Analog-P}}) + (E_{\text{TS-P}} \\ &\quad + E_{\text{Eq-P}} + E_{\text{FS-P}} + E_{\text{PS-P}}) \, . \end{aligned} \tag{4.22}$$

Note that the encoder and decoder do not operate on preamble symbols, and therefore do not contribute to (4.22).

The total energy per information bit for the point-to-point wireless system can now be written as

$$E^{\text{Total}} = E^{\text{Data}} + E^{\text{PreAm}} \, . \tag{4.23}$$

The goal in the simulations in Section IV is to evaluate this total energy as a function of distance to determine an optimal minimal energy configuration of M, r_c, and received $\frac{E_{\text{b}}}{N_0}$. Note that these three variables are sufficient to then generate the system bandwidth W and cyclic prefix length l.

Analytical Approximation for Energy Consumption

We now formulate an analytical approximation to (4.23) so that an approximated energy curve can be quickly generated, and possibly be used for further analysis. For a selected location (i.e. fixed distance d) and data rate R_d, the energy cost for data transmission is a function of three configuration parameters: modulation order (M), code rate (r_{c}) and operating SNR per bit ($\frac{E_{\text{b}}}{N_0}$).

Several other parameters in the energy model do depend on these three key parameters. In the digital energy modeling, the cyclic prefix length l (equal to the number of channel taps) depends on both M and r_{c}. Both the encoder and decoder energy models are a function of r_c. In the analog energy modeling, the following segments with associated parameters from Table 1 are functions of M or l: PA (PAPR), DAC (W and r_{DAC}), ADC (W and r_{ADC}) and BA (W).

The goal of the approximation will be to remove the combinatoric dependency on M and r_{c} (i.e. choice of modulation order and code rate) from the energy equation. However, we will allow for any $\log_2(M)r_{\text{c}}$ term in the approximation, as this term is proportional to spectral efficiency and will approximated as a simple linear function of $\frac{E_{\text{b}}}{N_0}$ in the next section using system simulations.

The following five approximations are made to eliminate the dependence on M, r_c and l:

AP1: The equalizer block length N_{Eq} is sufficiently long enough such that $N_{\text{Eq}} \gg l$, and hence $N_{\text{Eq}} + l \approx N_{\text{Eq}}$. This removes the dependency of l in time synchronization and in the required bandwidth W that affect the DAC, ADC and BA powers.

AP2: We remove the PAPR's dependence on M in the PA power model by choosing the intermediate value $M = 16$ in the calculation (PAPR = 1.88).

AP3: In a similar fashion, we use the ADC and DAC resolutions for 16-QAM to remove dependence on M: $r_{\text{DAC}} = 5$ and $r_{\text{ADC}} = 7$.

AP4: For the decoder energy, the second constant term is dropped due to being much less significant, and the energy is approximated as

$$E_{\text{Dec}} \approx \frac{f_{av}\ w_c}{r_{\text{c}}} C_{\text{Dec}\,1} = \frac{f_{av}\ w_c\ \log_2(M)}{r_{\text{c}} \log_2(M)} C_{\text{Dec}\,1}\ , \tag{4.24}$$

where the $\log_2(M)$ term in numerator is then fixed using $M = 16$ as done above.

AP5: The encoder energy is ignored as it is dominated by all other digital segment energies as shown in simulations results in Section 4.

We now use these approximations and the summed terms in (4.21) to express $\hat{E}^{\text{Data}}$ as

$$\hat{E}^{\text{Data}} = \text{A}_1 d^{\gamma} e^{\text{a}\frac{E_{\text{b}}}{N_0}} + \frac{\text{B}_1}{\log_2(M) r_{\text{c}}} + \frac{\text{D}_1}{R_{\text{d}}} \quad \text{(in nJ/bit)} \tag{4.25}$$

where,

$$\mathrm{A}_1 \;= \tfrac{1}{\eta_{\text{PA}}}\,(1-\lambda)\,C_{\text{PA}}\;\;.\,1.88\times 10^6\;, \tag{4.26}$$

$$\begin{aligned}\mathrm{B}_1 \;&=\; 2\,(1+\alpha)\,\Big(2C_{\text{DAC}}\;\;.\,5+2C_{\text{ADC}}\;\;.\,7+2C_{\text{BA}}\Big)\times 10^6\\ &\quad+\Big(C_{\text{Eq-D}\,1}\,\log_2(N_{\text{Eq}})+C_{\text{Eq-D}\,2}+C_{\text{TS}}+C_{\text{FS-D}}+C_{\text{PS-D}}\\ &\quad+f_{av}\;w_c\,4C_{\text{Dec}\,1}\Big)\times 10^{-3}\end{aligned} \tag{4.27}$$

and

$$\mathrm{D}_1 \;= (1-\lambda)\,\big(4C_{\text{Mixer}}+2C_{\text{Syn}}+C_{\text{LNA}}\big)\times 10^6 \tag{4.28}$$

Note that the analog power model parameters (Table 4.2) were initially presented in mW, therefore in order to convert them to nJ it was multiplied with a scaler 10^6. Similarly digital energy model parameters (Table 4.8) were multiplied by 10^{-3} to convert pJ to nJ.

The parameter A_1 is derived from the PA energy model included in the $E^{\text{Tx}}_{\text{Analog-D}}$ term. The term B_1 is calculated using the DAC, ADC and BA energy models in $E^{\text{Tx}}_{\text{Analog-D}}$, $E^{\text{Rx}}_{\text{Analog-D}}$ and all digital energy models. The parameter D_1 is derived from the mixer, synthesizer and LNA energy models in the $E^{\text{Tx}}_{\text{Analog-D}}$ and $E^{\text{Rx}}_{\text{Analog-D}}$ terms. We assume $\lambda = 0.1$ for the simulations in the next section, and using the previously presented values in Table 4.2 and 4.8, the parameters A_1, B_1 and C_1 are calculated to be 1.88×10^{-7}, 6.09 and 7.87×10^6, respectively.

We now use the preamble energy (4.22) using the above approximations to express $\hat{E}^{\text{PreAm}}$ as

$$\hat{E}^{\text{PreAm}} \;=\; \mathrm{A}_2 d^{\gamma} e^{\mathrm{a}\frac{E_\mathrm{b}}{N_0}}+\frac{\mathrm{B}_2}{\log_2(M)r_\mathrm{c}}+\frac{\mathrm{D}_2}{R_\mathrm{d}}\quad \text{(in nJ/bit)} \tag{4.29}$$

where,

$$\mathrm{A}_2 \;= \tfrac{1}{\eta_{\text{PA}}}\,\lambda\,C_{\text{PA}}\;\;.\,1.88\times 10^6\;, \tag{4.30}$$

$$\begin{aligned}
\mathrm{B}_2 \;=\; & \frac{\lambda}{1-\lambda}\ .\Big[2\,(1+\alpha)\,\big(2C_{\text{DAC}}\ .5 + 2C_{\text{ADC}}\ .7 + 2C_{\text{BA}}\big)\times 10^{6} \\
& +\big(C_{\text{Eq-P}\,1}\ \log_2(N_{\text{Eq}}) + C_{\text{Eq-P}\,2} + C_{\text{TS}} + C_{\text{FS-P}\,1}\log_2(N_{\text{FS}}) \\
& +C_{\text{FS-P}\,2} + C_{\text{PS-P}}\big)\times 10^{-3}\Big] \qquad (4.31)
\end{aligned}$$

and

$$\mathrm{D}_2 \;= \lambda\left(4C_{\text{Mixer}} + 2C_{\text{Syn}} + C_{\text{LNA}}\right)\times 10^{6} \qquad (4.32)$$

The factor $\frac{\lambda}{1-\lambda}$ above comes from the preamble to data symbol normalization. The parameters A_2 and D_2 are defined using analog power modules similar to calculating A_1 and D_1. The parameter B_2 is calculated in similar way as B_1 except for preambles not using coding. Again assuming $\lambda = 0.1$ and using Table 4.2 and 4.8, the parameters A_2, B_2 and C_2 are calculated to be 0.21×10^{-7}, 0.582 and 0.875×10^{6}, respectively.

The total energy per information bit (4.23) can now be approximated using data (4.25) and preamble (4.29) energy approximations as,

$$\hat{E}^{\text{Total}} = (\mathrm{A}_1 + \mathrm{A}_2)e^{\mathrm{a}\frac{E_{\mathrm{b}}}{N_0}}\, d^{\gamma} + \frac{\mathrm{B}_1 + \mathrm{B}_2}{r_{\mathrm{c}}\log_2(M)} + \frac{\mathrm{D}_1 + \mathrm{D}_2}{R_{\mathrm{d}}} \qquad (4.33)$$

This provides a closed-form analytical expression for the total energy consumption of a practical wireless link.

4.4 Energy consumption investigation of a point-to-point transmission

We now investigate the energy consumption using system simulations and numerical evaluations. We also complete our analytical approximation to total energy by using a model of the available code rate and modulation order configurations, and derive a minimum-energy approximation from this as a function of $\frac{E_{\mathrm{b}}}{N_0}$.

The relationship between the spectral efficiency and the received SNR per bit depends on many factors, including the channel model and the LDPC code. In our system, we fix the target data rate at 5 Mbps and calculated various RF bandwidths and the resulting number of channel taps to support the error-control codes for three M-QAM modulation formats. We simulated a LDPC-coded system over $10,000$ random channel realizations to observe the required $\frac{E_b}{N_0}$ to achieve a target BER of 10^{-4}. We discarded 0-4% of channel realizations when a BER for a particular estimated channel shows higher than 0.001 at a high SNR where almost all of the other channels have 0 errors. We assume τ = 4.3 μs, $\gamma = 3$ and λ = 0.1, and assume the channel remains constant during the transmission of a block as the channel coherence time is quite high compared to block transmission time.

Table 4.9: System parameters for different transmission configurations to achieve a BER of 10^{-4} and a data rate of 5Mbps.

Modulation M	**Bandwidth** W **(MHz)**	**Channel taps** l	**Code rate** r_c	**Code**	**Required** $\frac{E_b}{N_0}$ **(dB)**
4-QAM	21.44	30	0.40	(7500,3000)	9.8
4-QAM	17.06	24	0.50	(6000,3000)	10.5
4-QAM	14.88	21	0.57	(5250,3000)	10.9
4-QAM	13.44	19	0.63	(4750,3000)	11.4
4-QAM	12.72	18	0.67	(4500,3000)	11.8
4-QAM	12.00	17	0.71	(4250,3000)	12.5
4-QAM	11.28	16	0.75	(4000,3000)	12.7
4-QAM	10.57	15	0.80	(3750,3000)	13.4
4-QAM	9.86	14	0.86	(3500,3000)	14.4
4-QAM	9.14	13	0.92	(3250,3000)	15.6
4-QAM	8.43	12	1	uncoded	19.6
16-QAM	8.43	12	0.50	(3000,1500)	14.0
16-QAM	7.01	10	0.60	(2500,1500)	16.1
16-QAM	5.60	8	0.75	(2000,1500)	17.2
16-QAM	4.89	7	0.86	(1750,1500)	20.4
16-QAM	4.19	6	1	uncoded	24.4
64-QAM	7.01	10	0.40	(2500,1000)	19.3
64-QAM	5.60	8	0.50	(2000,1000)	22.2
64-QAM	4.89	7	0.57	(1750,1000)	23.6
64-QAM	4.19	6	0.67	(1500,1000)	25.1
64-QAM	3.49	5	0.80	(1250,1000)	28.1
64-QAM	2.79	4	1	uncoded	31.8

The simulated system includes imperfect channel estimation and equalization using the algorithms in Section 4.2.2. Perfect synchronization has been assumed in these simulations and the synchronization algorithms are used solely for energy modelling in the results in this section. This is because the synchronization estimates are random variables as well. With imperfect synchronization, the BER computations dramatically degrade with just one off-the-mark estimate. For example, even a small frequency offset out of the capture range of the PLL for phase synchronization can completely randomize the incoming bit stream. When our eventual goal is to compare energy consumption for a set BER, it then makes sense to assume perfect synchronization parameters[8].

The simulation results in Table 4.9 show that the required SNR per bit can be reduced using a modulation scheme with low spectral efficiency such as 4-QAM, along with a low rate code. However, this requires a higher bandwidth compared to using higher-order modulation schemes. Another important factor is that SNR per bit is influenced by the ISI, which increases with bandwidth (and hence, the number of channel taps) and results in BER performance reduction. The lowest $\frac{E_\mathrm{b}}{N_0}$ operation requires approximately eight times more bandwidth compared to the highest $\frac{E_\mathrm{b}}{N_0}$ operation. The results also reveal that approximately similar signal bandwidths can be used to operate at two different $\frac{E_\mathrm{b}}{N_0}$'s depending on the modulation scheme and the code rate. The use of LDPC codes in our system also results in significant savings of the required SNR per bit and a wider SNR-per-bit operating range compared to our previous work [89] where only RS codes were used.

4.4.1 Energy minimisation using an analytical approximation

We now seek to use the analytical approximation of total energy consumption in Section 4.3.3 to determine an approximate optimal operating $\frac{E_\mathrm{b}}{N_0}$ as a function of only distance d. The goal is to test the validity of the approximation by comparing it to the energies calculated from our earlier models.

We start by using the results in Table 4.9 to find a relationship between $r_\mathrm{c}\log_2(M)$ and $\frac{E_\mathrm{b}}{N_0}$ for our system can be approximated using the following curve-fitting approach,

---

[8] By adopting such a strategy, we are basically eliminating cases where channel and/or synchronization are very poor and retransmissions are required.

$$r_{\mathrm{c}} \log_2(M) \quad = \quad \mathrm{b}_1 \frac{E_{\mathrm{b}}}{N_0} + \mathrm{b}_2 \tag{4.34}$$

where the curve fitting parameters b_1 and b_2 are calculated as 0.2116 and -1.244 using least squared-error approach and $\frac{E_{\mathrm{b}}}{N_0}$ is given in decibels as defined in the previous section. We plotted the actual values and approximations in Fig. 4.8.

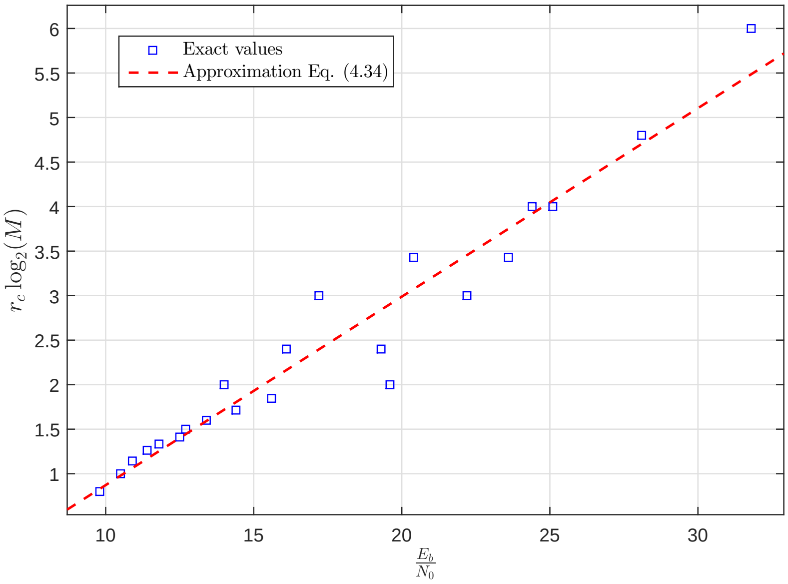

Figure 4.8: Curve fitting approximations of Eq. (4.34).

We can re-write (4.33) using the curve fitting approximation as follows,

$$\hat{E}^{\mathrm{Total}} \quad \approx \quad (\mathrm{A}_1 + \mathrm{A}_2) e^{\mathrm{a}\frac{E_{\mathrm{b}}}{N_0}} d^{\gamma} + \frac{\mathrm{B}_1 + \mathrm{B}_2}{\mathrm{b}_1 \frac{E_{\mathrm{b}}}{N_0} + \mathrm{b}_2} + \frac{\mathrm{D}_1 + \mathrm{D}_2}{R_{\mathrm{d}}} \tag{4.35}$$

The optimal SNR per bit that minimizes the total energy consumption can be obtained setting the derivative of (4.35) with respect to $\frac{E_{\mathrm{b}}}{N_0}$ to zero, which produces the following equation,

$$\mathrm{a}(\mathrm{A}_1 + \mathrm{A}_2)\, d^{\gamma}\, e^{\mathrm{a}\frac{E_{\mathrm{b}}}{N_0}} - \frac{\mathrm{b}_1(\mathrm{B}_1 + \mathrm{B}_2)}{\left(\mathrm{b}_1 \frac{E_{\mathrm{b}}}{N_0} + \mathrm{b}_2\right)^2} \quad = \quad 0 \tag{4.36}$$

The expression can be re-written as,

$$e^{\mathrm{a}\frac{E_\mathrm{b}}{N_0}}\left(\mathrm{b}_1\frac{E_\mathrm{b}}{N_0}+\mathrm{b}_2\right)^2 = \frac{\mathrm{b}_1(\mathrm{B}_1+\mathrm{B}_2)}{\mathrm{a}(\mathrm{A}_1+\mathrm{A}_2)\,d^\gamma} \tag{4.37}$$

By substituting, $t=\mathrm{b}_1\frac{E_\mathrm{b}}{N_0}+\mathrm{b}_2$ into (4.37), the following expression can be obtained which can be solvable using the Lambert function $\mathbf{W}$.

$$\frac{\mathrm{a}t}{2\mathrm{b}_1}e^{\frac{\mathrm{a}t}{2\mathrm{b}_1}} = \sqrt{\frac{\mathrm{a}(\mathrm{B}_1+\mathrm{B}_2)}{4\,\mathrm{b}_1\,(\mathrm{A}_1+\mathrm{A}_2)\,d^\gamma}e^{\frac{\mathrm{ab}_2}{\mathrm{b}_1}}}\,, \tag{4.38}$$

where $\mathrm{a}=\ln(10)$ as defined in the PA model in Table 4.2. The optimal solution for (4.38) is given by,

$$\left(\frac{E_\mathrm{b}}{N_0}\right)^* = \frac{2\mathrm{b}_1\,\mathbf{W}\left(\sqrt{\frac{\mathrm{a}\,(\mathrm{B}_1+\mathrm{B}_2)}{4\,\mathrm{b}_1\,(\mathrm{A}_1+\mathrm{A}_2)\,d^\gamma}\,e^{\frac{\mathrm{ab}_2}{\mathrm{b}_1}}}\right)-\mathrm{ab}_2}{\mathrm{ab}_1} \tag{4.39}$$

where, $\mathbf{W}$ provides the solutions of $y=\mathbf{W}(y)e^{\mathbf{W}(y)}$, which can be calculated using a wide range of available mathematical tools.

4.4.2 Simulation results

We now use numerical evaluation over the available data points in Table 4.9 to find solutions within the available $\frac{E_\mathrm{b}}{N_0}$ values. We assume the following parameters; τ = 4.3 μs and λ = 0.1. We assume the channel remains constant during the transmission of a block as the channel coherence time is quite high compared to block transmission time.

We start with Figs. 4.9 and 4.10 which present two example transceiver energy consumptions using two different system configurations and a transmission distance of 30 m. Fig. 4.9 summarizes the energy consumed by various parts of the transceiver when the receiver operates at $\frac{E_\mathrm{b}}{N_0}=13.4$ dB with 4-QAM modulation and code rate 0.8. The transceiver consumes a total energy of 5.3 nJ per bit, where the analog components consume about 77% of this total energy while the digital consumes about 23%. When the operating $\frac{E_\mathrm{b}}{N_0}$ is increased to 17.2 dB and uses 16-QAM with code rate 0.75 (as in Fig.

4.10), the digital energy percentage drops to 20%, and the total energy consumption and bandwidth become reduced to 4.3 nJ/bit and 5.6 MHz, respectively. A key difference between the two configurations is the PA energy, which is higher for the lower energy configuration. Furthermore, in both configurations and due to the short distance, the receiver energy consumption exceeds that of the transmitter.

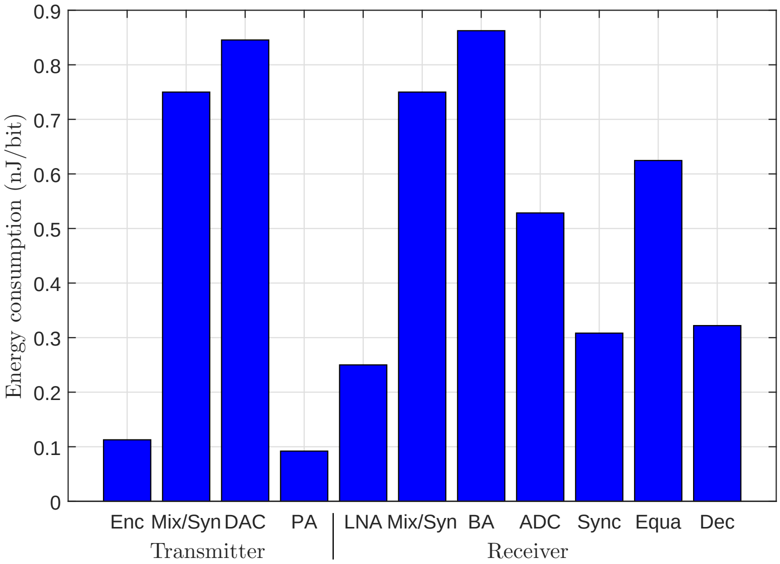

Figure 4.9: Energy consumption breakdown when the receiver operates at $\frac{E_\text{b}}{N_0} = 13.4$ dB with bandwidth 10.57 MHz at a distance of 30 m and data rate of 5 Mbps.

Fig. 4.11 shows the total energy consumption E^{Total} according to the actual energy models in (4.23) as a function of received $\frac{E_\text{b}}{N_0}$ when transmitted over a distance of 30 m. The total energy consumption is 9.5 nJ per bit when the receiver operates at the lowest $\frac{E_\text{b}}{N_0}$ of 9.8 dB using 4-QAM. As the operating $\frac{E_\text{b}}{N_0}$ is increased over the 4-QAM modulation scheme until 19.6 dB, the total energy gradually decreases to 4.7 nJ per bit which corresponds to uncoded transmission. For the low SNR-per-bit region, the total energy is dominated by the circuit processing energy and not the PA as shown in Fig. 4.9. A lower SNR-per-bit operation requires a higher symbol rate (and hence a higher RF bandwidth), which increases the energy consumption percentage of the ADC, DAC, LNA, BA and all digital components.

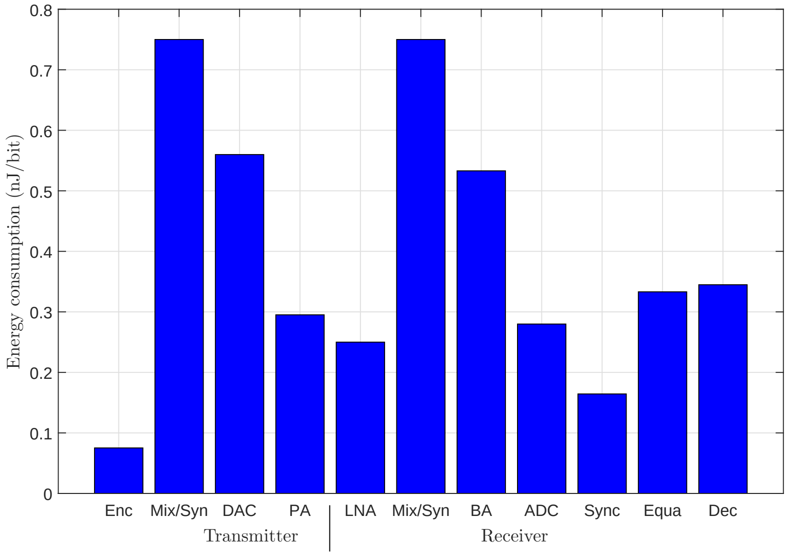

Figure 4.10: Energy consumption breakdown when the receiver operates at $\frac{E_b}{N_0} = 17.2$ dB with bandwidth 5.60 MHz at a distance of 30 m and data rate of 5 Mbps.

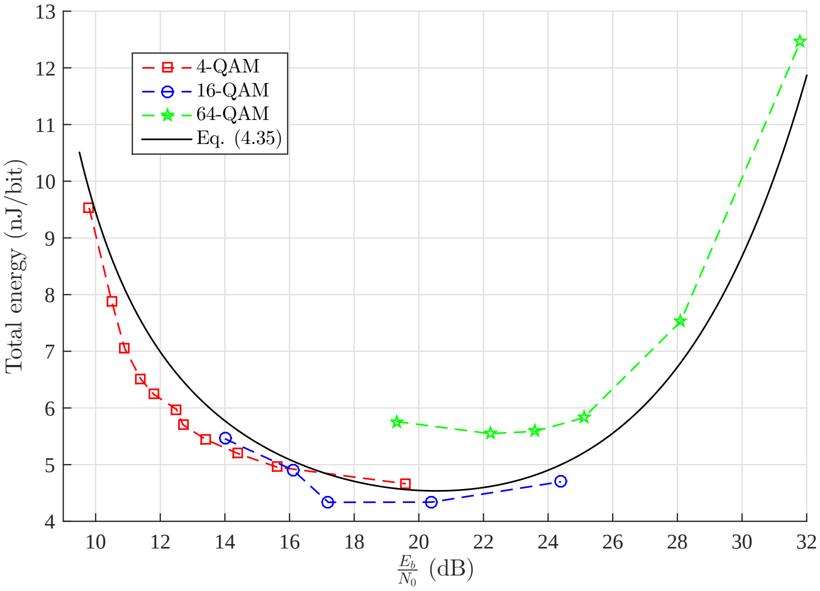

Figure 4.11: Total energy consumption versus the receiver $\frac{E_b}{N_0}$ for a distance of 30 m and data rate of 5 Mbps.

The total energy consumption of 16-QAM transmission behave differently. The consumed energy per bit decreases up until $\frac{E_\text{b}}{N_0} = 17.2$ dB, and begins to increase after this point. When 64-QAM is used, there is a slight energy drop initially, followed by a sharp increase in energy with increasing $\frac{E_\text{b}}{N_0}$. This is due to the high PAPR and requirement of a high transmit power to maintain a higher $\frac{E_\text{b}}{N_0}$. PA energy is the dominant factor here, and therefore total energy increases with the operating SNR per bit.

The approximate analytical energy consumption derived in (4.35) is sketched in Fig. 4.11 as the solid black line. It deviates slightly from the actual values, but is a reasonable approximation for the wide range of $\frac{E_\text{b}}{N_0}$ values considered. The small gaps in the approximation in the lower and higher $\frac{E_\text{b}}{N_0}$ regions are mostly due to approximations AP2–AP4 in Section 4.3.3 being based on a fixed intermediate value of $M = 16$ (and therefore fixed values of r_DAC and r_ADC). A better fit in Fig. 4.11 could be achieved with even a simple continuous approximation of M, r_DAC and $r_\text{ADC}7$ as a function of $\frac{E_\text{b}}{N_0}$ with the help of Table (4.35) as a guide for modulation order versus $\frac{E_\text{b}}{N_0}$.

Fig. 4.12 illustrates the total energy consumption as a function of RF bandwidth for a fixed distance of 30 m and a data rate of 5 Mbps. In the low bandwidth region, where 64-QAM can be used, the energy consumption decreases with increase in bandwidth. 64-QAM requires a higher transmit energy compared to the processing energy and therefore, by increasing the bandwidth and reducing the operating SNR per bit (as in Fig. 4.11) the total energy can be decreased for 64-QAM.

However, as the signal processing energy is more dominant in 4-QAM and 16-QAM systems, total energy consumption increases with an increase in bandwidth. Results show that a bandwidth expansion from 2.79 MHz to 4.19 MHz and a modulation scheme change from 64-QAM to 16-QAM could achieve an energy savings close to 60%. Fig. 4.11 and 4.12 present the trade-offs between rising of signal processing energy with transmit energy savings achieved by lowering the SNR per bit.

Fig. 4.13 shows the optimal minimum-energy operating $\frac{E_\text{b}}{N_0}$ and bandwidth as a function of distance using our energy models. The two dash-dot vertical lines at distances of 11 m and 53 m indicate the two distances where the optimal modulation order switches between 64-QAM or 16-QAM and 16-QAM or 4-QAM, respectively. The decaying dashed

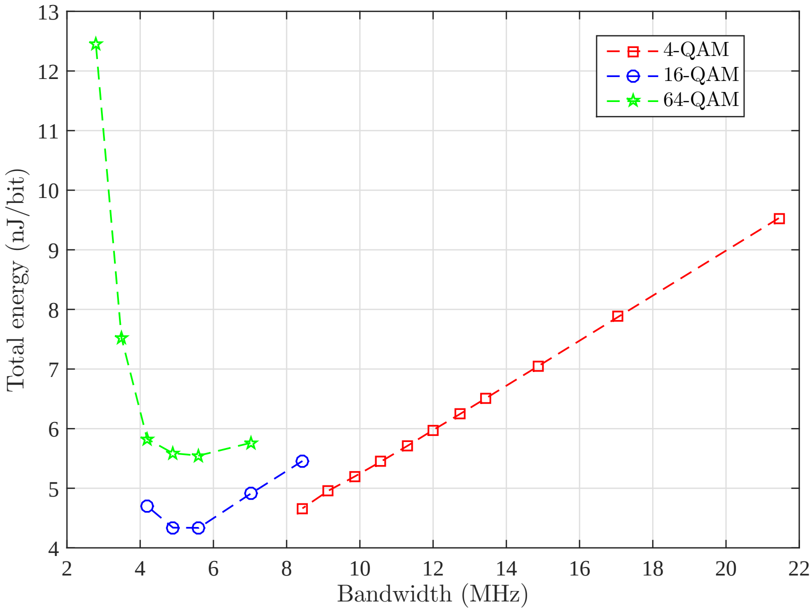

Figure 4.12: Total energy consumption versus the allocated bandwidth for a distance of 30 m and data rate of 5 Mbps.

line is the optimal operating $\frac{E_b^*}{N_0}$ as a function of distance in (4.39) that was derived from the closed-form analytical approximation in (4.33). Results show a close agreement with the numerical evaluated energy models, and the approximation can help predict code rates (using (4.34)) and their resulting bandwidths for $\frac{E_b}{N_0}$ operating values between those from the limited number of code rate choices in our simulations.

As expected, the optimal $\frac{E_b}{N_0}$ is inversely proportional to the transmit distance, while the optimal bandwidth expands to reduce energy consumption as distance increases. Transmit energy dominates the total energy for long distances, where it is important to reduce the received SNR per bit and allocate a wide bandwidth to achieve minimal total energy consumption. Results show that 64-QAM is energy efficient only for very short distances (less than 11 m) due to its high receiver SNR-per-bit requirement. 16-QAM is energy efficient for distances between 11 m and 53 m, while 4-QAM is more suitable for distances beyond 53 m for the example scenario considered here. Such results and the modelling process can be used in low-power wireless systems when allocating resources, i.e. provide smaller bandwidths to nearby users and wider bandwidths to users at longer

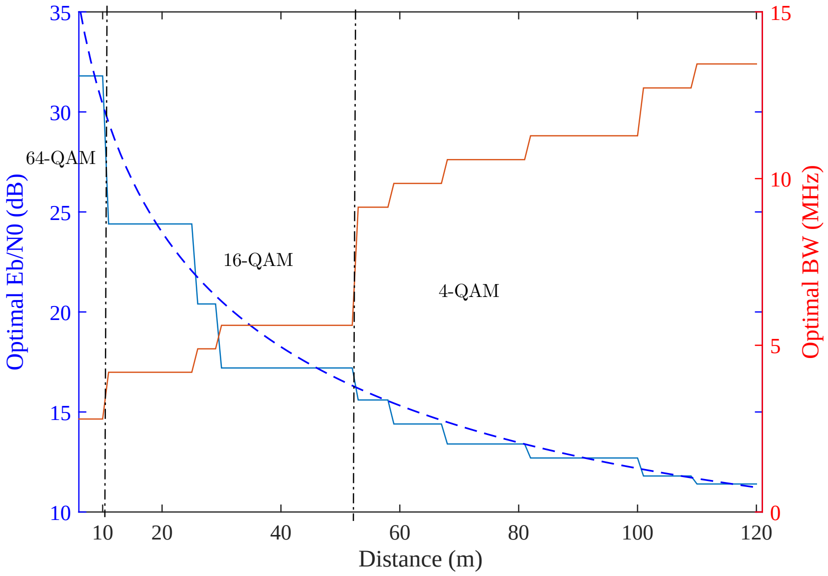

Figure 4.13: Optimal bandwidth and $\frac{E_b}{N_0}$ versus distance for most energy efficient transmission for a data rate of 5 Mbps.

distances.

Fig. 4.14 illustrates the energy consumption of analog segments in the transmitter and receiver, as well as the digital segments in the receiver as a percentage for different distances. The system is configured optimally for each distance according to Fig. 4.13. The digital energy consumption in the transmitter is only contributed by the encoder in our model and since it is very small (as shown in Fig. 4.9 and 4.10) we do not include it here. The analog transmit energy (and its percentage of overall energy) fluctuates in the first 55 m due to two modulation order and code rate changes. From 55 m onwards, the 4-QAM is the fixed modulation and there is an increasing energy trend. At the exact distance of a code rate decrease, the analog transmit energy decreases slightly due to less transmit power being compensated by a stronger bit-error correcting capability.

The digital received energy increases (not strictly though) as a function of distance. The increases in energy only occur when there is a change in M or code rate (r_c), and the energy is flat for distances in between. The percentage of overall energy increases sharply after 25 m when the minimal energy configuration first uses a code rate less than 1. The digital receiver percentage of overall energy reaches as high as 19.8% and begins to slowly decrease as the analog transmit energy begins to dominate the overall energy.

The analog received energy also increases (not strictly though) as a function of distance. Increases occur at distances where the optimal bandwidth increases as shown in Figure 4.13. At the shortest distances, the analog receive percentage of overall energy is a significant factor because it only partially depends on distance (via the ADC's and baseband amplifier's dependence on modulation order and bandwidth, respectively) and has a static energy component from the mixer, synthesizer, and LNA. As distance increases, this percentage has a decreasing trend due to the analog received energy only mildly increasing compared to analog transmit and digital receive energies. In particular, the analog receive energy increases by 63% from $d = 30$ m to $d = 150$ m, while the digital receiver and analog transmitter energies increase by factors of 2.1 and 5.2, respectively.

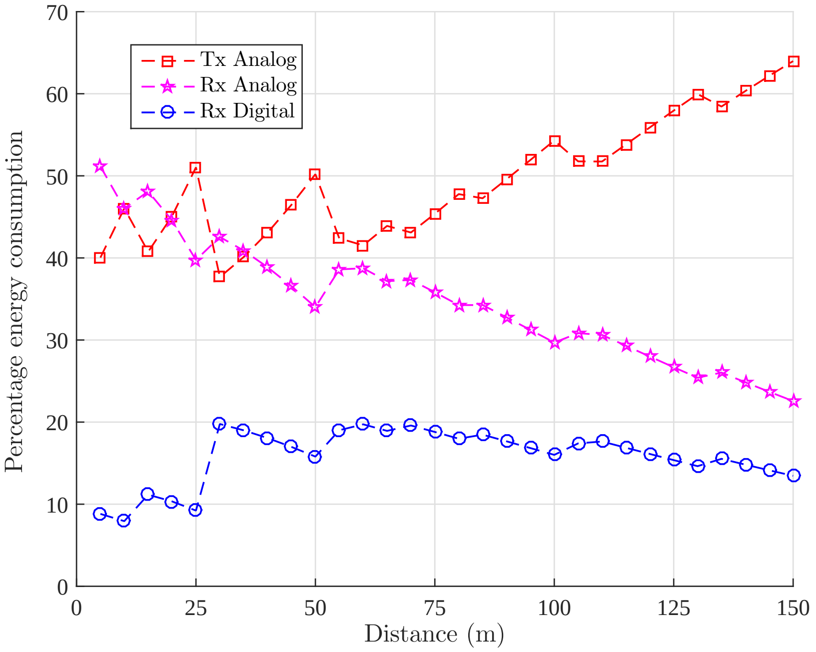

Figure 4.14: Energy consumption of transmitter and receiver analog and digital segments as a percentage when operated at optimal configurations as in Fig. 4.13 (distance = 30 m, data rate = 5 Mbps).

Finally, we consider future hardware implementations and predict the energy consumption for upcoming CMOS technologies. It is clear that with the development of efficient semiconductor components, circuit energy consumption will be reduced. CMOS technologies of 32 nm scale have already been introduced and 22 nm scale is being tested. Using the analog and digital CMOS technology scaling rules used earlier in the chapter assuming an uncoded 16-QAM transmission with the same requirements as in the above, we calculated the energy costs and present them in Fig. 4.15. The energy consumption for digital signal processing would decrease by 51% with the use of 22 nm technology, while the analog energy consumption would reduce by only 21%, and the total energy would fall by 27%. This might seemingly allow the minimum-energy configuration to rely more on receiver digital processing and a bit less on analog transmission power through lower-rate codes. However, note that lowering the code rate requires an increase in bandwidth to keep the same information rate, which results in requiring more analog power. Due to this interdependence and analog energy consumption being the majority factor, simulations based on 32 nm and 22 nm technologies have shown similar $\frac{E_b}{N_0}$ and bandwidth versus distance results as those in Fig. 4.13.

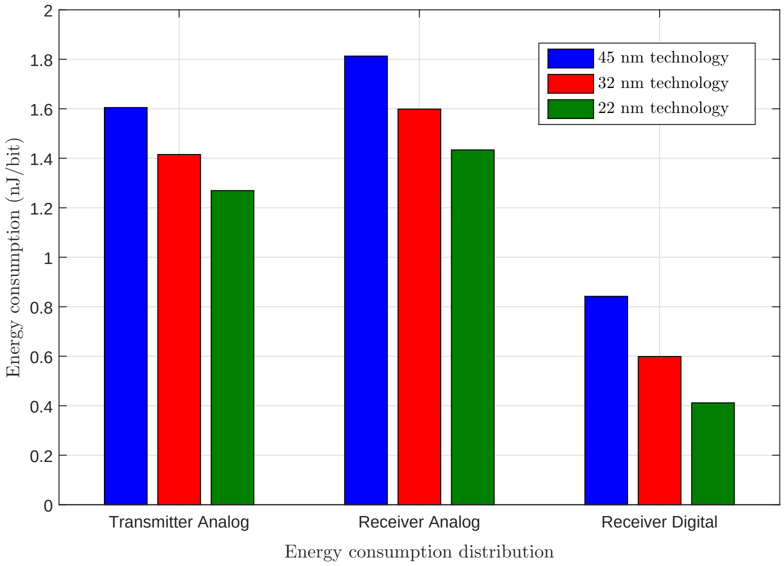

Figure 4.15: Energy consumption prediction for upcoming CMOS technologies (Here the transmission distance is assumed to be 30 m, data rate to be 5 Mbps and the receiver $\frac{E_b}{N_0}$ to be 17.2 dB).

4.5 Conclusions

A detailed energy modelling of the digital components (along with analog components) has resulted in a more complete energy model of a point-to-point, burst-mode wireless system compared to existing works. This allows for the analysis of energy consumption as a function of design parameters (bandwidth, modulation order, code rate, transmit power) and physical parameters (distance, channel model, and pathloss). For a given physical scenario and data-rate requirement, the optimal minimum-energy configuration can be determined as an optimal bandwidth and received $\frac{E_b}{N_0}$ that represent the design parameters. Eq. (4.33) is a key contribution because it provides an analytical approximation of total energy as a function of receiver $\frac{E_b}{N_0}$ and spectral efficiency which we could used to derive an expression for the optimal $\frac{E_b}{N_0}$.

The goal of the chosen system and its parameter configuration was to work towards a minimum-energy wireless point-to-point system. A single-carrier system was chosen due to a lower PAPR than OFDM systems, while the frequency-domain equalizer (FDE) allows the receiver to still have the performance advantage of an OFDM equalizer. As the transmitter energy is highly dependent on PAPR, single-carrier transmission is a better candidate for systems where energy efficiency is the main focus.

Shorter distances were considered in this chapter, and a prime application for our analysis is between devices in an internet-of-things (IoT) network, where burst-mode transmission is expected and energy consumption (possibly battery lifetime) is of extreme importance. At the shortest of distances with a fixed data rate, our results indicate that the receiver components were the dominant energy factor and analog transmit power is less constrained. In particular, these results show that digital energy consumption makes up a relevant portion of both the receiver's and overall system's energy consumption (as high as 24.6%). Furthermore, this percentage varies non-monotonically as a function of distance, as analog RX energy increases monotonically (as bandwidth increases with distance), while the digital energy can increase at distances where the optimal energy configuration changes (i.e. modulation order or code rate change).

A promising extension of this chapter is to consider relay networks, where one or more devices in an IoT network could serve as relays between source and destination nodes. Our framework could be used to determine the optimal energy configuration of the source transmitter and relays, including the number of required relays, type of relay (amplify or decode/detect and forward) and where the optimal relay locations are. Our modelling approach and the optimum-$\frac{E_\mathrm{b}}{N_0}$ concept may possibly be extended to a LTE network, where our receiver models are altered to that of a LTE receiver and a LTE base station energy model [80] is used.

4.6 Appendix

4.6.1 Equalizer energy model parameter derivation

When the equalizer is in data mode, Tasks I, III, IV and V result in the following total number of multiplies, adds and register accesses:

Multiplies: $8N_\mathrm{Eq}\log_2 N_\mathrm{Eq} + 27N_\mathrm{Eq} + 2$

Adds: $12N_\mathrm{Eq}\log_2 N_\mathrm{Eq} + 24N_\mathrm{Eq} + 2$

Register accesses: $4N_\mathrm{Eq}$

Using Table 4.3, the energy per preamble block is then computed as

$$\begin{aligned}\text{Energy per block} &= 7.41 \cdot (8N_\mathrm{Eq}\log_2 N_\mathrm{Eq} + 27N_\mathrm{Eq} + 2) + \\ &\quad 0.93 \cdot (12N_\mathrm{Eq}\log_2 N_\mathrm{Eq} + 24N_\mathrm{Eq} + 2) + 1.23 \cdot 4N_\mathrm{Eq}\end{aligned}$$

There are $r_\mathrm{c}\ \log_2(M)\ N_\mathrm{Eq}$ total number of data bits in N_Eq size equalizer block,

$$\text{Energy per bit } (E_\text{Eq-D}) = \frac{\text{Energy per block}}{r_\mathrm{c}\ \log_2(M)\ N_\mathrm{Eq}}$$

$$E_\text{Eq-D} = \frac{1}{r_\mathrm{c}}\left(70.4 \cdot \log_2 N_\mathrm{Eq} + 227.3 + \frac{16.7}{N_\mathrm{Eq}}\right)$$

The last term of the above equation, $\frac{16.7}{N_\mathrm{Eq}}$, is negligible as N_Eq is large in practice (512, 1024,...). Therefore, we ignore the last term and present two constants $C_\text{Eq-D1} = 70.4$ and

$C_{\text{Eq-D}\,2} = 227.3$ as coefficients to represent the above equation as,

$$E_{\text{Eq-D}} \;=\; \frac{1}{r_{\text{c}}\;\log_2(M)}\left[C_{\text{Eq-D}\,1}\;\log_2(N_{\text{Eq}}) + C_{\text{Eq-D}\,2}\right]$$

Chapter 5

Energy Modeling and Optimization of Cooperative Relay Transmission

Cooperative relays have been used in many wireless applications to reduce transmit power as well as to add diversity at the receiver. However, the energy efficiency trade-offs of relay networks have not been thoroughly investigated using a complete energy model of the system. In this chapter, we present an energy model for a cooperative single-relay system for two relay strategies: amplify-and-forward (AF) and detect-and-forward (DF). The proposed energy model consists of relative power allocation, relay location, spectral efficiency, data rate, transmission distance, and target error rate as parameters. Using this energy model, we optimize the location of the relay and power allocations to minimize the total energy consumption. The optimum location is found in two-dimensional space for constrained and unconstrained scenarios. The optimum location for an AF system can be found independently of the modulation scheme, while the optimum location for a DF system depends on the modulation scheme. We then optimize the total energy consumption over the spectral efficiency and derive expressions for the optimal spectral efficiency values, and verify our results using numerical simulations. Finally, we consider both single-hop (direction transmission) and two-hop (single-relay) transmission and present the optimal scheme and associated parameters as a function of source-to-destination distance.

5.1 Introduction

COOPERATIVE relay transmission has been used to improve the performance of wireless systems as well as to increase their coverage area [105]. The main function of a relay is to capture the incoming signal from the source and send it to the next relay or the destination. The relayed signals can be processed by the destination in multiple ways; they can be combined or used individually according to various available strategies [105, 106].

Relays generate independent channel paths between the source and destination. A major aspect of cooperative communication is the operation of the received signals at the relay and how they are forwarded on to the next node [105, 107]. The cooperative protocols of relay networks can be divided into two main categories based on their operation: amplify & forward (AF) and decode & forward. AF relays receive a signal from an incoming node, amplify the signal, and then forward it on to the next node. AF relays only amplify their received signals and do not perform any signal detection or decoding. Usually, AF is used as a fixed-wireless relaying approach, where it simply forwards the incoming signal.

DF relays detect the received signal first, followed by transmitting the signal to the next node. These relays are also known as regenerative relays as they attempt to fully reconstruct the original source signal again. In order to obtain closed-form analytical expressions, most of the related literature assume only signal detection at the relay without considering channel decoders. We follow the same procedure in our system, and hence adopt the terminology *detect & forward* (DF) instead of decode & forward. Therefore, uncoded transmission is used in the work that follows.

DF systems can be operated in various ways, with fixed DF and selective DF being the two common approaches. Fixed DF relay systems [105], where relays re-transmit all the times irrespective of perfect detection, are more suited when the source-destination link is weak and the source-relay link is quite strong. Otherwise, higher number of errors can be detected at the relay and can propagate to the destination and result in high error rates. Maximum-likelihood detection algorithms are available for fixed DF systems, but the receiver implementations is quite complex [108]. Therefore, selective transmission strategies [105] are proposed in DF systems where the relay transmits only when it detects the signal perfectly. When the relay does transmit a signal, the destination will combine the received signal from both the source and relay using maximal-ratio combining (MRC) techniques [109].

Most of the available literature on relay systems focus on either improving the final error probability or increasing the transmission capacity [107, 110–115]. Power allocation and relay positioning are jointly optimized by Zhang et al. for multi-relay cooperative AF and DF relay systems to minimize the outage probability [112]. The authors discuss two types of operations: combining all relays and selecting the best relay to minimize errors. Similarly, power allocation of both AF and DF relay systems is optimized by Liu et al. to minimize the symbol error rate after deriving closed-form expressions [107]. Zhao et al. performed power and relay location optimization for wireless multi-cast transmission using distribution relay selection and genie-aided relay selection schemes [113]. Lau et al. propose an optimum power allocation scheme for BPSK-modulated relay system under BER constraints and present upper bounds for the achievable power reduction gains [114]. Differentially-modulated AF relays are studied by Cho et al., and the system is optimized using a joint power and location allocation scheme [115].

Traditional research on the energy efficiency of wireless systems has mainly focused on power amplifier energy consumption, which is proportional to the transmit radio energy. Recent work, however, has shown that circuit energy or signal processing energy can be a significant contributor of the total energy in certain scenarios [33, 116]. In relay systems, several publications present energy optimization solutions that consider circuit energy consumption [107, 117–119]. Waqar et al. present an analysis of such energy model for a multi-hop AF non-cooperative relay network [117]. The authors adopt a non-cooperative strategy at the destination which results in equal power allocation and mid-point located relays. The authors assume a fixed circuit power consumption and jointly optimize the total energy as a function of the number of relays and spectral efficiency for a BER-constrained environment. However, non-cooperative systems, while less complex, do not benefit from diversity (especially in fading environments) and have higher error rates in comparison with cooperative systems. Kakitani et al. also consider only a fixed circuit power when analyzing the energy efficiency of single-hop and multi-hop relay networks for AF and DF systems [118]. However, their approach uses a fixed modulation scheme to investigate energy consumption instead of considering a more flexible rate system with a variable modulation. Furthermore, as in [117], assuming a fixed circuit power consumption can effect accuracy, especially in low power systems. Liu et al. [107] discussed the energy efficiency in sensor networks between direct transmission, AF relay and DF relay cooperations by assuming static circuit energy consumption under outage probability constraints. Chen et al. carried out a detailed energy efficiency comparison for both types of relay systems using outage probability analyses [119]. The authors assumed data retransmission whenever the final detection fails. However, this research is limited by the assumption of equal transmit power at the source and relay to reduce the system complexity. Energy efficiency of relay selection strategies and trade-offs between the energy consumed on data transmission and channel state information (CSI) acquisition are studied by Madan et al. [120]. Of the above, the works of [107,119] use numerical simulations to solve their optimization problems.

To the best of our knowledge, accurate circuit energy models based on computational complexity, spectral efficiency and data rate have not been used in any previous works related to cooperative relays. In the remainder of this chapter, we present an analytical framework to optimize the energy efficiency of AF and DF cooperative systems. Our contributions with respect to previous publications are as follows.

- We present a more comprehensive model for circuit energy consumption which are derived using our previous work in Chapter 4. We then approximate the circuit energy as a function of data rate and modulation scheme. This allows us to formulate a closed-form total energy consumption model for BER-constrained and throughput-constrained cooperative AF and DF relay systems.

- We propose to minimize the energy consumption of our system by introducing a multi-dimensional optimization problem that considers the following parameters: power allocation for both source and relay, location of the relay, and spectral efficiency.

- We solve the optimization problem in two steps: First, location is optimized considering both constrained and unconstrained scenarios. We then minimize the total energy consumption as a function of modulation order. The slight difference between AF and DF systems results in a specific optimization approach for each.

- Numerical simulations verify our analyses, and finally, we propose an optimal cooperation strategy as a function of distance for energy-efficient transmission.

The remainder of this chapter is organized as follows; Section 5.2 presents the single-relay system model. Section 5.3 and 5.4 present the models for the total energy consumption for AF and DF relay systems, respectively, along with energy minimization approaches for each. These approaches are numerically evaluated and verified Section 5.6. Finally, implications of our results and concluding remarks are discussed in Section 5.7. Section 5.8 contains the details of convexity of optimization functions and the radio energy derivations for direct transmission.

5.2 System Model

In our system, we consider a general scenario where a relay (R) is placed in a two-dimensional area with respect to source (S) and destination (D) as shown in Figure 5.1. The distances between the source-destination, source-relay and relay-destination are defined as $d_{s,d}$, $d_{s,r}$ and $d_{r,d}$, respectively. We define βl, where $0 < \beta < 1$, as the horizontal distance between the source and relay, and $(1-\beta)l$ as the horizontal relay-to-destination distance. The vertical relay distance, δl, is the distance component orthogonal to the direct path between the source and destination.[1] Together, β and δ provide a *relative* location of the relay with respect to the source-destination distance l. With basic geometry, we then rewrite the distances as

$$d_{s,d} = l \ , \quad d_{s,r} = \sqrt{\beta^2 + \delta^2}\, l \ , \quad d_{r,d} = \sqrt{(1-\beta)^2 + \delta^2}\, l \ . \tag{5.1}$$

In our work we make the following assumptions:

- Our system time-shares the resources between the relay links using two time instances for each transmission: First, between the source and relay/destination, and second, between the relay and destination. In each transmission time slot, a data rate of two times the average system throughput is required in order to achieve the same throughput as a direct transmission system.

---

[1] We only consider the region of δ from -1 to 1, as anything beyond this requires the source to transmit farther to the relay than to the destination. Such a scenario is not practical in an energy-efficiency sense as it would not require a relay in the first place.

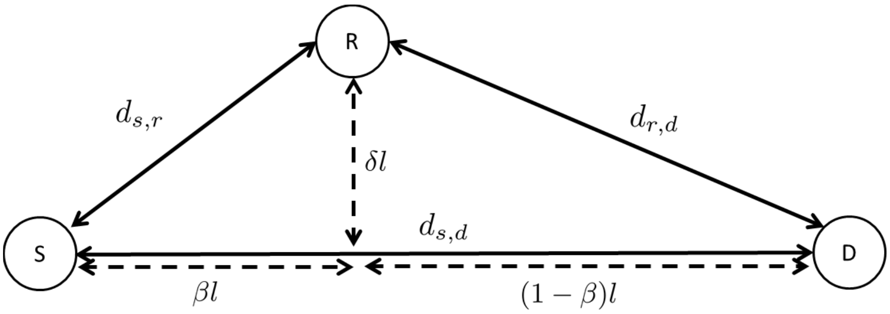

Figure 5.1: Diagram of the single relay system.

- All transmission links are modelled as flat-fading channels with mutually independent coefficients that follow the Rayleigh distribution and remain constant for the duration of a symbol.

- Channel state information is available at each receiver and the environment is interference-free.

- We only consider square-QAM modulation, and use exact BER expressions in our analyses. In this chapter, we refer to spectral efficiency as b, the number of bits per square-QAM symbol.[2] While the standard definition of spectral efficiency is the ratio of information bit rate to RF bandwidth measured in bits/sec/Hz, the forthcoming results are more easily viewed in terms of bits/symbol. Furthermore, as the standard spectral efficiency is proportional to b when the excess bandwidth of the Nyquist pulse shaping filter is fixed, it is easier to see spectral efficiency through b [45]. We consider four modulation schemes: 4-QAM, 16-QAM, 64-QAM and 256-QAM, thereby giving b values of 2, 4, or 8. We assume that for a fixed data throughput, the transmission bandwidth can be adjusted accordingly or a given modulation scheme.

- The system transmits at data rates in the range of 0.5–5 Mbps.

- Perfect receiver synchronization is assumed at the relay and the destination.

- The destination use maximal-ratio combining on the signals received from the relay

---

[2] Non-square QAM constellations, such as 32-QAM or 128-QAM, could be considered as well as their BER can be well approximated by square-QAM BER expressions.

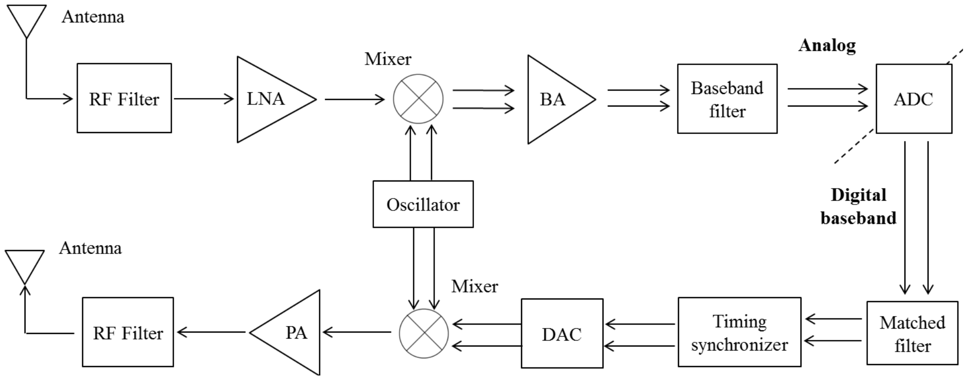

Figure 5.2: Block diagram of the AF relay transceiver.

and source.

5.3 Energy Modelling of Amplify-and-Forward (AF) Relaying Systems

In this section, we develop a total system energy model for our proposed AF relay system. We start with an overview of the AF relay transceiver, and then separately model the power amplifier (PA) and remaining circuit energies.

A block diagram of the AF relay node in our proposed system is shown in Figure 5.2. As an AF relay only re-transmits its received signal, it does not perform any symbol detection. Instead, it down converts, samples, up converts and amplifies during the process of re-transmission. Its received signal is first filtered using a band-pass filter and then amplified using a low-noise amplifier (LNA). The filter output is then down-converted to baseband and re-amplified using a baseband amplifier prior to the sampling process. An analog-to-digital converter (ADC) samples the analog signal and is followed by a timing recovery unit which maximizes the SNR of the received signal. The samples are then converted back to an analog signal using a digital-to-analog converter (DAC), and this signal is then modulated onto a transmit carrier frequency, amplified by the PA, and transmitted using a single antenna.

We denote the average required data throughput as R_{d}, and that direct transmission requires a bandwidth of W. The two variables are related by

$$R_{\mathrm{d}} = \frac{W}{2(1+\epsilon)} b \,, \tag{5.2}$$

where ϵ is denoted as the excess bandwidth of the Nyquist pulse. However, as the relayed transmission uses two transmission instances, in order to maintain the same throughput as a direct transmission system, it must transmit with twice the throughput, i.e. it requires twice the bandwidth for a given modulation scheme.

5.3.1 AF Power Amplifier Energy Modelling

We focus now on the energy consumed by the PA at both the source and relay. We begin by considering a point-to-point link and denote the following variables:

- E_{PA} is the power amplifier energy consumption per bit
- E_{Tx} is the power amplifier output energy per bit
- E_{Rx} is the received energy per bit
- η is the power amplifier efficiency
- L_0 is the constant in the pathloss model [121]
- γ is the path-loss exponent
- l is the transmission distance

The peak-to-average power ratio for square-QAM constellations is given by [34]

$$\mathrm{PAPR}(b) = 1.4\sqrt{\frac{3(2^{b/2}-1)}{2^{b/2}+1}}$$

We then write the PA output energy as follows:

$$E_{\mathrm{Tx}} = \sqrt{\frac{2^{b/2}+1}{3(2^{b/2}-1)}} \frac{\eta E_{\mathrm{PA}}}{1.4} \tag{5.3}$$

Efficiency of a PA cannot usually be represented by a single number in reality as it depends on various factors including the load. However, in order to obtain a closed-form solution to our problem, we assume a fixed efficiency (η) for the PA. Base station PAs are usually very inefficient and are predicted to operate with just 50% efficiency in 2020 [122]. The PA efficiencies in recent works lie within a wide range with maximum efficiencies of 33% in [123], 35% in [124] and 65% in [125]. We assume a PA efficiency efficiency (η) of 50% in this work.

Using the propagation model presented in [121], we can write the PA output energy and received energy as follows:

$$E_{\mathrm{Rx}} \;=\; E_{\mathrm{Tx}} L_0 l^{-\gamma} \tag{5.4}$$

Using (5.3) and (5.4), we can now calculate the energy consumption of the power amplifier as follows:

$$E_{\mathrm{PA}} \;=\; 1.4\sqrt{\frac{3(2^{b/2}-1)}{2^{b/2}+1}\frac{E_{\mathrm{Rx}}}{Ll^{-\gamma}}}\;, \tag{5.5}$$

where $L = L_0\eta$ is a constant.

An average symbol-error rate (SER) expression for cooperative AF transmission is derived in [107] assuming high-SNR operation[3]. We use the same expression as in [107] along with two assumptions: (1) Gray-coded symbol mapping is used; (2) A symbol error occurs only at neighboring symbol regions. Combined, the two assumptions result in a symbol error resulting in a single bit error, and this allows us to derive a closed-form approximation for BER later in this chapter. This BER approximation is accurate at high SNRs, is valid for any square M-QAM modulation scheme, and is a function of the spectral efficiency $b = \log_2 M$. The obtained BER of our cooperative AF transmission can

---

[3] The objective of this chapter is to minimize the total PA energy, and minimize the total energy which include both radio energy and signal processing energy. The approximation of high SNR holds for low BER values such as 10-4, but may not valid for higher BER values as higher BER can be achieved in low SNR.

be written using Eq. (5.85) in [107] and (5.5) as follows:

$$\mathrm{P_e} \approx \frac{B(b){N_0}^2}{E_{\mathrm{S}}Ld_{s,d}^{-\gamma}}\left(\frac{1}{E_{\mathrm{S}}Ld_{s,r}^{-\gamma}}+\frac{1}{E_{\mathrm{R}}Ld_{r,d}^{-\gamma}}\right), \tag{5.6}$$

where the PA energy per bit at the source and relay are represented by E_{S} and E_{R}, respectively, and N_0 represents the receiver noise spectral density multiplied into the receiver noise figure (RNF) at the receiver side of the relay and destination. The pathloss exponent γ is typically in the range $2 < \gamma < 6$ in practice, and the M-QAM modulation dependent constant $B(b)$ is based on Eq. 5.85 in [107] and (5.5), and is written as follows:

$$B(b) = \frac{23.52(2^b-1)(2^{b/2}-1)^2}{9b^3 2^b}\left(\frac{3(2^b-1)}{8}+\frac{(2^{b/2}-1)^2}{\pi}\right) \tag{5.7}$$

We denote the total PA energy consumption from both the source and relay as E_{tr}^{AF}. We use a weighting variable α to denote the relative PA power allocations for the source and relay. We now write the PA energy consumption of the source as $E_{\mathrm{S}} = \alpha E_{\mathrm{tr}}^{AF}$, and the relay as $E_{\mathrm{R}} = (1-\alpha)E_{\mathrm{tr}}^{AF}$, where $0 < \alpha < 1$. Substituting these energies and the distances defined in (5.1) into (5.6), followed by solving for E_{tr}^{AF}, results in

$$E_{\mathrm{tr}}^{AF} = \frac{N_0 l^{\gamma}}{L}\sqrt{\frac{B(b)}{\mathrm{P_e}}\mathrm{f}^{\mathrm{AF}}(\alpha,\beta,\delta)}, \tag{5.8}$$

where,

$$\mathrm{f}^{\mathrm{AF}}(\alpha,\beta,\delta) = \frac{(\beta^2+\delta^2)^{\gamma/2}}{\alpha^2}+\frac{((1-\beta)^2+\delta^2)^{\gamma/2}}{\alpha(1-\alpha)} \tag{5.9}$$

5.3.2 AF Circuit Energy Modelling

A summary of the energy models of a wireless transceiver[4] is presented in Table 5.1 based on the work in Chapter 4. According to the assumptions and our system model, we

---

[4] The digital pulse-shaping and receiver matched filters are neglected in our energy model. Both filters have less computations than other digital blocks, especially when exploiting the symmetry of the raised-root cosine filters.

Table 5.1: Power and energy models for wireless transceivers (from Table 4.2 and Table 4.8 in Chapter 4).

Component	**Power / energy model**	**Parameter values**
Mixer	$P_{\text{Mixer}} = C_{\text{Mixer}}$	$C_{\text{Mixer}} = 1.25$ mW
Oscillator	$P_{\text{Oscil}} = C_{\text{Oscil}}$	$C_{\text{Oscil}} = 1.25$ mW
Low noise amplifier	$P_{\text{LNA}} = C_{\text{LNA}}$	$C_{\text{LNA}} = 1.25$ mW
Digital-to-Analog converter	$P_{\text{DAC}} = C_{\text{DAC}} W$ [5]	$C_{\text{DAC}} = 0.25$ mW/MHz
Analog-to-Digital converter	$P_{\text{ADC}} = C_{\text{ADC}} W$ [5]	$C_{\text{ADC}} = 0.23$ mW/MHz
Baseband Amplifier	$P_{\text{BA}} = C_{\text{BA}} W$	$C_{\text{BA}} = 0.125$ mW/MHz
Timing Synchronizer	$E_{\text{TS}} = \frac{C_{\text{TS}}}{b}$	$C_{\text{TS}} = 0.235$ nJ
Frequency Synchronizer	$E_{\text{FS}} = \frac{C_{\text{FS}}}{b}$	$C_{\text{FS}} = 0.053$ nJ
Phase Synchronizer	$E_{\text{PS}} = \frac{C_{\text{PS}}}{b}$	$C_{\text{PS}} = 0.099$ nJ

define the circuit energy consumption of the relay as follows:

$$\begin{aligned} E_{\text{c,R}}^{\text{AF}} &= \frac{P_{\text{LNA}} + 4P_{\text{Mixer}} + 2P_{\text{Oscil}} + 2P_{\text{BA}} + 2P_{\text{ADC}} + 2P_{\text{DAC}}}{2R_{\text{d}}} + E_{\text{TS}} && (5.10) \\ &= \frac{4C_{\text{Mixer}} + 2C_{\text{Oscil}} + C_{\text{LNA}} + 2W(2C_{\text{BA}} + 2C_{\text{ADC}} + 2C_{\text{DAC}})}{2R_{\text{d}}} + \frac{C_{\text{TS}}}{b}, && (5.11) \end{aligned}$$

where P_{X} denotes the power consumption of analog component X and E_{X} denotes the energy consumption per information bit of component X. The integer in front of each P_{X} and E_{X} represents the number of such components in the considered system. The detailed models and parameter values are presented in Chapter 4. The source performs the function of a transmitter as presented in Figure 4.1 in Chapter 4[6]. The energy consumption of the source is written by adding the energy costs of the individual components

---

[5] We assumed fixed DAC and ADC resolutions of 5 and 7 bits, respectively. These values are irrespective of the modulation scheme in order to make E_{DAC} and E_{ADC} simpler linear models.

[6] We ignore the encoder block as we are focusing on uncoded transmission.

as

$$E_{\text{c,S}}^{AF} = \frac{2C_{\text{Mixer}} + C_{\text{Oscil}} + 2W \times 2C_{\text{DAC}}}{2R_{\text{d}}} \tag{5.12}$$

The destination performs the function of a receiver as presented in Figure 4.2 in Chapter 4,[7] but consumes twice the energy of a single receiver as it needs to process the received signals at two instances; first from the source, and second from the relay. The energy consumption of the destination is written by adding the energy costs of the individual circuit modules as

$$E_{\text{c,D}}^{AF} = \frac{4C_{\text{Mixer}} + 2C_{\text{Oscil}} + 2C_{\text{LNA}} + 2W(4C_{\text{BA}} + 4C_{\text{ADC}})}{2R_{\text{d}}} + \frac{2C_{\text{TS}} + 2C_{\text{FS}} + 2C_{\text{PS}}}{b} \tag{5.13}$$

The total circuit energy consumption of the AF cooperative system comprised of source, relay and destination nodes is now written by adding (5.10), (5.12) and (5.13), giving

$$E_{\text{c}}^{AF} = \frac{10C_{\text{Mixer}} + 5C_{\text{Oscil}} + 3C_{\text{LNA}} + 2W(6C_{\text{BA}} + 6C_{\text{ADC}} + 4C_{\text{DAC}})}{2R_{\text{d}}} + \frac{3C_{\text{TS}} + 2C_{\text{FS}} + 2C_{\text{PS}}}{b} \tag{5.14}$$

We simplify the above equation using Table 5.1, (5.2) and (5.14) to the following:

$$E_{\text{c}}^{AF} = \frac{C_1^{\text{AF}}}{R_{\text{d}}} + \frac{C_2^{\text{AF}}}{b}\ , \tag{5.15}$$

where the constants C_1^{AF} and C_2^{AF} are defined as,

$$C_1^{\text{AF}} = \frac{10C_{\text{Mixer}} + 5C_{\text{Oscil}} + 3C_{\text{LNA}}}{2} \times 10^6 \tag{5.16}$$

and

$$C_2^{\text{AF}} = 2\,(1+\alpha)\left(6C_{\text{BA}} + 6C_{\text{ADC}} + 4C_{\text{DAC}}\right) \times 10^6 + \left(3C_{\text{TS}} + 2C_{\text{FS}} + 2C_{\text{PS}}\right) \times 10^{-3}\ . \tag{5.17}$$

---

[7] We ignore the equalizer and decoder blocks as we are focusing on uncoded transmission in a single-tap channel.

C_1^{AF} and C_2^{AF} are calculated as 11.25×10^6 and 4.98 by using the models presented in Table 5.1 and assuming $\epsilon = 0.25$.

The total energy consumption for an AF system can now be written as a summation of PA energy (5.8) and circuit energy (5.15) as

$$E_{\text{total}}^{AF}(\alpha, \beta, \delta, b) \;=\; \frac{N_0 l^\gamma}{L}\sqrt{\frac{B(b)}{\mathrm{P_e}}\mathrm{f}^{\mathrm{AF}}(\alpha, \beta, \delta)} + \frac{C_1^{\mathrm{AF}}}{R_{\mathrm{d}}} + \frac{C_2^{\mathrm{AF}}}{b} \tag{5.18}$$

Looking closely at this equation, we see that minimizing $\mathrm{f}^{\mathrm{AF}}(\alpha, \beta, \delta)$ results in the optimal relative location (β^*,δ^*) and relative power allocation (α^*) that minimizes E_{tr}^{AF}. The first key result here is that the minimal-energy b^* is therefore independent of of the relative location and power allocation. The second key result is that the distance l from source to destination does not affect the optimal relative relay configuration parameters, which was the primary reason for their introduction into the analysis.

5.4 Energy Modelling of Detect-and-Forward (DF) Relaying Systems

We now investigate the energy consumption of a cooperative DF relay system. We first use SER expressions presented in [107] to derive the required transmit energy to achieve a desired BER. We make the same assumptions as in Section 5.3, and further to this, assume that the relay transmits only if it perfectly detects the signal. Otherwise, the relay remains silent in the second time slot and the destination uses only the signal received from the source to detect the transmitted data.

We present block diagrams of the receiver and transmitter segments of the DF relay in Figure 5.3 and Figure 5.4, respectively. A DF relay performs several additional functions compared to an AF relay. At the receiver end of the relay, carrier frequency and phase synchronization are performed. Following coherent detection, the detected signal is then re-modulated and transmitted as shown in Figure 5.4.

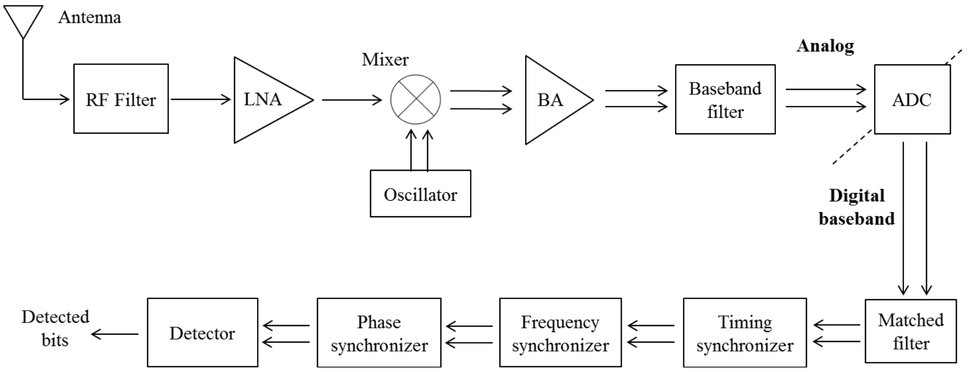

Figure 5.3: Block diagram of a DF relay receiver end.

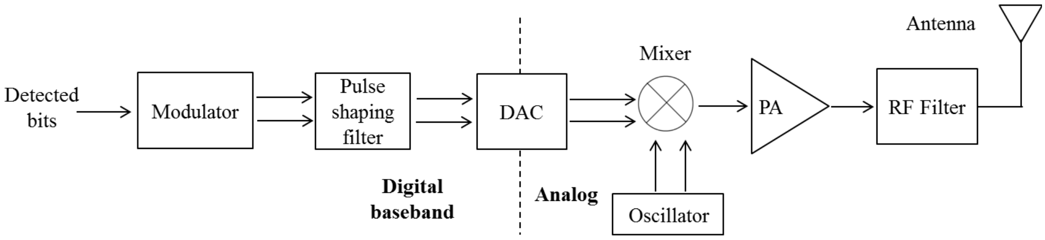

Figure 5.4: Block diagram of a DF relay transmitter end.

5.4.1 DF Power Amplifier Energy Modelling

When the relay detects the signal perfectly, the destination combines signals coming from both the source and the relay using maximal-ratio combining. Therefore, the final BER depends on the probability of accurate detection at the relay, which is a function of parameters such as relay location (β and δ), power allocation (α) of source and relay and spectral efficiency (b). However, the relative relay configuration parameters (β, δ, α) cannot be separated from spectral efficiency b as in (5.6) since the probability of the relay transmission depends on successful detection, which is a function of b. The final BER of a DF system can be written by using Eq. 5.35 in [107] and (5.5) to give

$$\mathrm{P_e} \ = \ \frac{{N_0}^2}{E_\mathrm{S} L d_{s,d}^{-\gamma}} \left(\frac{A(b)}{E_\mathrm{S} L d_{s,r}^{-\gamma}} + \frac{B(b)}{E_\mathrm{R} L d_{r,d}^{-\gamma}} \right) , \tag{5.19}$$

where the variables E_S, E_R, L, γ, N_0 and $B(b)$ carry the same definitions from Section 5.3. The spectral-efficiency-dependent term $A(b)$ is obtained by using both Eq. 5.35 in [107] and (5.5), resulting in

$$A(b) \;=\; \frac{23.52\,(2^b-1)(2^{b/2}-1)^2}{9\,b^3\,2^{2b}}\left(\frac{(2^b-1)}{2}+\frac{(2^{b/2}-1)^2}{\pi}\right)^2 \tag{5.20}$$

We denote E_{tr}^{DF} as the total combined PA energy consumption from both the source and relay. The power allocation of the source and relay are then written as $E_{\text{S}} = \alpha E_{\text{tr}}^{DF}$ and $E_{\text{R}} = (1-\alpha)E_{\text{tr}}^{DF}$, respectively, where again $0 < \alpha < 1$. Substituting these energies and the distances defined in (5.1) into (5.19), followed by solving for E_{tr}^{DF}, results in

$$E_{\text{tr}}^{DF} \;=\; \frac{N_0 l^\gamma}{L}\sqrt{\frac{1}{\text{P}_\text{e}}\text{f}^{\text{DF}}(\alpha,\beta,\delta,b)}\,, \tag{5.21}$$

where

$$\text{f}^{\text{DF}}(\alpha,\beta,\delta,b) = \frac{A(b)(\beta^2+\delta^2)^{\gamma/2}}{\alpha^2} + \frac{B(b)((1-\beta)^2+\delta^2)^{\gamma/2}}{\alpha(1-\alpha)} \tag{5.22}$$

5.4.2 DF Circuit Energy Modelling

According to the system model, we derived the circuit energy consumption of the relay by adding the energy of all the analog and digital segments as follows:

$$E_{\text{c,R}}^{\text{DF}} = \frac{P_{\text{LNA}} + 4P_{\text{Mixer}} + 2P_{\text{Oscil}} + 2P_{\text{BA}} + 2P_{\text{ADC}} + 2P_{\text{DAC}}}{2R_{\text{d}}} + E_{\text{TS}} + E_{\text{FS}} + E_{\text{PS}} \tag{5.23}$$

$$= \frac{4C_{\text{Mixer}} + 2C_{\text{Oscil}} + C_{\text{LNA}} + 2W(2C_{\text{BA}} + 2C_{\text{ADC}} + 2C_{\text{DAC}})}{2R_{\text{d}}} + \frac{C_{\text{TS}} + C_{\text{FS}} + C_{\text{PS}}}{b} \tag{5.24}$$

The energy models of these segments are presented in Table 5.1 based on the models in Chapter 4. The total circuit energy consumption of the system comprised of all three nodes is obtained by adding the energy consumption of the circuit components at the source (5.12), relay (5.23) and destination (5.13) as follows,

$$E_{\mathrm{c}}^{\mathrm{DF}} = \frac{10C_{\mathrm{Mixer}} + 5C_{\mathrm{Oscil}} + 3C_{\mathrm{LNA}} + 2W(6C_{\mathrm{BA}} + 6C_{\mathrm{ADC}} + 4C_{\mathrm{DAC}})}{2R_{\mathrm{d}}} + \frac{3C_{\mathrm{TS}} + 3C_{\mathrm{FS}} + 3C_{\mathrm{PS}}}{b} \tag{5.25}$$

We simplify the above equation using Table 5.1 and (5.2) as follows:

$$E_{\mathrm{c}}^{DF} = \frac{C_1^{\mathrm{DF}}}{R_{\mathrm{d}}} + \frac{C_2^{\mathrm{DF}}}{b}, \tag{5.26}$$

where the constants C_1^{DF} and C_2^{DF} are defined as,

$$C_1^{\mathrm{DF}} = \frac{10C_{\mathrm{Mixer}} + 5C_{\mathrm{Oscil}} + 3C_{\mathrm{LNA}}}{2} \times 10^6 \tag{5.27}$$

and

$$C_2^{\mathrm{DF}} = 2\,(1+\alpha)\left(6C_{\mathrm{BA}} + 6C_{\mathrm{ADC}} + 4C_{\mathrm{DAC}}\right) \times 10^6 + \left(3C_{\mathrm{TS}} + 3C_{\mathrm{FS}} + 3C_{\mathrm{PS}}\right) \times 10^{-3}\,. \tag{5.28}$$

The constants C_1^{DF} and C_2^{DF} are calculated as 11.25×10^6 and 5.14, respectively, using the models presented in Table 5.1 and assuming $\epsilon = 0.25$. The total energy consumption per bit of a DF system can be written as a summation of (5.21) and (5.26) as follows:

$$E_{\mathrm{total}}^{DF} = E_{\mathrm{tr}}^{DF} + E_{\mathrm{c}}^{DF} \tag{5.29}$$

$$= \frac{N_0 l^{\gamma}}{L}\sqrt{\frac{1}{\mathrm{P_e}}\mathrm{f}^{\mathrm{DF}}(\alpha,\beta,\delta,b)} + \frac{C_1^{\mathrm{DF}}}{R_{\mathrm{d}}} + \frac{C_2^{\mathrm{DF}}}{b} \tag{5.30}$$

Looking closely at this equation, we see that the minimal-energy relay configuration values (α^*, β^*,δ^*) are no longer independent of b as in the AF case. Furthermore, since the minimal-energy b^* will depend on the source-destination distance l, we no longer have (α^*, β^*,δ^*) being independent of l as they were in the AF case.

5.5 Optimum Location and Power Allocation Scheme (OLPAS) and Total Energy Minimization

Our goal is to determine the optimum relative relay location parameters (β^* and δ^*), relative power allocation (α^*), and optimum spectral efficiency b^* that minimizes the energy consumption of the relay system for a given information rate R_d, source-destination distance l, and the other physical transmission parameters in our model (i.e. pathloss exponent γ, PA efficiency η, and pathloss constant L_0). We formulate the optimization problem in the DF or AF case as:

$$\begin{aligned} \underset{\alpha,\beta,\delta,b}{\text{minimize}} \quad & E^{xF}_{\text{total}}(\alpha,\beta,\delta,b) \\ \text{subject to} \quad & b = \{2,4,6,8\}, \\ & 0 < \alpha < 1, \\ & 0 < \beta < 1, \\ & -1 < \delta < 1 \end{aligned} \tag{5.31}$$

where 'x' in E^{xF}_{total} refers to either AF or DF depending upon which system is under consideration.

In both the AF and DF cases, we analyze the following three cases and find the optimal minimal-energy configuration $(\alpha^*, \beta^*, \delta^*, b^*)$:

1. Relative location is fixed, while relative power allocation (α) is a free variable.

2. Both relative location ($0 < \beta < 1$, $-1 < \delta < 1$) and relative power allocation ($0 < \alpha < 1$) have no additional constraints.

3. The relative location has additional constraints where ($\beta_1 < \beta < \beta_2$ and $\delta_1 < \delta < \delta_2$). Furthermore, $0 < \beta_1 < \beta_2 < 1$ and $-1 < \delta_1 < \delta_2 < 1$. This results in the location space to be a rectangular subset of the space in Case 2.

5.5.1 OLPAS-AF

The global solution for the optimization problem (5.31) can be solved in two steps: First, $\mathrm{f}^{\mathrm{AF}}(\alpha, \beta, \delta)$ can be minimized independently of other variables. Second, The solutions of the first step is substituted into (5.31) and then minimized over all possible b.

The optimum relative location can be found by minimizing function $\mathrm{f}^{\mathrm{AF}}(\alpha, \beta, \delta)$ over the possible range of (α, β, δ) given in the last section. We first consider the second derivatives of $\mathrm{f}^{\mathrm{AF}}(\alpha, \beta, \delta)$ with respect to the individual parameters α, β and δ , i.e. $\frac{\partial^2 \mathrm{f}^{\mathrm{AF}}}{\partial \alpha^2}$, $\frac{\partial^2 \mathrm{f}^{\mathrm{AF}}}{\partial \beta^2}$ and $\frac{\partial^2 \mathrm{f}^{\mathrm{AF}}}{\partial \delta^2}$. We prove in Appendix 5.8.1 that $\frac{\partial^2 \mathrm{f}^{\mathrm{AF}}}{\partial ..^2} > 0$ for all 3 individual parameters. however, given the complexity of $\mathrm{f}^{\mathrm{af}}(\alpha, \beta, \delta)$, it is difficult to analytically prove convexity through its Hessian $\nabla^2 \mathrm{f}^{\mathrm{af}}$, and numerical simulation was used to verify convexity as discussed in Appendix 5.8.1.

We now give the relative power allocation and location solutions for the three possible cases:

- Case 1: In this case the relative locations (i.e. distances) are fixed. Due to the convexity of f^{AF}, by finding α such that $\frac{\partial \mathrm{f}^{\mathrm{AF}}}{\partial \alpha} = 0$, the optimum relative power allocation α^* is found as a function of relative distances (β and δ). These solutions are equivalent to Eqs. 5.86 and 5.87 in [107] to minimize the SER.

$$\alpha^* = \frac{((1-\beta)^2 + \delta^2)^{\gamma/4} + \sqrt{((1-\beta)^2 + \delta^2)^{\gamma/2} + 8(\beta^2 + \delta^2)^{\gamma/2}}}{3((1-\beta)^2 + \delta^2)^{\gamma/4} + \sqrt{((1-\beta)^2 + \delta^2)^{\gamma/2} + 8(\beta^2 + \delta^2)^{\gamma/2}}} \tag{5.32}$$

- Case 2: We now consider all available regions for α, β and δ to the globally optimum solution to (5.31) for the AF case.

  The optimal relative vertical distance is determined by finding δ such that $\frac{\partial \mathrm{f}^{\mathrm{AF}}}{\partial \delta} = 0$. By inspection of (5.9), it can be seen that the optimal $\delta^* = 0$, and this result is expected as f^{AF} is symmetrical around $\delta = 0$. Therefore, the optimal relay configuration is on a direct line between the source and destination. We can then substitute δ^* into $\mathrm{f}^{\mathrm{AF}}(\cdot)$, and by using its convexity, the optimal α^* and β^* are then found by jointly solving $\frac{\partial \mathrm{f}^{\mathrm{AF}}}{\partial \alpha} = 0$ and $\frac{\partial \mathrm{f}^{\mathrm{AF}}}{\partial \beta} = 0$. The result is the following two equations which can be solved numerically to obtain β^* and α^*

$$(1-\beta^*)^{\gamma-2}(1+\beta^*) - {\beta^*}^{\gamma-1} = 0 \tag{5.33}$$

$$\alpha^* = \frac{{\beta^*}^{\gamma-1}}{{\beta^*}^{\gamma-1} + (1-\beta^*)^{\gamma-1}} \tag{5.34}$$

A plot of optimal parameters β^* and α^* versus pathloss exponent γ is shown in Figure 5.5. We observe that the source needs more power allocation (more than 75%) when the pathloss exponents are between two and seven. This also implies that the relay should move closer to destination to minimize the transmit energy. These results are different from non-diversity systems (such as [117]) where the optimal power allocation (α^*) and location (β^*) is found to be 0.5.

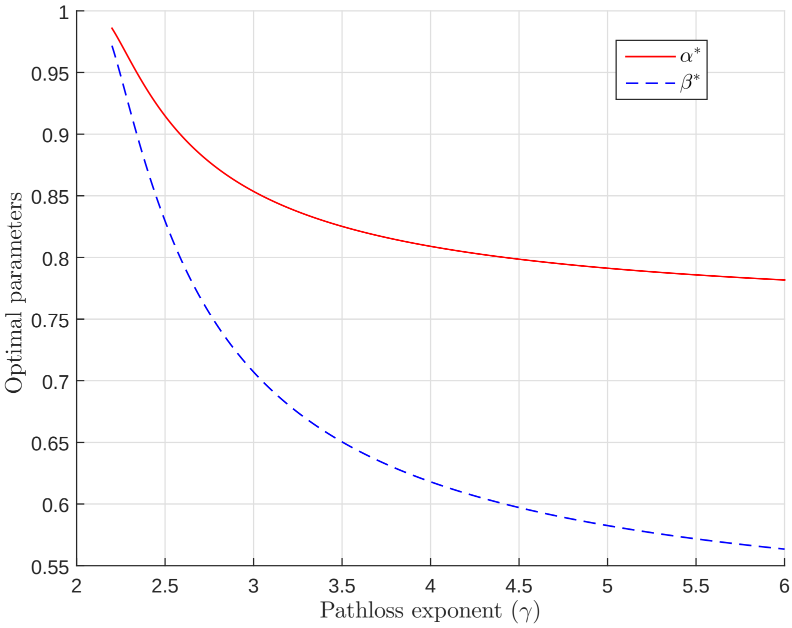

Figure 5.5: Optimal parameters α^* and β^* that minimize the total transmit energy as a function of pathloss exponent.

- Case 3: Here the relative location is constrained: $\beta_1 < \beta < \beta_2$ and $\delta_1 < \delta < \delta_2$. The optimal solution that minimizes $\mathrm{f}^{\mathrm{AF}}(\alpha, \beta, \delta)$ can be determined by using the Karush-Kuhn-Tucker (KKT) sufficient conditions [126]. This is summarized as follows:

- The optimal vertical distance is found as $\delta^* = \min|\delta|$. This value minimizes the source–relay and relay–destination distances.
- In order to find optimal horizontal distance β^*, the unconstrained optimal solution $\bar{\beta}$ is found first by solving the following equation:

$$(1-\bar{\beta})(1-\bar{\beta})^{\gamma/2-2}\{2(1-\bar{\beta})(\bar{\beta}^2+\delta^{*2})+\bar{\beta}((1-\bar{\beta})^2+\delta^{*2})\} \\ -\bar{\beta}^2(\bar{\beta}^2+\delta^{*2})^{\gamma/2-1}=0 \qquad (5.35)$$

  This equation was obtained by jointly solving $\frac{\partial \mathrm{f}^{\mathrm{AF}}}{\partial \alpha}=0$ and $\frac{\partial \mathrm{f}^{\mathrm{AF}}}{\partial \beta}=0$.
- If $\bar{\beta}$ lies within $(\beta_1\,,\beta_2)$, then the constrained optimal solution $\beta^*=\bar{\beta}$. Otherwise, β^* is equal to the closest of β_1 or β_2 to $\bar{\beta}$.
- Finally, the optimal relative power allocation parameter α^* is determined by solving $\frac{\partial \mathrm{f}^{\mathrm{DF}}}{\partial \alpha}=0$ using the previously determined β^* and δ^*. The result is the following equation:

$$\alpha^*=\frac{\beta^*(\beta^{*2}+\delta^{*2})^{\gamma/2-1}}{\beta^*(\beta^{*2}+\delta^{*2})^{\gamma/2-1}+(1-\beta^*)((1-\beta^*)^2+\delta^{*2})^{\gamma/2-1}} \qquad (5.36)$$

5.5.2 AF energy minimization as a function of b

We can re-write (5.18) using the optimized relative location and relative power allocation solution as follows:

$$E^{AF}_{\text{total}} = \frac{N_0 l^\gamma}{L} C^{\mathrm{AF}}_{\text{opt}}\sqrt{\frac{B(b)}{\mathrm{P_e}}}+\frac{C^{\mathrm{AF}}_1}{R_{\mathrm{d}}}+\frac{C^{\mathrm{AF}}_2}{b}\,, \qquad (5.37)$$

where the constant $C^{\mathrm{AF}}_{\text{opt}}$ is used to represent the value of $\sqrt{\mathrm{f}^{\mathrm{AF}}(\alpha^*,\beta^*,\delta^*)}$. We now have E^{AF}_{total} as a function of spectral efficiency b, which our model casts as an even integer.

We temporarily relax b and treat it as a continuous variable to make (5.37) a differentiable function. Numerical evaluation of $\sqrt{B(b)}$ shows that it is a convex function of b for $b>0$ and hence the first term of (5.37) is convex. The second term is not a function of b and is constant for a given data rate, while the third term is a convex function for $b > 0$. Therefore, since the sum of convex functions is also convex, we can conclude that (5.37) is a convex function of b and there exits an optimal spectral efficiency $b_{\mathrm{p}}^{*} > 0$ that minimizes energy consumption.

We now approximate $\sqrt{B(b)}$ in (5.37) using an exponential curve fitting function as follows:

$$p_1 \mathrm{e}^{p_2 b} + p_3 \ \approx \ \sqrt{B(b)}\,, \tag{5.38}$$

where the parameters p_1, p_2 and p_3 are calculated according to possible values of b. This approximation simplifies the total energy expression to

$$E_{\text{total}}^{AF} \ \approx \ \frac{N_0 l^{\gamma}}{L\sqrt{\mathrm{P_e}}} C_{\text{opt}}^{\text{AF}} \left(p_1 \mathrm{e}^{p_2 b} + p_3\right) + \frac{C_1^{\text{AF}}}{R_{\text{d}}} + \frac{C_2^{\text{AF}}}{b} \tag{5.39}$$

We use this approximation to create a new optimization problem where the total energy in (5.37) is replaced and is easier to solve analytically. By differentiating (5.39) with respect to be b and setting the result equal to 0, we obtain the following expression

$${b_{\mathrm{p}}^{*}}^{2} \mathrm{e}^{p_2 b_{\mathrm{p}}^{*}} = \frac{C_2^{\text{AF}} L (\mathrm{P_e})^{0.5}}{p_1 p_2 N_0 l^{\gamma} C_{\text{opt}}^{\text{AF}}} \tag{5.40}$$

The optimal solution b_{p}^{*} can then be found to be

$$b_{\mathrm{p}}^{*} = \frac{2\mathrm{W}\left(\sqrt{\frac{p_2 C_2^{\text{AF}} L (\mathrm{P_e})^{1/2}}{4 p_1 N_0 l^{\gamma} C_{\text{opt}}^{\text{AF}}}}\right)}{p_2}\,, \tag{5.41}$$

where W is the Lambert-W function [127]. We found general curve fitting parameters as $p_1 = 0.194$, $p_2 = 0.533$ and $p_3 = 0.046$ to find b_{p}^{*}. Figure 5.6 shows the curve fit with these parameters for the function $\sqrt{B(b)}$, and the approximation in (5.38) is seen as very tight with the actual values of the function $\sqrt{B(b)}$. As such, using (5.38) instead of $\sqrt{B(b)}$ will yield indiscernible results as shown later in this chapter.

We can now allocate the optimum available spectral efficiency b^{*} from the available

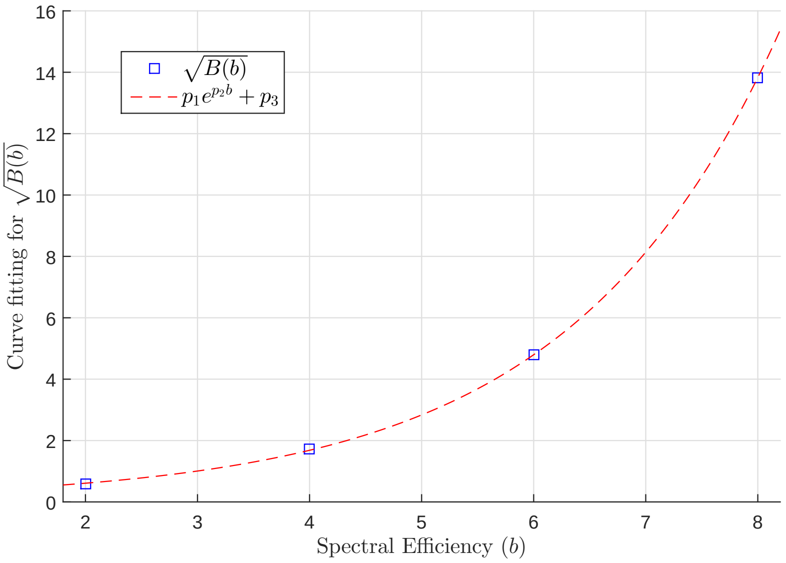

Figure 5.6: Curve fitting approximation $\sqrt{B(b)}$ for AF relay transmission.

square M-QAM constellations as follows:

$$b^* = \begin{cases} 2, & \text{if } b_{\mathrm{p}}^* \leq 2 \\ \tilde{b}, & \text{if } 2 \leq b_{\mathrm{p}}^* \leq 8 \\ 8, & \text{if } b_{\mathrm{p}}^* \geq 8 \end{cases}, \tag{5.42}$$

where $\tilde{b}$ is either $\lceil b_{\mathrm{p}}^* \rceil$ or $\lfloor b_{\mathrm{p}}^* \rfloor$, whichever gives the minimum energy consumption. Note that the $\lceil\,\rceil$ and $\lfloor\,\rfloor$ operators give the lower and higher available spectral efficiencies in b. The optimum total energy consumption can now be calculated by substituting b^* in (5.37).

5.5.3 OLPAS-DF

Unlike in the AF relaying case, the optimum relative location and power allocation depends on $\mathrm{f}^{\mathrm{DF}}(\alpha, \beta, \delta, b)$, which is a function of b. As we assume only a limited number of options for b, we can find the optimum parameters α^*, β^*, and δ^* for each given $b \in \{2, 4, 6, 8\}$. By evaluating these four choices, the optimal b^* and associated relative location and power parameters can be determined that minimize the total energy consumption.

The second derivatives of $\mathrm{f}^{\mathrm{DF}}(\alpha, \beta, \delta, b)$ with respect to either α, β and δ are positive for all four b values. However, like in the AF case, it is difficult to analytically prove convexity through its Hessian $\nabla^2 \mathrm{f}^{\mathrm{df}}$, and numerical simulation was used to verify convexity as discussed in Appendix 5.8.1.

As previously done in the AF relaying case, we consider 3 cases according to specific parameter selections for the OLPAS-DF scheme:

- Case 1: The relay location is fixed, and therefore β and δ can be treated as constants. We utilize the convexity of $\mathrm{f}^{\mathrm{DF}}(\cdot)$ to find the optimum relative power allocation α^* by solving $\frac{\partial \mathrm{f}^{\mathrm{DF}}}{\partial \alpha} = 0$ for a given value of b, which results in the following solution for α^*.

$$\alpha^* = \frac{\left((1-\beta)^2+\delta^2\right)^{\gamma/4} + \sqrt{\left((1-\beta)^2+\delta^2\right)^{\gamma/2} + 8A(b)/B(b)(\beta^2+\delta^2)^{\gamma/2}}}{3\left((1-\beta)^2+\delta^2\right)^{\gamma/4} + \sqrt{\left((1-\beta)^2+\delta^2\right)^{\gamma/2} + 8A(b)/B(b)(\beta^2+\delta^2)^{\gamma/2}}} \tag{5.43}$$

  This solution is similar to Eqs. 5.36 and 5.37 in [107] which are derived to obtain the minimum SER.

- Case 2: We find the globally-optimum solution assuming the original constraints defined for α, β and δ in (5.31). Similar to the AF system, we find the optimum relative vertical distance δ^* is zero (i.e. straight line between source and destination) by solving $\frac{\partial \mathrm{f}^{\mathrm{DF}}}{\partial \delta} = 0$. We can then substitute δ^* into $\mathrm{f}^{\mathrm{DF}}(\cdot)$, and by using its convexity, the optimal α^* and β^* are then found by solving $\frac{\partial \mathrm{f}^{\mathrm{DF}}}{\partial \alpha} = 0$ and $\frac{\partial \mathrm{f}^{\mathrm{DF}}}{\partial \beta} = 0$. The result is the following two equations which are to be jointly solved numerically to obtain β^* and α^* for all four values of b:

$$B(b)(1-\beta^*)^{\gamma-2}(1+\beta^*) - A(b)\beta^{*\gamma-1} = 0 \tag{5.44}$$

$$\alpha^* = \frac{A(b)\beta^{*\gamma-1}}{A(b)\beta^{*\gamma-1} + B(b)(1-\beta^*)^{\gamma-1}} \tag{5.45}$$

  We obtained optimal parameters for 4-QAM and 256-QAM as a function of the pathloss exponent γ, and the results are illustrated in Figure 5.7. The figure shows that for the considered pathlosses, DF systems are more energy efficient when the relay is moved towards the destination (i.e. $\beta > 0.5$), and when more power is allocated to the source (i.e. $\alpha > 0.5$). It is important to note that the major difference between AF and DF systems according to the OLPAS scheme is that both α^* and β^* reduce as the spectral efficiency b increases in DF systems, while they remain same in AF systems regardless of b.

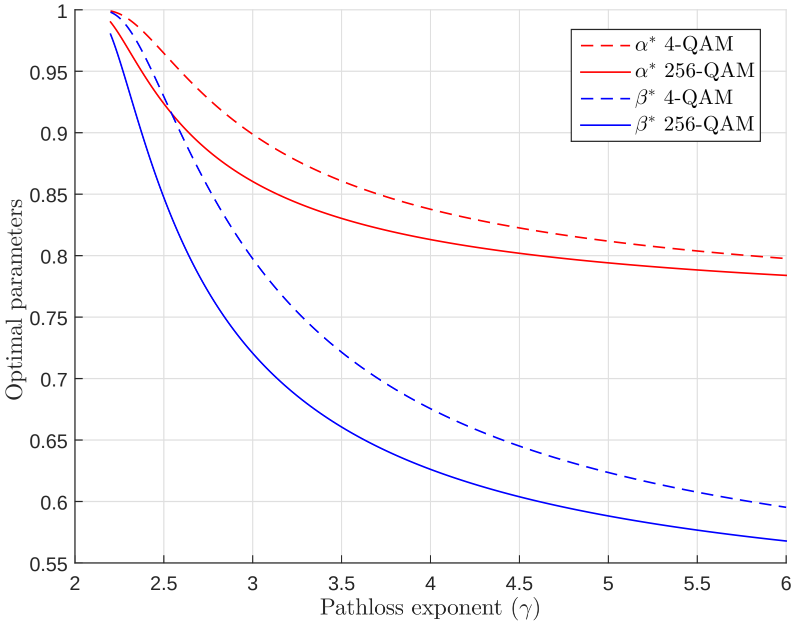

Figure 5.7: Optimal parameters α^* and β^* versus pathloss exponent γ that minimize the total transmit energy of a DF system.

- Case 3: Here the relative relay location is constrained by $\beta_1 < \beta < \beta_2$ and $\delta_1 < \delta < \delta_2$. The optimal solutions of $\mathrm{f}^{\mathrm{DF}}(\alpha, \beta, \delta, b)$ can be determined by Karush-Kuhn-Tucker (KKT) sufficient conditions [126]. It is summarized as follows:
  - The optimal vertical distance is found as $\delta^* = \min|\delta|$. This results in minimizing the source–relay and relay–destination distances.
  - The optimal horizontal distance β^* is found using the unconstrained optimal

solution $\bar{\beta}$, which is numerically solved for using the following equation.

$$\begin{aligned} B(b)(1-\bar{\beta})(1-\bar{\beta})^{\gamma/2-2}\{2(1-\bar{\beta})(\bar{\beta}^2+\delta^{*2})+\bar{\beta}((1-\bar{\beta})^2+\delta^{*2})\} \\ -A(b)\bar{\beta}^2(\bar{\beta}^2+\delta^{*2})^{\gamma/2-1} &= 0 \end{aligned} \tag{5.46}$$

This equation was obtained by jointly solving $\frac{\partial \mathrm{f}^{\mathrm{DF}}}{\partial \alpha} = 0$ and $\frac{\partial \mathrm{f}^{\mathrm{DF}}}{\partial \beta} = 0$.

- If $\bar{\beta}$ lies within $(\beta_1\ , \beta_2)$, then the constrained optimal solution is assigned as $\beta^* = \bar{\beta}$. Otherwise, β^* is equal to closest of β_1 or β_2 to $\bar{\beta}$.
- Finally, the optimal relative power allocation α^*, is calculated by solving $\frac{\partial \mathrm{f}^{\mathrm{DF}}}{\partial \alpha} = 0$ using the previously determined β^* and δ^*. The result is the following equation:

$$\alpha^* = \frac{A(b)\beta^*(\beta^{*2}+\delta^{*2})^{\gamma/2-1}}{A(b)\beta^*(\beta^{*2}+\delta^{*2})^{\gamma/2-1} + B(b)(1-\beta^*)((1-\beta^*)^2+\delta^{*2})^{\gamma/2-1}} \tag{5.47}$$

5.5.4 DF energy minimization as a function of b

As discussed in the previous subsection, we calculate four different optimal parameter sets for the four values of b. We re-write (5.30) for a given b using location and power optimized solutions as

$$E_{\text{total}}^{DF} = \frac{N_0 l^\gamma}{L}\sqrt{\frac{1}{\mathrm{P_e}}\mathrm{f}^{\mathrm{DF}}(\alpha^*, \beta^*, \delta^*, b)} + \frac{C_1^{\mathrm{DF}}}{R_{\mathrm{d}}} + \frac{C_2^{\mathrm{DF}}}{b} \tag{5.48}$$

We now temporarily relax b and treat it as a continuous variable to make (5.48) a differentiable function of b. Proving the convexity of E_{total}^{DF} as a function of $b > 0$ is difficult due to the square root in the first term and $\sqrt{\mathrm{f}^{\mathrm{DF}}(\alpha^*, \beta^*, \delta^*, b)}$ being a function of $B(b)$ and $A(b)$ from (5.7) and (5.20), respectively. Furthermore, it is not sufficient to show that $\mathrm{f}^{\mathrm{DF}}()$ is a convex function because $\sqrt{x}$ is a concave function for $x > 0$. Numerical simulation of $\sqrt{\mathrm{f}^{\mathrm{DF}}(\alpha^*, \beta^*, \delta^*, b)}$ was performed under Case 2's parameter space and over the range of pathloss exponents $2 < \gamma < 6$ with a resolution of 0.01 on γ and b.[8] Using the set of

---

[8] Under Case 3 and certain region constrictions on β and δ that are likely not practical, E_{total}^{DF} is not a convex function of continuous-valued $b > 0$. In this case, one can compute E_{total}^{DF} for all possible b values and choose the minimum-energy configuration directly.

optimal parameters α^*, β^* and $\delta^* = 0$ that resulted from a given b and γ, convexity was verified as a function of b. Similar to the AF case, the remaining terms in (5.48) are convex with respect to b, and therefore we can conclude that (5.37) is a convex function of b and there exits an optimal spectral efficiency $b_{\mathrm{p}}^* > 0$ that minimizes energy consumption.

We now approximate $\sqrt{\mathrm{f}^{\mathrm{DF}}(\alpha^*, \beta^*, \delta^*, b)}$ in (5.48) using an exponential curve fitting function of b as follows:

$$p_4 \mathrm{e}^{p_5 b} + p_6 \;\approx\; \sqrt{\mathrm{f}^{\mathrm{DF}}(\alpha^*, \beta^*, \delta^*, b)}\,, \tag{5.49}$$

where the parameters p_4, p_5 and p_6 are calculated according to possible values of b.

This approximation simplifies the total energy consumption in (5.48) to

$$E_{\text{total}}^{DF} \;\approx\; \frac{N_0 l^\gamma}{L\sqrt{\mathrm{P_e}}}\left(p_4 \mathrm{e}^{p_5 b} + p_6\right) + \frac{C_1^{\mathrm{DF}}}{R_{\mathrm{d}}} + \frac{C_2^{\mathrm{DF}}}{b} \tag{5.50}$$

As in Section 5.3, we now use this approximation to create an analytically solvable new optimization problem. By differentiating (5.50) with respect to be b and setting the result equal to 0, we obtain the following expression.

$$b_{\mathrm{p}}^{*\,2} \mathrm{e}^{p_5 b_{\mathrm{p}}^*} = \frac{C_2^{\mathrm{DF}} L \sqrt{(\mathrm{P_e})}}{p_4 p_5 N_0 l^\gamma} \tag{5.51}$$

Rearranging this equation, the optimal solution that minimizes the approximation of E_{total}^{DF} in (5.50) is found to be

$$b_{\mathrm{p}}^* = \frac{2\mathrm{W}\left(\sqrt{\frac{p_5 C_2^{\mathrm{DF}} L (\mathrm{P_e})^{0.5}}{4 p_4 N_0 l^\gamma}}\right)}{p_5}\,, \tag{5.52}$$

where W is the Lambert-W function. This continuous result is then mapped to the closest available discrete spectral efficiency.

Assuming a pathloss exponent of $\gamma = 3.5$ and the Case 2 with unconstrained location, we calculated the general curve fitting parameters as $p_4 = 0.133$, $p_5 = 0.534$ and $p_6 = -0.029$. Optimal relative power allocation parameter α^* values were calculated to be

0.86, 0.84, 0.83 and 0.83 for the four discrete spectral efficiencies 2, 4, 6 and 8, respectively. The optimal relative location parameter β^* values were calculated to be 0.72, 0.68, 0.67 and 0.66 for the same four values of b, respectively. We then use the mapping proposed in (5.42) to allocate the optimum available spectral efficiency b^* using b_{p}^*. The curve fitting function for this scenario is illustrated in Figure 5.8, and shows that our approximation in (5.49) is very tight with the actual values of the function $\sqrt{\text{f}^{\text{DF}}(\alpha^*, \beta^*, \delta^*, b)}$. Using (5.49) instead of $\sqrt{\text{f}^{\text{DF}}(\alpha^*, \beta^*, \delta^*, b)}$ will therefore yield indiscernible results as shown later in this chapter.

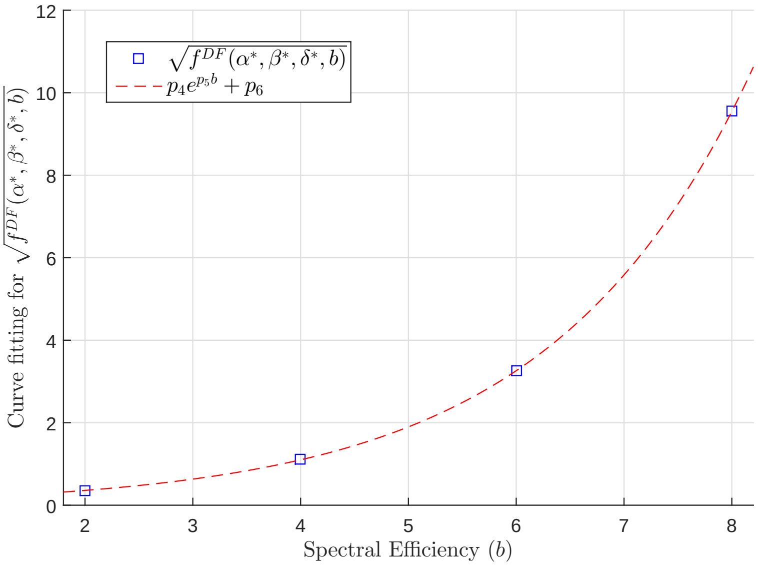

Figure 5.8: Curve fitting approximation of $\sqrt{\text{f}^{\text{DF}}(\alpha^*, \beta^*, \delta^*, b)}$ for DF relay transmission.

After finding b^*, the optimal total energy consumption can be calculated by (5.48) using $E_{\text{total}}^{DF}(\alpha^*, \beta^*, \delta^*, b^*)$.

5.6 Numerical Evaluation

We now use the above expressions to investigate the energy consumption of AF and DF relay systems.

5.6.1 Performance of OLPAS compared to other schemes

We first look at the energy gains achieved by the OLPAS scheme compared to two conventional one-dimensional optimization approaches. The first is equal-energy allocation, where both source and relay have the same power allocation (i.e. $\alpha = 0.5$) and location is optimized. The second is middle-location allocation, where the relay is located halfway between the source and destination (i.e. $\beta = 0.5$ and $\delta = 0$) and power allocation is optimized. Figure 5.9 represents the effective output of $\mathrm{f}^{\mathrm{AF}}(\alpha, \beta, 0)$ in the radio energy consumption of OLPAS and these two resource allocation strategies for AF transmission The figure shows that the OLPAS schemes saves energy compared to both other schemes

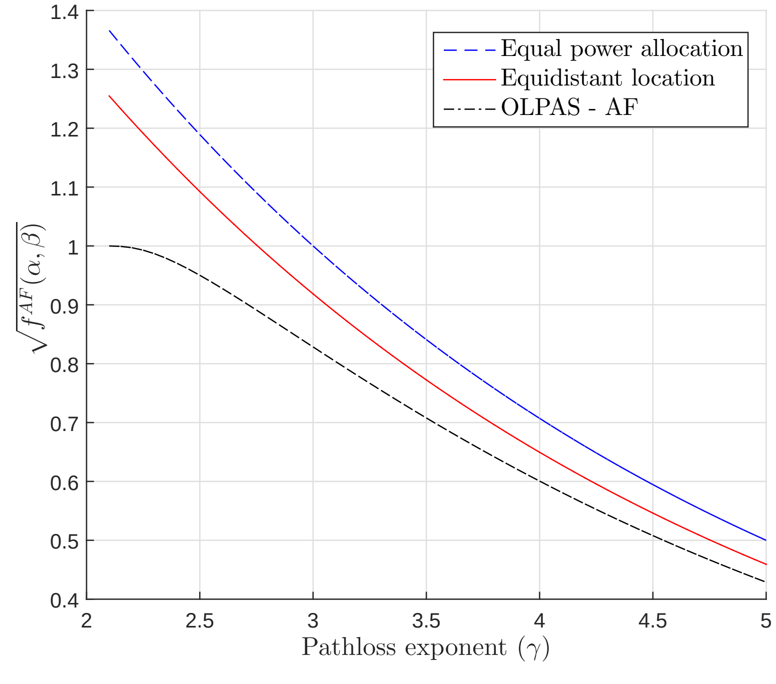

Figure 5.9: Radio energy consumption for the OLPAS-AF scheme, equal-energy scheme, and middle-location scheme versus pathloss γ.

for all pathloss considering. However, the gain achieved by our proposed scheme reduces when pathloss exponent is high. Another important note is that power optimization appears to be more important than location optimization due to the middle-location strategy being more efficient than the equal-energy strategy.

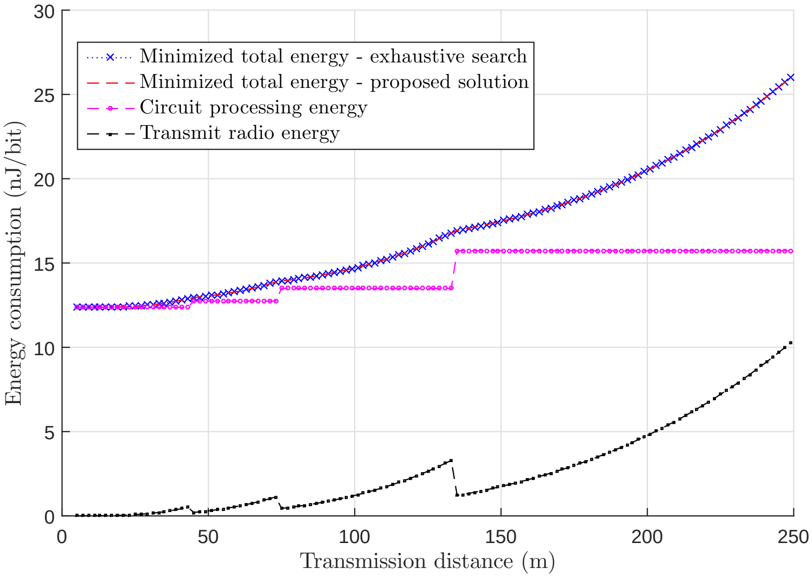

Figure 5.10: Total minimized energy consumption of AF system using exhaustive search and approximations, energy breakdown of total transmission.

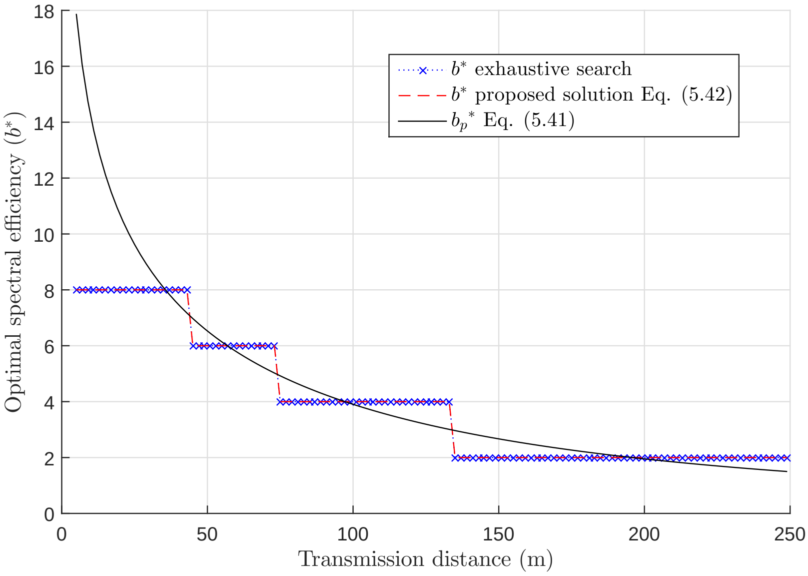

Figure 5.11: Optimum spectral efficiency using exhaustive search, (5.41) and proposed solution.

5.6.2 Performance of the proposed optimizing approach

In this section, we investigate the accuracy of our proposed optimization methodology for AF systems using numerical evaluation. We compare the performance of our proposed approach with exhaustive search results of (5.37). We also investigate the energy breakdown between the power amplifier transmission energy and circuit processing energy. Results for an AF system are presented in Figure 5.10 assuming a pathloss exponent of 3.5 [117]. We do not present the results for DF systems as they show a similar pattern as in AF. In this simulation, our approach using the approximation in (5.39) achieves the optimal solutions from an exhaustive search, but with a lower complexity. It can also be seen that the total energy increases exponentially with distance, which is expected. The shapes of the curves in Figure 5.10 change at a few occasions due to a change in modulation scheme as a function of distance (see Figure 5.11). The breakdown between the power amplifier energy and circuit processing energy highlights the importance of having a modulation-dependent energy model.

At short distances, the radio energy is small, and therefore the lowest circuit processing energy is chosen by increasing the spectral efficiency to minimize the total energy. As the distance increases and radio energy dominates the total energy, a higher portion of the energy budget is allocated to radio energy. This results in a reduction in spectral efficiency (b) in order to reduce the dominant energy component, and while this does increase the circuit energy, the trade-off is beneficial as it reduces the radio energy by a greater amount. This trend is more visible at distances above 80 m in Figure 5.10.

Figure 5.11 shows the optimal spectral efficiency as a function of distance. The continuous b solution of (5.41) is plotted along with the final solution of our approach and the exhaustive search result. This figure also verifies that our algorithm produces the optimal results in terms of energy efficiency.

At short distances 256-QAM provides the most energy efficient transmission, and as the distance increases the optimal modulation order reduces. Specifically, the reduction from to 64-QAM, to 16-QAM and to 4-QAM occur at the distances of 45 m, 73 m and 134 m, respectively.

5.6.3 Performance comparison of various transmission schemes

We now investigate energy efficiencies of three transmission systems: AF relaying, DF relaying and direct transmission. We set a target average BER $P_e = 10^{-4}$ with target data rate $R_{\mathrm{d}} = 1$ Mbps, and assume a pathloss exponent of $\gamma = 3.5$. Receiver noise spectral density of -174 dBm/Hz and receiver noise figure of 9 dB [104], and path-loss propagation constant $L_0 = 10^{-3}$ [121] are assumed. The optimal parameters α^* are β^* are chosen according to the OLPAS schemes with $\delta = 0$.

In order to compare the performance of cooperative-relayed transmission with direct transmission under the same Rayleigh channel conditions, we derived an expression for the power amplifier energy consumption $E_{\mathrm{tr}}^{\mathrm{Dir}}$ to achieve a given BER of $\mathrm{P_e}$. This is given as follows:

$$E_{\mathrm{tr}}^{\mathrm{Dir}} = \frac{1.4\, N_0\, (2^b-1)^{1/2} (2^{b/2}-1)^2}{\sqrt{3}\mathrm{P_e} L l^{-\gamma}\, b^2 2^b} \left[\left(1+\frac{2}{\pi}\right) 2^{b/2} + \left(1-\frac{2}{\pi}\right) \right] , \tag{5.53}$$

and a derivation is presented in Appendix 5.8.2. The circuit energy consumption of direct transmission[9] is found by adding the energy costs of components from the source and the destination as follows:

$$E_{\mathrm{c}}^{\mathrm{Dir}} = \frac{4C_{\mathrm{Mixer}} + 2C_{\mathrm{Oscil}} + C_{\mathrm{LNA}} + W(2C_{\mathrm{BA}} + 2C_{\mathrm{ADC}} + 2C_{\mathrm{DAC}})}{R_{\mathrm{d}}} + \frac{C_{\mathrm{TS}} + C_{\mathrm{FS}} + C_{\mathrm{PS}}}{b} \tag{5.54}$$

$$E_{\mathrm{c}}^{\mathrm{Dir}} = \frac{C_1^{\mathrm{Dir}}}{R_{\mathrm{d}}} + \frac{C_2^{\mathrm{Dir}}}{b} , \tag{5.55}$$

where the constants C_1^{Dir} and C_2^{Dir} are defined as,

$$C_1^{\mathrm{Dir}} = \frac{4C_{\mathrm{Mixer}} + 2C_{\mathrm{Oscil}} + C_{\mathrm{LNA}}}{2} \times 10^6 \tag{5.56}$$

and

$$C_2^{\mathrm{Dir}} = 2\,(1+\alpha)\left(2C_{\mathrm{BA}} + 2C_{\mathrm{ADC}} + 2C_{\mathrm{DAC}}\right) \times 10^6 + \left(C_{\mathrm{TS}} + C_{\mathrm{FS}} + C_{\mathrm{PS}}\right) \times 10^{-3} . \tag{5.57}$$

The constants C_1^{Dir} and C_2^{Dir} are calculated as 4.375×10^6 and 3.45, respectively.

---

[9] The circuit energy model in Chapter 4 includes energy consumption of an equalizer, an encoder and a decoder. However, since we do not consider these segments in our system, we ignore their energy costs.

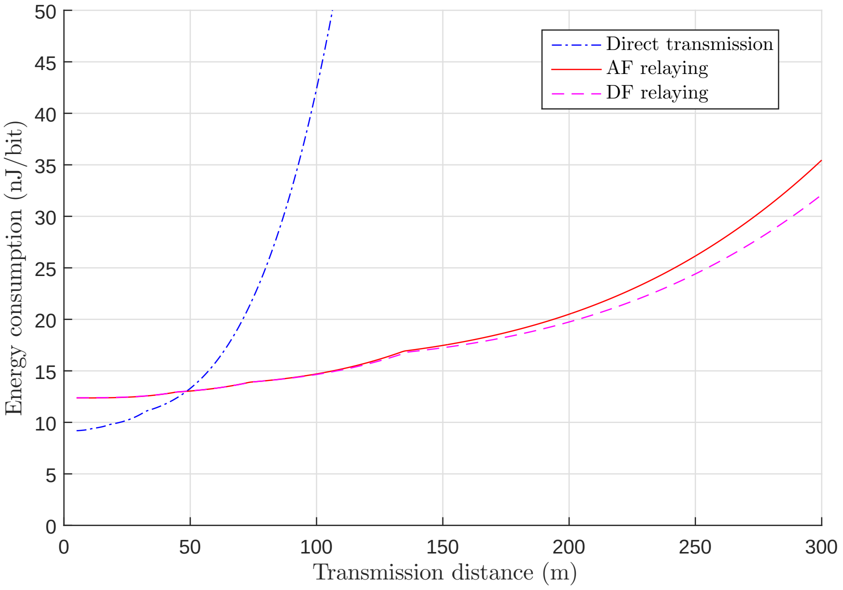

Figure 5.12: Total energy for AF, DF and direct transmission versus distance.

By adding (5.53) and (5.55), we find the total energy consumption for the direct transmission as follows:

$$E_{\text{total}}^{Dir} = \frac{1.4\, N_0\, (2^b-1)^{1/2}(2^{b/2}-1)^2}{\sqrt{3}\mathrm{P_e} L l^{-\gamma}\, b^2\, 2^b} \left[\left(1+\frac{2}{\pi}\right)2^{b/2} + \left(1-\frac{2}{\pi}\right)\right] + \frac{C_1^{\text{Dir}}}{R_{\text{d}}} + \frac{C_2^{\text{Dir}}}{b} \quad (5.58)$$

The total energy consumption, including both circuit processing energy and power amplifier energy is plotted as a function of transmission distance in Figure 5.12. Here we considered all available M-QAM constellations and manually picked the most efficient modulation scheme. The circuit energy required with AF and DF systems are approximately the same as both contain the same analog operations, which are energy-dominant over digital processing operations. In direct transmission, the circuit energy cost is approximately half of the cost in relay systems. Therefore, for shorter distances (< 50 m) direct transmission consumes less total energy than the two relay systems. DF relay systems consume slightly more energy than AF till about 62 m, where AF then starts consuming more energy at longer distances. The shape of the AF and DF curves changes at several points due to the change in modulation scheme to optimize the total energy. We also notice that the relaying energy consumption increases rapidly after 200 m, which hints that additional relays may possibly reduce the transmission energy at such longer distances.

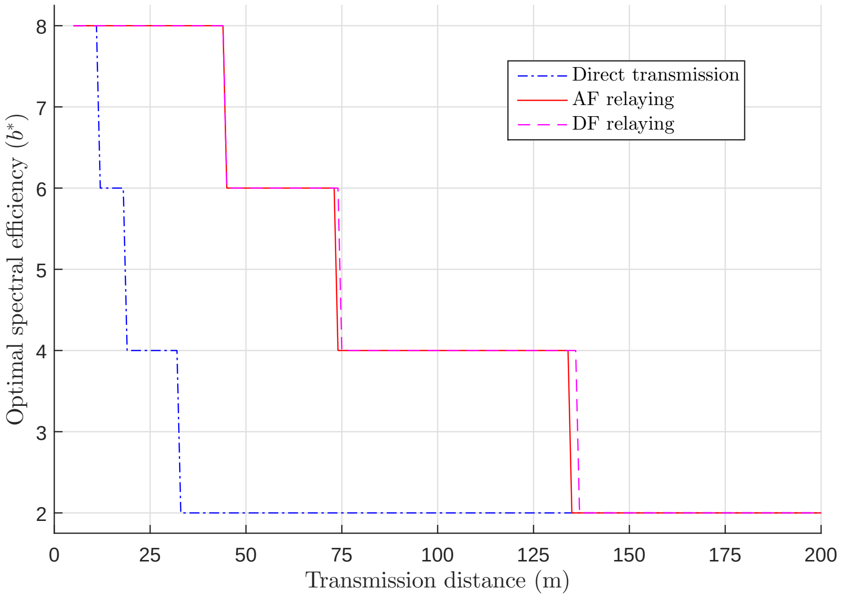

Figure 5.13: Optimum spectral efficiency versus distance for AF, DF and direct transmission.

The spectral efficiency adapted by each of the three transmission schemes at various distances is presented in Figure 5.13. Higher-order modulation is much more energy efficient for shorter distances, while lower-order modulation suits longer range transmission. The optimal spectral efficiency for both AF and DF are nearly the same except for a small gaps around around 75 m and 134 m. Analyzing both Figure 5.12 and Figure 5.13, it can be seen that relaying with 256-QAM or 64-QAM may not be suitable as direction transmission for distances below 50 m. Of course, such a result will vary with the chosen target BER and data rate, but the main point is likely to remain valid: if higher modulation order is possible for the given BER constraint, it is likely that a relay simply is not required.

Figure 5.14 shows the energy percentage breakdown of the PA, other analog circuitry, and digital segments for the optimal-energy configuration as a function of distance. We can see that the optimal transmission scheme switches to relay from direct transmission

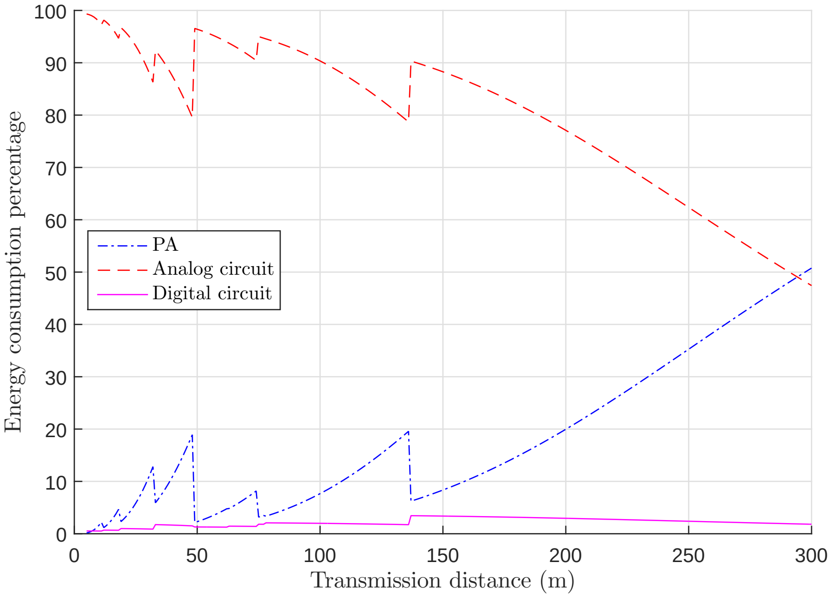

Figure 5.14: Energy consumption percentage for optimal transmission.

at around 50 m when the PA power begins to increase more rapidly. Adding a relay at this point reduces the total PA power, but it results in an increase to the remaining analog and digital energies. However, when the relay strategy switches to AF and DF in the considered distance, a significant percentage difference cannot be observed due to their analog circuit energy consumption being same and digital energy of DF being slightly higher. PA energy is considerably lower around distances 50-70 m. However, when the optimal modulation changes from 6 to 4 to 2 at 75 m and 134 m, respectively, the PA energy is reduced in DF relay transmission at the expense of analog and digital circuit energy.

Figure 5.15 summarizes the energy efficiency investigation of cooperative-relayed transmission and direct transmission by proposing the optimal selected scheme as a function of distance. For short distances of up to 50 m, direct transmission requires the least energy, while cooperative relayed transmission is more energy efficient for longer distances. AF is slightly more efficient than DF at short distances up to 62 m, and more efficient than direct transmission after 50 m. Specifically, it is DF transmission that is chosen beyond 62 m due to its low PA energy requirement at long distance transmission.

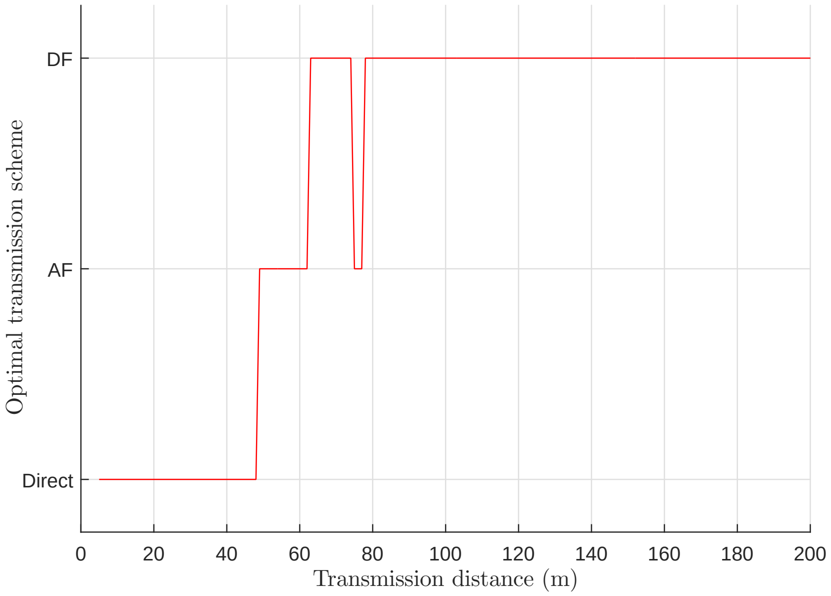

Figure 5.15: Optimal transmission strategy vs transmission distance.

AF briefly becomes the most efficient scheme again at around 75 m when it shifts from 64-QAM to 16-QAM, thus reducing its PA energy. However, DF shifts to 16-QAM only with only a few additional meters of distance, and becomes most energy efficiency from that point and further distances.

5.7 Conclusions

We derived energy models for dual-hop (single-relay) cooperative systems in which location of the relay is defined in a two-dimensional space. Using our energy models, we showed that both AF and DF systems have an optimal location and optimal power allocation which minimize the total energy consumption. In AF, the location and power allocation can be optimized independently from the spectral efficiency, circuit processing energy and other variables, such as BER and amplifier efficiency. We were able to optimize the energy over spectral efficiency using some mathematical approximations. Energy optimization in DF systems, however, is more complex because location and power are not independent of spectral efficiency and some other variables. It therefore requires evaluation over spectral efficiency through either an exhaustive search or a more efficient approximation method.

However, the decode–and–forward systems usually required a lower SNR at the receivers after combining and with a higher computational complexity. Therefore, the processing energy–radio energy trade-off would be more visible in AF system versus decode–and–forward system investigation and the results may include AF relays as an optimal solution in Figure 5.15.

In our system, we assumed a Rayleigh faded (non–line–of–sight-LOS) channel model. When the distance is short, LOS component could be available and the Rician channel model could be adopted. In such cases a lower transmit power might be needed since usually Rician channels have a dominant LOS component which improves the performance at the same SNR for a Rayleigh channel. However, at short distances the total energy is dominated by the circuit processing energy and therefore, assuming a Rician channel may not change the overall results significantly.

Based on our analysis and numerical results, single-relay systems can have rapidly increasing energy consumptions even at relatively short distances (e.g., beyond 200 m in our simulation example). Therefore, we will next consider the energy efficiency of multi-relay transmission and any cooperation and diversity trade-offs.

5.8 Appendix

5.8.1 Convexity of $\mathrm{f}^{\mathbf{AF}}(\alpha, \beta, \delta)$ with respect to α, β and δ

The function f^{AF} is defined as,

$$\mathrm{f}^{\mathrm{AF}}(\alpha,\beta,\delta) = \frac{(\beta^2+\delta^2)^{\gamma/2}}{\alpha^2} + \frac{[(1-\beta)^2+\delta^2]^{\gamma/2}}{\alpha(1-\alpha)} \tag{5.59}$$

The partial derivative of f^{AF} with respect to α is

$$\frac{\partial \mathrm{f}^{\mathrm{AF}}}{\partial\alpha} = \frac{-2(\beta^2+\delta^2)^{\gamma/2}}{\alpha^3} - \frac{[(1-\beta)^2+\delta^2]^{\gamma/2}(1-2\alpha)}{\alpha^2(1-\alpha)^2} \tag{5.60}$$

The second order partial derivative of f^{AF} with respect to α is then

$$\frac{\partial^2 \mathrm{f}^{\mathrm{AF}}}{\partial \alpha^2} = \frac{6(\beta^2+\delta^2)^{\gamma/2}}{\alpha^6} + \frac{2[(1-\beta)^2+\delta^2]^{\gamma/2}[(1-2\alpha)^2+\alpha(1-\alpha)]}{\alpha^3(1-\alpha)^3} \tag{5.61}$$

The value of $\frac{\partial^2 \mathrm{f}^{\mathrm{AF}}}{\partial \alpha^2}$ is always positive for the given parameter ranges.

The partial derivative of f^{AF} with respect to β is

$$\frac{\partial \mathrm{f}^{\mathrm{AF}}}{\partial \beta} = \frac{\gamma\beta(\beta^2+\delta^2)^{\gamma/2-1}}{\alpha^2} - \frac{\gamma[(1-\beta)^2+\delta^2]^{\gamma/2-1}(1-\beta)}{\alpha(1-\alpha)} \tag{5.62}$$

The second order partial derivative of f^{AF} with respect to β is

$$\frac{\partial^2 \mathrm{f}^{\mathrm{AF}}}{\partial \beta^2} = \frac{\gamma(\beta^2+\delta^2)^{\gamma/2-2}[\delta^2+(\gamma-1)\beta^2]}{\alpha^2} + \frac{\gamma[(1-\beta)^2+\delta^2]^{\gamma/2-2}[\delta^2+(\gamma-1)(1-\beta)^2]}{\alpha(1-\alpha)} \tag{5.63}$$

The value of $\frac{\partial^2 \mathrm{f}^{\mathrm{AF}}}{\partial \beta^2}$ is always positive for the given parameter ranges.

The partial derivative of f^{AF} with respect to δ is

$$\frac{\partial \mathrm{f}^{\mathrm{AF}}}{\partial \delta} = \frac{\gamma\delta(\beta^2+\delta^2)^{\gamma/2-1}}{\alpha^2} + \frac{\gamma\delta[(1-\beta)^2+\delta^2]^{\gamma/2-1}}{\alpha(1-\alpha)} \tag{5.64}$$

The second order partial derivative of f^{AF} with respect to δ is

$$\frac{\partial^2 \mathrm{f}^{\mathrm{AF}}}{\partial \delta^2} = \frac{\gamma(\beta^2+\delta^2)^{\gamma/2-2}[\beta^2+(\gamma-1)\delta^2]}{\alpha^2} + \frac{\gamma[(1-\beta)^2+\delta^2]^{\gamma/2-2}[(1-\beta)^2+(\gamma-1)\delta^2]}{\alpha(1-\alpha)} \tag{5.65}$$

The $\frac{\partial^2 \mathrm{f}^{\mathrm{AF}}}{\partial \delta^2}$ is always positive for the given parameter regions $0 < \alpha < 1$, $0 < \beta < 1$, and $-1 < \delta < 1$.

As the set of second derivatives in (5.61), (5.63) and (5.65) are positive, and numerical solutions exist for the first derivatives that satisfy $\frac{\partial \mathrm{f}^{\mathrm{AF}}}{\partial \alpha} = 0$, $\frac{\partial \mathrm{f}^{\mathrm{AF}}}{\partial \beta} = 0$, and $\frac{\partial \mathrm{f}^{\mathrm{AF}}}{\partial \delta} = 0$ for the given parameter regions, it can be concluded that f^{AF} is a convex function of each *individual* variable (α, β and δ).

f^{AF} is a convex function of all three parameters if its Hessian matrix ($\nabla^2 \mathrm{f}^{\mathrm{AF}}$) is positive semi-definite [126] for all α, β and δ in the given parameter regions. The Hessian $\nabla^2 \mathrm{f}^{\mathrm{AF}}$

is defined as [126],

$$\nabla^2 \mathrm{f}^{\mathrm{AF}} = \begin{bmatrix} \frac{\partial^2 \mathrm{f}^{\mathrm{AF}}}{\partial \alpha^2} & \frac{\partial^2 \mathrm{f}^{\mathrm{AF}}}{\partial \alpha \partial \beta} & \frac{\partial^2 \mathrm{f}^{\mathrm{AF}}}{\partial \alpha \partial \delta} \\ \frac{\partial^2 \mathrm{f}^{\mathrm{AF}}}{\partial \beta \partial \alpha} & \frac{\partial^2 \mathrm{f}^{\mathrm{AF}}}{\partial \beta^2} & \frac{\partial^2 \mathrm{f}^{\mathrm{AF}}}{\partial \beta \partial \delta} \\ \frac{\partial^2 \mathrm{f}^{\mathrm{AF}}}{\partial \delta \partial \alpha} & \frac{\partial^2 \mathrm{f}^{\mathrm{AF}}}{\partial \delta \partial \beta} & \frac{\partial^2 \mathrm{f}^{\mathrm{AF}}}{\partial \delta^2} \end{bmatrix} \tag{5.66}$$

Since it is difficult to show that $\nabla^2 \mathrm{f}^{\mathrm{AF}}$ is positive semi-definite by using a general analytical framework, we instead use numerical simulations to verify convexity up to a resolution of 0.01 for the parameters α, β and δ in their defined ranges and the pathloss exponent in the range $(2 < \gamma < 6)$. We observed that $\nabla^2 \mathrm{f}^{\mathrm{AF}}$ was positive semi-definite in all cases.

Similar simulations were used to verify the convexity of $\mathrm{f}^{\mathrm{DF}}(\alpha, \beta, \delta, b)$ up to the same 0.01 resolution and for all available spectral efficiencies b.

5.8.2 Transmit Energy per bit for direct transmission

The symbol error rate for Rayleigh faded single link is derived by Simon et al. [128] and given as

$$P_s = \frac{4K_1}{\pi} \int_0^{\pi/2} \frac{1}{1 + \frac{K_2}{\sin^2\theta} \frac{E_{\mathrm{Rx}}}{N_0}} d\theta - \frac{4{K_1}^2}{\pi} \int_0^{\pi/4} \frac{1}{1 + \frac{K_2}{\sin^2\theta} \frac{E_{\mathrm{Rx}}}{N_0}} d\theta \, , \tag{5.67}$$

where $\frac{E_{\mathrm{Rx}}}{N_0}$ is the received SNR per bit and the modulation-dependent constants are defined as $K_1 = 1 - 2^{-b/2}$ and $K_2 = \frac{1.5b}{2^b - 1}$. Assuming the system operates in a high SNR region, we introduce the following approximation:

$$1 + \frac{K_2}{\sin^2\theta} \frac{E_{\mathrm{Rx}}}{N_0} \approx \frac{K_2}{\sin^2\theta} \frac{E_{\mathrm{Rx}}}{N_0}$$

This allows the for the simplification of (5.67) to

$$P_s \;=\; \frac{4K_1N_0}{\pi K_2 E_{\text{Rx}}}\int_0^{\pi/2}\sin^2\theta d\theta - \frac{4{K_1}^2N_0}{\pi K_2 E_{\text{Rx}}}\int_0^{\pi/4}\sin^2\theta d\theta \tag{5.68}$$

Evaluating these integrals results in

$$P_s \;=\; \frac{N_0\,(2^b-1)(2^{b/2}-1)}{3E_{\text{Rx}}\,b\,2^b}\left[\left(1+\frac{2}{\pi}\right)2^{b/2}+\left(1-\frac{2}{\pi}\right)\right] \tag{5.69}$$

Using (5.69) and by substituting the power amplifier energy-consumption-based expression from (5.5) for E_{Rx}, we obtain the following BER expression for direct transmission:

$$\mathrm{P_e} \;=\; \frac{1.4\,N_0\sqrt{\left(2^{b/2}-1\right)^5(2^{b/2}+1)}}{\sqrt{3}E_{\text{tr}}^{\text{Dir}}Ll^{-\gamma}\,b^2\,2^b}\left[\left(1+\frac{2}{\pi}\right)2^{b/2}+\left(1-\frac{2}{\pi}\right)\right], \tag{5.70}$$

where $E_{\text{tr}}^{\text{Dir}}$ is the power amplifier energy consumption in direct transmission. Rearranging terms in the equation results in

$$E_{\text{tr}}^{\text{Dir}} \;=\; \frac{1.4\,N_0\,\left(2^b-1\right)^{1/2}\left(2^{b/2}-1\right)^2}{\sqrt{3}\mathrm{P_e}Ll^{-\gamma}\,b^2\,2^b}\left[\left(1+\frac{2}{\pi}\right)2^{b/2}+\left(1-\frac{2}{\pi}\right)\right] \tag{5.71}$$

Chapter 6

Energy Modeling and Optimization of Dual-Relay Systems

In this chapter, we present an energy model for a cooperative dual-relay system using detect-and-forward (DF) protocol with receiver diversity. Energy consumption is based on models of both analog and digital components for transmission and reception. A quartic transmit power amplifier (PA) energy equation is derived that is a function of the following parameters: relay location, relative transmit power allocation amongst the relays, spectral efficiency, transmission distance, pathloss, and target bit-error rate (BER). The energies of the remaining circuit components are added to form a multi-relay DF system energy equation, which is then numerically evaluated to minimize total energy by finding the optimal relay locations, relay transmit PA power allocations, and spectral efficiency. Results are compared to our previous work in Chapter 5 that considered the energy of direct transmission and a single-relay system, and the minimum-energy system as a function of source-destination distance is considered.

6.1 Introduction

THe previous chapter showed that single cooperative relay can be used to reduce energy consumption of wireless transmission. Specifically, the detect-and-forward (DF) protocol showed higher energy efficiency compared to the amplify-and-forward (AF) protocol. In this chapter, we observe that further energy savings can be achieved by a dual-relay system. Previous results show that for longer distances, total energy is dominated by transmission energy, and therefore, this energy consumption should be more focused on such scenarios. This has been recognized in the research literature, as more relays are proposed to reduce the power consumption of wireless transmission in

[106, 107, 117].

There are various strategies used in multi-hop relaying systems to increase the performance in terms of error rate and capacity. Several studies have focused on AF relays that utilize the multi-link diversity [106, 129, 130], but when the signals are combined at the destination, the final SNR produces a complex expression of channel gains, which results in underivable error rate and outage probability expressions. Most of the work related to AF multi-hop systems, therefore, ignore the optimization of the power allocation and relay locations; however, some research has focused on single-link diversity at the receiver end [131] and contributes simpler analytical expressions that can be used to optimize power allocation [110]. In general, however, AF relays are not used when the number of hops is large, as more noise is amplified with each additional link.

DF is more popular in multi-hop transmission, especially when the number of hops is large [106, 117]. The energy efficiency of multi-hop DF relay systems was analyzed for fixed-circuit power consumption and outage probability constraints in [118]. Liu et al. [107] discussed symbol-error rate (SER) performance and energy efficiency aspects of multi-hop relays without considering location or power allocation. A detailed investigation of multi-hop systems' energy consumption is shown in Waqar et al. [117], but only single-link diversity is assumed.

With the exception of a limited study in Liu et al. [107][1], and to the best of our knowledge, system parameters such as relay locations and power allocations have not been jointly optimized for multi-hop systems when full diversity is utilized. We address this issue by focusing on a two-relay system and using numerical analysis to find optimal energy configurations.

We use the circuit energy models presented in Chapter 5 to analyze and optimize the system energy consumption and compare with single-hop (direct transmission) and two-hop (single-relay) systems. We compare energy consumption by modifying such variables like target BER, spectral efficiency and the environment's pathloss exponent.

The rest of the chapter is organized as follows; Section 6.2 presents the four-node system model and description of our energy model. The locations and power allocations

---

[1] Liu et al. studied the best locations and power allocations assuming static circuit energy consumption to minimize SER by considering a few example scenarios.

are optimized in Section 6.3 to minimize energy consumption. Section 6.4 uses numerical simulations to analyze energy consumption for scenarios where either throughput or bandwidth are constrained. Finally, implications of our results and future work are discussed in Section 6.5.

6.2 System Model and Energy Model

Our system is comprised of two relays (R1 and R2) placed on a straight line between the source (S) and the destination (D) as shown in Figure 6.1. We define the distances between the node i and j as $d_{i,j}$. In order to locate the relative positions independent of the actual distances, we can also model all distances in comparison with $d_{S,D}$ as follows: First, we define $d_{S,D} = l$ as the distance between source and destination, along with the β_1 and β_2 as the normalized distances (by l) between source and relay 1 and source and relay 2. This allows us to express the distance between all nodes as follows:

$$d_{S,D} = l\ ,\ d_{S,R1} = \beta_1 l\ ,\ d_{S,R2} = \beta_2 l\ ,\ d_{R1,R2} = (\beta_2 - \beta_1) l\ ,$$

$$d_{R1,D} = (1-\beta_1) l\ , d_{R2,D} = (1-\beta_2) l\ ,$$

where $0 < \beta_1, \beta_2 < 1$.

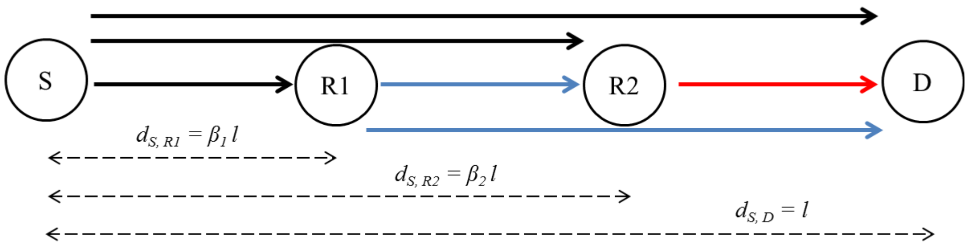

Figure 6.1: Block diagram of the cooperative two-relay multi-hop system.

We use the following system assumptions in our analysis:

- The system time-shares resources between relay links using three time instances for each transmission: first, between the source and the relays/destination; second, between the relay 1 and the relay 2/destination; and third, between the relay 2 and the destination. In each transmission time slot, a data rate of three times the average system throughput is required in order to achieve the same throughput as a direct transmission system.

- Selective relaying only occurs when a DF relay detects bits perfectly to simplify the forthcoming analysis.
- All transmission links are modelled as flat-fading channels with mutually independent coefficients that follow the Rayleigh distribution and remain constant for the duration of a symbol.
- Channel state information is available at each receiver and the environment is interference-free.
- We only consider square-QAM modulation, and we use exact BER expressions in our analysis. In this chapter, we define the spectral efficiency b as the number of bits per square-QAM symbol, while the standard definition of spectral efficiency is the ratio of equivalent bit rate to RF bandwidth - measured in bits/sec/Hz, forthcoming results are more easily viewed in terms of bits/symbol. As the standard spectral efficiency is proportional to b when the excess bandwidth of the Nyquist pulse shaping filter is fixed, it is easier to see spectral efficiency through b [45]. We consider four modulation schemes 4-QAM. 16-QAM, 64-QAM and 256-QAM which give 2, 4, 6 and 8 values for b.
- System transmit data rates are in the range of 0.5–5 Mbps.
- Perfect receiver synchronization is assumed at all relays and the destination.
- Relay 2 and the destination use maximal-ratio combining on the signals received from the relay(s) and source.

We denote R_{d} as the average required throughput of two-relay system. Therefore, in one time instance the system needs to transmit $3R_{\text{d}}$. Assuming a transmit Nyquist pulse with excess bandwidth ϵ, we define the transmission radio bandwidth used in this system as $3W$. The bandwidth and rate are related as

$$R_{\text{d}} = \frac{W}{2(1+\epsilon)} b \tag{6.1}$$

A block diagrams of our proposed transmitter in the source/relays is presented in Figure 6.2. The information is first modulated and sends through a pulse shaping filter prior to converting to an an analog signal using a digital-to-analog converter (DAC). This signal is then modulated onto a transmit carrier frequency and amplified using the power amplifier (PA) before transmission using a single antenna.

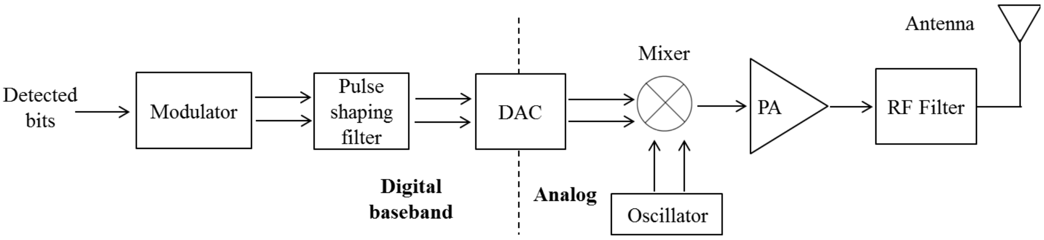

Figure 6.2: Block diagram of a DF relay transmitter end.

The received signal at the relays/destination undergoes the functions presented in Figure 6.3. The received signal is first filtered using a band-pass filter and then amplified using a low-noise amplifier (LNA). The filter output is then down-converted to baseband and re-amplified using a baseband amplifier prior to the sampling process. An analog-to-digital converter (ADC) is used to sample the analog signal and is followed by a timing recovery unit which maximizes the SNR of the received signal. The sampled signal is fed through frequency recovery and phase recovery units prior to detection in order to remove the constellation rotations due to carrier frequency and phase offsets.

Due to the complexity of the forthcoming analysis, we separate the energy modelling of the power amplifiers and the remainder of the analog and digital circuitry.

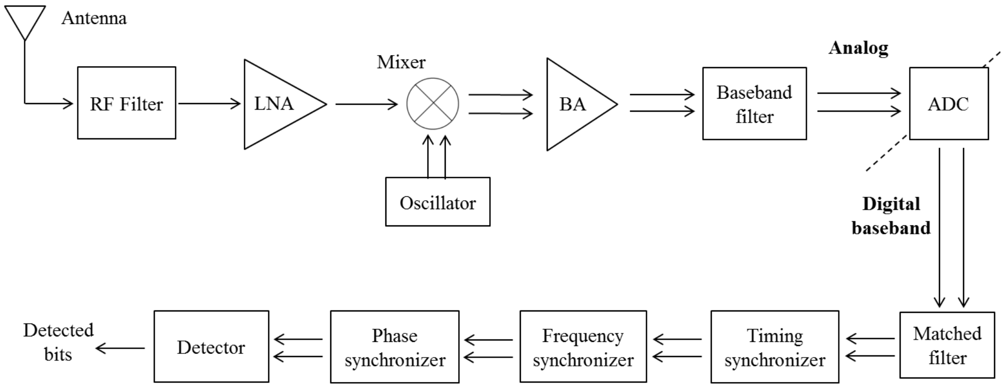

Figure 6.3: Block diagram of a DF relay receiver end.

6.2.1 Total Power Amplifier Energy Model

We first define the average received SNR per bit at node j from the transmitted signal by node i is written as

$$\Gamma_{\mathrm{i,j}} = \frac{E_{\mathrm{Rx}}}{N_0} = \frac{E_i L d_{i,j}^{-\gamma}}{N_0 \xi} , \tag{6.2}$$

where E_{Rx} is the average received energy per bit,[2] E_{i} is the transmitter power amplifier (PA) energy consumption per bit for node i, $d_{\mathrm{i,j}}$ is the distance between nodes i and j, γ is the pathloss exponent, and ξ is the peak-to-average power ratio defined as $\xi = 1.4\sqrt{\frac{3(2^{b/2}-1)}{2^{b/2}+1}}$ for QAM modulated sinusoidal carriers [34]. $L = L_0\eta$ is a propagation constant, where L_0 is a constant in the pathloss model [121] and η is the PA efficiency. N_0 represents the receiver noise spectral density multiplied into the receiver noise figure (RNF).

The average SER for a single link between transmitter node i and receiver node j with an average SNR per bit $\Gamma_{i,j}$ over Rayleigh distributed channel gains is given by [132] as

$$P_S = F\left(1 + \frac{A\Gamma_{i,j}}{\sin^2\theta}\right) , \tag{6.3}$$

---

[2] E_{Rx} can found using the transmitter output energy E_{Tx} as $E_{\mathrm{Rx}} = E_{\mathrm{Tx}} L l^{-\gamma}$ [121]. The transmit power amplifier energy consumption per bit E_{i} can be found as $E_{\mathrm{i}} = \xi E_{\mathrm{Tx}}$.

where $F(x(\theta))$ is defined as

$$F\left(x(\theta)\right) \;=\; \frac{4K}{\pi}\int_0^{\pi/2}\frac{1}{x(\theta)}d\theta \,-\, \frac{4K^2}{\pi}\int_0^{\pi/4}\frac{1}{x(\theta)}d\theta\ ,$$

and b is the spectral efficiency defined as the number of bits per transmitted QAM symbol, and the modulation dependent constants A and K are defined as

$$A = 1.5b/(2^b - 1) \text{ and } K = 1 - 2^{-b/2}\ , \tag{6.4}$$

respectively.

For n received signals using maximal-ratio combining, the average SER can be written as follows [107]:

$$P_S \;=\; F\left(\left(1+\frac{A\Gamma_{i_1,j_1}}{\sin^2\theta}\right)\cdot\left(1+\frac{A\Gamma_{i_2,j_2}}{\sin^2\theta}\right)\cdot\ldots\cdot\left(1+\frac{A\Gamma_{i_n,j_n}}{\sin^2\theta}\right)\right) \tag{6.5}$$

The final SER at the destination's detector can be derived using the conditional probability of error detection at the relays. There are four possible scenarios to consider:

1. Both relay 1 and relay 2 detect incorrectly. The average SNR at relay 1, relay 2 and destination result only from the signal coming from the source.

2. Relay 1 detects incorrectly, while relay 2 detects correctly. The average SNRs at relay 1 and relay 2 result only from the source, while the average SNR at the destination results from the signals coming from both the source and relay 2.

3. Relay 1 detects correctly, while relay 2 detects incorrectly. The average SNR at relay 1 results from the source signal, while the average SNRs at relay 2 and the destination result from the signals coming from both the source and relay 1.

4. Both relay 1 and relay 2 detect correctly. The average SNR at relay 1 results from the source signal, the average SNR at relay 2 results from both the source and relay 1 signals, and the average SNR at the destination is the result of the signals from the source and both the relays.

Using the above four cases, we mathematically represent the SER as follows:

$$\begin{aligned} P_S \;=\;& \mathrm{P}_{\mathrm{R1}}(\Gamma_{\mathrm{S,R1}})\,\mathrm{P}_{\mathrm{R2}}(\Gamma_{\mathrm{S,R2}})\,\mathrm{P}_{\mathrm{D}}(\Gamma_{\mathrm{S,D}}) \\ & + \mathrm{P}_{\mathrm{R1}}(\Gamma_{\mathrm{S,R1}})\,(1-\mathrm{P}_{\mathrm{R2}}(\Gamma_{\mathrm{S,R2}}))\,\mathrm{P}_{\mathrm{D}}(\Gamma_{\mathrm{S,D}}+\Gamma_{\mathrm{R2,D}}) \\ & + (1-\mathrm{P}_{\mathrm{R1}}(\Gamma_{\mathrm{S,R1}}))\,\mathrm{P}_{\mathrm{R2}}(\Gamma_{\mathrm{S,R2}}+\Gamma_{\mathrm{R1,R2}})\,\mathrm{P}_{\mathrm{D}}(\Gamma_{\mathrm{S,D}}+\Gamma_{\mathrm{R1,D}}) \\ & + (1-\mathrm{P}_{\mathrm{R1}}(\Gamma_{\mathrm{S,R1}}))\,(1-\mathrm{P}_{\mathrm{R2}}(\Gamma_{\mathrm{S,R2}}+\Gamma_{\mathrm{R1,R2}}))\,\mathrm{P}_{\mathrm{D}}(\Gamma_{\mathrm{S,D}}+\Gamma_{\mathrm{R1,D}}+\Gamma_{\mathrm{R2,D}})\,, \quad (6.6) \end{aligned}$$

where $\mathrm{P_j}(\Gamma_{\mathrm{i,j}})$ represents the symbol error probability at node j when the signal is received from node i.

We now consider a high-SNR approximation to simplify the SER expression so that we can utilize it in our system energy optimization[3]. We start with the following approximation that is valid at high SNRs:

$$1+\frac{A\Gamma_{i,j}}{\sin^2\theta} \approx \frac{A\Gamma_{i,j}}{\sin^2\theta}$$

This can be used to simplify (6.5) to

$$P_S \;=\; F\left(\frac{A^n\Gamma_{i_1,j_1}\Gamma_{i_2,j_2}...\Gamma_{i_n,j_n}}{\sin^{2n}\theta}\right) \qquad (6.7)$$

Using the high-SNR approximation $(1-\mathrm{P}_i(j)) \approx 1$ along with (6.2) and (6.7), we can simplify (6.6) to

$$\begin{aligned} P_S \;=\; & \frac{\mathrm{N}_0^3 d^{\gamma}_{\mathrm{S,R1}} d^{\gamma}_{\mathrm{S,R2}} d^{\gamma}_{\mathrm{S,D}} X_1^3}{L^3 B^3 E_{\mathrm{S}}^3} + \frac{\mathrm{N}_0^3 d^{\gamma}_{\mathrm{S,R1}} d^{\gamma}_{\mathrm{R2,D}} d^{\gamma}_{\mathrm{S,D}} X_1 X_2}{L^3 B^3 E_{\mathrm{S}}^2 E_{\mathrm{R2}}} + \frac{\mathrm{N}_0^4 d^{\gamma}_{\mathrm{S,R2}} d^{\gamma}_{\mathrm{R1,R2}} d^{\gamma}_{\mathrm{S,D}} d^{\gamma}_{\mathrm{R1,D}} X_2^2}{L^4 B^4 E_{\mathrm{S}}^2 E_{\mathrm{R1}}^2} \\ & + \frac{\mathrm{N}_0^3 d^{\gamma}_{\mathrm{S,D}} d^{\gamma}_{\mathrm{R1,D}} d^{\gamma}_{\mathrm{R2,D}} X_3}{L^3 B^3 E_{\mathrm{S}} E_{\mathrm{R1}} E_{\mathrm{R2}}}\,, \quad (6.8) \end{aligned}$$

where the modulation-dependent constants are defined as $X_{\mathrm{n}} = F(\sin^{-2n}\theta)$ for $n = \{1,2,3\}$, and the modulation dependent constant B is defined as A/ξ. We denote E to be the total PA energy consumption (per bit) from the source and two relays, and use α_1 and α_2 to represent the relative power allocation to the first and second relays, respectively.

---

[3] The approximation of high SNR holds for low BER values such as 10^{-4}, but may not valid for higher BER values as higher BER can be achieved in low SNR.

We can write the energy allocation for the source and two relays as

$$E_{\mathrm{S}} = (1-\alpha_1-\alpha_2)E \ \ , \quad E_{\mathrm{R1}} = \alpha_1 E \ \ , \quad E_{\mathrm{R2}} = \alpha_2 E \ , \tag{6.9}$$

where the parameters are constrained by $0 < \alpha_1, \alpha_2 < 1$ and $0 < \alpha_1 + \alpha_2 < 1$.

By substituting these radio energies and the link distances into (6.8), we obtain the following expression:

$$\begin{aligned} P_S \;=\; & \frac{\mathrm{N}_0^3 l^{3\gamma}}{L^3 B^3 E^3}\left\{ \frac{X_1^3 \beta_1^\gamma \beta_2^\gamma}{(1-\alpha_1-\alpha_2)^3} + \frac{X_1 X_2 \beta_1^\gamma (1-\beta_2)^\gamma}{(1-\alpha_1-\alpha_2)^2 \alpha_2} + \frac{\mathrm{N}_0\, l^\gamma X_2^2 \beta_2^\gamma (\beta_2-\beta_1)^\gamma (1-\beta_1)^\gamma}{LBE(1-\alpha_1-\alpha_2)^2 \alpha_1^2} \right. \\ & \left. + \frac{X_3 (1-\beta_1)^\gamma (1-\beta_2)^\gamma}{(1-\alpha_1-\alpha_2)\alpha_1\alpha_2} \right\} \end{aligned} \tag{6.10}$$

Assuming the BER is equal to SER divided by the number of bits per symbol[4] (i.e. $P_e = P_s/b$), and by interchanging the variables in (6.10), we obtain the following quartic equation of total PA energy E.

$$\begin{aligned} E^4 \;-\; & \frac{\mathrm{N}_0^3 l^{3\gamma}}{L^3 B^3 P_e b}\left\{ \frac{X_1^3 \beta_1^\gamma \beta_2^\gamma}{(1-\alpha_1-\alpha_2)^3} + \frac{X_1 X_2 \beta_1^\gamma (1-\beta_2)^\gamma}{(1-\alpha_1-\alpha_2)^2 \alpha_2} + \frac{X_3 (1-\beta_1)^\gamma (1-\beta_2)^\gamma}{(1-\alpha_1-\alpha_2)\alpha_1\alpha_2} \right\} E \\ & - \frac{\mathrm{N}_0^4 l^{4\gamma} X_2^2 \beta_2^\gamma (\beta_2-\beta_1)^\gamma (1-\beta_1)^\gamma}{L^4 B^4 P_e b (1-\alpha_1-\alpha_2)^2 \alpha_1^2} \;=\; 0 \end{aligned} \tag{6.11}$$

In analyzing this result, we observe that the first coefficient of the equation is positive, while the second and third coefficients are negative. By applying Descartes' rule of signs [133] on (6.11), we identify that only one positive real root exists for transmit energy E. This root can be found using basic quartic equation solving approaches as presented in PlanetMath online article [134].

The solution for the total PA transmit energy E is too complex to present analytically; therefore, we represent this energy in a general form as follows:

$$E \;=\; \frac{\mathrm{N}_0 l^\gamma}{LB} f(b, \gamma, P_e, \alpha_1, \alpha_2, \beta_1, \beta_2) \ , \tag{6.12}$$

---

[4] When Gray-coded symbol mapping is used at high-SNRs, it can be assumed that the bit errors occur only via an incorrect detection at a neighboring adjacent symbol.

where the function $f(b, \gamma, P_e, \alpha_1, \alpha_2, \beta_1, \beta_2)$ is defined using system variables b, γ, P_e, and relay parameters such as power allocation (α_1 and α_2) and relay locations (β_1 and β_2).

6.2.2 Circuit Energy Model

Focusing on the circuit energy consumption, we need to model the energy of all components and understand when they are operating. The receiver in the first relay operates only during the first time slot, while the receiver of the second relay operates in both the first and second time slots. The destination receives the signal from source and two relays over all three time slots. Transmission from the source, first relay and the second relay occur at the first, second and third time slots, respectively. The previous statement on relay transmission is only true when the selective-relaying conditions are satisfied. We assume this is always true to simplify the energy modelling, and note that due to our high SNR assumption, the probability of a relay not transmitting will be very low.

The circuit energy models of the remaining active components in a wireless transceiver were developed in the Chapter 4 and 5. A summary of these energy models is presented in Table 6.1[5]. We denote P_{X} and E_{X} to be component X's power and energy consumptions per information bit, respectively.

According to the system model presented in Figures 6.2 and 6.3 and the models in Chapter 5, we write the circuit energy consumption per information bit of nth relay by summing the energy from each component as follows:

$$\begin{aligned} E_{\text{c}}^{\text{Relay-n}} &= \frac{(2+2n)P_{\text{Mixer}} + (1+n)P_{\text{Oscil}} + nP_{\text{LNA}} + 2nP_{\text{BA}} + 2nP_{\text{ADC}} + 2P_{\text{DAC}}}{3R_{\text{d}}} \\ &\quad + n(E_{\text{TS}} + E_{\text{FS}} + E_{\text{PS}}) \qquad (6.13) \\ &= \frac{(2+2n)C_{\text{Mixer}} + (1+n)C_{\text{Oscil}} + nC_{\text{LNA}} + 3W(2nC_{\text{BA}} + 2nC_{\text{ADC}} + 2C_{\text{DAC}})}{3R_{\text{d}}}, \\ &\quad + \frac{n(C_{\text{TS}} + C_{\text{FS}} + C_{\text{PS}})}{b} \qquad (6.14) \end{aligned}$$

---

[5] The digital pulse-shaping and receiver matched filters are neglected in our energy model. Both filters have less computations than other digital blocks, especially when exploiting the symmetry of the raised-root cosine filters.

Table 6.1: Power and energy models for wireless transceivers (from Section 5.3).

Component	**Power / energy model**	**Parameter values**
Mixer	$P_{\text{Mixer}} = C_{\text{Mixer}}$	$C_{\text{Mixer}} = 1.25\ \text{mW}$
Oscillator	$P_{\text{Oscil}} = C_{\text{Oscil}}$	$C_{\text{Oscil}} = 1.25\ \text{mW}$
Low Noise Amplifier	$P_{\text{LNA}} = C_{\text{LNA}}$	$C_{\text{LNA}} = 1.25\ \text{mW}$
Digital-to-Analog Converter	$P_{\text{DAC}} = C_{\text{DAC}}W$ [6]	$C_{\text{DAC}} = 0.25\ \text{mW/MHz}$
Analog-to-Digital Converter	$P_{\text{ADC}} = C_{\text{ADC}}W$ [6]	$C_{\text{ADC}} = 0.23\ \text{mW/MHz}$
Baseband Amplifier	$P_{\text{BA}} = C_{\text{BA}}W$	$C_{\text{BA}} = 0.125\ \text{mW/MHz}$
Timing Synchronizer	$E_{\text{TS}} = \frac{C_{\text{TS}}}{b}$	$C_{\text{TS}} = 0.235\ \text{nJ}$
Frequency Synchronizer	$E_{\text{FS}} = \frac{C_{\text{FS}}}{b}$	$C_{\text{FS}} = 0.053\ \text{nJ}$
Phase Synchronizer	$E_{\text{PS}} = \frac{C_{\text{PS}}}{b}$	$C_{\text{PS}} = 0.099\ \text{nJ}$

where the integer in front of P_{X} and E_{X} terms represents the number of such components in the relay.

The source performs functions only as a transmitter with circuit energy as derived in Eq. (5.12) in Chapter 5

$$E_{\text{c,S}}^{MR} = \frac{2C_{\text{Mixer}} + C_{\text{Oscil}} + 3W \times 2C_{\text{DAC}}}{3R_{\text{d}}} \tag{6.15}$$

The destination performs the function of a receiver, but consumes three time the energy of a single receiver as it needs to process the received signals at three instances; the source and two relays. Its energy consumption is written by adding the energy costs of

---

[6] We assumed fixed DAC and ADC resolutions of 5 and 7 bits, respectively. These values are irrespective of the modulation scheme in order to make E_{DAC} and E_{ADC} simpler linear models.

the individual components as

$$E_{\mathrm{c,D}}^{MR} = \frac{6C_{\mathrm{Mixer}} + 3C_{\mathrm{Oscil}} + 3C_{\mathrm{LNA}} + 3W(6C_{\mathrm{BA}} + 6C_{\mathrm{ADC}})}{3R_{\mathrm{d}}} + \frac{3C_{\mathrm{TS}} + 3C_{\mathrm{FS}} + 3C_{\mathrm{PS}}}{b} \tag{6.16}$$

The total circuit energy consumption of the complete system can then be written by adding the components from the source (6.15), destination (6.16) and two relays (adding (6.13) for both n =1 and 2) as follows

$$\begin{aligned} E_{\mathrm{c}}^{\mathrm{MR}} &= \frac{18C_{\mathrm{Mixer}} + 9C_{\mathrm{Oscil}} + 6C_{\mathrm{LNA}} + 3W(12C_{\mathrm{BA}} + 12C_{\mathrm{ADC}} + 6C_{\mathrm{DAC}})}{3R_{\mathrm{d}}} \\ &+ \frac{6(C_{\mathrm{TS}} + C_{\mathrm{FS}} + C_{\mathrm{PS}})}{b} \end{aligned} \tag{6.17}$$

We can simplify the above equation by grouping terms, the resulting circuit energy per bit model is

$$E_{\mathrm{c}}^{\mathrm{MR}} = \frac{C_1^{\mathrm{MR}}}{R_{\mathrm{d}}} + \frac{C_2^{\mathrm{MR}}}{b} , \tag{6.18}$$

where the constants C_1^{MR} and C_2^{MR} are defined as,

$$C_1^{\mathrm{MR}} = \left(6C_{\mathrm{Mixer}} + 3C_{\mathrm{Oscil}} + 2C_{\mathrm{LNA}}\right) \times 10^6 \tag{6.19}$$

and

$$C_2^{\mathrm{MR}} = 2\,(1+\alpha)\left(12C_{\mathrm{BA}} + 12C_{\mathrm{ADC}} + 6C_{\mathrm{DAC}}\right) \times 10^6 + \left(6C_{\mathrm{TS}} + 6C_{\mathrm{FS}} + 6C_{\mathrm{PS}}\right) \times 10^{-3} \tag{6.20}$$

The constants C_1^{MR} and C_2^{MR} are calculated as 13.75×10^6 and 7.21 using the numerical constants from Table 6.1 into this equation, and assuming $\epsilon = 0.25$.

The total energy consumption of the dual-relay system can now be written using (6.12) and (6.18) as follows:

$$E_{\mathrm{total}}^{\mathrm{MR}} = \frac{\mathrm{N}_0 l^{\gamma}}{LB} f(b, \gamma, P_e, \alpha_1, \alpha_2, \beta_1, \beta_2) + \frac{C_1^{\mathrm{MR}}}{R_{\mathrm{d}}} + \frac{C_2^{\mathrm{MR}}}{b} \tag{6.21}$$

6.3 Relay location and power allocation optimization for dual-relay systems

In this section, we investigate the optimal power allocation and relay locations to minimize the required transmit energy. We present numerical results to benchmark our proposed approach against conventional equal-power and equidistant-location approaches.

We use a numerical search to optimize the power allocation and relay locations because the function $f(b, \gamma, P_e, \alpha_1, \alpha_2, \beta_1, \beta_2)$ in (6.12) is too complex to minimize analytically. We therefore simulate over all the possible values of α_1, α_2, β_1 and β_2 and obtain the optimal values for a range of pathloss exponents, BER and spectral efficiency. Our simulations considered the power allocation and relative location to a resolution of 1% (i.e. 0.01 relative to 1).

Figure 6.4 presents the optimal location and power allocation parameters as a function of pathloss exponent for 4-QAM modulation and a target BER of 10^{-4}. It can be observed that the source requires the most power (i.e. α_0 in the range of 0.69 – 0.89) while the second relay requires a small power (i.e. α_2 between 0.01 to 0.11) for the given pathloss region of interest. As the pathloss coefficient increases, power allocation to the relays increases, while the source power allocation decreases. This is due to the fact that the the received SNR difference between the relays and destination increases when the pathloss increases. In other words, the relays are able to detect data more accurately than the destination, and therefore, the relaying signals are more relied upon in high attenuating environments. Hence more power is allocated to the relays with increasing pathloss.

In terms of the optimal relay locations, the first relay is situated near the middle with a relative distance β_1 in the range of 0.41–0.72, while the second relay is located quite close to the destination (i.e. β_2 in the range of 0.76–0.99). Note that an equidistant location strategy is not optimal, and as the pathloss coefficient increases, both relays are shifted towards the source for optimal energy efficiency. This is due to the same issue discussed above, where the relays are able to detect data more accurately than the destination when the pathloss exponent is increased. In addition, as more power is allocated to the relays, less power is allocated to the source and therefore, the relays need to be moved closer to

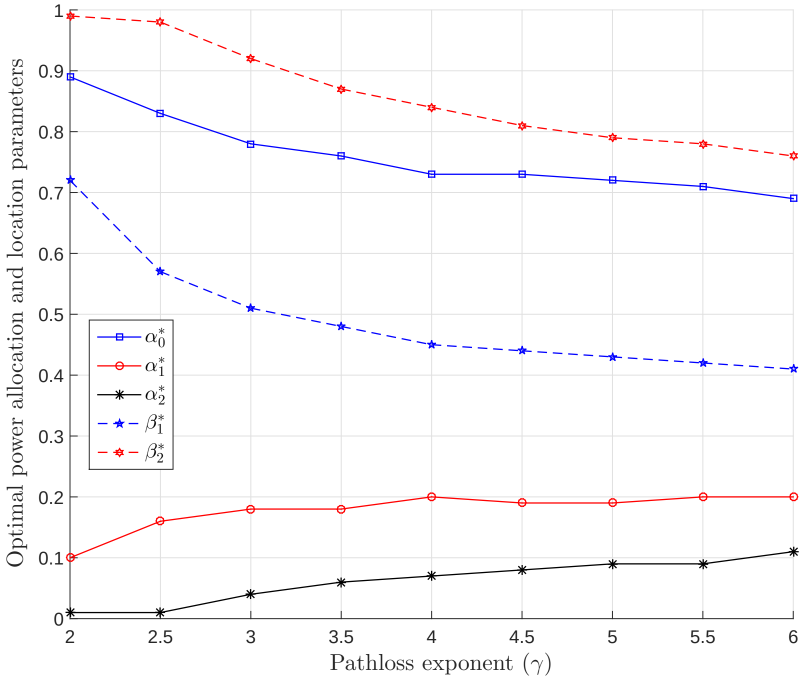

Figure 6.4: Optimal power allocation and location parameters versus pathloss exponent ($P_e = 10^{-4}$ and 4-QAM modulation).

source to acquire a signal with a better SNR.

Figure 6.5 shows the value of the jointly-optimized function $f(b, \gamma, P_e, \alpha_1^*, \alpha_2^*, \beta_1^*, \beta_2^*)$ compared with the function's values for equal-power allocation ($\alpha_0 = \alpha_1 = \alpha_2 = 1/3$) and equidistant-located relays ($\beta_1 = 1/3$, $\beta_2 = 2/3$). It can be clearly seen that the joint optimization always reduces the transmit energy consumption by a factor of 3 or more compared to the equal-power equidistant-relay case.

Figure 6.6 shows the behavior of the optimal system parameters as a function of QAM modulation order for a pathloss exponent of 3.5 and a 10^{-4} target BER. The optimal power allocation to the source reduces slightly from 0.76 to 0.71 as the spectral efficiency increases from 2 to 8 bits/symbol. On the other hand, the power allocations of the second relay rises slightly with spectral efficiency while the power allocation of the first relays fluctuates within a limited region. The optimal location of the first relay is closer to the source, but the second relay is always very close to the destination. As the spectral efficiency increases the relays' optimal locations are slightly shifted towards the source.

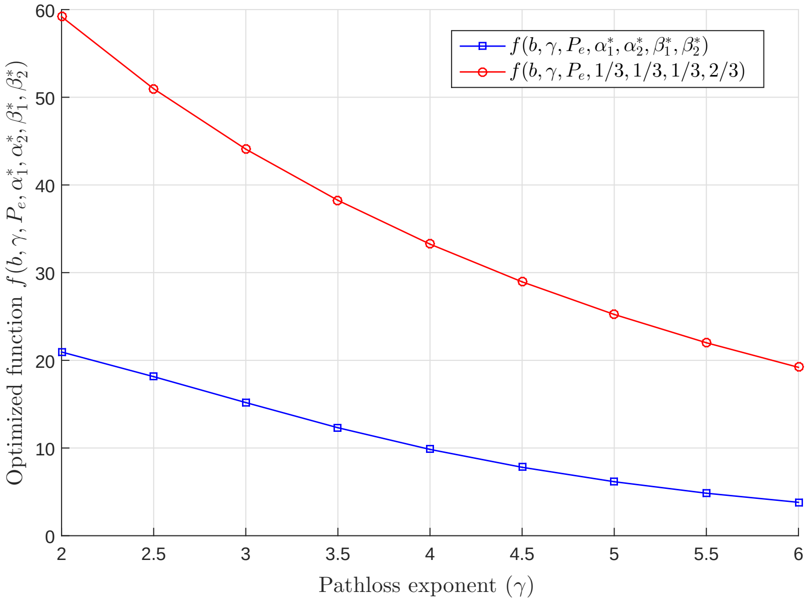

Figure 6.5: The function $f(b,\gamma,P_e,\alpha_1,\alpha_2,\beta_1,\beta_2)$ versus pathloss exponent ($P_e = 10^{-4}$ and 4-QAM modulation).

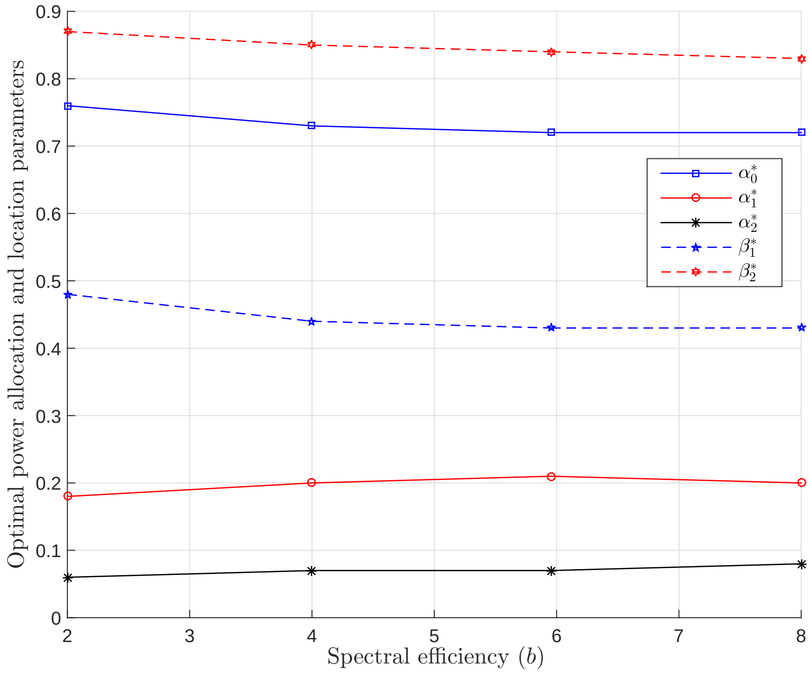

Figure 6.6: Optimal power allocation and location parameters versus spectral efficiency ($P_e = 10^{-4}$ and $\gamma = 3.5$).

The most interesting observation is that all power allocations and location parameters lie within a narrow range for all spectral efficiencies. For high spectral efficiencies such as 256, the last term in (6.11) with a factor of B^{-4} becomes more dominant over the second term (coefficient of E) with a factor of B^{-3} (B is inversely proportional with b). This influences the optimality of relay locations and power allocations.

Figure 6.7 shows the optimal location and power allocation parameters as a function of target BER, where 4-QAM modulation is used along with a pathloss exponent of 3.5. Due to the high SNR approximations used in the preceding analysis, our expressions are only valid for small BER values. As such, we considered a BER range of 10^{-8} to 10^{-3} in our simulations. Results show that as BER increases, the source's and second-relay's power allocation increases, while the first relay power allocation decreases. In terms of location, the first relay moves toward the destination with increasing BER, while the second relay moves toward the source. Clearly, BER has a significant impact on the optimal parameter allocation.

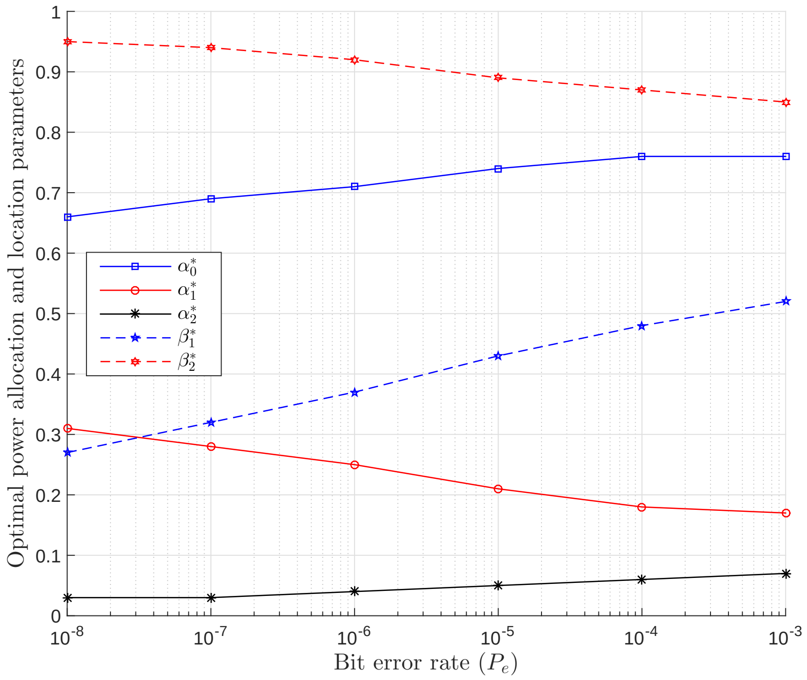

Figure 6.7: Optimal power allocation and location parameters versus target BER (4-QAM and γ = 3.5).

6.4 Energy minimization of fixed–throughput and fixed–bandwidth 2-relay systems

We now investigate the total energy consumption of the system from two perspectives. First, the system has a fixed-throughput, and bandwidth can be varied according to the selected modulation scheme. In the second approach, we fix bandwidth and allow throughput to change. From a practical perspective, adapting the data rate instead of the bandwidth is a more feasible approach, as bandwidth may be a scarce resource.

Note that the transmit energy consumption per bit (6.12) is independent of total throughput for a fixed modulation[7]. Therefore, transmit energy in (6.12) depends on the spectral efficiency (via b), and the circuit energy consumption in (6.18) depends on both the spectral efficiency (via b) and throughput.

In the fixed–throughput approach, the first term in the circuit energy model in (6.18) remains the same for a given modulation scheme, while in the fixed–bandwidth approach, the same term changes according to the throughput. However, in the second scenario, the terms in (6.18) change as bandwidth is fixed and the data rate is changed according to the spectral efficiency. We have assumed receiver noise spectral density of -174 dBm/Hz and receiver noise figure of 9 dB [104], path-loss propagation constant $L_0 = 10^{-3}$ [121], and $\eta = 0.5$.

6.4.1 Fixed-Throughput Case

We set a target data rate of 1 Mbps, pathloss exponent $\gamma = 3.5$, a target average BER of 10^{-4}, and evaluate energy and required bandwidth as a function of distance l. Optimal relay locations and power allocations are obtained via a numerical search to optimize (6.12) for all $b \in \{2, 4, 6, 8\}$, followed by finding the optimal b^* and associated $(\alpha_1^*, \alpha_2^*, \beta_1^*, \beta_2^*)$ that minimizes the energy consumption per bit for a given distance l. The minimal energy consumption of single relay system (5.30) and direct transmission system (5.58) are also obtained as in Chapter 5. Figure 6.8 illustrates the minimal total energy consumption of three systems as a function of distance.

---

[7] We consider energy per bit, which is obtained by total power consumption divided by the throughput.

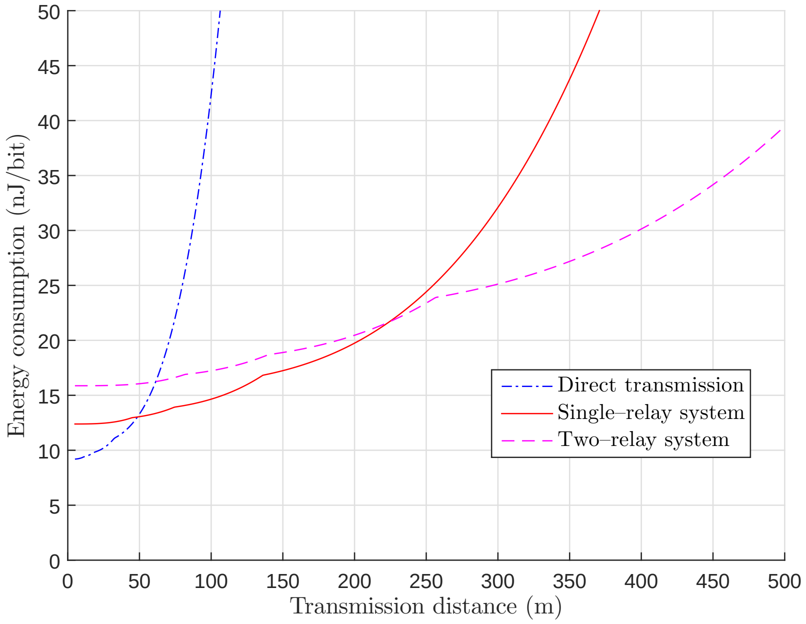

Figure 6.8: Optimized total energy consumption vs distance ($P_e = 10^{-4}$, $R_\mathrm{d} = 1$ Mbps and $\gamma = 3.5$).

These results are essentially an extension of those in Figure 5.15 in Chapter 5 for a two-relay system. At short distances, direct transmission is the most efficient system, but its energy quickly increases beyond 50 m due to the PA needing to overcome the distance-dependent pathloss. The single-relay system then becomes the more efficient system at this distance, and remains so until the exponentially-increasing pathloss requires more radiated energy from its PAs. The exponential increase of the single-relay system is not as fast as direct transmission due to diversity combining enabling lower PA energy consumption. As a result, the system switch point at 225 m from single- to dual-relaying is far more than the 50 m switch point from direct to single-relay transmission.

The optimal spectral efficiency for the three systems is plotted as a function of distance in Figure 6.9. The basic pattern of adopting higher-order modulation schemes at low distances and lower-order modulation schemes at longer distances is reflected in this graph. It is important to note that the two-relay system utilizes higher-order modulation at longer distances than the other systems. The main reason for this behavior is that the second term in (6.18) reduces with high spectral efficiency and the circuit energy is more

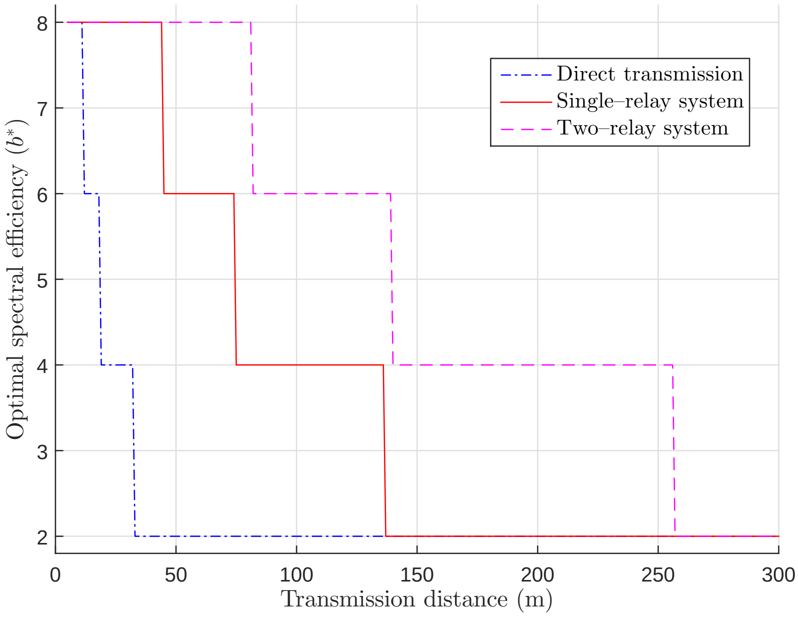

Figure 6.9: Optimal spectral efficiency vs distance (P_e = 10^{-4}, R_d = 1 Mbps and $\gamma = 3.5$).

dominant in multi-relay systems at short distances.

Figure 6.10 shows the minimal-energy bandwidth required for the 1 Mbps throughput as a function of distance. Up until 50 m, direct transmission's b^* decreases from 8 to 6 to 4 to 2 bits/symbol, and the corresponding bandwidth increases at each transition. Single-relay systems require twice the bandwidth of direct transmission due to using two time slots, but the bandwidth decreases from 1.25 MHz to 0.833 MHz at 50 m when single relaying becomes optimal. The reason here is that b^* increases to 6 bits/symbol at this switch point, and later decreases to 4 and 2 bits/symbol at approximately 75 m and 135m, respectively. The same pattern can be observed at the switching point of single- to dual-relay transmission at about 200 m where b^* increases to 4 bits/symbol and results in a lower bandwidth compared to the single-relay case. Further away, b^* decreases to 2 bits/symbol at approximately 260 m and 100% more bandwidth is needed to support the same throughput using a dual-relay system. These results typify the standard pattern of adopting higher-order modulation at shorter distances and lower-order modulation at distance increases.

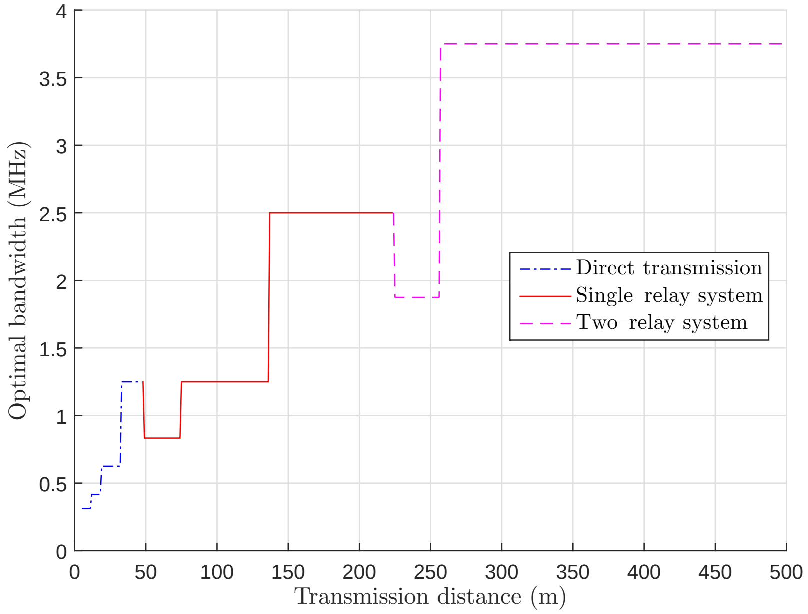

Figure 6.10: Optimal bandwidth vs distance ($P_e = 10^{-4}$, $R_\mathrm{d} = 1$ Mbps and $\gamma = 3.5$).

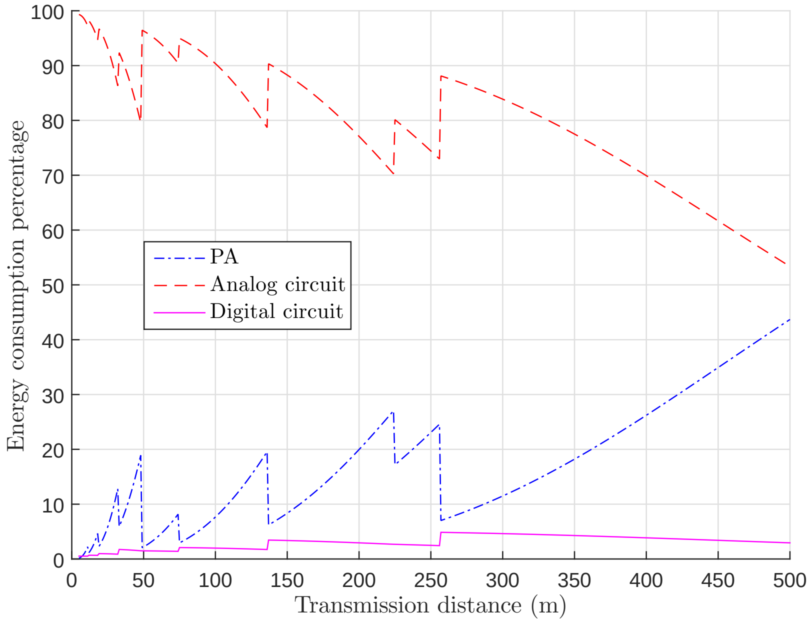

Figure 6.11: Optimal minimal-energy bandwidth vs distance ($P_e = 10^{-4}$, $R_\mathrm{d} = 1$ Mbps and $\gamma = 3.5$).

Figure 6.11 shows the energy percentage breakdown of the PA, other analog circuitry, and digital components for the minimal-energy configuration as a function of distance.

We can see that the relay switch points at 50 m and 225 m occur when the PA power begins to increase more rapidly. While adding a relay at these distances reduces the total PA power, it causes an increase to the remaining analog and digital circuit energies. The other peaks in PA energy curve occur when modulation is lowered within the same transmission system at the expense of analog and digital circuit energy.

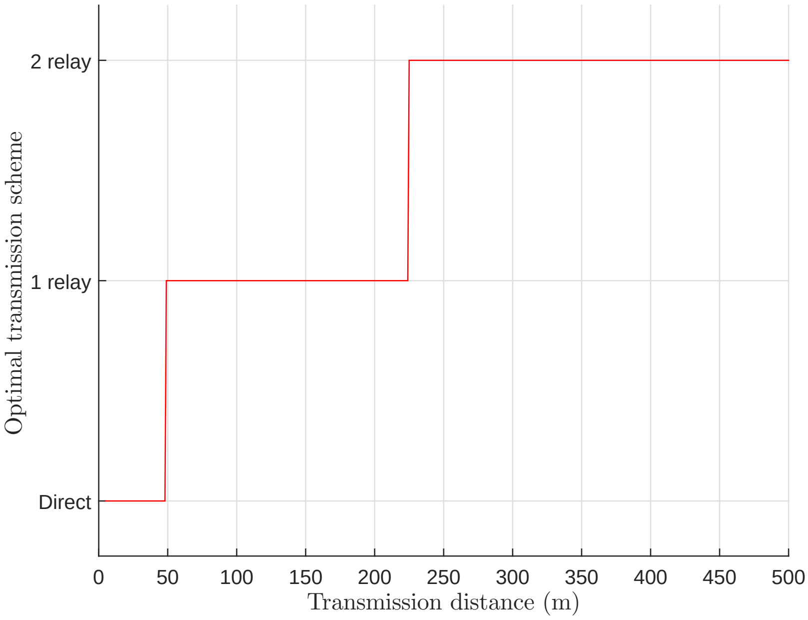

Figure 6.12: Optimal transmission scheme vs distance (P_e = 10^{-4}, R_d = 1 Mbps and γ = 3.5).

Figure 6.12 summarizes the results of the optimal transmission scheme versus distance for an average throughput of 1 Mbps and BER of 10^{-4}. This result clearly demonstrates the use of distributing energy to intermediate nodes and using diversity in order to reduce the transmit energy at the expense of additional circuit processing energy.

6.4.2 Fixed–Bandwidth case

Figure 6.13 shows total energy consumption as a function of distance for three systems with a fixed 2.5 MHz bandwidth and a variable throughput R_d. The second terms in (6.18)–(5.30) now increase as R_d decreases, allowing b to decrease more slowly with dis-

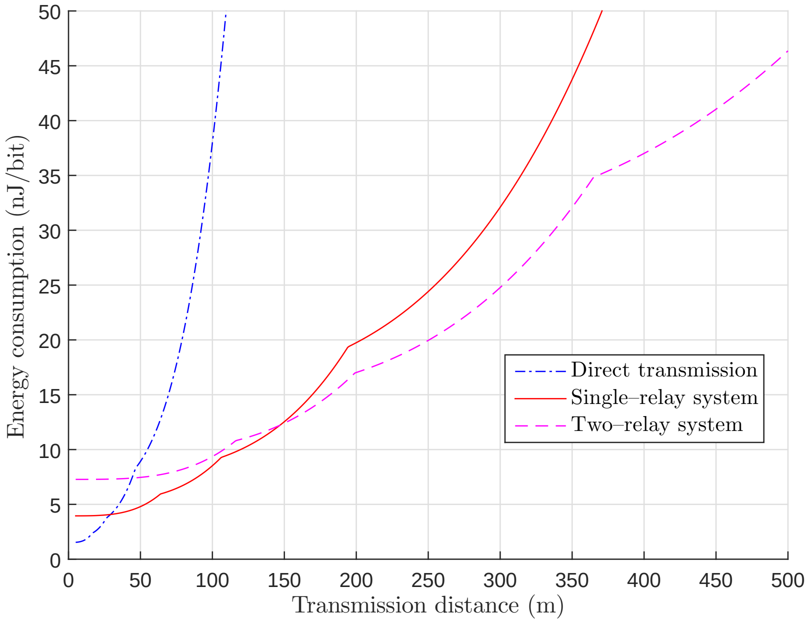

Figure 6.13: Optimized total energy consumption vs distance ($P_e = 10^{-4}$, $W = 2.5$ MHz and $\gamma = 3.5$).

tance than the fixed-throughput case. At short distances, direct transmission is most efficient system as expected. This is similar to Figure 6.8, but the energy consumption of the single-relay and dual-relay systems are slightly closer to each other over a short range of distance (100 m to 160 m). Dual relaying is most efficient from 150 m as its transmit energy is reduced by having 3 hops.

The minimal-energy throughput versus distance is illustrated in Figure 6.14 for the three transmission strategies. As expected, higher throughputs are more efficient at short distances due to lower pathloss allowing for higher receiver SNRs and spectral efficiency. At longer distances, however, a stronger pathloss results in lower received SNRs being more energy efficient, resulting in a decreased spectral efficiency and lower throughput for a fixed bandwidth. This reasoning and a similar result is also seen in Figure 6.9, where the optimal spectral efficiency is plotted as a function of distance for the throughput-constrained scenario.

Figure 6.15 shows the optimal transmission strategy versus distance for the same bandwidth-constrained system as above and summarizes the results of this Section. It can

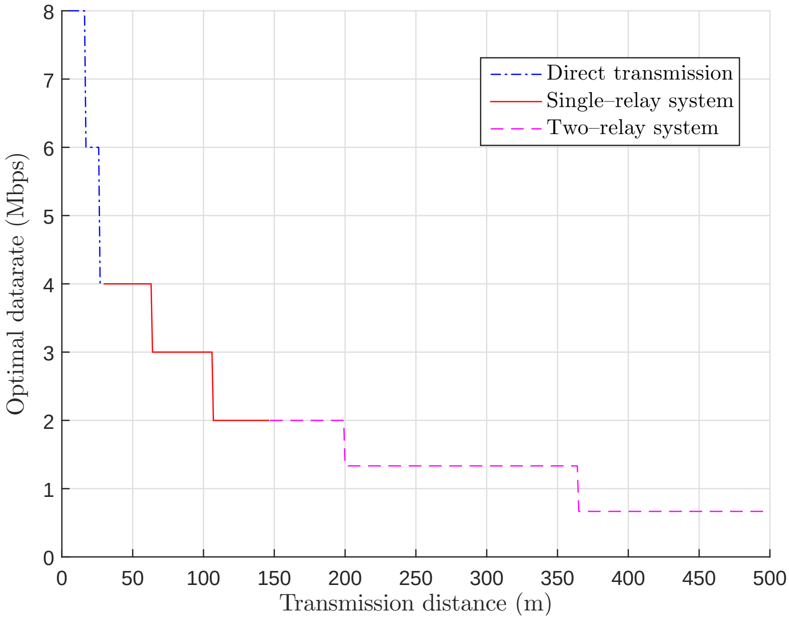

Figure 6.14: Optimal data rate vs distance ($P_e = 10^{-4}$, $W = 2.5$ MHz and $\gamma = 3.5$).

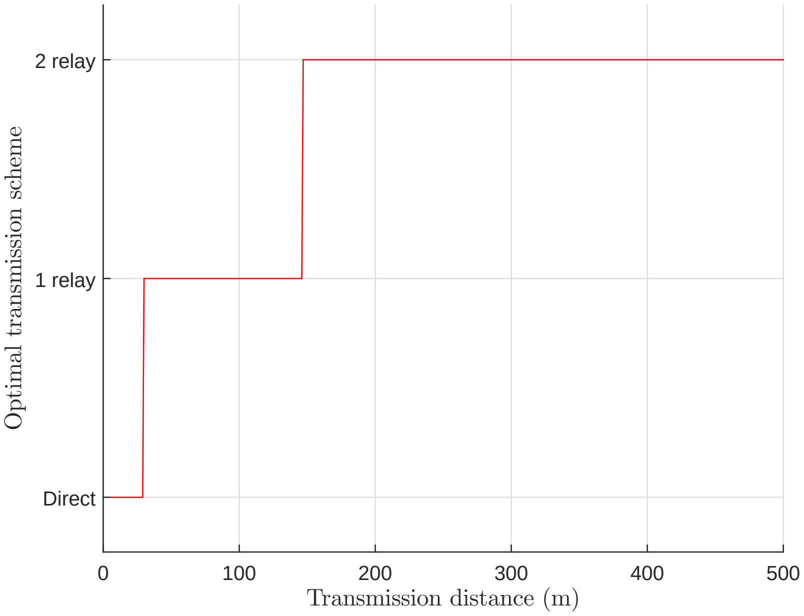

Figure 6.15: Optimal transmission scheme vs distance ($P_e = 10^{-4}$, $W = 2.5$ MHz and $\gamma = 3.5$).

be concluded that relayed transmission provides an energy efficient solution for long distance communication when a target throughput is not a primary concern. The transmit-circuit energy trade-off of single-relay and two-relay systems is also noticeable as their energy consumptions are different when compared with the throughput-constrained results in Figure 6.12.

6.5 Conclusions

In this chapter, we developed an energy model for dual-relay DF transmission system and evaluated its energy consumption in comparison to direct and single-relay DF transmission. Due to the high-complexity relationship between total transmit energy and the relay locations and their power allocations, it required numerical evaluation to optimize the dual-relay parameters. As expected, the use of additional relays helps reduce the total system energy consumption as distance increases in order to overcome the exponential pathloss.

Results indicate that when full diversity is utilized at the relays and destination, more power should be allocated to the initial nodes as that signal will be utilized by the relay node(s) that follows. When moving from the source towards the destination, the distances between the neighboring nodes gets reduced, e.g., the distance between the source and first relay is the longest and the distance between the second relay and destination is the shortest. Both equal power allocation amongst the transmitters and equidistant spacing of the relays is clearly suboptimal from an energy-efficiency perspective.

Going beyond our work, finding the transmit energy of a three-relay system is much more complex than a two-relay system as it results in a sextic equation[8] (The quadratic equation (6.11) becomes a sextic equation). Due to this complexity, we have not investigated this system or beyond three relays. However, our conclusions regarding the power allocation and relay positioning likely remain valid for multi-hop systems with larger number of relays and full diversity.

Our results on fixed-throughput and fixed-bandwidth systems reveal the importance of using multiple hops to reduce the energy consumption. Previously, relays were mostly used to achieve diversity and increase performance by reducing the BER [105, 106, 130,

---

[8] A sextic equation is a polynomial equation of degree six.

131].

The proposed framework could be applied to future IoT networks where energy might be the most significant concern and high, but bursty throughputs may be required. Optimizing the relay-network configuration can help maximize battery and/or energy harvesting lifetimes.

Chapter 7

Conclusions and Future Work

THIS chapter summarizes the key contributions of this thesis and discusses some future directions for research in the area of energy modeling and optimization of wireless systems.

7.1 Conclusions

This thesis investigates the energy consumption of wireless systems and presents total energy minimization solutions for point-to-point transmission and relay transmission systems. Our motivation was to analyze the energy consumption of the wireless physical layer as a function of practical parameters such as receiver SNR, modulation scheme, data rate, code rate, RF bandwidth, distance and pathloss exponent.

In modeling the wireless system energy consumption as a function of SNR, we first observed the synchronization capability at low SNR operation. We investigated synchronization system architectures and evaluated the performance of various estimation algorithms as a function of SNR. The most appropriate architectures and algorithms were selected to operate at in the low-SNR region.

We identified the need of preamble to acquire the initial synchronization parameters such as timing offset, carrier frequency offset and phase offset, and this was especially true for the low-SNR region. We recommend the use of non-data aided algorithms and decision-directed algorithms during data transmission to track the synchronization parameters. We recommend that timing synchronization should be performed first, as timing errors can be recovered prior to carrier recovery. We selected the absolute value nonlinearity (AVN) based feed-forward timing estimator [59] or the Gardner TED [57] for the timing recovery system. We then propose that frequency recovery should be performed using the feed-forward Mengali & Morelli estimator [64] during preamble transmission. This estimate can be used to correct the frequency errors during the data transmission with the aid of the phase recovery system. We recommend a feedback loop with decision-directed ML carrier recovery loop [51] to be used. Otherwise, for 4-QAM systems, we also recommend the feed-forward Viterbi and Viterbi estimator [7].

Next, we analyzed the computational complexity of synchronization systems and developed energy models. These energy models were then used to compare the energy efficiency of different estimation algorithms to achieve a given MSE performance. By using this new metric, we evaluated the synchronization algorithms from an actual energy efficiency perspective. Although, the real energy consumption values can only be measured by implementing the circuits on simulators or actual hardware, we considered the required number of arithmetic operations and memory accesses that provide an accurate estimate compared with just arithmetic calculation based developments.

We then used the synchronization system energy models along with other digital signal processing (DSP) segment energy models and a transmit energy model to investigate the energy consumption of a point-to-point wireless transmission system. We considered a multipath environment with Rayleigh-faded channel coefficients. An approximative analytical expression –a summation of two exponential functions of SNR – was applied to find an optimal solution to minimize the total energy consumption. The results reveal that an optimum SNR and an optimum bandwidth can be found from an energy-efficiency perspective for a given user requirement.

We then focused on relay transmission by using the energy models of point-to-point communication. We initially developed an optimization problem for amplify-and-forward (AF) and detect-and-forward (DF) cooperative single-relay systems. Our optimization problem was formulated on the basis of the source and relay power allocations, relay location and spectral efficiency. We showed that both AF and DF systems have an optimal location and optimal power allocation that minimizes the total energy consumption. In AF systems, the location and power allocation can be optimized independently from the spectral efficiency, but the same parameters in the DF system depend on spectral efficiency. Total energy consumption was then minimized from a spectral-efficiency perspective for both AF and DF systems when considering transmit energy and circuit processing energy. Using mathematical approximations, we were able to optimize energy consumption over spectral efficiency. On the basis of our analysis and numerical results, direct transmission is more energy efficient at shorter distances, but single-relay systems save energy in relatively longer distance transmission. However, even the single relay system's energy consumption increases after certain longer distances (e.g., beyond 200 m in our simulation example). We, therefore, next focused on multi-relay transmission to reduce the energy consumption at longer distances.

The energy efficiency of cooperative multi-relay systems was then evaluated by considering DF protocol with full diversity at the relays and destination. An energy model for a two-relay transmission system was developed. Due to the highly complex relationship between total transmit energy and the relay locations and their power allocations, numerical simulations were used to optimize these parameters. We then compared the total energy consumption of single-hop, two-hop and three-hop systems using numerical evaluation for two cases: throughput-constrained and bandwidth-constrained transmission. Our observations reveal that the total energy consumption of long distance transmission can be reduced by adding more relays with energy distributed amongst the additional nodes and using diversity to combat channel fading. The simulation outcomes also suggest that when full diversity is utilized at the relays and destination, more power should be allocated to the initial nodes as that signal will be utilized by the relay node(s) that follows. In terms of the relay locations, the initial relays should be positioned closer to the source, but the final relays should be located closer to the destination. The distances between the nodes are reduced towards the destination end.

7.2 Future Work

Before concluding this thesis, we briefly present some ideas that will motivate future studies on this topic.

7.2.1 Modeling the Energy Consumption of an IoT Gateway

In future IoT networks, wireless access will be used to connect millions of low powered devices [135–137]. An IoT gateway is proposed to connect a number of wireless sensors into the IoT network [137, 138]. These sensor devices can be use to provide a wide range of applications such as video surveillance, environmental condition monitoring, e-health, home automation, etc. Each application will have its own requirements in terms of quality-of-service and resources. For example, a video sensing camera requires a higher transmission rate with a low latency, but a temperature and humid sensor requires only a limited transmission rate and can afford a higher latency. Therefore, when connecting these different devices, the IoT gateway needs to optimize the physical layer resource allocations. Hence, physical layer energy models need to be developed as a function of bandwidth, spectral efficiency, operating SNR and other parameters in order to optimize the energy efficiency. The point-to-point communication energy we presented in Chapter 4 can be used to derive energy models for Internet-of-Things (IoT) gateways. Additional constraints such as multi-user data rates and bit-error rates, will need to be considered when allocating optimal bandwidths and modulation schemes.

7.2.2 Cellular Network Energy Efficiency Improvement by traffic offloading using relay transmission

The power consumption of cellular networks has been increasing due to the rapid growth of connected devices as well as ever–rising traffic demands. Larger network densification and higher spectral efficiencies have been adapted to satisfy these requirements. Such approaches have consequently resulted in increasing the power consumption of mobile networks, especially in base stations. Several methodologies are presented to reduce the power consumption of base stations [28, 30, 139]. The power consumption of various types of base stations are modeled up to different levels in the literature [80, 122, 140].

The use of relays to offload some demand on base stations has gained an attention [28, 141]. This approach effectively reduces cell sizes and the transmission distances between the base station and user equipment. The energy models we presented in Chapter 5 and 6 can be merged with base station power models (e.g. [140]) to formulate an energy minimization problem for the network with a base station and relays. Furthermore, in services such as broadcasting, selected users can be assigned as relays to forward data onto other users [142]. The energy consumption of such systems can be investigated using our models and optimal solutions can be derived.

7.2.3 Investigating the Trade-offs in Energy Harvesting Networks

Future wireless networks are set to use energy harvesting technologies to generate to required energy within wireless nodes. Unlike typical wireless devices which are operated using batteries, energy harvesting devices have strict limitations on the energy related parameters (i.e. maximum available energy and the time duration of energy availability) [143]. Therefore, it is essential to have more accurate energy models for transmitter and receiver segments as a function of system parameters (i.e. bandwidth, transmit power/received SNR, spectral efficiency). Our CMOS based energy models of single–hop and multi–hop systems can be used with different system architectures proposed by Lu et al. [144] in order to obtain practical energy optimization solutions for energy harvesting networks.

Bibliography

[1] M. Oerder and H. Meyr, “Digital filter and square timing recovery,” *IEEE Transactions on Communications*, vol. 36, no. 5, pp. 605–612, 1988.

[2] W.-P. Zhu, Y. Yan, M. O. Ahmad, and M. Swamy, “Feedforward symbol timing recovery technique using two samples per symbol,” *IEEE Transactions on Circuits and Systems I: Regular Papers*, vol. 52, no. 11, pp. 2490–2500, 2005.

[3] S. Kay, “A fast and accurate single frequency estimator,” *IEEE Transactions on Acoustics, Speech and Signal Processing*, vol. 37, no. 12, pp. 1987–1990, 1989.

[4] M. Luise and R. Reggiannini, “Carrier frequency recovery in all–digital modems for burst–mode transmissions,” *IEEE Transactions on Communications*, vol. 43, no. 234, pp. 1169–1178, 1995.

[5] M. Morelli and U. Mengali, “Feedforward frequency estimation for PSK: a tutorial review,” *European Transactions on Telecommunications*, vol. 9, no. 2, pp. 103–116, 1998.

[6] M. Fitz, “Further results in the fast estimation of a single frequency,” *IEEE Transactions on Communications*, vol. 42, no. 234, pp. 862–864, Apr. 1994.

[7] A. Viterbi, “Nonlinear estimation of PSK–modulated carrier phase with application to burst digital transmission,” *IEEE Transactions on Information Theory*, vol. 29, no. 4, pp. 543–551, 1983.

[8] “Cisco visual networking index: Forecast and methodology, 2011–2016,” Cisco I, Tech. Rep., 2012.

[9] D. Evans, "The internet of things: How the next evolution of the internet is changing everything," *CISCO white paper*, vol. 1, p. 14, 2011.

[10] W. Vereecken, W. Van Heddeghem, M. Deruyck, B. Puype, B. Lannoo, W. Joseph, D. Colle, L. Martens, and P. Demeester, "Power consumption in telecommunication networks: overview and reduction strategies," *IEEE Communications Magazine*, vol. 49, no. 6, pp. 62–69, 2011.

[11] M. Webb *et al.*, "Smart 2020: Enabling the low carbon economy in the information age," *The Climate Group. London*, vol. 1, no. 1, pp. 1–1, 2008.

[12] A. Fehske, G. Fettweis, J. Malmodin, and G. Biczók, "The global footprint of mobile communications: The ecological and economic perspective," *IEEE Communications Magazine*, vol. 49, no. 8, pp. 55–62, 2011.

[13] E. Oh, B. Krishnamachari, X. Liu, and Z. Niu, "Toward dynamic energy–efficient operation of cellular network infrastructure," *IEEE Communications Magazine*, vol. 49, no. 6, pp. 56–61, 2011.

[14] G. Fettweis and E. Zimmermann, "ICT energy consumption-trends and challenges," in *11th International Symposium on Wireless Personal Multimedia Communications*, vol. 2, no. 4, 2008, p. 6.

[15] J. Baliga, R. Ayre, W. V. Sorin, K. Hinton, and R. S. Tucker, "Energy consumption in access networks," in *Optical Fiber Communication Conference*. Optical Society of America, 2008, p. OThT6.

[16] J. Baliga, R. Ayre, K. Hinton, and R. S. Tucker, "Energy consumption in wired and wireless access networks," *IEEE Communications Magazine*, vol. 49, no. 6, pp. 70–77, 2011.

[17] J. Baliga, R. W. Ayre, K. Hinton, and R. S. Tucker, "Green cloud computing: Balancing energy in processing, storage, and transport," *Proceedings of the IEEE*, vol. 99, no. 1, pp. 149–167, 2011.

[18] C. Han, T. Harrold, S. Armour, I. Krikidis, S. Videv, P. M. Grant, H. Haas, J. S. Thompson, I. Ku, C.-X. Wang *et al.*, "Green radio: radio techniques to enable energy–efficient wireless networks," *IEEE Communications Magazine*, vol. 49, no. 6, pp. 46–54, 2011.

[19] S. Aleksić and A. Lovrić, "Power consumption of wired access network technologies," in *IEEE 7th International Symposium on Communication Systems Networks and Digital Signal Processing (CSNDSP 2010)*, 2010, pp. 147–151.

[20] Y. Chen, S. Zhang, S. Xu, and G. Li, "Fundamental trade–offs on green wireless networks," *IEEE Communications Magazine*, vol. 49, no. 6, pp. 30–37, June 2011.

[21] Z. Hasan, H. Boostanimehr, and V. Bhargava, "Green cellular networks: A survey, some research issues and challenges," *IEEE Communications Surveys Tutorials*, vol. 13, no. 4, pp. 524 –540, quarter 2011.

[22] J. Zyren and W. McCoy, "Overview of the 3GPP long term evolution physical layer," *Freescale Semiconductor, Inc., white paper*, 2007.

[23] D. Kilper, "Energy efficient networks," in *Optical Fiber Communication Conference*. Optical Society of America, 2011, p. OWI5.

[24] R. Tafazolli, "EARTH–energy aware radio and network technologies," *Proc. Next Generation Wireless Green Networks Wksp*, 2009.

[25] GreenTouch. GreenTouch consortium. [Online]. Available: http://http://www.greentouch.org/

[26] C. E. Shannon, "The zero error capacity of a noisy channel," *IRE Transactions on Information Theory,*, vol. 2, no. 3, pp. 8–19, 1956.

[27] V. Chandrasekhar, J. Andrews, and A. Gatherer, "Femtocell networks: a survey," *IEEE Communications Magazine*, vol. 46, no. 9, pp. 59–67, 2008.

[28] Z. Hasan, H. Boostanimehr, and V. K. Bhargava, "Green cellular networks: A survey, some research issues and challenges," *IEEE Communications Surveys & Tutorials*, vol. 13, no. 4, pp. 524–540, 2011.

[29] G. Y. Li, Z. Xu, C. Xiong, C. Yang, S. Zhang, Y. Chen, and S. Xu, "Energy–efficient wireless communications: tutorial, survey, and open issues," *IEEE Wireless Communications*, vol. 18, no. 6, pp. 28–35, 2011.

[30] D. Feng, C. Jiang, G. Lim, L. J. Cimini, G. Feng, and G. Y. Li, "A survey of energy–efficient wireless communications," *IEEE Communications Surveys & Tutorials*, vol. 15, no. 1, pp. 167–178, 2013.

[31] F. Meshkati, H. V. Poor, and S. C. Schwartz, "Energy–efficient resource allocation in wireless networks," *IEEE Signal Processing Magazine*, vol. 24, no. 3, pp. 58–68, 2007.

[32] W. Stark, H. Wang, A. Worthen, S. Lafortune, and D. Teneketzis, "Low–energy wireless communication network design," *IEEE Wireless Communications*, vol. 9, no. 4, pp. 60–72, 2002.

[33] S. Cui, A. J. Goldsmith, and A. Bahai, "Energy–constrained modulation optimization," *IEEE Transactions on Wireless Communications*, vol. 4, no. 5, pp. 2349–2360, 2005.

[34] Y. Li, B. Bakkaloglu, and C. Chakrabarti, "A system level energy model and energy–quality evaluation for integrated transceiver front–ends," *IEEE Transactions of Very Large Scale Integration Systems*, vol. 15, no. 1, pp. 90–103, 2007.

[35] C. Desset and A. Fort, "Selection of channel coding for low–power wireless systems," in *IEEE Vehicular Technology Conference*, vol. 3, 2003, pp. 1920–1924.

[36] S. L. Howard, C. Schlegel, and K. Iniewski, "Error control coding in low–power wireless sensor networks: When is ECC energy–efficient?" *EURASIP Journal on Wireless Communications and Networking*, pp. 1–14, 2006.

[37] P. Grover, A. Sahai, and J.-H. Park, "Simple models for power optimization across transmission, equalization and decoding," in *European Signal Processing Conference (EUSIPO)*, 2011.

[38] P. Grover, K. Woyach, and A. Sahai, "Towards a communication–theoretic understanding of system–level power consumption," *IEEE Journal on Selected Areas in Communications*, vol. 29, no. 8, pp. 1744–1755, 2011.

[39] P. Grover, A. Goldsmith, and A. Sahai, "Fundamental limits on the power consumption of encoding and decoding," in *EEE International Symposium on Information Theory Proceedings (ISIT 2012)*, 2012, pp. 2716–2720.

[40] C. D. Thompson, "A complexity theory for VLSI," Ph.D. dissertation, Carnegie-Mellon University, 1980.

[41] F. Kienle, N. Wehn, and H. Meyr, "On complexity, energy–and implementation–efficiency of channel decoders," *IEEE Transactions on Communications*, vol. 59, no. 12, pp. 3301–3310, 2011.

[42] C. Xiong, G. Y. Li, Y. Liu, and S. Xu, "When and how should decoding power be considered for achieving high energy efficiency?" in *IEEE 23rd International Symposium on Personal Indoor and Mobile Radio Communications (PIMRC 2012)*, 2012, pp. 2427–2431.

[43] B. S. G. Pillai, B. Sedighi, K. Guan, N. P. Anthapadmanabhan, W. Shieh, K. J. Hinton, and R. S. Tucker, "End–to–end energy modeling and analysis of long–haul coherent transmission systems," *IEEE Journal of Lightwave Technology*, vol. 32, no. 18, pp. 3093–3111, 2014.

[44] S. Verdú, "Spectral efficiency in the wideband regime," *IEEE Transactions on Information Theory*, vol. 48, no. 6, pp. 1319–1343, 2002.

[45] M. Rice, *Digital communications: a discrete–time approach*. Pearson Education India, 2009.

[46] C. R. Johnson Jr, W. A. Sethares, and A. G. Klein, *Software receiver design: build your own digital communication system in five easy steps*. Cambridge University Press, 2011.

[47] D. Falconer, S. L. Ariyavisitakul, A. Benyamin-Seeyar, and B. Eidson, "Frequency domain equalization for single–carrier broadband wireless systems," *IEEE Communications Magazine*, vol. 40, no. 4, pp. 58–66, 2002.

[48] T. S. Rappaport *et al.*, *Wireless communications: principles and practice*. prentice hall PTR New Jersey, 1996, vol. 2.

[49] C. Myer, M. Moeneclay, and S. Fechtel, *Digital communication receivers*. Wiley series in telecommunications and signal processing. Wiley, 1995.

[50] J. Proakis and M. Salehi, *Digital Communications*. McGraw-Hill, 2007.

[51] U. Mengali, *Synchronization techniques for digital receivers*. New York: Plenum Press, 1997.

[52] F. M. Gardner, "Hangup in phase–lock loops," *IEEE Transactions on Communications*, vol. 25, no. 10, pp. 1210–1214, 1977.

[53] M. Andronico, S. Casale, and A. L. Corte, "A feed–forward technique for initial reference parameter estimation in burst mode PSK demodulation," *European transactions on telecommunications*, vol. 9, no. 6, pp. 537–549, 1998.

[54] F. J. Harris and M. Rice, "Multirate digital filters for symbol timing synchronization in software defined radios," *IEEE Journal on Selected Areas in Communications*, vol. 19, no. 12, pp. 2346–2357, 2001.

[55] F. M. Gardner, "Interpolation in digital modems. I. fundamentals," *IEEE Transactions on Communications*, vol. 41, no. 3, pp. 501–507, 1993.

[56] W. C. Lindsey and M. K. Simon, *Telecommunication systems engineering*. Courier Corporation, 1973.

[57] F. M. Gardner, "A BPSK/QPSK timing–error detector for sampled receivers," *IEEE Transactions on Communications*, vol. 34, pp. 423–429, 1986.

[58] K. Mueller and M. Muller, "Timing recovery in digital synchronous data receivers," *IEEE Transactions on Communications*, vol. 24, no. 5, pp. 516–531, 1976.

[59] M. Morelli, A. D'Andrea, and U. Mengali, "Feedforward ML–based timing estimation with PSK signals," *IEEE Communications Letters*, vol. 1, no. 3, pp. 80–82, 1997.

[60] S. J. Lee, "A new non–data–aided feedforward symbol timing estimator using two samples per symbol," *IEEE Communications Letters*, vol. 6, no. 5, pp. 205–207, 2002.

[61] K. Bucket and M. Moeneclaey, "Effect of random carrier phase and timing errors on the detection of narrowband M–PSK and bandlimited DS/SS M–PSK signals," *IEEE Transactions on Communications*, vol. 43, no. 234, pp. 1260–1263, 1995.

[62] F. M. Gardner, *Phaselock techniques*. John Wiley & Sons, 2005.

[63] B. C. Lovell and R. C. Williamson, "The statistical performance of some instantaneous frequency estimators," *IEEE Transactions on Signal Processing*, vol. 40, no. 7, pp. 1708–1723, 1992.

[64] U. Mengali and M. Morelli, "Data–aided frequency estimation for burst digital transmission," *IEEE Transactions on Communications*, vol. 45, no. 1, pp. 23–25, 1997.

[65] J. M. Palmer and M. Rice, "Frequency estimation using multiple disjoint pilot blocks in burst–mode communications," in *IEEE Global Telecommunications Conference (GLOBECOM 2008)*, 2008, pp. 1–5.

[66] F. Classen and H. Meyr, "Two frequency estimation schemes operating independently of timing information," in *IEEE Global Telecommunications Conference (GLOBECOM'93)*, 1993, pp. 1996–2000.

[67] A. A. D'Amico, A. N. D'Andrea, and R. Regiannini, "Efficient non–data–aided carrier and clock recovery for satellite DVB at very low signal–to–noise ratios," *IEEE Journal on Selected Areas in Communications*, vol. 19, no. 12, pp. 2320–2330, 2001.

[68] W. N. HE *et al.*, *CMOS VLSI Design: A Circuits And Systems Perspective, 3/E*. Pearson Education India, 2006.

[69] K. K. Parhi, *VLSI digital signal processing systems: design and implementation*. John Wiley & Sons, 2007.

[70] A. P. Chandrakasan, S. Sheng, and R. W. Brodersen, "Low–power CMOS digital design," *IEICE Transactions on Electronics*, vol. 75, no. 4, pp. 371–382, 1992.

[71] T. Lengauer and K. Mehlhorn, "On the complexity of VLSI computations," in *VLSI systems and computations*. Springer, 1981, pp. 89–99.

[72] L. Biard and D. Noguet, "Reed–solomon codes for low power communications," *Journal of Communications*, vol. 3, no. 2, 2008.

[73] F. Bruekers, "Symmetry and efficiency in complex FIR filters," *Philips Research Laboratories, Eindhoven*, 2009.

[74] Xlinix. (2014) Xilinx LogiCORE complex mulitplier product specification. [Online]. Available: http://www.xilinx.com/support/documentation/ip_documentation/cmpy/v6_0/pg104-cmpy.pdf

[75] R. Andraka, "A survey of CORDIC algorithms for FPGA based computers," in *ACM/SIGDA sixth international symposium on Field programmable gate arrays*. ACM, 1998, pp. 191–200.

[76] D. J. Frank, R. H. Dennard, E. Nowak, P. M. Solomon, Y. Taur, and H.-S. P. Wong, "Device scaling limits of si mosfets and their application dependencies," *Proceedings of the IEEE*, vol. 89, no. 3, pp. 259–288, 2001.

[77] L. Erup, F. M. Gardner, and R. A. Harris, "Interpolation in digital modems. II. implementation and performance," *IEEE Transactions on Communications*, vol. 41, no. 6, pp. 998–1008, 1993.

[78] A. V. Oppenheim, R. W. Schafer, J. R. Buck *et al.*, *Discrete–time signal processing*. Prentice-hall Englewood Cliffs, 1989, vol. 2.

[79] "Hyperconnectivity and the approaching zettabyte era," Cisco Visual Networking Index, Tech. Rep., 2010.

[80] C. Desset, B. Debaillie, V. Giannini, A. Fehske, G. Auer, H. Holtkamp, W. Wajda, D. Sabella, F. Richter, M. J. Gonzalez *et al.*, "Flexible power modeling of LTE base

stations," in *IEEE Wireless Communications and Networking Conference (WCNC)*, 2012, pp. 2858–2862.

[81] S. Zhang, Y. Chen, and S. Xu, "Improving energy efficiency through bandwidth, power, and adaptive modulation," in *IEEE Vehicular Technology Conference*, Sept 2010, pp. 1–5.

[82] G. He, S. Zhang, Y. Chen, and S. Xu, "Energy efficiency and deployment efficiency tradeoff for heterogeneous wireless networks," in *IEEE Global Telecommunications Conference*, Dec 2012, pp. 3189–3194.

[83] S. Zhang, G. He, Y. Chen, and S. Xu, "On the bandwidth–power tradeoff for heterogeneous networks with site sleeping and inter–cell interference," in *IEEE Wireless Communications and Networking Conference*, April 2013, pp. 3794–3799.

[84] F. Rosas, G. Brante, R. Demo Souza, and C. Oberli, "Optimizing the code rate for achieving energy-efficient wireless communications," in *IEEE Wireless Communications and Networking Conference (WCNC)*, 2014, pp. 775–780.

[85] S. Mirabbasi and K. Martin, "Classical and modern receiver architectures," *IEEE Communications Magazine*, vol. 38, no. 11, pp. 132–139, 2000.

[86] M. V. Clark, "Adaptive frequency–domain equalization and diversity combining for broadband wireless communications," *IEEE Journal on Selected Areas in Communications*, vol. 16, no. 8, pp. 1385–1395, 1998.

[87] M. Morelli, L. Sanguinetti, and U. Mengali, "Channel estimation for adaptive frequency–domain equalization," *IEEE Transactions on Wireless Communications*, vol. 4, no. 5, pp. 2508–2518, 2005.

[88] T. K. Moon, "Error correction coding," *Mathematical Methods and Algorithms. Jhon Wiley and Son*, 2005.

[89] D. Kudavithana, Q. Chaudhari, B. Krongold, and J. Evans, "On the energy efficiency of coherent communication in multipath fading channels," in *IEEE Global*

Telecommunications Conference (Globecom 2014) - 2nd Workshop on Green Broadband access: energy efficient wireless and wired network solutions, Dec. 2014.

[90] S. Myung, K. Yang, and J. Kim, "Quasi–cyclic LDPC codes for fast encoding," *IEEE Transactions on Information Theory*, vol. 51, no. 8, pp. 2894–2901, 2005.

[91] J. Chen, A. Dholakia, E. Eleftheriou, M. P. Fossorier, and X.-Y. Hu, "Reduced–complexity decoding of LDPC codes," *IEEE Transactions on Communications*, vol. 53, no. 8, pp. 1288–1299, 2005.

[92] C. Garuda and M. Ismail, "A multiband CMOS RF front–end for 4G WiMAX and WLAN applications," in *IEEE International Symposium on Circuits and Systems (ISCAS 2006)*, 2006, pp. 4–pp.

[93] Y. Ke, J. Craninckx, and G. Gielen, "A design approach for power–optimized fully reconfigurable A/D converter for 4G radios," *IEEE Transactions on Circuits and Systems*, vol. 55, no. 3, pp. 229–233, 2008.

[94] A. Liscidini, M. Brandolini, D. Sanzogni, and R. Castello, "A 0.13 μm CMOS front–end, for DCS1800/UMTS/802.11 bg with multiband positive feedback low–noise amplifier," *IEEE Journal of Solid-State Circuits*, vol. 41, no. 4, pp. 981–989, 2006.

[95] S. Rodriguez, A. Rusu, and M. Ismail, "WiMAX/LTE receiver front–end in 90nm CMOS," in *IEEE International Symposium on Circuits and Systems (ISCAS 2009)*, 2009, pp. 1036–1039.

[96] D. Jakonis, K. Folkesson, J. Dbrowski, P. Eriksson, and C. Svensson, "A 2.4–GHz rf sampling receiver front–end in 0.18–μm CMOS," *IEEE Journal of Solid-State Circuits*, vol. 40, no. 6, pp. 1265–1277, 2005.

[97] S. Soldà, M. Caruso, A. Bevilacqua, A. Gerosa, D. Vogrig, and A. Neviani, "A 5 Mb/s UWB–IR transceiver front–end for wireless sensor networks in 0.13 CMOS," *IEEE Journal of Solid-State Circuits*, vol. 46, no. 7, pp. 1636–1647, 2011.

[98] H. Samavati, H. R. Rategh, and T. H. Lee, "A 5–GHz CMOS wireless LAN receiver front end," *IEEE Journal of Solid-State Circuits*, vol. 35, no. 5, pp. 765–772, 2000.

[99] H. Seo, I. Choi, C. Park, J. Yoon, and B. Kim, “A wideband digital RF receiver front–end employing a new discrete–time filter for m–WiMAX,” *IEEE Journal of Solid-State Circuits*, vol. 47, no. 5, pp. 1165–1174, 2012.

[100] M. Demirkan, S. P. Bruss, and R. R. Spencer, “Design of wide tuning–range CMOS VCOs using switched coupled–inductors,” *IEEE Journal of Solid-State Circuits*, vol. 43, no. 5, pp. 1156–1163, 2008.

[101] R. B. Staszewski, S. Vemulapalli, P. Vallur, J. Wallberg, and P. T. Balsara, “1.3 V 20 ps time–to–digital converter for frequency synthesis in 90-nm CMOS,” *IEEE Transactions on Circuits and Systems*, vol. 53, no. 3, pp. 220–224, 2006.

[102] S. Hyvonen, K. Bhatia, and E. Rosenbaum, “An ESD–protected, 2.45/5.25–GHz dual-band CMOS LNA with series LC loads and a 0.5 V supply,” in *IEEE Radio Frequency integrated Circuits (RFIC) Symposium*, 2005, pp. 43–46.

[103] N. Ghittori, A. Vigna, P. Malcovati, S. D’Amico, and A. Baschirotto, “1.2–V low–power multi–mode DAC+ filter blocks for reconfigurable (WLAN/UMTS, WLAN/Bluetooth) transmitters,” *IEEE Journal of Solid-State Circuits*, vol. 41, no. 9, pp. 1970–1982, 2006.

[104] GreenTouch, *Mobile Communication WG,Architecture Doc 2: Reference scenarios,*, 2013.

[105] J. N. Laneman, D. N. Tse, and G. W. Wornell, “Cooperative diversity in wireless networks: Efficient protocols and outage behavior,” *IEEE Transactions on Information Theory*, vol. 50, no. 12, pp. 3062–3080, 2004.

[106] J. Boyer, D. D. Falconer, and H. Yanikomeroglu, “Multihop diversity in wireless relaying channels,” *IEEE Transactions on Communications*, vol. 52, no. 10, pp. 1820–1830, 2004.

[107] K. R. Liu, *Cooperative communications and networking*. Cambridge university press, 2009.

[108] T. Wang, A. Cano, G. B. Giannakis, and J. N. Laneman, "High–performance cooperative demodulation with decode–and–forward relays," *IEEE Transactions on Communications*, vol. 55, no. 7, pp. 1427–1438, 2007.

[109] D. Brennan, "Linear diversity combining techniques," *IEEE Proceedings of the IRE*, vol. 47, no. 6, pp. 1075–1102, 1959.

[110] G. Farhadi and N. C. Beaulieu, "Power–optimized amplify–and–forward multi–hop relaying systems," *IEEE Transactions on Wireless Communications*, vol. 8, no. 9, pp. 4634–4643, 2009.

[111] K. Vardhe, D. Reynolds, and B. D. Woerner, "Joint power allocation and relay selection for multiuser cooperative communication," *IEEE Transactions on Wireless Communications*, vol. 9, no. 4, pp. 1255–1260, 2010.

[112] X. J. Zhang and Y. Gong, "Joint power allocation and relay positioning in multi–relay cooperative systems," *IET Communications*, vol. 3, no. 10, pp. 1683–1692, 2009.

[113] H. V. Zhao and W. Su, "Cooperative wireless multicast: performance analysis and power/location optimization," *IEEE Transactions on Wireless Communications*, vol. 9, no. 6, pp. 2088–2100, 2010.

[114] A. P. T. Lau and S. Cui, "Joint power minimization in wireless relay channels," *IEEE Transactions on Wireless Communications*, vol. 6, no. 8, pp. 2820–2824, 2007.

[115] W. Cho, R. Cao, and L. Yang, "Optimum resource allocation for amplify–and–forward relay networks with differential modulation," *IEEE Transactions on Signal Processing*, vol. 56, no. 11, pp. 5680–5691, 2008.

[116] D. Kudavithana, Q. Chaudhari, and B. Krongold, "On the energy-efficiency of point-to-point wireless transmission," *Elsevier Physical Commmunications*, 2015, submitted.

[117] O. Waqar, M. A. Imran, M. Dianati, and R. Tafazolli, "Energy consumption analysis and optimization of BER–constrained amplify–and–forward relay networks," *IEEE Transactions on Vehicular Technology*, vol. 63, no. 3, pp. 1256–1269, 2014.

[118] M. T. Kakitani, G. Brante, R. D. Souza, and A. Munaretto, "Comparing the energy efficiency of single–hop, multi–hop and incremental decode–and-forward in multi–relay wireless sensor networks," in *IEEE 22nd International Symposium on Personal Indoor and Mobile Radio Communications (PIMRC 2011)*, 2011, pp. 970–974.

[119] Q. Chen and M. C. Gursoy, "Energy efficiency analysis in amplify–and–forward and decode-and-forward cooperative networks," in *IEEE Wireless Communications and Networking Conference (WCNC 2010)*, 2010, pp. 1–6.

[120] R. Madan, N. B. Mehta, A. F. Molisch, and J. Zhang, "Energy–efficient cooperative relaying over fading channels with simple relay selection," *IEEE Transactions on Wireless Communications*, vol. 7, no. 8, pp. 3013–3025, 2008.

[121] Y. Chen, S. Zhang, and S. Xu, "Characterizing energy efficiency and deployment efficiency relations for green architecture design," in *IEEE International Conference on Communications Workshops (ICC 2010)*, 2010, pp. 1–5.

[122] B. Debaillie, C. Desset, and F. Louagie, "A flexible and future–proof power model for cellular base stations," in *IEEE Vehicular Technology Conference Spring (VTC-Spring)*, 2014.

[123] E. Kaymaksut and P. Reynaert, "Transformer–based uneven doherty power amplifier in 90 nm CMOS for WLAN applications," *IEEE Journal of Solid-State Circuits*, vol. 47, no. 7, pp. 1659–1671, 2012.

[124] A. Afsahi, A. Behzad, V. Magoon, and L. E. Larson, "Linearized dual–band power amplifiers with integrated baluns in 65 nm CMOS for a 2x2 802.11 n MIMO WLAN SoC," *IEEE Journal of Solid-State Circuits*, vol. 45, no. 5, pp. 955–966, 2010.

[125] Y. Li, J. Lopez, C. Schecht, R. Wu, and D. Y. Lie, "Design of high efficiency monolithic power amplifier with envelope–tracking and transistor resizing for broadband wireless applications," *IEEE Journal of Solid-State Circuits*, vol. 47, no. 9, pp. 2007–2018, 2012.

[126] S. Boyd and L. Vandenberghe, *Convex optimization*. Cambridge university press, 2004.

[127] E. W. Weisstein, “Lambert w-function. from mathworlda wolfram web resource,” 2004.

[128] M. K. Simon and M.-S. Alouini, “A unified approach to the performance analysis of digital communication over generalized fading channels,” *Proceedings of the IEEE*, vol. 86, no. 9, pp. 1860–1877, 1998.

[129] K. Schwieger and G. Fettweis, “Power and energy consumption for multi–hop protocols: A sensor network point of view,” in *International Workshop on Wireless Ad-hoc Network*, 2005.

[130] C. Conne and I.-M. Kim, “Outage probability of multi–hop amplify–and–forward relay systems,” *IEEE Transactions on Wireless Communications*, vol. 9, no. 3, pp. 1139–1149, 2010.

[131] S. S. Ikki and S. Aïssa, “Multihop wireless relaying systems in the presence of cochannel interferences: Performance analysis and design optimization,” *IEEE Transactions on Vehicular Technology*, vol. 61, no. 2, pp. 566–573, 2012.

[132] M. K. Simon and M.-S. Alouini, *Digital communication over fading channels*. John Wiley & Sons, 2005, vol. 95.

[133] D. J. Grabiner, “Descartes’ rule of signs: Another construction,” *American Mathematical Monthly*, pp. 854–856, 1999.

[134] PlanetMath. (1999) Quartic formula. [Online]. Available: http://planetmath.org/QuarticFormula

[135] L. Atzori, A. Iera, and G. Morabito, “The internet of things: A survey,” *Elsevier Computer networks*, vol. 54, no. 15, pp. 2787–2805, 2010.

[136] M. Zorzi, A. Gluhak, S. Lange, and A. Bassi, “From today’s intranet of things to a future internet of things: a wireless–and mobility–related view,” *IEEE Wireless Communications*, vol. 17, no. 6, pp. 44–51, 2010.

[137] J. Gubbi, R. Buyya, S. Marusic, and M. Palaniswami, "Internet of Things (IoT): A vision, architectural elements, and future directions," *Elsevier Future Generation Computer Systems*, vol. 29, no. 7, pp. 1645–1660, 2013.

[138] Q. Zhu, R. Wang, Q. Chen, Y. Liu, and W. Qin, "IoT gateway: Bridgingwireless sensor networks into internet of things," in *IEEE/IFIP 8th International Conference on Embedded and Ubiquitous Computing (EUC)*, 2010, pp. 347–352.

[139] A. P. Bianzino, C. Chaudet, D. Rossi, and J.-L. Rougier, "A survey of green networking research," *IEEE Communications Surveys & Tutorials*, vol. 14, no. 1, pp. 3–20, 2012.

[140] H. Holtkamp, G. Auer, V. Giannini, and H. Haas, "A parameterized base station power model," *IEEE Communications Letters*, vol. 17, no. 11, pp. 2033–2035, 2013.

[141] N. Ristanovic, J.-Y. L. Boudec, A. Chaintreau, and V. Erramilli, "Energy efficient offloading of 3G networks," in *IEEE 8th International Conference on Mobile Adhoc and Sensor Systems (MASS)*, 2011, pp. 202–211.

[142] F. Ingelrest, D. Simplot-Ryl, and I. Stojmenovic, "Optimal transmission radius for energy efficient broadcasting protocols in ad hoc and sensor networks," *IEEE Transactions on Parallel and Distributed Systems*, vol. 17, no. 6, pp. 536–547, 2006.

[143] A. Kansal, J. Hsu, S. Zahedi, and M. B. Srivastava, "Power management in energy harvesting sensor networks," *ACM Transactions on Embedded Computing Systems (TECS)*, vol. 6, no. 4, p. 32, 2007.

[144] X. Lu, P. Wang, D. Niyato, D. I. Kim, and Z. Han, "Wireless networks with rf energy harvesting: A contemporary survey," *IEEE Communications Surveys & Tutorials*, vol. 17, no. 2, pp. 757–789, 2015.

Author/s:
Kudavithana, Dinuka

Title:
Energy efficient wireless system design

Date:
2015

Persistent Link:
http://hdl.handle.net/11343/91674

File Description:
Energy Efficient Wireless System Design